University of Windsor
Scholarship at UWindsor

Electronic Theses and Dissertations

Theses, Dissertations, and Major Papers

1989

A Charge Simulation Based Computer-Aided Design Implementation of High Voltage Systems Modelling

Hanafy Mahmoud Ismail
University of Windsor

Follow this and additional works at: https://scholar.uwindsor.ca/etd

Part of the Electrical and Computer Engineering Commons

Recommended Citation

A CHARGE SIMULATION BASED
COMPUTER-AIDED DESIGN IMPLEMENTATION
OF HIGH VOLTAGE SYSTEMS MODELLING

BY

HANAFY MAHMOUD ISMAIL

A CHARGE SIMULATION BASED COMPUTER-AIDED DESIGN IMPLEMENTATION

OF HIGH VOLTAGE SYSTEMS MODELLING

by

HANAFY MAHMOUD ISMAIL

A Dissertation
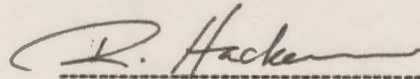
submitted to the
Faculty of Graduate Studies and Research
through the Department of
Electrical Engineering in Partial Fulfillment
of the requirements for the degree
of Doctorate of Philosophy at
the University of Windsor

Windsor, Ontario, Canada
1989

ACB 8371

APPROVED BY :

Prof. P. H. Alexander

Dr. R. Hackam

Dr. R. J. Harrington

Dr. C. MacInnis, Dean of Eng.

Dr. A. C. Smith

Dr. A. Watson

DEDICATION

TO MY PARENTS, MY WIFE HODA AND MY

LOVELY DAUGHTER ANGIE

ABSTRACT

A Charge Simulation based Computer-Aided Design (CAD) Package which facilitates the development of a charge simulation model for high voltage (HV) systems consisting of a number of electrodes and one or two dielectric regions has been developed. The package calculates the potential and electric field distributions for practical systems. It avoids the necessity for creating individual programs for each system studied by allowing the geometry to be specified using a minimum of entered data.

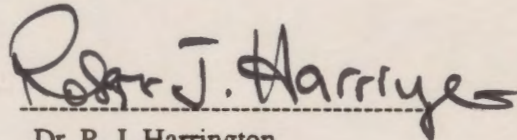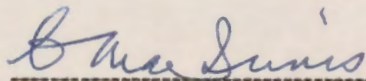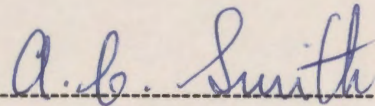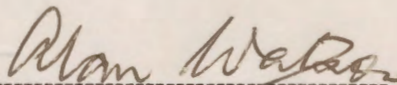The application of the CAD package to several electrode systems which have analytical solutions is presented. Good agreement, generally within 0.5% was found between the fields produced by the Charge Simulation Method (CSM) and the analytical results.

A study of the effect of several parameters controlling the charge simulation model is conducted to determine their optimum ranges. Recommendations for these values are made. It is found that for best simulation, discontinuities in alignment of the simulating charges should be avoided.

The rod-plane gap configuration and a HV shielding system are modelled and results are compared with existing literature values. Some simulation quality measures which have not previously been published are given.

The computation of fields in a sphere/slab arrangement is conducted and results are presented for a wide range of permittivity ratios and gap spacings. It is found that the maximum electric field strength occurs at the triple point for high dielectric constant unrecessed slabs, and away from the axis for low dielectric constant slabs.

Two high voltage systems which have not been analyzed before using the CSM are studied. One is a rotationally symmetrical triggering electrode configuration. The other is a 22 - shed

polymer insulator with a grading ring included to reduce the non-linearity of the voltage distribution. In the triggering electrode system it is found that both the main gap distance and the pilot gap distance affect the potential and the field distributions along the axial main gap line. The location of the maximum electric field changes with both gaps and always occurs on the hemispherical part of the triggering electrode, but not necessarily at the tip.

Optimum values for the location and size of the grading ring are determined for the polymer insulator.

The simulations of additional complicated three-dimensional field problems with and without axial symmetry using the CSM are presented. A tilted rod-electrode versus ground plane and a hemispherical capped rod electrode versus a grounded plane with another offset hemispherically capped electrode embedded are modelled. A detailed examination of the field distribution for a triggering high voltage system without axial symmetry is also presented.

ACKNOWLEDGEMENTS

ABBREVIATIONS AND NOTATION

Abbreviations:

----

cm	centimeter
Diff	Difference
Discr	Discrepancy
EHV	Extra high voltage
HV	High voltage
kV	Kilo volt
LV	Low voltage
Max	Maximum
Min	Minimum
mm	millimeter
MPE	Maximum potential error
MTFD	Maximum tangential field difference
MV	Mega volt
Pot	Potential
pu	Per unit
Sym	Symmetric
Tang	Tangential
UHV	Ultra high voltage
Unsym	Unsymmetric
#	Number

Notation:

A_g	Cross section radius of the grading ring
a_x, a_y, a_z	Unit vectors in the x, y and z directions
a_i, b_i, c_i, d_i	Coefficients of a cubic spline function
[a,b]	Interval for the Chebyshev distribution of points
B_a	Assignment factor
D	Diameter of the electrode, m
D_a	Distance between two successive contour points, m
E	Total electric field intensity, V/m
E_i	Electric field component at the i-th point, V/m
E'	Normalized total electric field
E_n	Normal electric field, V/m
E_t	Tangential electric field, V/m
E_{av}	Average electric field, V/m
E'_n	Normalized normal field
E'_t	Normalized tangential field
E_{max}	Maximum electric field, V/m
E'_{max}	Normalized maximum electric field
F_{ij}	Field coefficient factor
g	Gap separation between two spheres or gap distance, m
G	Gap distance, m
G/r	Gap spacing/corner radius
H_g	Height of the grading ring from the HV electrode, m
i	Index used for positioning contour points
j	Index used for positioning charges
l	Distance from the high voltage electrode, m

l'	Normalized gap distance measured from the tip of the triggering electrode
n	Total number of contour points or charges
n_b	Number of boundary points on the dielectric interface
n_c	Number of charges on the curved portion of the standard electrode
n_e	Number of charges on the electrodes
n_{ea}	Number of charges on the air side
n_{ed}	Number of charges on the dielectric side
n/L	Number of charges per unit length
P_{ij}	Potential coefficient at location i due to a charge located at position j
Q	Total charge on the isolated sphere, C
Q_j	Charge located at position j, C
r	Radius of the sphere or corner radius, m
R	Radius of the electrode, m
R/r	Ratio of the the electrode radius to corner radius
R_g	Mean radius of the grading ring, m
R_o	Radius of the isolated sphere, m
R_t	Radius of the trigger electrode, m
r'	Distance from the isolated sphere center to the point where the potential is to be calculated, m
r_1	Radius of the high voltage sphere, m
r_2	Radius of the low voltage sphere, m
s	Distance between the centers of the spheres, m
S_a	Distance between a contour point and a charge, m
S(x)	A cubic spline function
S'(x)	First derivative of S(x)
S''(x)	Second derivative of S(x)
T_x , T_y , T_z	Translation distances from the coordinate axes, m

V	Potential, V
V_c	Calculated potential, V
V_d	Potential difference between two spheres, V
V_e	Electrode or contour points potential, V
V_h	Potential of the triggering system HV electrode, V
V_i	Potential at the i-th contour point, V
V_{ij}	Computed potential at the i-th contour point due to the j-th charge, V
V_l	Potential of the triggering system LV electrode, V
V_o	Potential of the isolated sphere, V
V_t	Triggering electrode potential, V
V'	Normalized potential
V_1	Potential of the high voltage electrode in the non-axial triggering system, V
V_2	Potential of the low voltage electrode in the non-axial triggering system, V
(x,y,z)	Initial position of a point or a charge
(x',y',z')	Final position of a point or a charge
ρ	Volume charge density, C/m_3
ε	Permittivity of the medium, F/m
∇	Gradient operator
ε_r	Relative dielectric constant of the material
δV	Error in potential
θ	Rotation angle in degrees
$\%$	Percentage
$\varepsilon_2 / \varepsilon_1$	Permittivity ratio of the dielectric slab to the surrounding medium
ϕ	Potential, V
ϕ'	Normalized potential

TABLE OF CONTENTS

TABLE OF CONTENTS

Chapter I

INTRODUCTION

1.1 Preamble

A knowledge of the electric field distribution is important in the design of high voltage system components. The predetermination of discharge voltages needs an accurate knowledge of the electric field in some special regions (normally those near the electrodes) of the configuration of interest.

In the study of corona and electrical breakdown of gases, the hemispherical capped rod-plane is sometimes used to investigate that phenomena due to the concentration of breakdown ionization at the rod tip [1]. A detailed investigation of the breakdown phenomenon of gases requires the calculation of the electric field distribution with reasonable accuracy in the entire interelectrode space.

In response to an increasing demand for electrical energy, operating transmission voltages have increased considerably over the last two decades. Effective designs at high voltages with minimum corona losses are possible only through an understanding of the properties of insulating materials and knowledge of electric fields and methods of reducing electric stress [2].

In the design of high voltage transmission lines, the knowledge of the electric field at the conductor surface as well as in the interelectrode space is essential to calculate the corona-onset voltage, corona loss and radio interference [3].

Insulating spacers are used to support high voltage conductors in vacuum and in gas insulated systems. It is well established that the electrical insulation of a vacuum gap bridged by a solid insulator fails at a lower voltage than the unbridged gap, and that the insulation failure occurs by a flashover across the insulator surface [4,5,6]. Usually the surface flashover of the

insulator is the limiting factor in the operation of the vacuum and gaseous insulated equipment. Therefore, it is useful to know the electric field and potential distribution along the insulator-vacuum (or gas) interface for determining the mechanisms leading to the flashover and their dependence on the field strength. The determination of the electric field distribution also aims at achieving better designs of optimum shapes of insulators from the viewpoint of achieving higher withstand voltages [7]. A high electric field, say at a poorly designed triple junction, may initiate electrons from the cathode at much lower applied voltage than if the geometry produced a lower electric field. The electrons emitted from the cathode junction may lead to a flashover of the gap when increasing the applied voltage [4].

The calculation of electric fields requires the solution of Laplace's and Poisson's equations with the boundary conditions satisfied [8]. The analytical solution of Laplace's equation can only be obtained for relatively simple charge distributions and conductor configurations. However, field distributions of physical systems that are frequently used in high voltage apparatus can not be generated by such simple charge distributions and therefore the analytical solution of Laplace's or Poisson's equations for these cases is very difficult, if not impossible.

The availability of digital computers with large memory has made it possible to determine accurately the design parameters and to evaluate the expected performance of devices by means of numerical techniques.

In recent years several numerical methods for solving partial differential equations and thus also Laplace's and Poisson's equations have become available. The available numerical methods are normally based on difference or integral concepts. The difference concept employs Laplace's and Poisson's equations in the space where the field is to be determined. This is done by dividing the whole space by a fine mesh. These include the Finite Difference Method [9-17] and the Finite Element Method [18-20]. The integral concept of the computation of fields is based on integration of Laplace's equation either by employing discrete charges, or by dividing the electrode surface into subsections with charges associated with each. This method of

computation is known as the Charge Simulation Method [21,22]. The Charge Simulation Method has been receiving attention during the past few years. It is a numerical method which uses a number of discrete modelling charges or finite charge distributions.

The conventional Charge Simulation Method (CSM) is a widely used and powerful method for numerical calculation of electric fields. It expresses a solution to Laplace's equation as a superposition of particular solutions (i.e. those due to discrete charges). These charges replace the physically distributed surface charges of the electrodes. They are placed outside the region where the field is to be calculated. The magnitudes of these charges must be calculated so that their integrated effect satisfies the boundary conditions of the particular configuration to an acceptable degree of accuracy. This method has been successfully applied to many high voltage field problems. It is applicable to any system that includes one or more homogeneous media and it is also suitable for the solution of three dimensional fields without any particular symmetry [21].

1.2   Statement of the Problem

It is acknowledged that there is a degree of complexity in setting up a problem using the conventional charge simulation method, and that the time required to prepare a problem for computation can sometimes be excessive. It is also known that the CSM is a direct method which involves a priori assumptions about the location of the equivalent charge distribution which are made on the basis of experience, and may be different for different researchers. The assumptions determine the degree of accuracy in the result. To attain a reasonable accuracy, some of the controlling parameters which affect the simulation may have to be adjusted and this takes much time in the conventional implementation of the Charge Simulation Method, since the user has to address the details of the geometry when the controlling parameters are changed. Therefore, emphasis is laid on the development of a Computer-Aided Design (CAD) package which allows a user to conveniently and rapidly define the geometry of a system consisting of a number of electrodes and one or two dielectric regions [23-24]. The package automatically calculates the

coordinates of contour points for cases for which the contour consists of straight lines, parts of circles or any other curved portion that can be adequately fitted using a cubic spline. The package forms the system of linear equations and solves it. Finally, the package presents the results in the form selected by the user from a broad range of alternatives. The package has been used to investigate general electrostatic field problems in two and three dimensions with and without axial symmetry. In this work a description of this package and its application are given.

To assess the accuracy obtained with this package, extensive studies of the quality of the solutions are undertaken. The amount of error and discrepancy data provided is much more extensive than that which has been available in the literature. This allows other workers to assess for themselves the quality of this model against their own requirements. Where applicable, numerical values of the fields are compared with the values previously determined in the literature.

1.3   *Organization of the Dissertation*

Chapter 2 gives a brief review of the different methods used in electrostatic field computations. It also gives a review of the available literature on the charge simulation technique. The applications of the method to single and two dielectric systems are reviewed in separate sections.

Chapter 3 introduces the theory of the Charge Simulation Method as a technique for solving electrostatic field problems. Computation of fields in two dielectric systems are discussed in detail in addition to the different solution quality measures of the CSM model. Some other modifications to the conventional charge simulation technique are also explained. Features of the CSM with reference to the other methods are discussed briefly at the end of this chapter.

Chapter 4 describes in detail an implementation of a general purpose Charge Simulation based Computer-Aided Design package. The input data required to generate the geometry, the input data required for charge simulation model generation and the different output options

available for the user are described. Mathematical approaches used in the implementation of the program package are briefly discussed. Finally, limitations associated with using the package are introduced.

Chapter 5 presents the application of the CAD package to several standard and practical electrode systems which have analytical solutions. A comparison between the analytical solution and the CSM solution is presented through graphs representing the difference between the potentials and fields of the two solutions.

A study of the effect of different parameters controlling the modelling of the charge simulation model is conducted to optimize the parameters using the CAD package and presented in chapter 6. This chapter also presents a comparison between full and partial modelling in the case of symmetry, and the effect of varying the gap separation on the solution quality measures.

Chapter 7 is on the modelling and refinement of several engineering systems using the CAD package. The rod-plane gap configuration and a high voltage shielding system are modelled and results are presented and compared with those previously presented in the literature. In addition, solution quality measures which have not previously been published are provided. The computation of fields in a sphere/slab arrangement (both plane and recessed dielectric slab) was conducted as an example of a two-dielectric two-dimensional field problem. Two high voltage systems which have not been analyzed before using the Charge Simulation Method are selected and simulated with the package and presented in this chapter. These systems include a triggering electrode configuration and a 22-shed long rod polymer insulator. The latter is also modelled with the inclusion of grading rings introduced to improve the voltage distribution along the insulator.

Chapter 8 is devoted to the application of the package to complicated three-dimensional field problems with and without axial symmetry. A tilted rod-electrode versus ground plane is simulated with the package. A hemispherical capped rod electrode versus a grounded plane having another hemispherical capped electrode embedded in it is modelled. A detailed and thorough examination of the field distribution for a triggering high voltage electrode system which represents a more complicated three-dimensional field problem is presented.

In chapter 9 the conclusions and recommendations for future work are given.

Chapter II

FIELD CALCULATION METHODS AND SURVEY OF LITERATURE

2.1 Summary of Field Calculation Methods

It is very important to know the potential and electric field distributions in the design of high voltage equipment. Inaccurate estimation of the field and potential distributions may result in a loss of accuracy and efficiency of the manufactured equipment. The prior knowledge of the potential and electric field distributions by means of computational techniques can be used to determine appropriate design parameters and to conduct a performance evaluation of devices.

In recent years several numerical methods for solving partial differential equations, including Laplace's and Poisson's equations have become available. There are inherent difficulties in solving partial differential equations for general two- or three-dimensional fields with mixed boundary conditions or for insulating materials with different permittivities and/or conductivities. Each of the different numerical methods, however, has inherent advantages and disadvantages [25]. The calculation of the potential and electric fields requires the solution of Laplace's and Poisson's equations with the boundary conditions satisfied. The field equations for an electrostatic field in a homogeneous medium is given by Poisson's equation:

$$\nabla^2 \phi = - \frac{\rho}{\varepsilon}$$

where

$\phi = potential,$

$\rho = volume\ charge\ density$, and

$\varepsilon = permitivity\ of\ the\ medium.$

For zero charge density Poisson's equation reduces to Laplace's equation:

$$\nabla^2 \phi = 0. \qquad\qquad (2\text{-}2)$$

In cartesian coordination equation (2-2) becomes

$$\nabla^2 \phi = \frac{\partial^2 \phi}{\partial x^2} + \frac{\partial^2 \phi}{\partial y^2} + \frac{\partial^2 \phi}{\partial z^2} = 0$$

This equation can be solved either by analytical or numerical techniques. When the solution of this equation is given as the potential $\phi(x, y, z)$, the electric field is calculated from the negative gradient of the potential

$$\vec{E} = -\vec{\nabla} \phi$$

$$= -\left(\frac{\partial \phi}{\partial x}\, \vec{a}_x + \frac{\partial \phi}{\partial y}\, \vec{a}_y + \frac{\partial \phi}{\partial z}\, \vec{a}_z \right)$$

However, many physical systems are so complicated that analytical solutions are seldom applicable and hence numerical methods are commonly used [26]. Two numerical methods are being extensively used in the calculation of electrostatic fields in high voltage systems. The first method is based on the difference technique. This is implemented by dividing the whole space into a fine mesh and Laplace's equation is then approximated at each mesh point by equations which relate the unknown potential of the mesh point to the unknown value at other mesh points and to known boundary potentials. These difference techniques include the Finite Difference and the Finite Element methods.

The Finite Difference and Finite Element methods have been very extensively described in the literature [9-20].

Difference techniques are very powerful when the region of interest contains a number of different materials or a dielectric constant which varies in space [18]. In more simple cases (such as the case where only conductors are present), difference techniques may be more cumbersome due to the large number of linear equations that must be solved [27]. Furthermore, Finite Element and Finite Difference methods are particularly suited for use in bounded regions, but many physical problems of interest are unbounded. However, attempts have been made to use difference techniques for the solution of electric field problems where the field is not bounded in

space but extends indefinitely [19,20]. In one of these methods an artificial finite boundary condition is initially introduced to obtain a solution and is then iteratively moved to more distant locations as the solution proceeds. In order to have a minimum effect of errors in specifying the known potentials on the calculated potential values in the region of interest, the artificial boundary must be placed far away from the region of major interest. Hence Laplace's equation must be solved for a larger region than the region of interest. Thus a larger number of equations must be solved which adds to the computation time [20].

The accuracy in the Finite Element Method depends on the number of divided elements, how they are divided, as well as on the approximation function. A potential approximation function valid in each element is used to allow the electrostatic energy of the entire field to be minimized by correct relation of the node point potential values. Variational principles are used to generate the necessary equations relating the node point potential values.

In the application to electric field problems within insulation systems, the advantages of the FEM may be summarized as follows:

1.   It is readily applicable to non-homogeneous systems (i.e. with materials of different permittivities) as well as to anisotropic systems.

2.   The shapes and sizes of the elements may be chosen to fit arbitrary boundaries and the grid size may easily be adapted to the gradient of the potentials, i.e. small elements can be placed into regions with high gradients and vice versa.

3.   Accuracy may also be improved using higher order elements, without complicating boundary conditions.

4.   Dielectric materials may also be treated as the case where conduction currents contribute to the potential distribution. This can be done by assuming a complex permittivity with real and imaginary parts.

For the calculation of electric field intensities within insulation systems, the only disadvantage of the FEM is related to the limited and a priori unknown accuracy which can be

achieved. For two-dimensional problems and highly divergent fields, a very large number of triangular elements or nodes would be necessary to obtain an adequate accuracy within the highly divergent field regions.

Another method used for potential and electric field calculations is the Mont Carlo Method [28]. In this method, Laplace's equation is solved for an unknown potential at any point as the expected boundary value at the intersection of simulated random walks starting from the point and terminating on the boundary.

The other approach to the solution of fields is the use of integrals of Laplace's or Poisson's equations either by dividing the electrode surface into subsections of charges or by using discrete charges. This is explained in the following sections.

2.1.1   Electrode Surface Subsectioning

The electrode surface is divided into subsections with their associated charges. It will be assumed here that the medium consists of several different homogeneous materials and that as a result, the only charges are the surface charges. If this is not the case, then volume charges must be considered [29]. The integral equation can be solved for the surface charge densities by approximating the integral as a sum of subsections considered on the entire electrode surface. The sum is set equal to the known potential at the centre of each subsection. As a result of this discretization process, a set of linear algebraic equations is obtained in terms of unknown segments of charges which when solved with a digital computer gives values of these charges. Once the charge densities are obtained , potential and electric field values can be evaluated at any point.

2.1.2   Discretization of Charges

The distributed surface charges of the electrode are replaced by discrete line, ring and point charges (instead of assuming them to be surface charges). These charges are placed outside the space in which the field is to be computed. The potentials due to these charges will be smoothly

varying (mathematically represents a well behaved function) at, and in front of, the surface and thus can simulate approximately the field of a surface charge.

This method of discretization is known as the Charge Simulation Method (CSM) and was first presented by Singer et al. [21]. It proved to be successful for many high voltage field problems. It is simple and applicable to any system that includes one or more homogeneous media. A special advantage of this method is the good applicability to three-dimensional fields without axial symmetry and to space charge problems.

A few papers have been published which deal with a combination method in which the Charge Simulation method is combined with the Finite Element method, for electric field calculations [30,31]. The combined method has the advantages of the Charge Simulation method and the Finite Element method with an overall improvement in the accuracy of the simulation. In the combination method, the field is divided into two regions, one covered by the Charge Simulation method and the other by the Finite Element method. These two regions are combined using the continuous conditions for potentials and electric flux densities at the boundary.

The combination method enables the calculation of an electric field which could not be solved with enough accuracy by an individual calculation method. For example, the combination method can be applied to non-enclosed fields with multiple-dielectrics, a space charge field, a field with leakage current and so on. In addition, modelling a part of a field with another method, can reduce the memory requirement of the computer and improve the calculation accuracy.

The work presented in this dissertation is based on Singer's technique of the Charge Simulation. A survey of the available literature on the charge simulation technique is therefore carried out in order to observe the applicability of the method to many high voltage field problems.

2.2   *The Conventional Charge Simulation Method*

The conventional Charge Simulation Method (CSM) consists of placing a number of discrete charges or a finite charge distribution outside the region where the field is to be calculated [21]. These charges are used to approximate the effect of the surface charges associated with the field of the physical system. Making use of the linearity of Laplace's equation in applying the Charge Simulation method, the solution to Laplace's equation is expressed as a superposition of particular solutions such as those for point, line or ring charges. Compared with the other methods, only boundary surfaces (electrode surfaces and medium interfaces) are subdivided and boundary charges (or charge densities) are taken as unknowns in the Charge Simulation method. It follows then that the amount of human time and effort needed for subdivision is greatly reduced in the CSM. Also the matrix equation thus obtained by discretization is one dimension smaller compared to the matrices obtained in the Finite Element or the Finite Difference methods. The electric field strength can be expressed explicitly in terms of the simulating charges (or charge densities) without resorting to the numerical differentiation of the potential. This last characteristic is very important because the field strength is more crucial in insulator design than the potential, and furthermore, numerical differentiation often results in significant errors.

The increasing availability of high speed digital computers allowed the Charge Simulation method to be extensively used in the calculation of electrostatic fields of high voltage systems. The Charge Simulation method is particularly appropriate for many high voltage problems that include one or more homogeneous media in unbounded regions [21,22]. This method is also suitable for modelling three dimensional fields with and without axial symmetry. Using the Charge Simulation method it is also possible to calculate electric fields for systems in which space charges are present.

2.3   Previous Applications of the CSM

2.3.1   Applications to One Dielectric HV Systems

Considerable attention has been given to electrode configurations used in high voltage experimentation by many authors. Singer et al. [21] calculated the electric field between a conductor strip and a plane as an example of a two dimensional field. The influence of an earthed cage on the field of a sphere-gap was also analyzed by Singer as an example of an axial symmetrical problem. He also applied the method to an electrode arrangement used for the shielding of high voltage apparatus to calculate the maximum electric field. Singer also explained the principle of the method applied to three-dimensional fields without axial symmetry by a single example, a rod-rod gap with a trigger electrode. He studied the effectiveness of the method for three-dimensional electric fields by applying the technique to two practical field problems of high voltage engineering: the influence of adjacent conductors on the field of a sphere-gap, and the field distribution near the bundle of a three phase overhead-line under the influence of the tower. Abou-Seada [1] applied the Charge Simulation method to the calculation of electric fields of a rod-rod gap. Parekh et al. [32] computed the electric field for rotationally symmetric electrodes. Yializis et al. [33] calculated the potential distribution for a rod-plane electrode configuration and presented an optimized version of the charge simulation technique. The objective function used by Yializis et al. was the accumulated squared potential error while the position of the charges and their values were the variables of optimization. Akazaki and Mishijima [34] examined the field distribution of multiple axisymmetric electrodes displacing and rotating the plane of the symmetric model charges. They made calculations for a three-dimensional axisymmetric gap for a tilted upper rod-plane electrode arrangement and the rod-plane with lower rod arrangement. Iravani and Raghuveer [35] suggested a method in which an optimization technique employing a modified objective function which minimized not only the accumulated squared potential error but also the tangential electric field along the conducting surface.

The application of the Charge Simulation method to single dielectric systems finds its greater use in the evaluation of the electric fields around high voltage overhead transmission lines. The existence of corona and radio interference around the insulator-line conductors is more acute with transmission at EHV and UHV levels [36]. Therefore, electric field calculations are made for bundle conductors used for such transmission lines. Abou-Seada and Nasser [37] used the method of Charge Simulation to calculate the electric field and potential around a twin subconductor bundle. In this method, the actual charge distribution on each subconductor surface was represented by several discrete line charges placed inside each subconductor. These line charges of unknown magnitude were placed on a fictitious cylinder whose radius was half of the subconductor radius. The correct angular positions of these line charges on the fictitious cylinder were determined by a trial and error method to achieve better accuracy of the results. The results obtained by Abou-Seada and Nasser gave an error of about one percent in the values of the direction of electric field. However, their method was applicable for the case of twin subconductor bundles. They also calculated the potential gradient of twin cylindrical bipolar conductors with various geometrical parameters [38]. Parekh et al. [39] described a method based on charge simulation which used arbitrary specifications of location of the images and boundary points and was applied to bundles of up to eight cylindrical subconductors.

2.3.2   Applications to Multiple Dielectric HV Systems

Electrical machines and high voltage devices often contain multi-dielectric insulation layers between conductors or cores, etc. For the design and testing of these devices, it is important to have accurate information on the electric field distribution within. The method of computation of potential and electrostatic fields in two dielectric arrangements was also developed by Singer et al. [21]. As an application of this method, they modelled a sphere electrode with a dielectric slab. For studies of the electric strength of solid insulating material, flat-slab specimens are often tested by such arrangements (i.e. a dielectric slab between a sphere and a plane). They also applied the method to a practical electrode arrangement used for shielding of high voltage apparatus, and to

the calculation of the field strength at the shielding electrodes of UHV transformers. Following the same concept of computation as proposed by Singer, Mukerjee and Roy [22] applied the method to the calculation of fields in a multiple dielectric three-dimensional system. They applied it to a parallel plate arrangement as a test example and then to a disc insulator, the shape of which was simplified to a truncated cone. Khaled [40] used the Charge Simulation method for computation of the corona onset voltage. The main feature of his work was the development of a new simulation model of the avalanche growth. Takuma [41] using the charge simulation technique studied the optimal profiles of disc-type spacers for gas insulation. He also studied the field behaviour near triple points in composite dielectrics [42]. Takuma et al. [43] calculated the electric field very accurately in configurations including volume resistance or surface resistance using the Charge Simulation method. They used the same numerical method (CSM) to study the effect of conduction on field behaviour near singular points in composite medium arrangements [44]. Takuma also used the Charge Simulation method to describe the field intensification at the contact point in various arrangements where a rounded electrode contacts a solid dielectric at a zero contact angle [45]. Nosseir and Zaky [46] described a method based on the charge simulation technique to evaluate electrical stresses in three core cables. In this method, each conductor was replaced by a line charge, assumed to vary sinusoidally with time and with a phase shift of 120 degrees between each pair of line charges. They expressed the mathematical expressions in terms of the cable geometrical parameters. The results were checked by using an electrolytic tank. Takashima and Ishibashi [47] described a way to determine the electric field of a point charge by the method of images in three or more dielectric layers on a plane conductor. They applied this method in combination with charge simulation to calculate the field of a spherical conductor enclosed by three concentric dielectric layers on a plane conductor [48]. In this method, ring charges in the spherical conductor together with their images were used for representing the field. Sakakibara [49] applied this method to the calculation of three-dimensional asymmetric fields for a post-type spacer with two dielectric media. A

simplified post-type spacer used in SF_6 gas insulated apparatus was modelled. A high voltage impulse test was also carried out by those authors to verify the validity of the method and the results were found to be in good agreement. Khan and Alexander [50] applied the Charge Simulation method to a typical transmission line disc insulator (unsimplified) section under pollution-free conditions. They used ring and line charges for the modelling of the field distribution in and around the insulator with an accuracy in the representation of electrode potentials well within 1% of the maximum potential difference. Elmoursi and Malik [51] investigated the electric field uniformity of a high voltage test electrode system by using the charge simulation technique. Iravani and Raghuveer [52] computed the potential distribution along a high voltage transmission line insulator chain (cap and pin type) taking into account the influence of tower, crossarm, conductor, and ground by using a combination of the integral equation and the Charge Simulation technique. Anis and Mohsen [53] extended the charge simulation technique for computing time-varying electric fields and potentials. They applied the extended method to three-cored gas-insulated (GIS) cables where the new treatment was shown to help in examining the problem of gas contaminations with conducting particles. Pillai et al. [54] studied the influence of radius of curvature, contact angle and material of solid insulator on the electric field in vacuum (and gaseous) gaps by using the charge simulation technique. Pillai and Hackam [55] computed the electric field and potential distributions of the interfacial boundary between the solid insulator and vacuum for different realistic surface charges by applying the charge simulation technique. They also used the method for calculating the electric field and the potential distributions for unequal spheres using symmetric and asymmetric applied voltages [56]. Pillai and Hackam [57] also applied the Charge Simulation method to investigate the surface flashover of conical insulators in vacuum. The electric field distribution along the interface of a solid insulator-vacuum (or gas) was analyzed by Pillai and Hackam for different solid insulator-electrode configurations with and without the presence of surface charges using the charge simulation technique [58,59]. They also used this method for improving the

performance of cylindrical solid insulators with concave curved edges in vacuum [60]. Salama and Hackam [61] presented a theoretical model, based on the charge simulation technique, from which design parameters and dimensions of polymer sheets can be obtained to construct substation inclosures. They applied this method to design grading rings for air-core power reactors for improving the impulse voltage distribution along the axial length of the reactors [62].

2.4   Other Modifications of the Charge Simulation Technique

It is highly desirable to get a high degree of precision in computing the potential at the electrode surface. However, improving the accuracy beyond a given limit is not worthwhile because of the increase in the computer time and memory requirement. An algorithm aimed at reducing the overall computer time and memory requirements, precision being equal, is valuable since, either the cost of a given computation could be reduced, or at a given cost, a more complex problem could be solved [50,63].

Several attempts have been made by several authors proposing optimization techniques to reduce the cost of numerical computation on the basis of a fixed degree of precision required. A function fitting-oriented modification to the Charge Simulation method for estimating electric field was introduced by Anis et al. [64] aiming at the reduction of computation time and cost. In this method, a multiple linear regression makes it possible to reduce the size of the simulating charge system without decreasing the number of selected boundary points. The direct optimization approach for the computation of electric fields, based on the charge simulation technique described by Yializis et al. [33], used the accumulated squared error in boundary potential values as the objective function. The positions of the charges and their values were chosen to be the variables of optimization subject to constraints imposed according to the geometry of the problem described. The objective function was minimized to 1%. However the optimization algorithm (Rosenbrok's optimization technique) used [65] is not the most rapidly converging technique and therefore savings in computation time did not result. Fast convergence

techniques such as Davidson's method modified by Fletcher and Powel [66] have been suggested for reducing computation time with comparable accuracy. According to the authors [33], other factors that could influence the computation time are the initial values of the optimization parameters and the effectiveness of the objective function. The latter parameter is important, since for more complex configurations it is possible that the minimum accumulated squared error may not be an efficient criterion. Chow and Charalambous [67] presented a similar approach but with unconstrained optimization. This approach has been applied to a number of geometries encountered in engineering applications. The objective function in this method was the mean square error in the boundary potential. The optimization technique used was due to Fletcher [68] which has the advantage that since it requires the gradient of the objective function, the electric field intensity on the conducting boundary is implicitly obtained. Therefore it can be extracted without further computation.

Mohsen and Abdel Salam [69] presented a development of the charge simulation technique for the calculation of electric field around conductor bundles of EHV transmission lines. In this method a known initial set of charges which are deduced from the analysis of a similar but simpler problem is introduced. These initial charges may be used in addition to a set of unknown charges which are determined from the boundary conditions. The better the initial charges, the lower will be the number of unknown charges. This is expected to lead to a considerable saving in computational time. Sakakibara et al. [49] described a modification of the Charge Simulation method applicable to three-dimensional asymmetric fields with two dielectric media. Since the formulation of a large potential coefficient matrix results in an extensive computation time and memory requirements, they have taken advantage of symmetry to reduce the size of the computational problem. Recently Iravani and Raghuveer [35] suggested a method which uses an optimization technique employing a modified objective function for numerical field calculations. Several other papers have been published which used the Charge Simulation method for optimizing the electrode geometries and the high voltage electric fields [70-73].

Chapter III

THE CHARGE SIMULATION METHOD

3.1   Theory of the Charge Simulation Method

The potential at a point in the region of interest can be expressed by two integrals over the bounding surface. These integrals can be interpreted as being associated with a distribution of charges and a distribution of dipoles. Since in actual electrostatic problems the boundaries are generally equipotentials (i.e., conductors or surfaces at infinity) no dipole layer is required and the potential can be expressed using only the surface charge [26]. However, the CSM replaces these surface charges by a finite number of discrete charges located outside the region where the field is to be calculated [21].

The type of the charges commonly used are ring charges which are used to model axially symmetrical profiles, line charges (finite or infinite) which are appropriate for cylindrical configurations that include regions with translated geometry, and point charges which, due to their spherically symmetrical field behaviour, suit spherically symmetrical surfaces. These three forms of charge arrangements for a particular high voltage electrode configuration cover almost all possible system configurations.

The distributed charge on the surface of a conductor is replaced by n charges arranged inside the conductor as shown in Figure 3.1a. If the conductor is located in the vicinity of the ground, then the effect of the ground must be taken into account. Since the potential of the ground is assumed to be zero, for each fictitious charge inside the conductor, an image charge of opposite polarity is appropriately placed with respect to the ground surface as shown in Fig. 3.1b.

In order to determine the magnitude of these charges, n points on the surface of the conductors (contour points) are chosen. It is required that the potential resulting from the superposition of the charges is equal to the conductor potential at that point:

$$\sum_{j=1}^{n} P_{ij} \, Q_j = V_i \qquad\qquad (i = 1, 2, \dots, n) \qquad\qquad (3\text{-}1)$$

where,

n   is the number of contour points (or charges),

P_{ij} is the the associated potential coefficient,

V_i is the potential at the i-th contour point.

The potential coefficient P_{ij} is defined as the potential at the i-th contour point due to a unit

charge located at the position of Q_j. The potential coefficients of line, ring and point charges are

given in Appendix A. Applying equation (3-1) to the n contour points leads to a system of linear

equations for n charges, which can be expressed in matrix form as:

$$[P] \, [Q] = [V] \qquad\qquad (3\text{-}2)$$
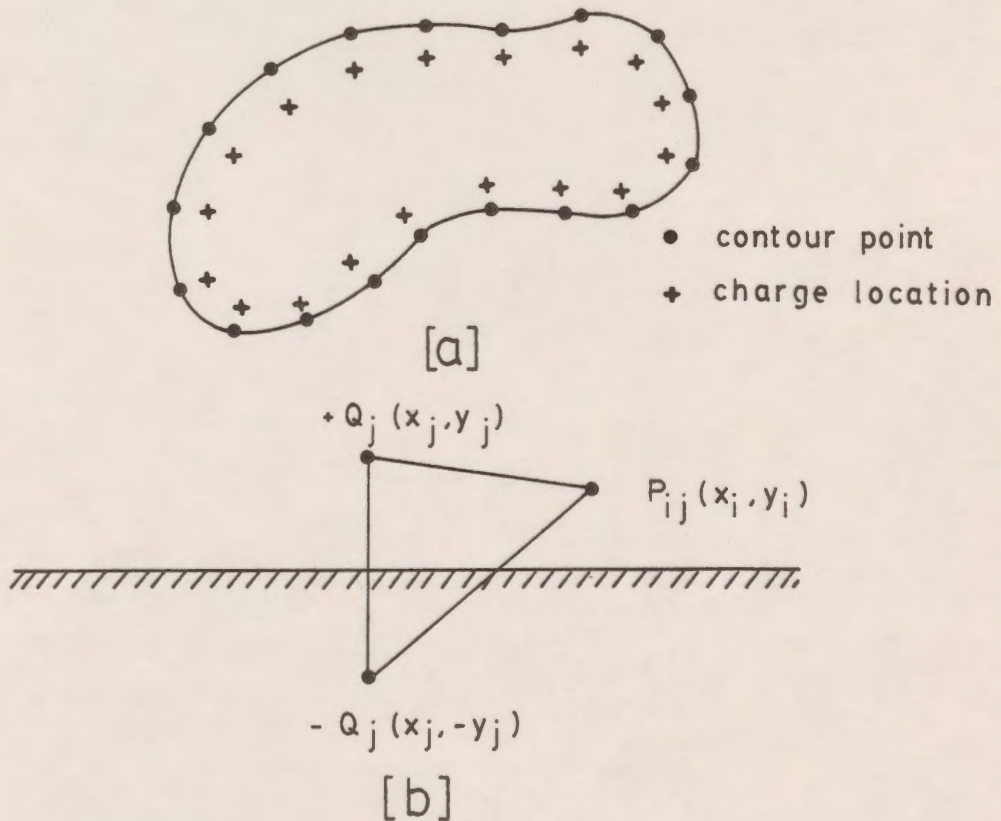

Figure 3.1: Principles of the Charge Simulation Method.
                 (a) modelling charges with contour points
                 (b) a point charge and its image

The matrix of potential coefficients [P] can be calculated; the potential matrix [V] is known at every contour point, and thus the magnitudes of the set of charges Q are the only unknown variables, which can readily be obtained from the solution of equation (3-2).

After obtaining the values of these charges, the potential at any point in the region of interest can be computed, which is regarded as being due to the integral effect of these charges. The potential V at any point due to the charges Q can be expressed as:

$$V = \sum_{j=1}^{n} P_j \, Q_j$$

where P_j is the potential at that point due to a unit charge located at the position j. The electric field intensity at any arbitrary point can be determined outside the boundary of the electrodes. This is achieved by a vectorial superposition of the contributions from every charge as given in the following equation

$$E_i = \sum_{j=1}^{n} F_{ij} \, Q_j$$

where,

E_i is the electric field component at the i-th point.

Q_j is the charge value at location j

F_{ij} is the field coefficient factor, which incorporates the appropriate component of the field vector.

The expression for the field coefficient for the different types of charges are given in the Appendix A.

The accuracy of the Charge Simulation method depends on several factors, the most important of which are the positions of the charges and of the corresponding contour points. An assignment factor is defined as

$$\beta_a = \frac{S_a}{D_a}$$

where D_a is the distance between two successive contour points and S_a the distance between the contour point and the corresponding charge as shown in Figure 3.2. Experience shows that for efficient computation β_a should be between 0.7 and 2.0 and its value depends upon the nature of the surface [21]. Another factor which affects the accuracy of the method is the density of the boundary points. To improve the accuracy in a certain region, generally a higher density of boundary points is placed in that region. A limit will be reached beyond which an increase in the number of the charges will have no significant effect on increasing the accuracy or the error in the simulation will be increased.
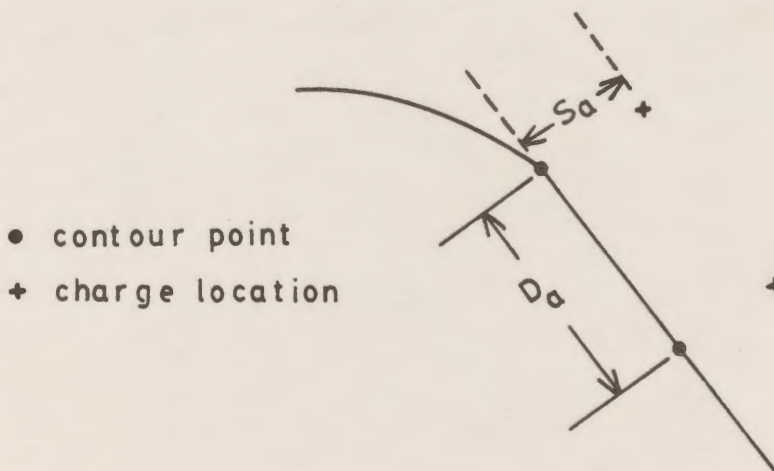

Figure 3.2: Relationship between contour points and charge locations.

Looking again to the matrix form (equation (3-2)) which describes the model in a system of linear equations, we will find that each element of the square matrix requires one storage element in the computer. Since a minimum of n(n+1) such elements are required for n modelling charges, the selection of the number of such charges is restricted by the storage capacity of the computer. An increased accuracy of the charge simulation technique is mostly obtained with an increased number of charges. In order to achieve higher accuracy, the CSM can be applied in the

following modified way for determination of the field and the potential in a symmetric system.

For each contour point one modelling charge is selected if the arrangement is wholly asymmetrical. Then the term P_{ij} describes the effect of only one charge. If the arrangement is symmetrical about the x-x or y-y axis, then two charges of equal value can be positioned symmetrically about the axis of symmetry, shown in Fig. 3.3a, and only one-half of the system need be analyzed for the field. Then P_{ij} is computed as the combined effect of both charges on the potential of the i-th contour point and the storage requirement is reduced appreciably. Again if the arrangement is symmetrical about both x-x and y-y axes then for each contour point, four equal charges can be positioned, as in Fig. 3.3b, and the term P_{ij} is the total effect of all four charges. For n selected contour points in one quadrant, effectively 4n charges are positioned and the computer storage requirement is proportionately reduced as compared to a totally asymmetrical system with 4n charges.
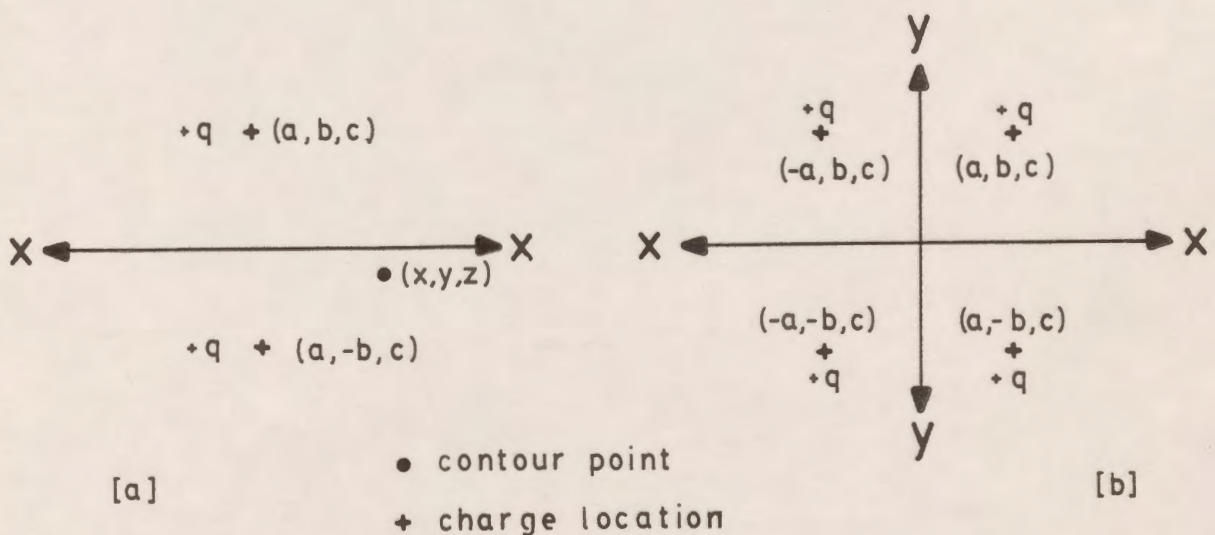

Figure 3.3: Charge distribution in symmetric system.
(a) symmetry about x-axis
(b) symmetry about both x and y axis.

3.2   Computation of Fields in Two-Dielectric HV Systems

A conductor is a substance containing electrons which are free to move under the action of an electric field distances which are large compared with atomic dimensions. The movement of the electrons in the substance occurs even when the electric fields are very small.

Unlike the conductor, a dielectric is defined as a substance containing an array of charges which will remain in equilibrium when the electric field is not zero inside the substance. Thus, a dielectric or an insulator is characterized by the fact that it does not contain free electrons in any appreciable numbers.

The behaviour of the electric field in a medium depends on the structure of the material. In a conducting medium the free charges appear as surface charge density on the exterior surface of the conductor. In dielectric materials or insulators, charges can only be displaced by small distances locally. However, a dielectric in an electric field can be viewed as a free-space region containing atomic-sized electric dipoles, or positive and negative bound charges, the centers of which do not quite coincide; these charges can be treated as any other sources of electrostatic field.

The characteristic which all dielectric materials (insulators) have in common, whether they are solid, liquid, or gas, is their ability to store electrical energy. This storage takes place by a shift in the relative positions of the internal positive and negative charges against the normal molecular and atomic forces. The actual mechanisms of the charge displacement differs in the various dielectric materials [8]. Some molecules, termed polar molecules, have a permanent displacement existing between the centers of "gravity" of the positive and negative charges, and each pair of charges acts as a dipole. Normally the dipoles are oriented in a random way throughout the interior of the material, and the action of the electric field is to align these molecules to some extent parallel to the electric field. A sufficiently strong field may even produce an additional displacement between the positive and negative charges. A nonpolar molecule does not have this dipole arrangement until after a field is applied. The negative and

positive charges shift in opposite directions against their mutual attraction and produce a dipole which is aligned with the electric field. In the interior of the dielectric material (insulator) the electrical effects of the molecules tend to cancel each other but on the surface of the dielectric boundary the dipoles produce net surface charges.

The effect of any surface charge distribution is equivalent to (or can be replaced by) the identical effect of other charges located beyond the surface as far as effects on "this side" of the surface are concerned. Therefore, a dielectric surface can be approximately simulated by discrete charges located appropriately on either side of the dielectric boundary. The magnitudes of these charges should be such that they satisfy the following conditions on the dielectric interface provided that the interface has no free charges and the two media are homogeneous and isotropic.

1. The potential at any point on the dielectric surface must be the same when computed from either side of the dielectric surface.

2. The normal component of the electric flux density at any point in either medium at the surface must be the same.

3. The tangential component of the electric field intensity at any point in either medium at the surface must be the same.

The last boundary condition is not imposed as an explicit condition in the solution because once the first condition is imposed and satisfied the last boundary condition will be automatically satisfied.

3.2.1   Computation Procedure

The procedure for computation of fields and potentials of a two-dielectric system, shown in Fig. 3.4 with relative permittivity ε_r, is as follows:

1. Electrodes (conductors) are replaced by a number of discrete charges n_e with the same number of contour (boundary) points on the electrode, of which n_{ea} contour points are on the side of the air and $n_e - n_{ea} = n_{ed}$ contour points are on the side of the dielectric. These n_e charges contribute to the potential and field strength in both sides.

2.   The dielectric boundary is replaced by n_b contour points with n_b charges in the dielectric and n_b in air. The charges in the dielectric contribute to the potential when it is evaluated at contour points on the air side of the conductors. The contributions of the charges in the air should be taken into account when evaluating the potential at contour points on the dielectric side of the conductors. There are thus $n_e + 2n_b$ equations involving these charges. These charges can be described as follows:

In conductor ------------> $1, \ldots , n_e$

In air   ------------> $n_e+1 , \ldots , n_e+n_b$

In dielectric ------------> $n_e+n_b+1 , \ldots , n_e+2n_b$

The points on the dielectric side of the conductor are labelled:

    $1,2, \ldots , n_{ed}$;

The points on the air side of the conductor are labelled:

$n_{ed}+1, n_{ed}+2 , \ldots , n_e$

The points on the air-dielectric interface are labelled:

$n_e+1, n_e+2, \ldots , n_e+n_b$

The symbols used are:

i   : index for contour points.

j   : index for the charges.

P_{ij} : The potential coefficient. This depends on the type of the charges, their location and the location of the point at which the potential is being specified.

Q_j : The discrete charge at the j-th location.

F_{ij} : The normal component of the electric field vector. It is defined as the contribution of the j-th charge to that component of the electric field vector which is normal to the dielectric boundary.
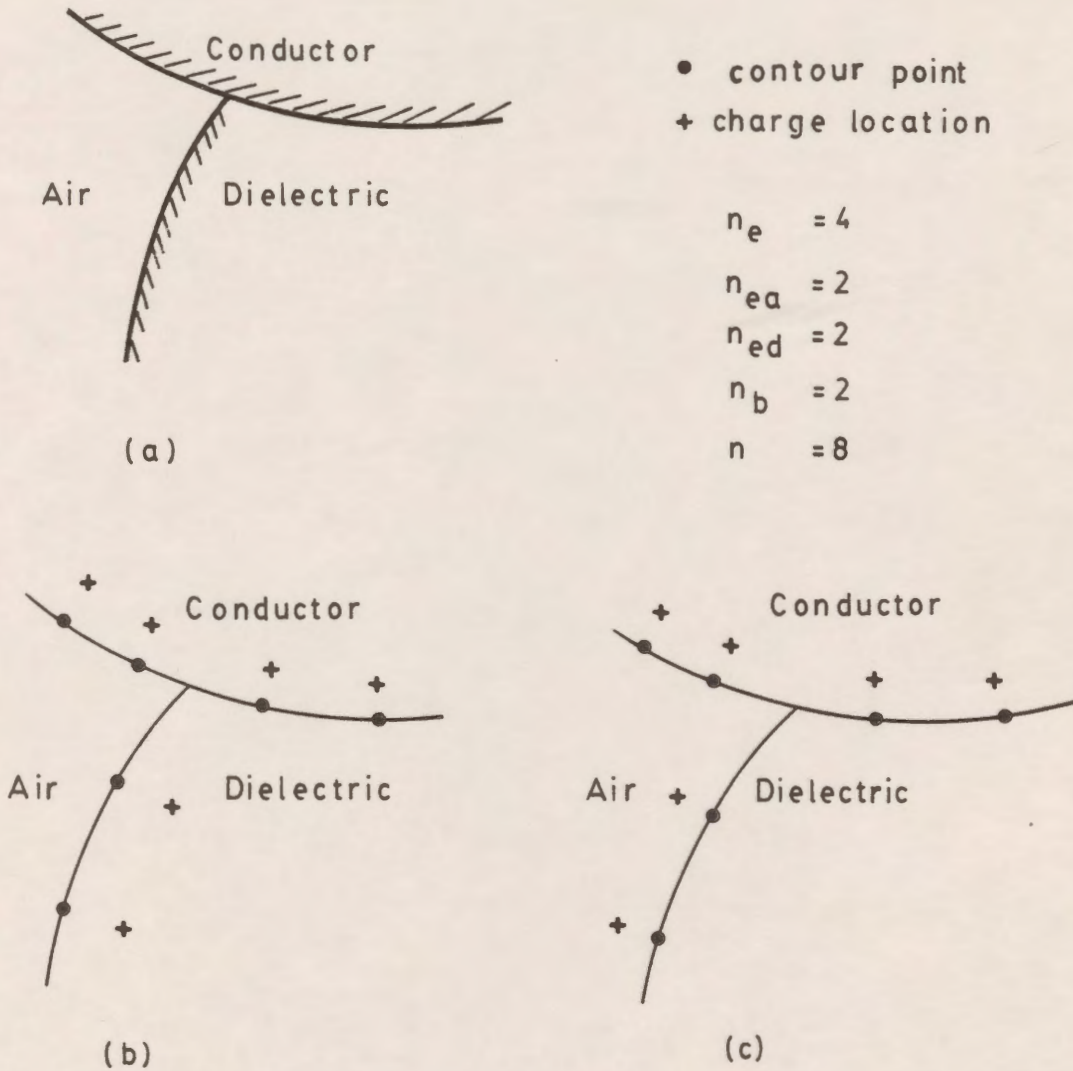
V_e : The conductor potential.

Figure 3.4: Procedure for computation of fields and potential of a two dielectric system.
    (a) conductor interfaced with dielectric material and air
    (b) charges contributing to potential at contour points on air/conductor side
    (c) charges contributing to potential at contour points on dielectric/conductor side

3.2.2   Formulation of the equations

The system of equations required for determination of the simulating charges can be formulated in the following manner:

1.   The potential V_e at the contour points on the dielectric side of the electrode is the integrated effect of all the n_e charges on the electrode and the n_b charges in air, that is,

$$\sum_{j=1}^{n_e} P_{ij} Q_j + \sum_{j=n_e+1}^{n_e+n_b} P_{ij} Q_j = V_e$$

   for $i = 1, 2, \ldots, n_{ed}$

2.   The potential V_e at the contour points on the air side of the electrode is the integrated effect of all the n_e electrode charges and the n_b charges in the dielectric. Therefore,

$$\sum_{j=1}^{n_e} P_{ij} Q_j + \sum_{j=n_e+n_b+1}^{n_e+2n_b} P_{ij} Q_j = V_e$$

   for $i = n_{ed}+1, \ldots, n_e$

3.   The potential at contour points on the dielectric boundary is unknown but the potential at each point on the boundary must be the same whether it is calculated from the region of air or from the dielectric region. Thus these equations can be written as:

$$\sum_{j=1}^{n_e} P_{ij} Q_j + \sum_{j=n_e+n_b+1}^{n_e+2n_b} P_{ij} Q_j = \sum_{j=1}^{n_e} P_{ij} Q_j + \sum_{j=n_e+1}^{n_e+n_b} P_{ij} Q_j$$

   or simplifying

$$\sum_{j=n_e+1}^{n_e+n_b} P_{ij} Q_j - \sum_{j=n_e+n_b+1}^{n_e+2n_b} P_{ij} Q_j = 0$$

   for $i = n_e+1, \ldots, n_e+n_b$

4.   At the contour points on the dielectric interface, the normal electric field intensity in air must be ε_r times that in the dielectric. If F_{ij} denotes the field intensity normal to the surface at the i-th contour point due to a unit charge at the position of Q_j, then the following equation applies:

$$\varepsilon_r \left[\sum_{j=1}^{n_e} F_{ij} \, Q_j + \sum_{j=n_e+1}^{n_e+n_b} F_{ij} \, Q_j \right] = \sum_{j=1}^{n_e} F_{ij} \, Q_j + \sum_{j=n_e+n_b+1}^{n_e+2n_b} F_{ij} \, Q_j$$

or

$$(\varepsilon_r - 1) \sum_{j=1}^{n_e} F_{ij} \, Q_j + \varepsilon_r \sum_{j=n_e+1}^{n_e+n_b} F_{ij} \, Q_j - \sum_{j=n_e+n_b+1}^{j=n_e+2n_b} F_{ij} \, Q_j = 0$$

for $i = n_e+1, \dots, n_e+n_b$

or

$$(\varepsilon_r - 1) \sum_{j=1}^{n_e} F_{lj} \, Q_j + \varepsilon_r \sum_{j=n_e+1}^{n_e+n_b} F_{lj} \, Q_j - \sum_{j=n_e+n_b+1}^{j=n_e+2n_b} F_{lj} \, Q_j = 0$$

for $i = n_e+n_b+1, \; n_e+n_b+2, \; \dots, n_e+2n_b$

where $l = i - n_b$

All the above $n_e + 2n_b$ equations can be written in a matrix form as shown in Fig. 3.5. One equation is written for every contour point on the conductor and two are written for each contour point on the dielectric boundary. Thus in the matrix form, the row number corresponds to the number of the contour point and the column number corresponds to the number of the charge.

Figure 3.5: Matrix representation of equations for application to two dielectric systems.

3.3   *Evaluation of the Charge Simulation Method*

Two factors which introduce errors in the fields computed using the CSM are the location and type of the simulating charges. Since these have been removed from the boundary which is where they properly belong, and since they are discrete instead of contineous distribution, some error is thus introduced. Therefore, there must be a check on how well the calculated set of charges satisfy the boundary conditions. For instance the potential at a number of check points located on the boundary can be calculated. The difference between these potentials and the given boundary potential is a measure of the accuracy of the simulation. If the coincidence between the actual conductor surface and the corresponding equipotential surface is sufficiently accurate, the electric fields at any point can be calculated from concise analytic expressions by superposition. The following quality measures are used to evaluate the accuracy of the Charge Simulation method:

1.   The potential error: this is the deviation of the calculated potentials from their specified

values on the conductor surface and is preferable to be less than 0.1% [22].

The significance of keeping the potential error below 0.1% is important since all

corona calculations are very sensitive to the values of electric fields. Very small errors

in the values of electric field might result in a very large error in the values of the

corona onset voltage, corona loss, and radio interference. The practical goal for

accuracy in the simulation of electrodes is limited by the manufacturing tolerances of

conductors. Similarly the accuracy of the simulation of dielectrics has as its practical

goal, the accuracy of the measurement of dielectric constant values. However, the

dielectric constant ε_r is not only limited by measurements but also by variation from

sample to sample and within the sample itself due to the presence of impurities.

The percentage potential error δV can be expressed as:

$$\delta V = \sum_{j=1}^{n} \frac{V_{ij} - V_e}{V_e} * 100$$

where,

V_{ij} is the computed potential at the i-th contour point due to the j-th charge.

V_e is the electrode potential, other than zero.

2.   The potential difference: this is defined as the difference between the potential along

the boundary of a grounded electrode (which is zero) and the calculated value resulting

from the CSM.

3.   The percentage normal field error: this error is defined as the difference between the

known normal electric field component and the calculated value resulting from the

CSM expressed in percentage of the known normal value.

4.   The tangential field difference: this is defined as the difference between the tangential field component along the surface of the conductor which is equal to zero and the calculated value of the tangential field (which has very small non-zero value due to the discreteness of the charges).

5.   The percentage potential discrepancy: this is defined as the difference between the potentials calculated on each side of the solid dielectric-vacuum (or gas) interface expressed in percentage of the average potential value. This error should be very small (typically less than 1%) [50].

6.   The percentage normal flux density discrepancy: it is defined as the difference in normal flux density solutions at the solid dielectric-gas interface evaluated from either side expressed in percentage of the average normal flux density.

7.   The percentage tangential field discrepancy: it is defined as the difference in the tangential fields calculated on each side of the interface of the solid dielectric-gas boundary expressed as a percentage of the average tangential field.

The tangential field discrepancy condition is a good check of how well the system has been modelled, since we recall that the continuity of the tangential field at the interface is not one of the imposed conditions, though indirectly implied by the continuity of the potential at the interface. It is usually higher than the previously described quality measures.

The difficulty associated with the charge simulation technique is that a critical placement of equivalent modelling charges is needed to obtain reasonable accuracy [50]. As a result, the best location of the equivalent charges is guided by experience. Thus the accuracy is usually checked after the problem is solved by determining how closely the boundary conditions are matched along all the interfaces. Also the accuracy in the solution is sensitive to the number of charges chosen for a particular problem. The suggestion that the larger the number of charges, the better is the solution, is not necessarily true. The situation depends to a major extent on the geometric complexity of the model and the number charge density [50]. Mukerjee and Roy [22] reported

that for a dielectric disc, an increase in the number of charges beyond a certain limit does not have a significant influence on the solution. Beasely et al. [25] made a comparative study of three methods - the Finite Element method, the Mont Carlo method, and the Charge Simulation method - and applied them to different geometries of a practical engineering nature. They concluded that for some very large and complex configurations it may not be possible to obtain satisfactory solutions using only one method. They suggested that in such cases the Mont Carlo method or the Charge Simulation method may be used to derive a first approximation followed by the Finite Element method within some reduced subregion of interest.

3.4   Features of the CSM With Reference to FDM

In summarizing the features of the Charge Simulation method with reference to the Finite Difference method, the following statements can be made.

For the specific tasks of field calculations within high voltage insulation systems, in which, in general, Dirichlet boundary conditions are given, all types of interfaces are predominantly curved and field distributions are of utmost interest in highly stressed areas, the inherent feature of CSM to simulate curved interfaces by relatively simple means is a major advantage.

Field regions need not be limited by a closed boundary, as the solution is not based upon a computation of potential within a given field space. Nevertheless, potential and even field stresses can be computed based upon analytical solutions within any point in the field region as soon as a proper charge distribution is found.

Proper charge distributions and thus field simulations need in general less computation time for digital computers, as fewer linear equations are involved and thus the potential coefficient matrix [P] is similar, though densely occupied, in comparison with adequate matrix equations within the Finite Difference method or the Finite Element method.

The accuracy of this method may be controlled more strictly quantitively.

With a reasonable amount of computation three-dimensional fields without any symmetry can be handled.

The greatest disadvantages of the CSM are related to multidielectric problems, though the current development based upon surface charges may greatly improve the method [74,75].

Chapter IV

CHARGE SIMULATION BASED COMPUTER-AIDED DESIGN

PACKAGE

4.1   General

The formulation of a model for field calculations of a high voltage system using the well-known Charge Simulation method has proved to be tedious and time consuming. Therefore, emphasis was laid on the development of a Computer-Aided Design (CAD) package which allows a user to conveniently (with a minimum of entered data) define the geometry of a system consisting of a number of electrodes and one or two dielectric regions. The package automatically generates a charge simulation model of the system by assigning the number and locations of the boundary points and charges to be used. Where desired, a cubic spline is fitted to boundary profiles defined by discrete points and identification of segment type which is provided by the user. The user can modify the model by redefining the system geometry, or by deleting, adding, or re-positioning boundary points and/or modelling charges. Decisions on revising the model can be based on quality measures of the results which the user selects. The resulting equations are solved and the results presented in the form(s) desired by the designer from a number of available options.

4.2   Package Capabilities

The capabilities of the CAD package are summarized in the following points:

1.   It allows a wide variety of problems to be formulated without having to address the details of the geometry through direct programming.

2.   One and two dielectric arrangements can be easily formulated.

3.   It allows three-dimensional field problems with and without axial symmetry to be readily analyzed.

4.   It allows consistent comparison among various trial models by keeping most of the parameters fixed at the default values during comparative analyses.

5.   Iterative refinement of charge simulation models can be achieved for complicated geometries.

6.   A large number of solution quality measures of the model can be examined.

7.   Field profiles can be produced for arbitrary paths or approximations of them.

8.   Equipotential contour maps and details in small windows can be produced for the single and two dielectric systems examined.

9.   Decisions can be directed to refining the model after defining the system or to studying alternative systems.

10.   A short time is required to analyze a model using the package compared to the time required to prepare a separate program for that model.

4.3   Input Data for Generation of the Geometry

The CAD package allows the user to conveniently define the geometry of the model to be examined. Three types of sections can be generated by the program. These include straight lines (horizontal, vertical or inclined), parts of circles and any other curved portion that can be adequately fitted using a cubic spline function.

Any system is initially defined by giving the package three parameters. The first parameter specifies the number of sections; the second, the total number of points which will describe those sections; and the third, is a number of parameters, each defines the number of points for each section. These parameters are fed to the package in addition to the coordinates of the points describing the modelled system. The type of the section will be automatically defined by the program according to the number of points in each section. The type of the section will be a

straight line if the number of the points is 2, a part of a circle if 3, and a curved part that will be fitted by a cubic spline if the segment is defined by more than three points.

Once the input data of the geometry is supplied to the program from a separate file or from the terminal, the package will automatically generate the geometry and display it on the screen of the terminal. The user can modify the geometry or revise the input data of the system and can take another look after the modification.

The program package allows the user to make translations and rotations for any point or section around any axis in the three dimensional space by giving the package the data required to make these operations in an interactive way. After making these operations the user can display the geometry on a terminal.

4.4   Input Data for Charge Simulation Model Generation

After generating the geometry, a charge simulation model of the system will be automatically created. The input data required consists of some parameters which are described in detail in the following paragraphs.

The first parameter given by the user is the number of contour points which is always the same as the number of the charges for each section in the modelled system. This gives the user the capability of varying the number of charges if a higher accuracy is required.

The second parameter defines the most effective controlling factor in the charge simulation model which is the assignment factor. This factor takes a positive or negative value according to how the charges should be located in the section. Positive assignment factors are given to the package if the charges will be allocated above a horizontal line segment, to the left of vertical or inclined line segment, above or to the left of a curved line that can be fitted by a cubic spline or to the left of a part of a circle if this part starts from the top to the bottom as in the case of spherical coordinates. Otherwise, negative assignment factors should be supplied to the package. The recommended range of the magnitude of the assignment factor is 0.7 to 1.5.

The third parameter defines the type of charges used to model each section. Three types of charges can be used in the package. These are ring charges, infinite line charges, and finite line charges. A combination of these charges can be used according to the shape of the geometry. Point charges are not included in the package because most of the modelled systems have rotational and translational symmetry. Even those systems which have not rotational symmetry are modelled by using ring charges with small radii.

Associated with each parameter defining the charge type there is another parameter which defines how that charge is located along the axis of symmetry. For the ring charges, this parameter is used to define whether the charge is perpendicular to the x, y, or z axis in the three-dimensional space. In the case of infinite and finite line charges, it is used to define whether the charges are parallel to the x, y, or z axis, respectively.

Three other parameters associated with each section in the model are used to specify the displacement of the axis of symmetry from the original reference axes x, y, and z.

If the system contains two dielectric regions, another two parameters are used to define the dielectric constant of the second dielectric material and the location of the section, i.e., whether or not this boundary section is adjacent to the air/vacuum region, adjacent to the second dielectric material or is an interface between the two materials.

The final parameter in the input data list is the specified potential associated with each modelled section. The package is implemented in such a way that the input voltage associated with each interface section between two dielectrics should be zero in the input data list. The CAD package is implemented in a way such that the user has the flexibility of entering the data of the modelled system in any way he desires. In other words, there is not any specific order for entering the data of the different sections of the model. This means that the user can start entering the data for any section and follow it by that for other sections in a random order. If the system contains two dielectric regions (dielectric / air or vacuum), the package will arrange the charges in such a way that the first set of charges will be located along the different sections of the

electrodes, the second set of charges will be located on the dielectric side of the interface(s) and the third set of charges will be located in the air side of the interface(s).

Once the input data are given to the program package, the package automatically calculates the coordinates of contour points and the corresponding charges, displays a graph of the contour points, charge locations or both together on the same graph according to the desire of the user. It allows the user to modify the location of the contour points and the corresponding charges by changing the number of points and the assignment factor in a boundary segment. It is recommended that the user see a plot of the charge locations in order to eliminate any undesired discontinuity in their alignment along the different sections of the system geometry.

After generating the contour points and the charge locations, the user can make translations and rotations of any set of contour points or charge locations around any axis in the three-dimensional space. After implementing these operations the user can display the modified contour and charge locations.

Two examples of input data for modelling two different systems are illustrated:

The first example is the hemispherical capped electrode above a grounded plane electrode as shown in Fig. 4.1. The data required to generate a charge simulation model for this problem consists of the number of sections to be modelled which are 2 in this example, the hemispherical part and the cylindrical part. The other parameter which should be given in the data set is the total number of points describing these sections which are 5 points and their coordinates specified in the 3-dimensional space; three points for the hemispherical part and two points for the cylindrical part. The displacements of the axis of symmetry of each section from the three reference axes are zeroes. The coordinates of the straight lines and any curve that can be fitted by a cubic spline fit are entered in cartesian coordinates while those for the parts of circles are entered in the spherical coordinate system. Both the hemispherical and the cylindrical parts are modelled using ring charges. The ring charges are perpendicular to the z-axis. Since the system is a single dielectric arrangement, no value is given to the parameter defining the dielectric

constant. Also no value is given to the parameter which defines the location of each section. The number of ring charges for the two sections are given to the package. The final parameter is the specified value of the potential associated with each section. The effect of the infinite grounded plane is taken into consideration by including the image charges. The package is implemented in such a way that the user has the choice to take the image charges into consideration by answering a prompting question. Table 4.1 summarizes the data input required to generate a complete charge simulation model of the system of Fig. 4.1. The data should be entered in the same order as they appear in the table.

The second example is a high voltage spherical electrode above a dielectric slab as shown in Fig. 4.2. The system has rotational symmetry about the z-axis and hence ring charges are used to model both the electrode and the dielectric slab. The number of points describing the arrangement is 5. Three are for the spherical electrode and two for the interface of the dielectric slab (the system consists only of two sections). The displacements of the axis of symmetry of each section from the three reference axes are zeroes. The ring charges are perpendicular to the z-axis for both sections. The number of ring charges modelling each section should be given to the package. Since this system is a two dielectric arrangement, the value of the dielectric constant of the second material should be specified. Also, the parameter which defines the location of the section should be given in the list of data input. The final parameters are the specified potentials for the spherical electrode $V = 1$ and $V = 0$ for potential discrepancy at the dielectric interface. Table 4.2 summarizes the data required to generate the geometry and to simulate the arrangement using the Charge Simulation Computer-Aided Design package.

As mentioned before, the user can model this arrangement starting with the data for the spherical electrode section and followed by the data for the interface or he can start by entering the data for the interface and follow that by the data for the spherical electrode section. Whatever section with which he begins, the order of the input data parameters for each section should be the same as they appear in the table. The effect of the grounded electrode is taken into consideration
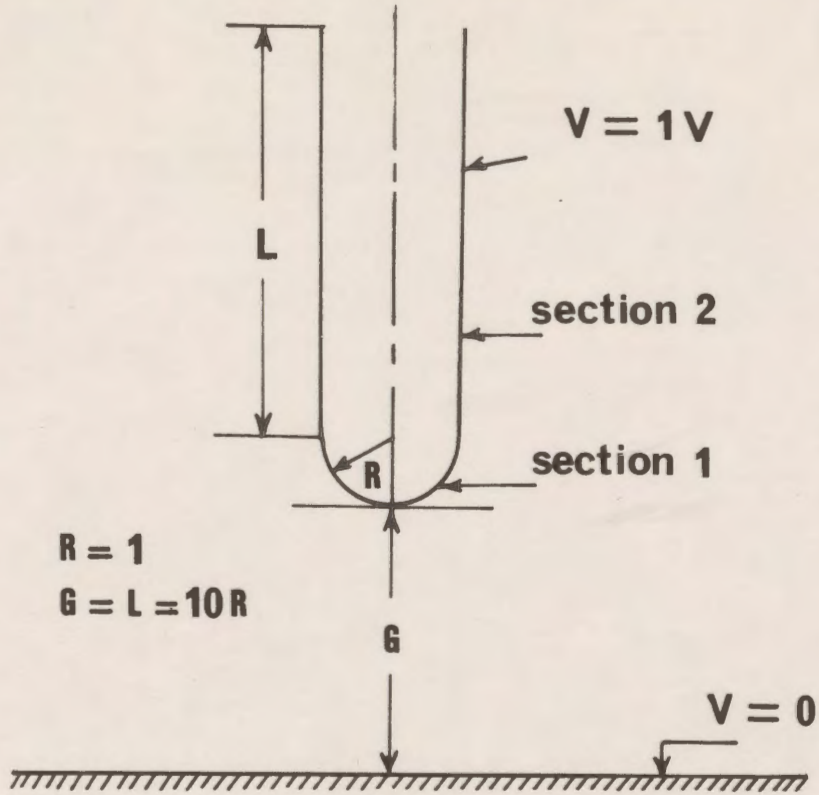
Figure 4.1: A hemispherical capped electrode above a grounded plane.
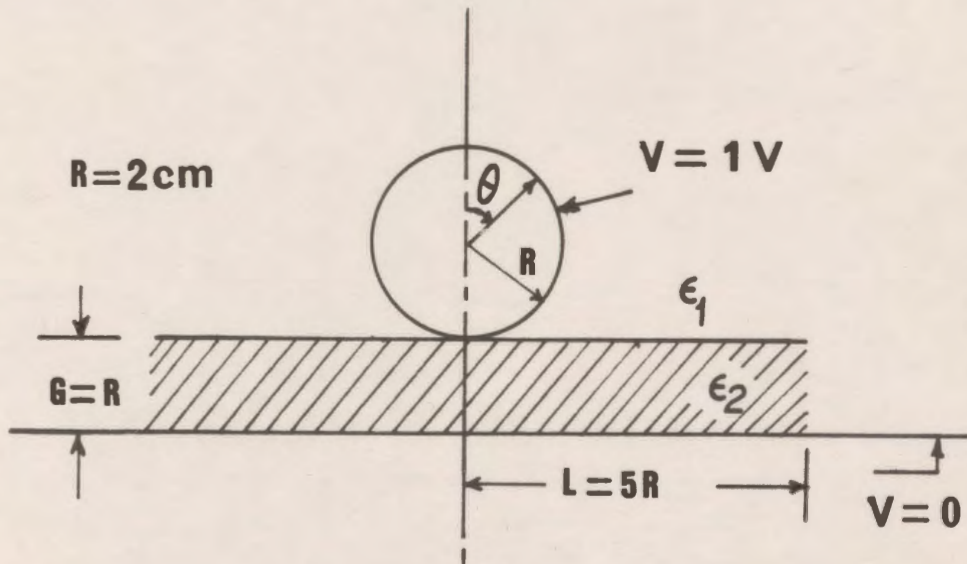
Figure 4.2: A high voltage spherical electrode above a plane dielectric slab.

n_{Ptot}	n_{stot}	ϵ_r	n_s	i	X_i	Y_i	Z_i	np(ns)	REX(ns)	REY(ns)	REZ(ns)	V(ns)	Kρ(ns)	Kz(ns)	Ks(ns)	αj(ns)	nb(ns)
5	2																
			1	1	0	0	11										
				2	1	90	90										
				3	1	180	90										
			2	4	0	1	11										
				5	0	1	21										
			1					3	0	0	0	1		1	3	1.25	8
			2					2	0	0	0	1		3	3	0.75	30

Table 4.1: Input data required to generate a charge simulation model of the system of Fig. 4.1.

n_{ptot}	n_{stot}	ϵ_r	n_s	i	X_i	Y_i	Z_i	$np(ns)$	$REX(ns)$	$REY(ns)$	$REZ(ns)$	$V(ns)$	$Kp(ns)$	$Ka(ns)$	$Ks(ns)$	$aj(ns)$	$nb(ns)$
5	2	3.8	1	1	0	0	4										
				2	2	0	90										
				3	2	0	180										
			2	4	0	0	2										
				5	0	10	2										
			1					3	0	0	0	1	3	1	3	1.25	30
			2					2	0	0	0	0	1	1	3	-0.75	20

Table 4.2: Input data required to generate a charge simulation model of the system of Fig. 4.2 without explicitly modelling the grounded electrode.

by including the image charges. Of course the user has the choice of modelling the grounded electrode instead of taking the images into consideration. In this case the data set in Table 4.2 should be modified such that the number of sections in the arrangement becomes 3 and the total number of points describing the system is 7. Also the data for the third section should be added to Table 4.2. A complete data set for modelling the arrangement without including the images but modelling the grounded electrode is shown in Table 4.3. Definitions of the symbols used in Figs. 4.1 and 4.2 and in the previous tables are given in Appendix B.

Figure 4.3a shows the distribution of contour points and charge locations for modelling the sphere/slab arrangement by taking the image charges due to the presence of the grounded electrode into consideration. Fig. 4.3b also shows the distribution of the contour points and charge locations for modelling the same arrangement, modelling the grounded electrode explicitly instead of using the image charges.

nPtot	nstct	ϵ_r	n_s	i	X_i	Y_i	Z_i	np(ns)	REX(ns)	REY(ns)	REZ(ns)	V(ns)	Kp(ns)	Kz(ns)	Ks(ns)	αj(ns)	nb(ns)
7	3	3.8															
			1	1	0	0	4										
				2	2	0	90										
				3	2	0	180										
			2	4	0	0	2										
				5	0	10	2										
			3	6	0	0	0										
				7	0	10	0										
			1					3	0	0	0	1	3	1	3	1.25	30
			2					2	0	0	0	0	2	1	3	– 0.75	20
			3					2	0	0	0	0	2	1	3	– 0.75	20

Table 4.3: Input data required to generate a charge simulation model of the system of Fig. 4.2 explicitly modelling the grounded electrode.
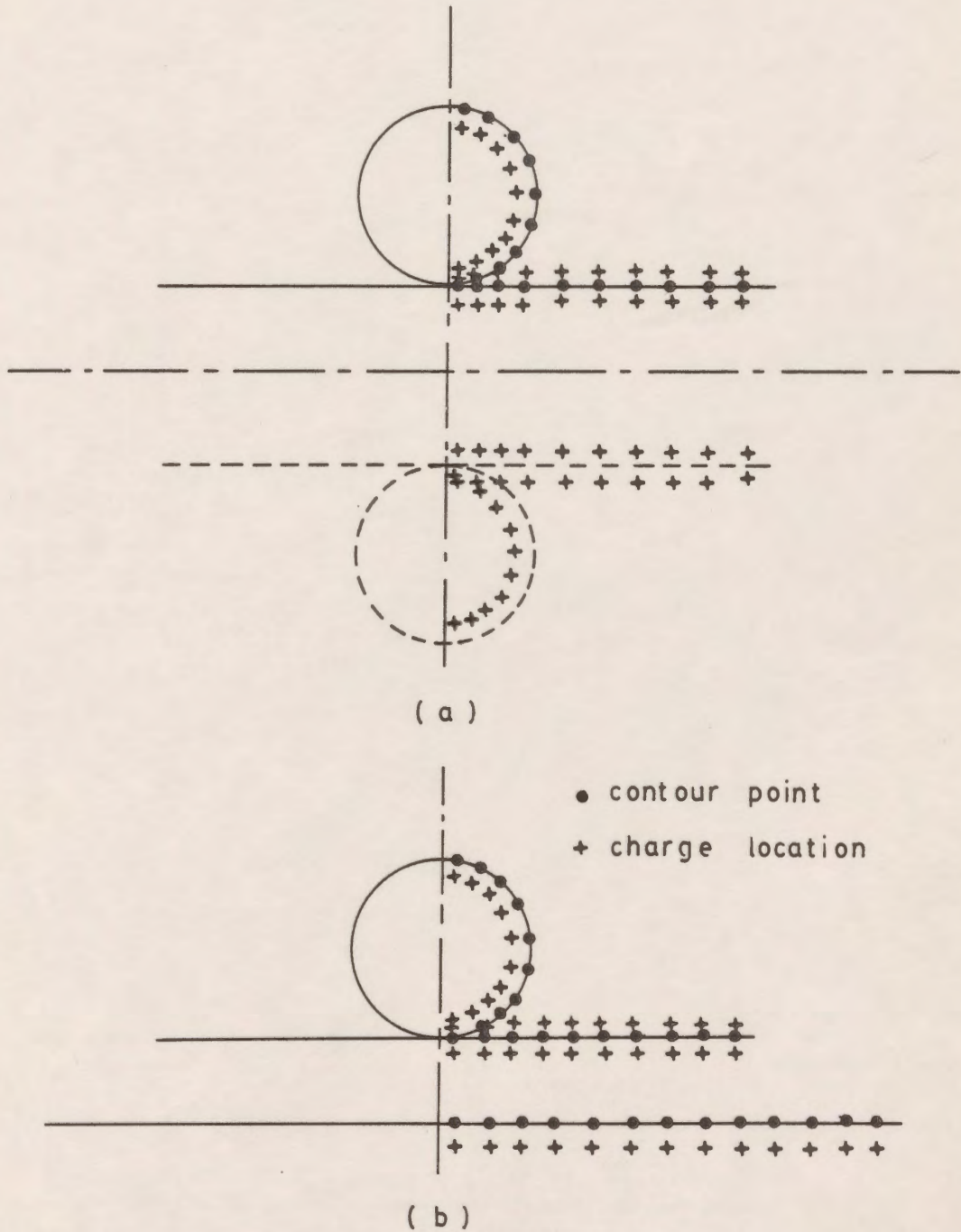
Figure 4.3: Distribution of contour points and charge locations.
(a) without modelling the grounded electrode explicitly
(b) explicitly modelling the grounded electrode

4.5   Output Options

4.5.1   Modelling Quality Measures

The criteria for evaluating the quality of the solution of the model are examined. These criteria are the potential error and the tangential electric field error at the electrodes, the potential discrepancy, the tangential field discrepancy and the normal field discrepancy along the dielectric interfaces. These segments of electrodes and interfaces can be any type of straight line, part of a circle, or any other curved part that can be fitted by a cubic spline function as described before. These errors and discrepancies can be determined and plotted along any portion of the described loci as the user desires.

4.5.2   Field Features Of Interest

The forms of the field features that can be selected for display are:

1.   A graph of electrostatic potential versus position along any path defined by the user. These paths are usually straight lines, parts of a circle or any other curved line that can be approximated by a cubic spline in the region of interest. Also, paths representing interfaces between different media are considered in the package.

2.   Graphs of electric field components along paths as defined in 1;

3.   Graphs of electric field magnitude along paths as defined in 1;

4.   Two dimensional equipotential contour plots in the region of interest.

4.5.3   Modification Of The Model

After considering the quality of the solution of the model, decisions can be directed to modifying it if the evaluation criteria are not within acceptable limits. The user can modify the model by deleting, adding, or re-positioning boundary points and/or modelling charges as deemed necessary. This can be done by changing the assignment factor and keeping the number of boundary points or charges fixed for repositioning the charges only or by changing the number of boundary points (or charges) keeping the assignment factor fixed or changing both for repositioning the charges and the contour points together.

4.6   Alternative Approaches for Programming

The basic requirements of the Computer-Aided Design package can be implemented in several ways, some of which are more convenient to the user, but which may be more challenging to achieve. Three alternative ways of programming will be discussed below.

4.6.1   Wylbur Implementation:

If the package is implemented in the Wylbur system, it will be of necessity a quasi-batch (as opposed to interactive) package. This is the most cumbersome for a user to use, since all decisions about user input must be made before the "run". If more flexibility is desired, this may be incorporated through the use of a sequence of segmented runs, for which output is examined at each stage in order to make decisions on parameter values and other user choices which will be used in the following stages.

4.6.2   CMS Implementation:

If the package is implemented using CMS (The Conversational Monitor System), there is a minimal change from using Wylbur, and also minimal additional flexibility is obtained. Since the runs can be "on-line", the segmenting referred to above can simply be pauses in the on-line run, at which points the user is prompted for the input required for the next stage after being presented with the results of the immediately prior stage of computer calculation. For example, the user inputs the information describing the geometry as numerical data, the package determines the coordinates of boundary points and charge locations, displays them in a graphical manner, and pauses to allow the user to decide whether to change any aspect of the model. These changes must be entered (again as numerical data), and the package released to compute the charge simulation solution for that model. Similar interaction takes place after each stage of calculation.

4.6.3   Text/Graphics Implementation

It should be apparent that the use of graphics to present the details of the model and the resulting field relationships is quite important. Using the capabilities of the CAD/CAM system, it is possible to implement the CAD package in a much more convenient way.

With the VT-240 medium resolution terminals, the graphical displays can be quite detailed, and colour could be used where it represents an advantageous method of displaying the results. Working with the VAX 11/785 in an on-line manner, a screen cursor could be controlled from the keyboard to find points on the screen corresponding to the location of charges and boundary points or to find the potential and the electric field at a specific point on the screen.

It is found that the most convenient implementation among the three alternative approaches is the last one. Therefore the Charge Simulation Computer-Aided Design package was implemented using the VAX 11/785 located in the CAD/CAM system, with access provided through a VT-240 terminal. FORTRAN 77 is used throughout the programming.

4.7   *Mathematical Aids Used in the CAD Package*

Mathematical techniques are required to implement the requirements of the Computer-Aided Design package. These include transformations method in the three-dimensional space, Chebyshev distribution of points and cubic spline interpolatory scheme. These techniques are discussed breifely in the following sections.

4.7.1   Three-Dimensional Transformations

Methods for translating and rotating objects in three dimensions are extended from two dimensional methods by including considerations for the z-coordinate [76]. A translation is now accomplished by specifying a three-dimensional translation vector. Extensions for three-dimensional rotations are less straightforward, since rotations can now be performed about an axis with any spatial orientation. Geometric transformation equations can be expressed in terms of transformation matrices. Any sequence of transformations is then represented as a single

matrix, formed by concatenating the matrices for the individual transformations in the sequence. Details of the three dimensional transformations and the matrices representations of translation and rotation implemented in the package are given in Appendix (C)

4.7.2   Chebyshev Distribution Of Points

The CAD package allows the charges to be located in one of two different distributions according to the user desire. The two alternatives are a uniform distribution which distributes the contour points and the corresponding charges at equally spaced points and a Chebyshev distribution. Although the Chebyshev distribution of points is based on minimizing the maximum error in a polynomial approximation to the smooth curve through those points, it is used here to determine (empirically) whether it results in any improvement in the potential error along boundary segments associated with those points [77]. Details of Chebyshev distribution is given in Appendix (D).

4.7.3   Cubic Spline Interpolatory Scheme

One of the capabilities of the CAD package is that it can be used to model systems which contain any curved sections which can be fitted by employing an appropriate interpolating scheme.

Several interpolation techniques are available for approximating functions and "smoothing" data such as Taylor's polynomials, interpolation polynomials, and splines. One of the most effective and direct ways to approximate a function defined at a finite set of points is to fit a polynomial of suitable degree to the discrete data. In addition to its simplicity, polynomial approximation has some advantageous properties. But the chief disadvantage is that it may become excessively oscillatory between the nodes as the number of points to be interpolated increases. To eliminate this drawback and also when the curve or data set has more erratic features, piecewise polynomial approximation and splines have some appealing advantages.

Specific situations for which splines afford advantages over interpolation polynomials are [78]:

1.   The number n of data points to be interpolated is moderate to large (e.g., n is greater than 20).

2.   The data points are associated with some known or unknown function F(x) the derivatives of which are large or do not exist.

3.   The data points arise from a natural or non-mathematical source.

Spline functions are piecewise polynomials with derivatives constrained at the common boundary points of the polynomial pieces for the purpose of making the resulting function smooth at the node points.

Cubic (degree 3) interpolating splines are the most common splines in the application literature. Reasons for this popularity include their ability to interpolate data with curves that look smooth. Lower-degree splines do not disguise the data points well, and higher-degree splines have the instabilities inherent in high- degree polynomials. Cubic splines appear to flow smoothly and indeed possess a minimum curvature property. The construction of a cubic spline interpolatory scheme is described in Appendix (E).

4.8   Limitations of the Package

The limitations of the CAD package are:

1.   Point charges are not implemented in the program since most of the modelled systems in this work have rotational and translational symmetry and therefore ring, finite and infinite line charges are used. The systems which have not symmetry about a common axis are modelled by using ring charges of small radii.

2.   The package is not implemented to model systems which have more than two dielectric media.

3.   Sinusoidal time varying fields are not considered in the package.

4.   There is no limitation on the numbers of charges and boundary points used. The only limitation regarding these numbers are the limitations on the computer capacity and storage memory. The approximate maximum number of charges which can be used without using disk storage during the run is 900 charges.

5.   The computation time is another imposed limitation on the package since as the number of modelling charges increases the execution time increases. Typical run times for 50, 100, and 150 charges are 4, 27, and 112 seconds, respectively while the run time for 500 charges is approximately 90 minutes.

6.   Three dimensional field plots are not implemented in this package.

7.   Space and surface charges are not taken into consideration.

Chapter V

VERIFICATION OF THE CHARGE SIMULATION BASED CAD

PACKAGE

5.1   General

The work presented in this chapter is based on the application of a Charge Simulation Computer-Aided-Design package for several standard electrode systems for calculating the potential and the electric field. A comparison is made with the results obtained from analytical solutions in order to check the validity and the accuracy of the numerical method. In addition, solution quality measures are provided.

5.2   Application of the CSM to Spherical Electrodes

5.2.1   Isolated Spherical Electrode

The CSM is applied to the isolated spherical electrode shown in Fig. 5.1. The sphere has a radius of 2 cm and an applied voltage of 1 V ($R_o = 2cm, V_o = 1V$). The sphere is simulated by 10 ring charges corresponding to 10 contour points distributed around the right hemispherical part of the electrode (from $\theta = 0°$ to $\theta = 180°$). Figure 5.2 shows the distribution of the contour points and the corresponding charges. The assignment factor is kept at 1.5 throughout the calculations.

The potential at any point in the space due to an isolated spherical conductor is given by,

$$V = \frac{V_o R_o}{r'} \tag{5-1}$$

where r' is the distance from the center of the sphere.

The potential is calculated using (5-1) and the CSM package. The difference between the two solutions is plotted as a function of θ for r'= R_o and $2R_o$ in Figs. 5.3 and 5.4 respectively.
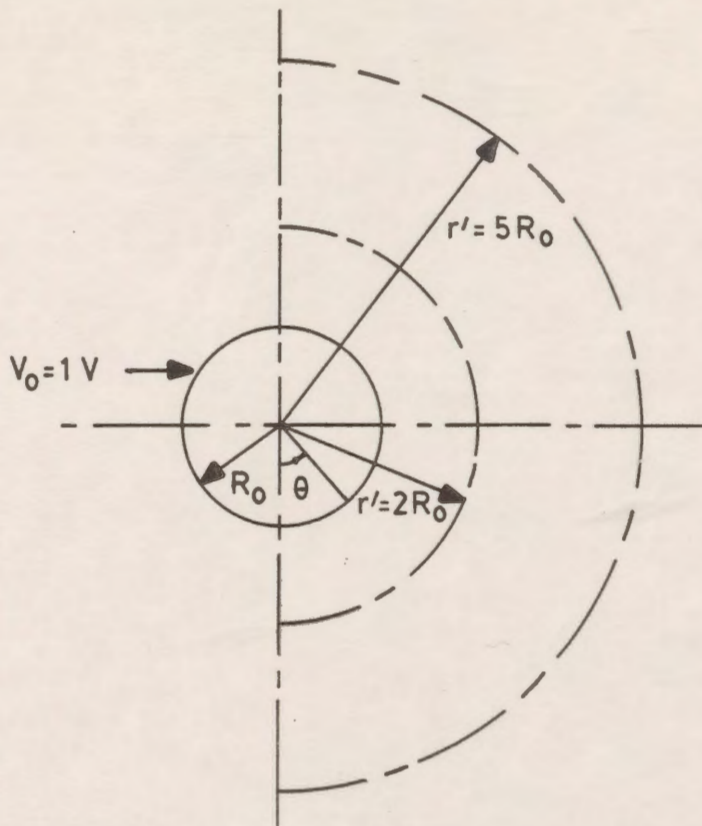
Figure 5.1: Isolated spherical electrode.
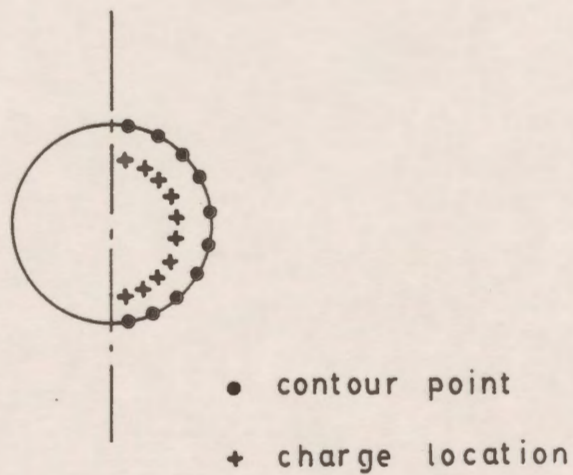
Figure 5.2: Distribution of contour points and charges in the isolated spherical electrode.

The electric field is given by,

$$E = -\frac{dV}{dr'} = \frac{V_o R_o}{r^2}$$

The normal field error which is defined as the difference between the analytical and the numerical solutions divided by the analytical value of the electric field is plotted as a function of θ for $r' = R_o$ and $2R_o$.

Fig. 5.3a shows the distribution of the potential error around the surface of half the sphere (from $\theta = 0°$ to $\theta = 180°$) as a percentage of the applied potential. The maximum error is found to be $0.2 * 10^{-3}\%$.

Fig. 5.3b shows also the distribution of the normal electric field error which has a maximum value of 0.002%.

Figs. 5.4a and 5.4b present the distribution of both the percentage potential and the normal field errors for a locus which has a radius of $r' = 2R_o$. It is clear from these figures that the errors decrease as the radius increases from the surface of the sphere.

The errors are also plotted in Figs. 5.5a and 5.5b, respectively for $r' = 5R_o$.

Figs. 5.6a and 5.6b show the distribution of the potential and the normal field errors for a radial line which extends from $r' = R_o$ up to $r' = 5R_o$ and $\theta = 30°$. It is clear that the maximum percentage errors are very small.

5.2.2 Isolated Spherical Electrode With Rotated Axis Of Symmetry

The CSM is applied to the same spherical electrode with the axis of symmetry rotated by $-45°$ about the x-axis. Fig. 5.7 shows the distribution of contour points and charge locations.

The distributions of the potential and the normal field errors around the modelled hemispherical part (from $\theta = 0°$ to $\theta = 180°$ after rotation) are shown in Figs. 5.8a and 5.8b, respectively.
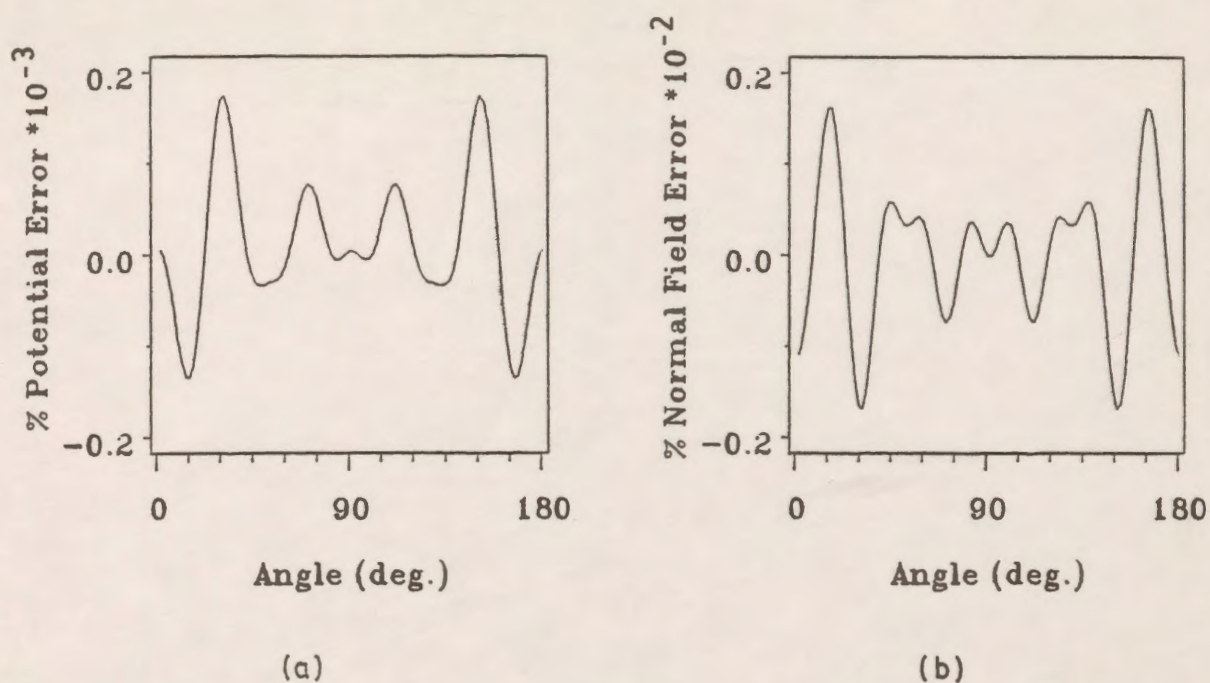
Figure 5.3: Distribution of errors on the isolated spherical electrode surface ($R_o = 2$ *cm.*).
(a) potential error distribution
(b) normal field error distribution
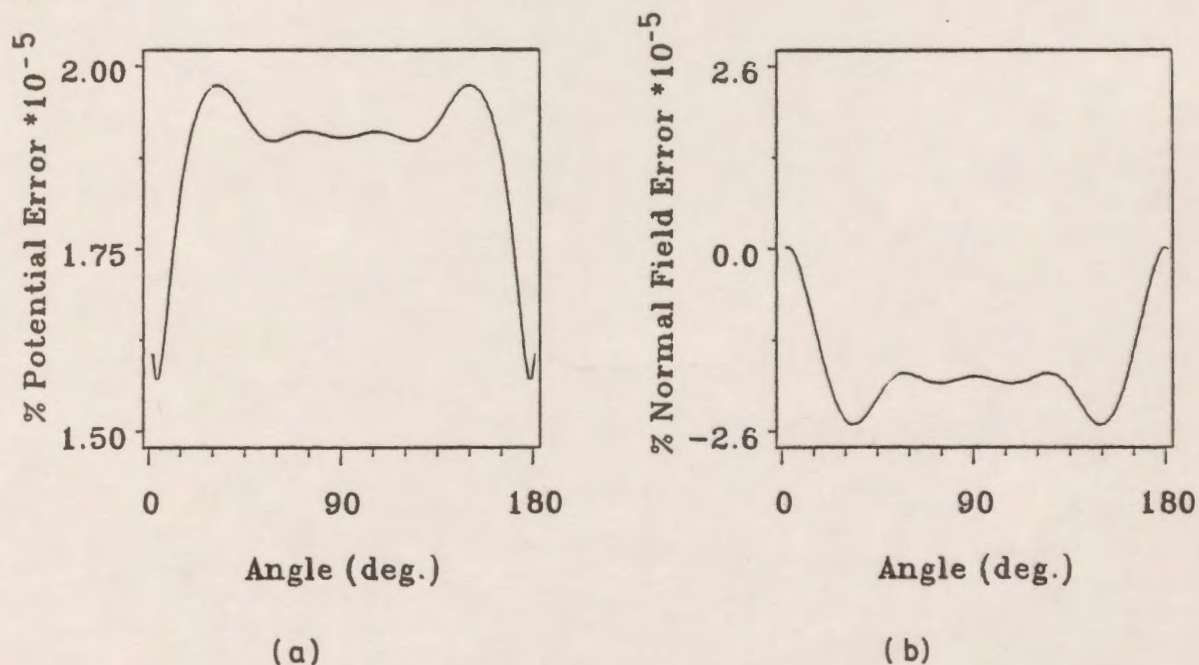
Figure 5.4: Distribution of errors on a locus (surface) of radius r'=2R_o.
(a) potential error distribution
(b) normal field error distribution
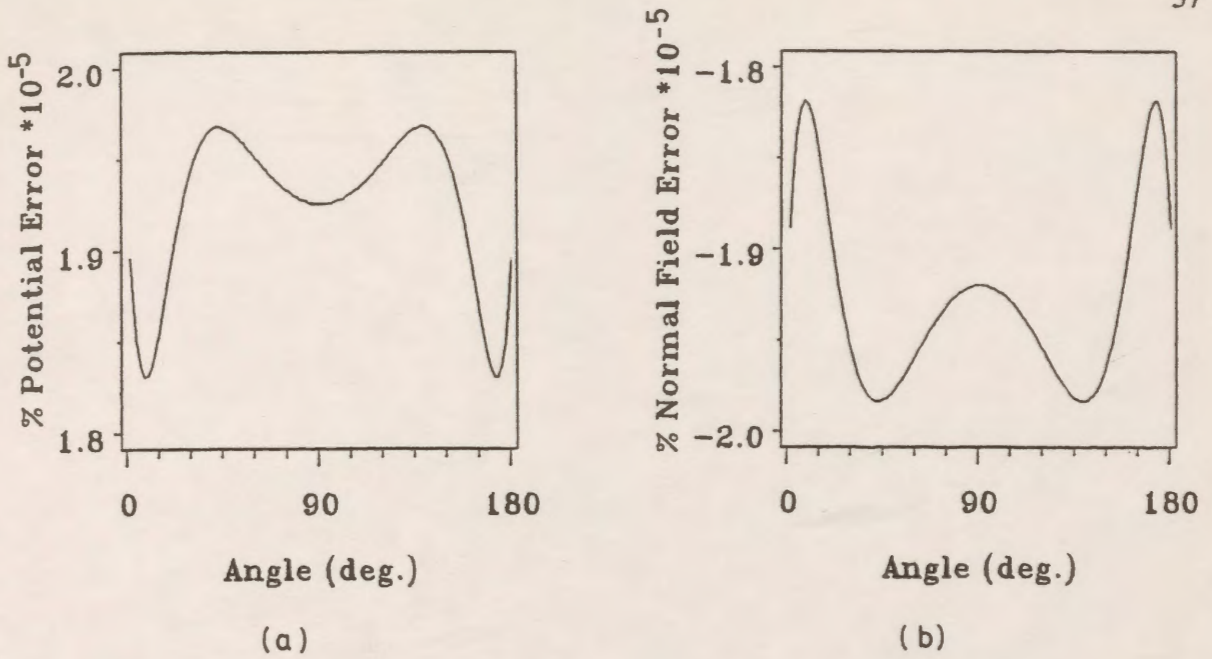
Figure 5.5: Distribution of errors on a locus (surface) of radius r'=5R$_o$.
      (a) potential error distribution
      (b) normal field error distribution
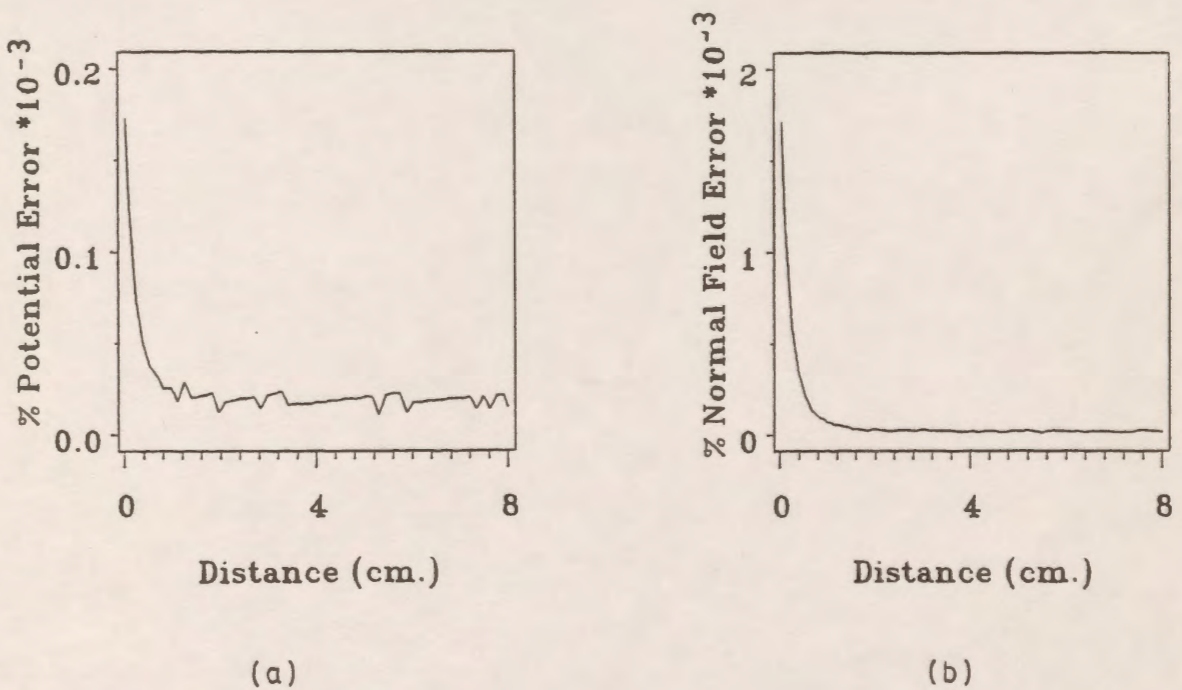
Figure 5.6: Distribution of errors along a radial line with a radius r'=5R$_o$ and θ=30°.
      (a) potential error distribution
      (b) normal field error distribution
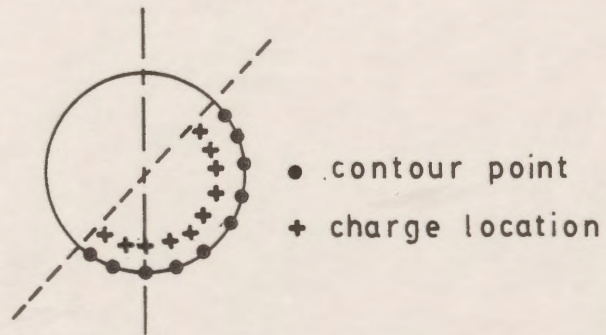
Figure 5.7: Isolated spherical electrode with rotated axis of symmetry.

Figs. 5.9a and 5.9b show the distribution of the potential and the normal field errors for the other half of the sphere which is specified from $\theta = 0^{\circ}$ to $\theta = -180^{\circ}$. It is clear that the errors are the same for both halves of the sphere since the sphere is isolated and this case corresponds exactly to the case of the sphere without rotation of the axis of symmetry.
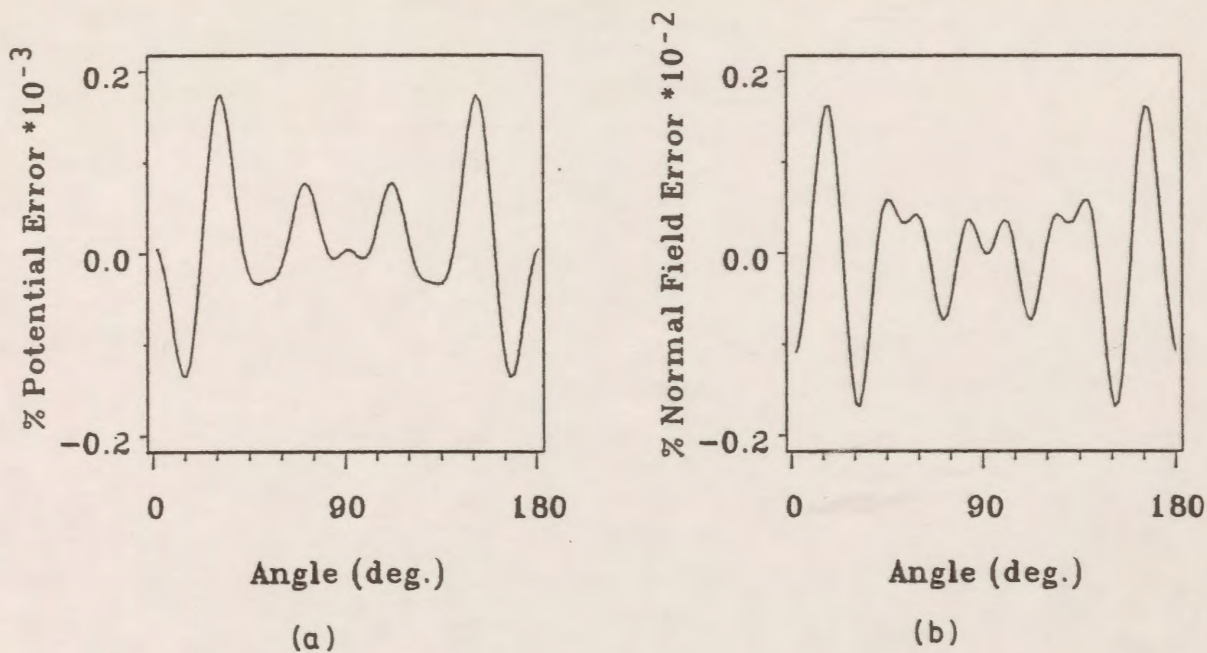
Figure 5.8: Distribution of errors on the right hemispherical electrode part at $r'=R_o$.
(a) potential error distribution
(b) normal field error distribution
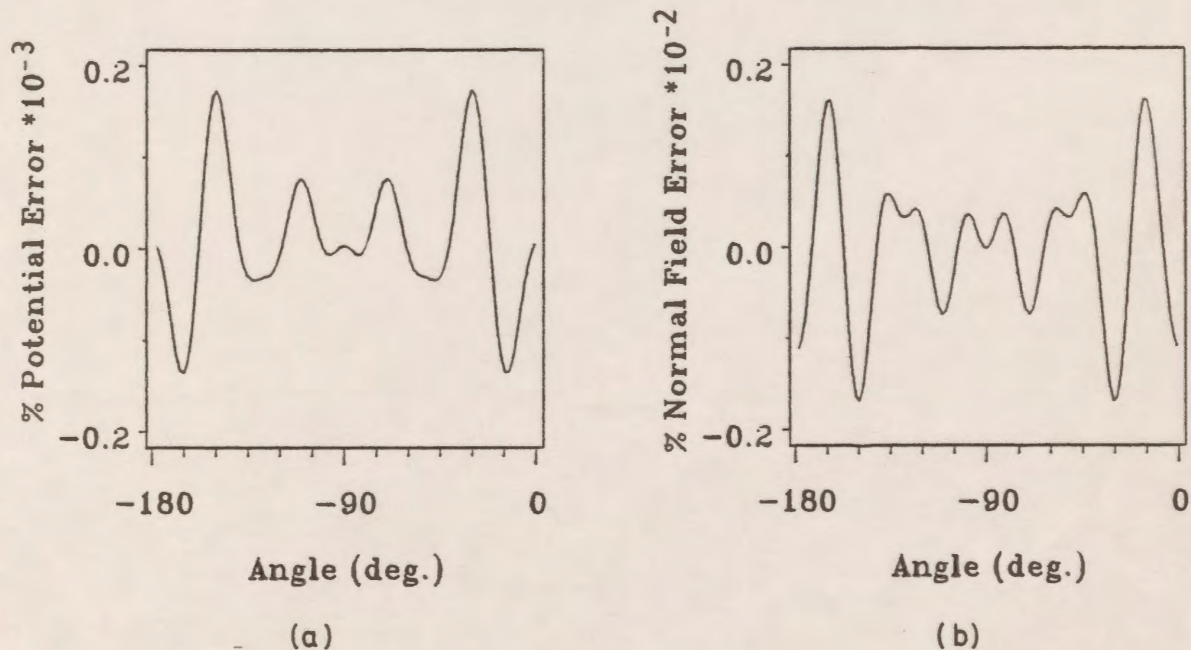
Figure 5.9: Distribution of errors on the left hemispherical electrode part at $r'=R_o$.
(a) potential error distribution
(b) normal field error distribution

5.2.3   Spherical Electrode With Rotated Axis Of Symmetry Above A grounded Plane.

5.2.3.1   Modelling Using One Set of Contour Boundary Points

The spherical electrode is modelled by using one set of contour points (and charges) distributed around that portion of the surface of the sphere which extends from $\theta = 0°$ to $\theta = 180°$ after rotation about the x-axis by -45°. Since the grounded plane is included, the spherical electrode model no longer has a symmetry around the main z-axis after rotation. Fig. 5.10 shows the contour points and charge locations for this case.

Figs. 5.11a and 5.11b show the percentage potential error and the tangential field difference distributions, respectively along the surface of the sphere (from $\theta = 0°$ to $\theta = 180°$ after rotation). Figs. 5.12a and 5.12b also show the same errors but for the other part of the sphere which has not been explicitly modelled. It is clear from these plots that the values of the errors are large compared to those values obtained for the spherical electrode without a grounded plane.
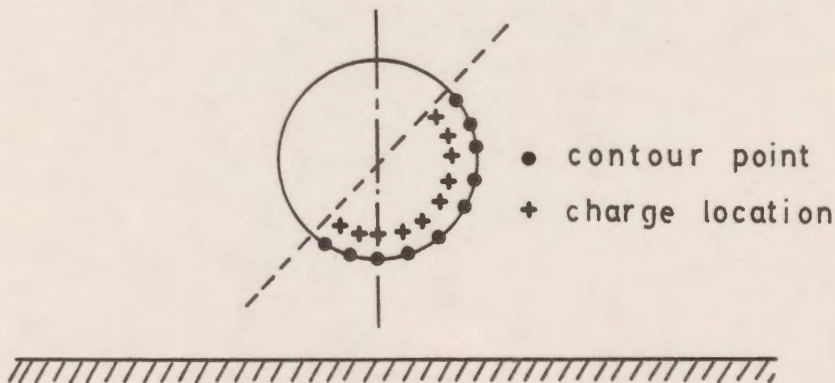
Figure 5.10:   Distribution of contour points and charges for the rotated spherical electrode above a ground plane.
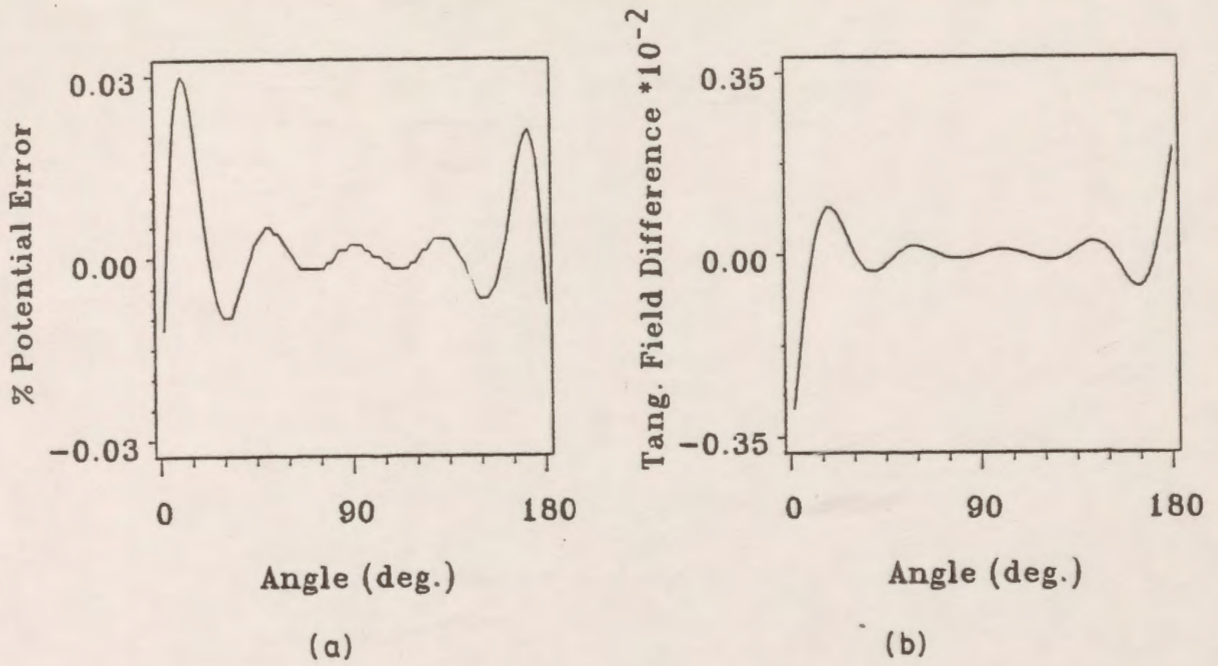
Figure 5.11: Distribution of errors on the right hemispherical part of Fig. 5.10 at r'=R_o.
(a) potential error distribution
(b) tangential field difference distribution
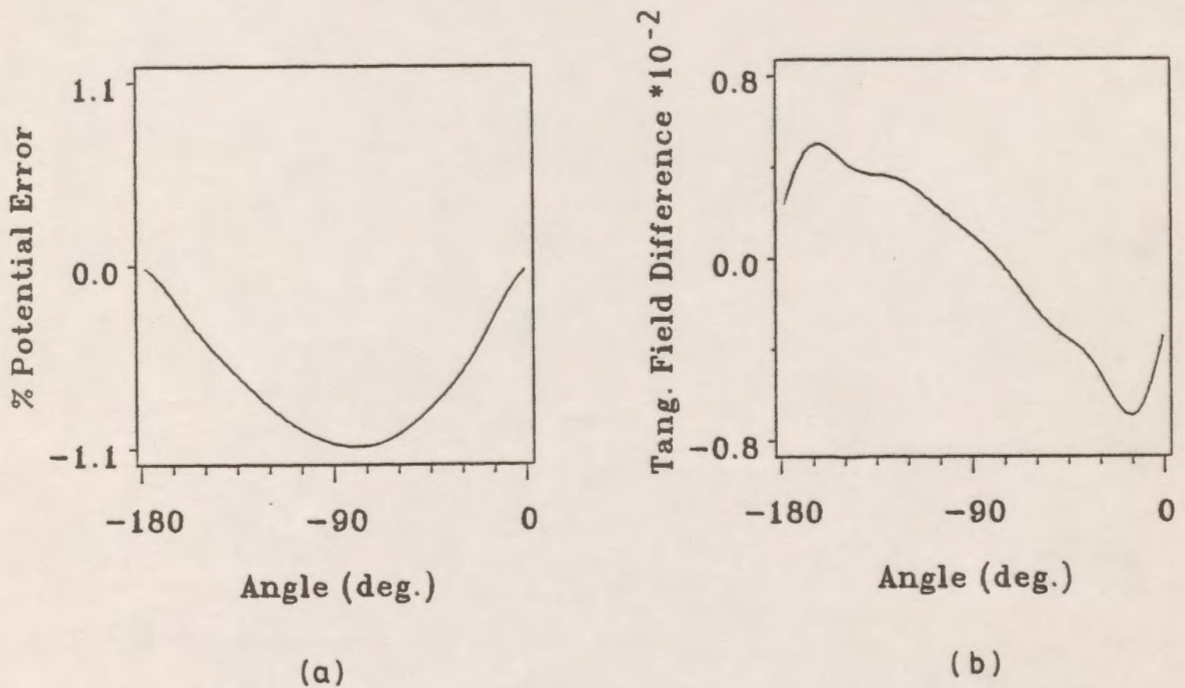
Figure 5.12: Distribution of errors on the left hemispherical part of Fig. 5.10 at r'=R_o.
(a) potential error distribution
(b) tangential field difference distribution

5.2.3.2 Modelling By Using Two Sets Of Contour Boundary points

The spherical electrode is modelled by using two sets of contour points (and ring charges) to compensate for the lack of symmetry when a grounded plane is included and the axis of symmetry is tilted by -45° around the x-axis as shown in Fig. 5.13. The two sets of contour points are used to apply the boundary conditions to a better distribution of points on the entire sphere surface. The ring charges are distributed such that there is a displacement between the centers of each pair of charges corresponding to boundary points on each side of the sphere. The symmetry is destroyed by tilting the axis to determine the degree to which small values of quality measures depend on symmetry.
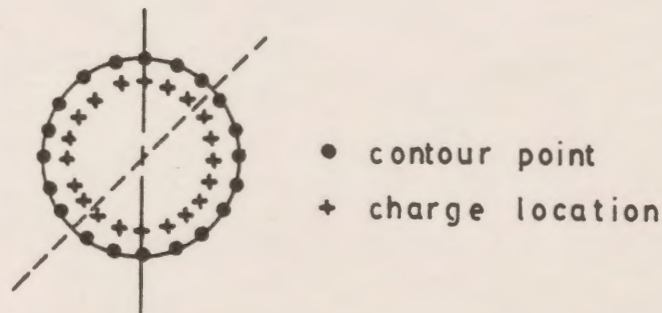
Figure 5.13: Distribution of contour points and charges around the whole electrode boundary.

Figs. 5.14a and 5.14b present the distribution of the potential error and the tangential field difference, respectively around the surface of the sphere from $\theta = 0°$ to $\theta = 180°$ after rotation. The distribution of the same errors along the other part of the sphere (from $\theta = 0°$ to $\theta = -180°$) after rotation is shown in Figs. 5.15a and 5.15b, respectively.

It is clear from Figs. 5.14 through 5.15 that the errors are very small since we compensated for the lack of symmetry by modelling the whole boundary of the spherical electrode in the y-z plane.
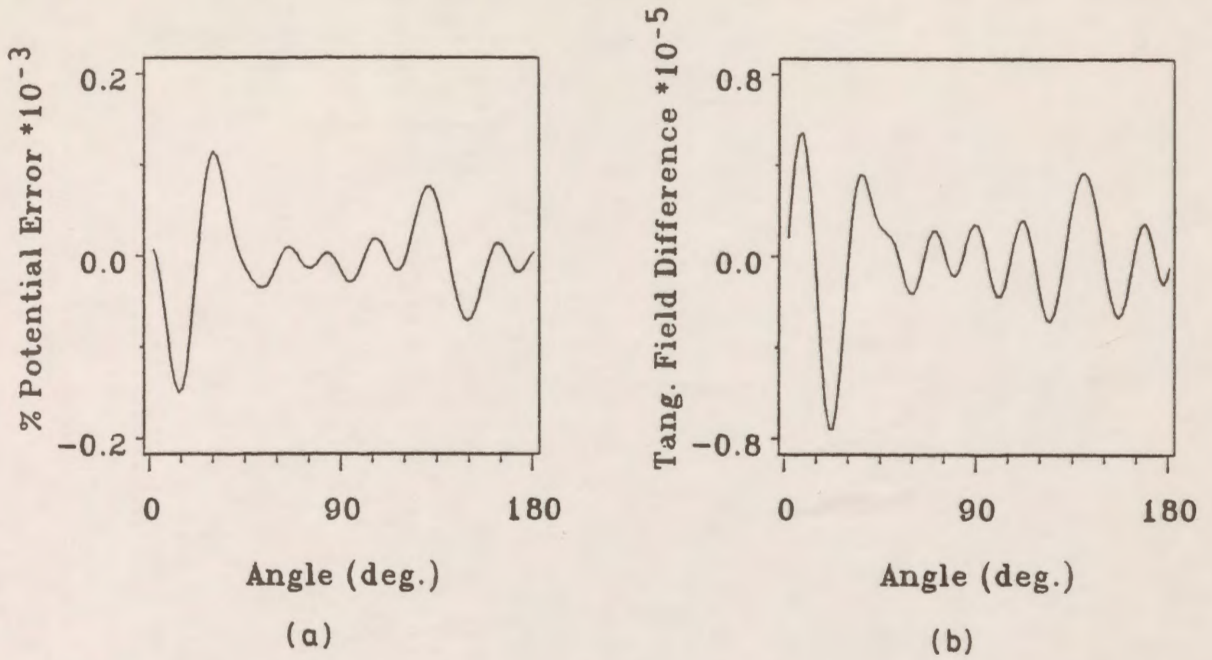
Figure 5.14: Distribution of errors on the right hemispherical part of Fig. 5.13 at r'=R_o.
(a) potential error distribution
(b) tangential field difference distribution
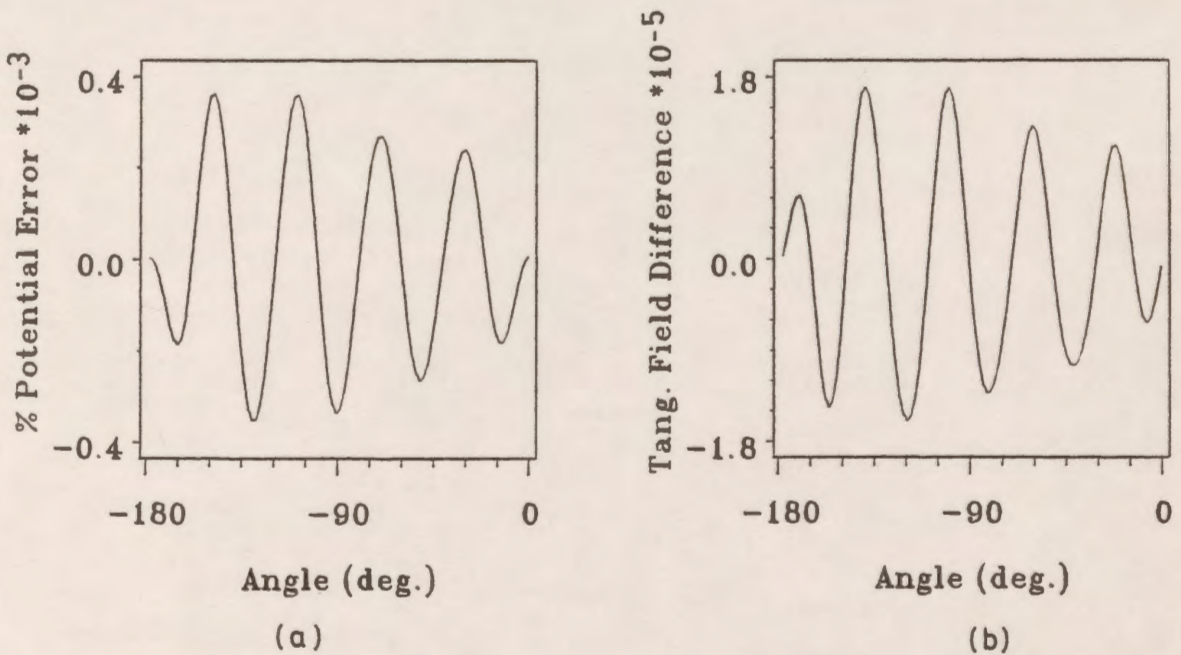
Figure 5.15: Distribution of errors on the left hemispherical part of Fig. 5.13 at r'=R_o.
(a) potential error distribution
(b) tangential field difference distribution

5.3 Calculation of the Electric Field in A sphere Gap

The electric field in a sphere gap is calculated by using the Charge Simulation Computer-Aided-Design package. A solution was obtained analytically through the direct solution of Laplace's equation in dipolar coordinates by Carter [79]. Detailed graphical solution quality measures of the Charge Simulation method for this system are provided. Two cases are studied: 1. symmetrically applied positive and negative voltages, and 2. unsymmetrical gap for which one electrode is grounded. The zero reference of the potential is at infinity for both cases.

5.3.1 Solution Quality Measures

The sphere gap may be used in two distinct ways: as a symmetrical gap, in which the spheres carry equal and opposite charges and are at equal and opposite potentials, and as an unsymmetrical gap, in which one sphere is earthed. Fig. 5.16 shows the two systems. The number of charges used for modelling is chosen as 3 charges per centimeter of arc length of a 1 cm radius spheres and the assignment factor is kept at 1.2 everywhere in the model.
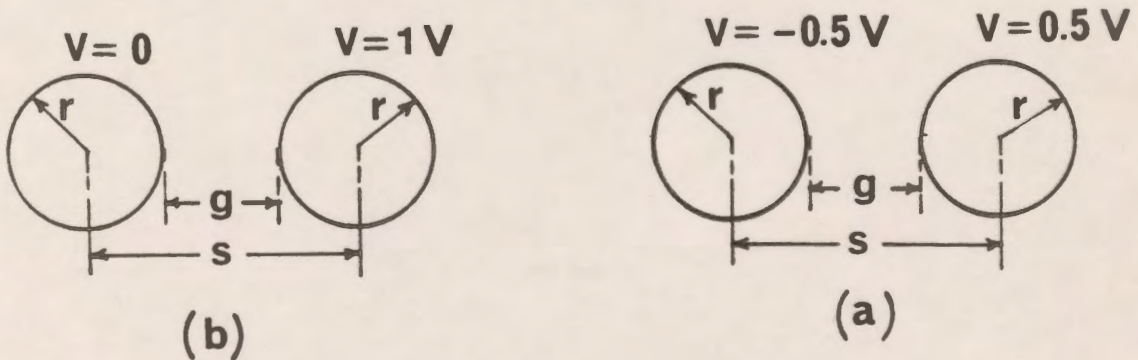
Figure 5.16: Different systems for field calculations.
(a) symmetrical gap form
(b) unsymmetrical gap form

Figs. 5.17a and 5.17b show the distribution of the potential error and the potential difference along the surfaces of the high and the low voltage spheres respectively, for the unsymmetrical gap. The maximum percentage potential error was found to be less than 0.004% on the surface of the HV sphere.

The tangential field difference distributions along the surfaces of the spheres are shown in Fig. 5.18. It is found also that the maximum value of that difference is approximately $0.4 * 10^{-3}$.

The potential errors and the tangential field differences are plotted for the symmetrical form of the gap spheres. Figs. 5.19a and 5.19b show the potential error distribution along the surface of the high and low voltage sphere, respectively. The maximum percentage error in the potential is less than 0.005%.

Fig. 5.20 shows the distribution of the tangential field difference around the surface of the high and low voltage spheres for the symmetrical gap spheres. The maximum tangential field difference was found to be less than $0.3 * 10^{-3}$.

The errors on the HV and LV spheres in the symmetrical system case are almost the same while these errors are not the same on the surfaces of the HV and LV spheres for the unsymmetrical system case.

5.3.2   Maximum Voltage Gradient in the Sphere Gap

For the symmetrical gap, the potential is constant over each of the two spheres and is taken as +0.5 V and -0.5 V. The spheres are separated by a distance g and each sphere has a radius r. For the unsymmetrical gap, one of the spheres (high-voltage sphere) is connected to 1.0 V and the other sphere (low- voltage sphere) is connected to 0.

The mean voltage gradient between the spheres along the line joining their point of nearest approach is defined as

$$E_{mean} = \frac{V_d}{g} = \frac{V_d}{s - 2r}$$
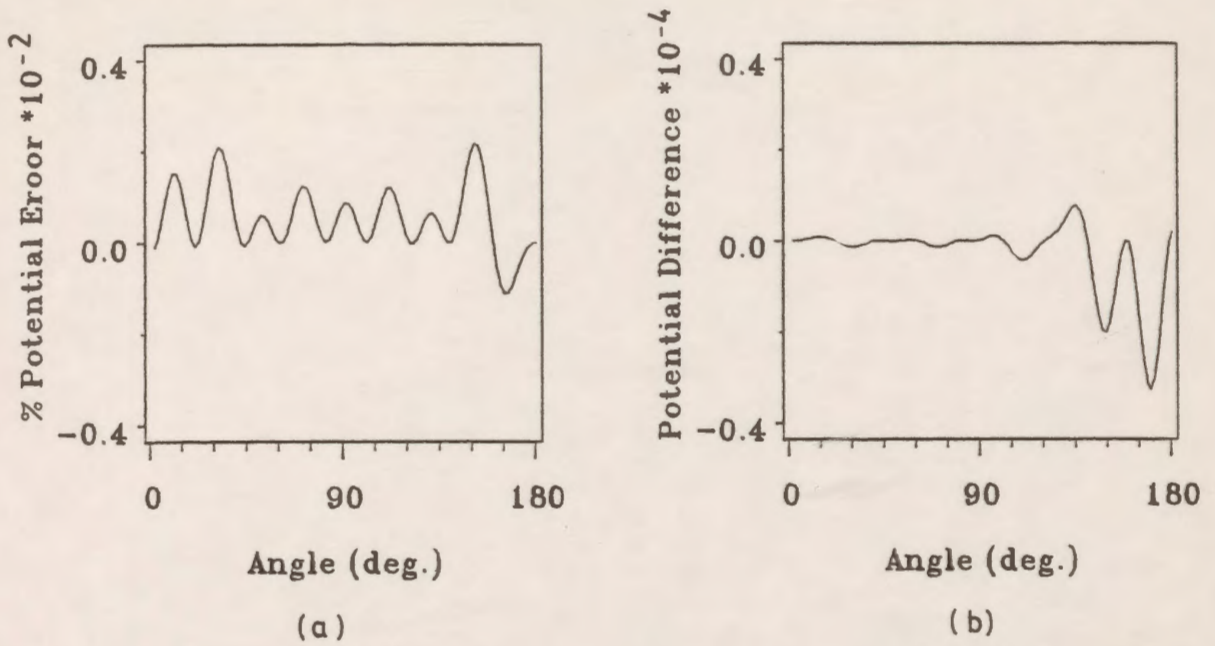
Figure 5.17: Potential error and potential difference distributions for the unsymmetrical gap form on the lower half surfaces of the spheres.
(a) error on the HV sphere
(b) difference on the LV sphere
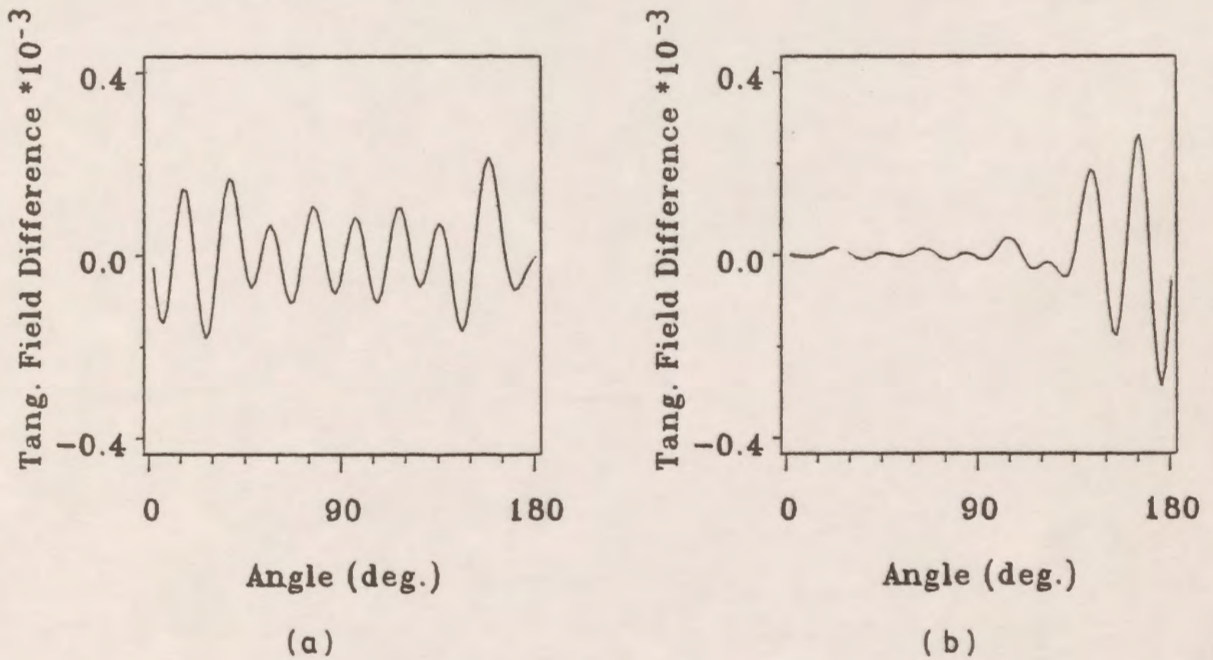
Figure 5.18: Tangential field difference distributions for the unsymmetrical gap form on the lower half surfaces of the spheres.
(a) difference on the HV sphere
(b) difference on the LV sphere
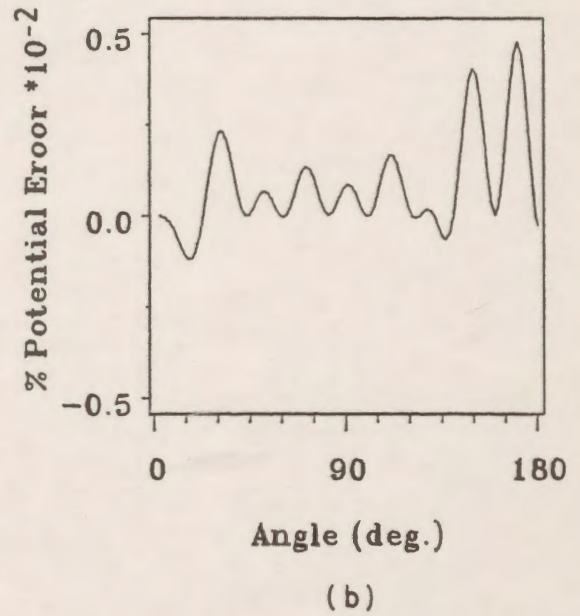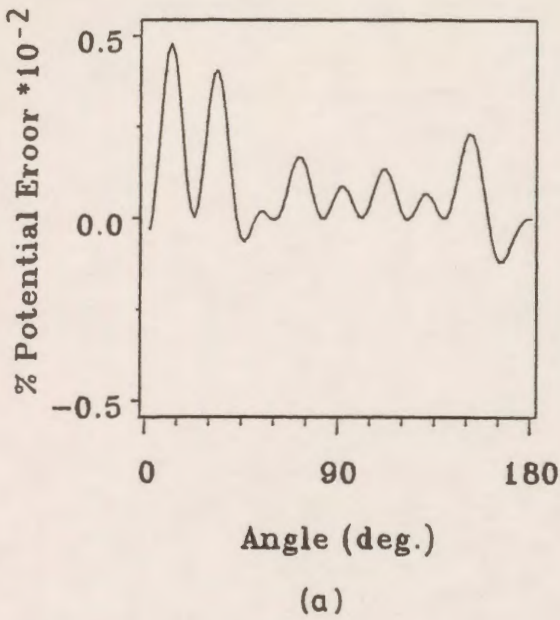
Figure 5.19: Potential error distributions for the symmetrical gap form on the lower half surfaces of the spheres.
(a) error on the HV sphere
(b) error on the LV sphere
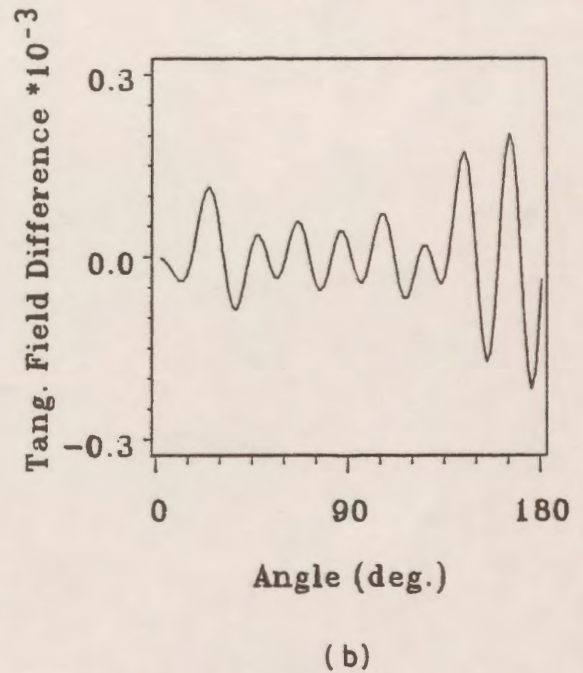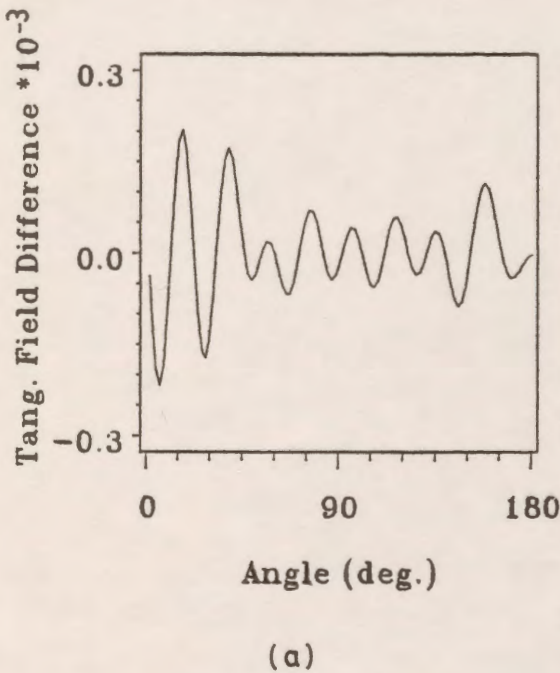
Figure 5.20: Tangential field difference distributions for the symmetrical gap form on the lower half surfaces of the spheres.
(a) difference on the HV sphere
(b) difference on the LV sphere

Where V_d is the potential difference between the spheres, s is the distance between the centers of the two spheres and r is the radius of the sphere.

The ratio E_{max}/E_{mean} is plotted in Fig. 5.21a as a function of the spacing/sphere-diameter ratio (g/2r) for the symmetrical and assymetrical forms of the gap. The radius of the sphere is kept constant at 10 cm while g is varied. This ratio is extended in this work to 2.0 from 1.4 as in Carter's paper.

For the case when the radius of the sphere is 10 cm and the gap distance is 20 cm (i.e. g/2r = 1.0), the calculated value of E_{max}/E_{mean} from the charge simulation technique is found to be 1.77 and 2.3384 for the symmetrical and asymmetrical gap, respectively while the values of E_{max}/E_{mean} taken from the analytical solution by Carter [79] are found to be 1.77 and 2.34 for the two cases, respectively.

The ratio E_{min}/E_{mean} is also plotted in Fig. 5.21b as a function of sphere-spacing/sphere-diameter ratio.
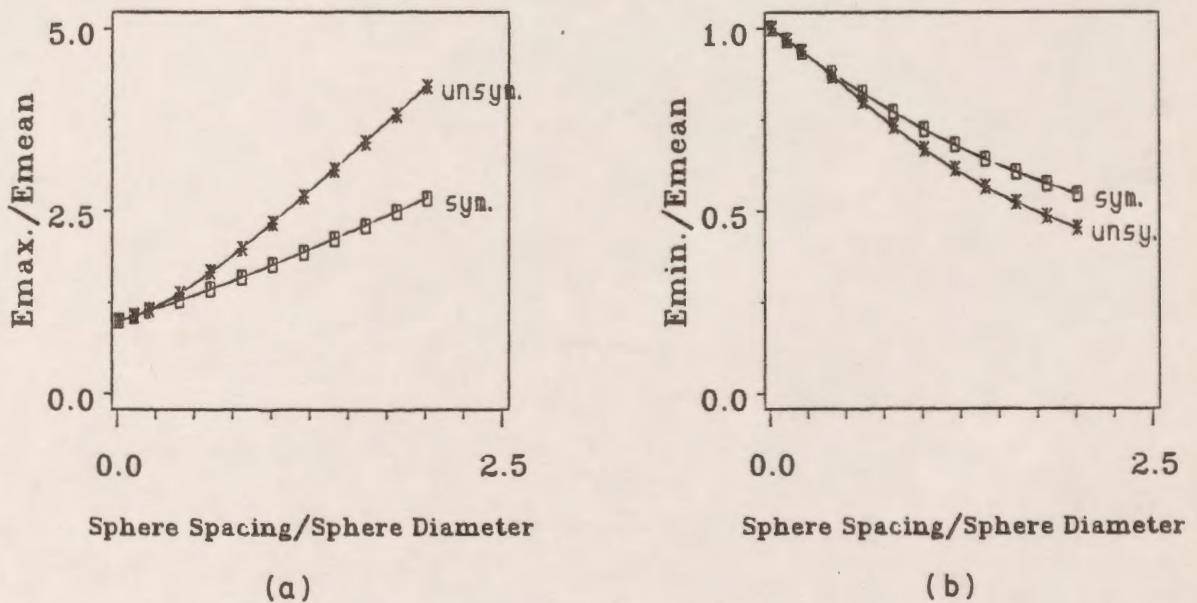
Figure 5.21: Variation of the electric field with the sphere-spacing/sphere-diameter ratio.
(a) maximum field variation
(b) minimum field variation

Fig. 5.22 shows the potential and the electric field distributions in the gap along the line joining the centers of the spheres for two different values of the ratio g/2r for the symmetrical gap form. It is clear from this figure that the nonlinearity in the potential distribution increases with increasing g/2r. Also the dissymmetry in the field distribution starts to appear as g/2r increases from 0.2 to 0.5.
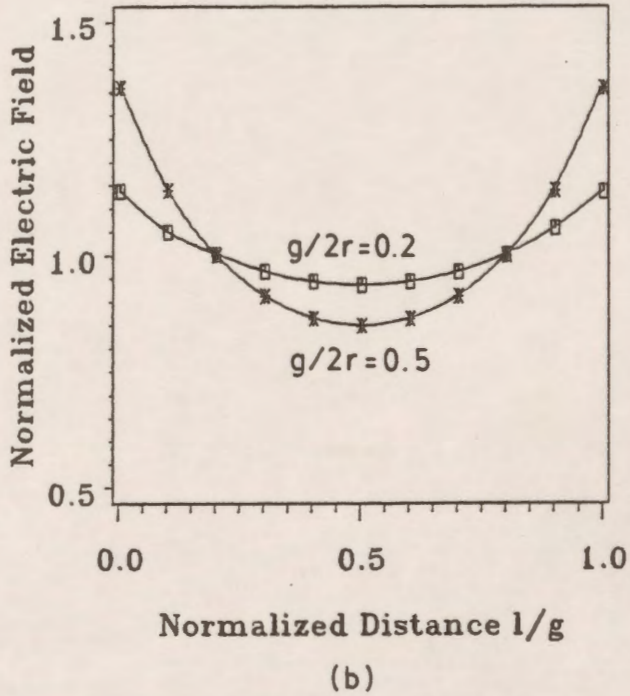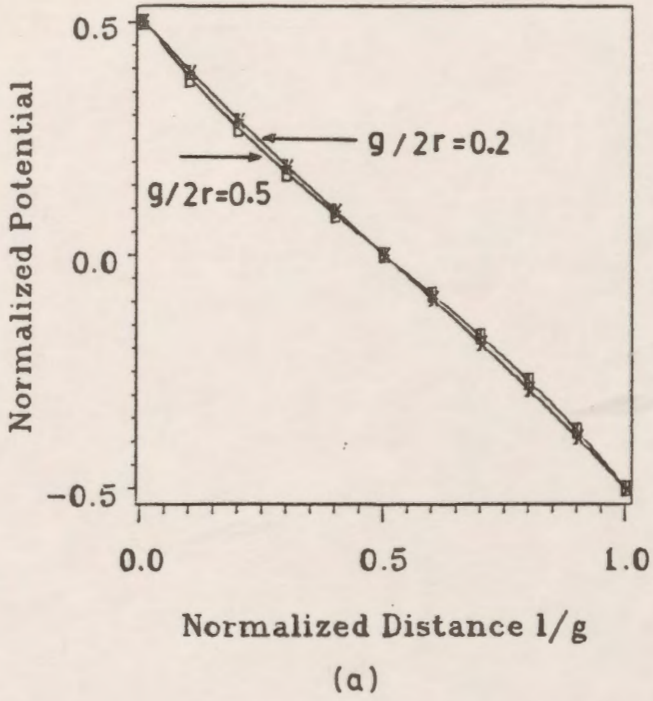
Figure 5.22: Potential and electric field distributions for the symmetrical gap form.
(a) potential distribution
(b) electric field distribution

5.4 Circular Cylinders and Spheres

The main concern in the calculation of the field between cylindrical and spherical electrodes is the points of maximum field intensity on the electrode surfaces [80]. Limited information concerning quantitative values of the potential gradient across the minimum-gap region has been published, for particular cases, by Pedersen [81] for equal spheres, and by Abou-Seada and Nasser [1] for a rod plane geometry. Shallal and Harrison [82] have given graphical values of the potential gradient for a particular sphere-plane geometry. Abou-Seada and Nasser [38] have applied the charge simulation technique to twin cylindrical bipolar conductors. Mattingley and Ryan [15] provided formulas, and tabulated data of the potential and potential gradients along the line of minimum electrode separation for standard electrode systems. They also presented various forward-,central- and backward difference equations for computing the fields for many arbitrarily shaped practical electrode systems.

In this work the Charge Simulation-based CAD package is applied to the same standard electrodes presented previously [15] to calculate the potential and the electric field distributions along the line of minimum electrode separation for a wide range of gap/radius ratios and for different ratios of the radii of the spheres and cylinders. For purposes of comparison, the notation is kept the same as in reference 15 throughout the study.

5.4.1 External Spheres

The CAD package is applied to the system shown in Fig. 5.23a which consists of two spheres separated by a distance g. The form of the gap is an unsymmetrical one in which one of the spheres is connected to 1.0 V and the other sphere is connected to 0. The distance along the line of the minimum electrode gap from the surface of the high voltage electrode is defined as l. The results are plotted and tabulated in a normalized format. For the sake of comparison with [15] we now define the normalized potential V' and the normalized electric field F as:

$$V' = \frac{V_c}{V},$$

and
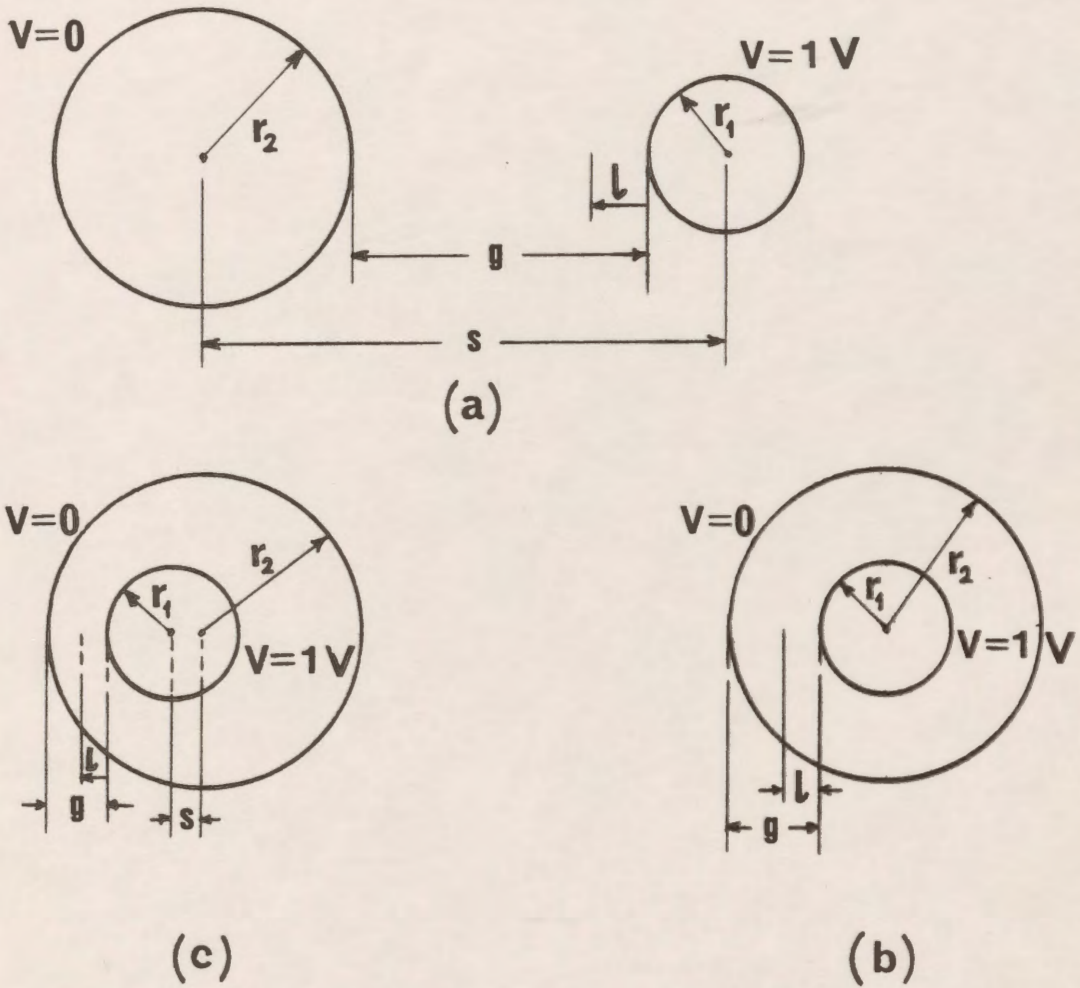
Figure 5.23:   Different systems for field calculations.
(a) external spheres
(b) concentric spheres and cylinders
(c) eccentric spheres and cylinders

$$F = \frac{r_1 E}{V},$$

where V is the voltage at the high-voltage electrode, which has a radius r_1, V_c and E are the calculated potential and electric field, respectively.

The analytical expressions for the potential and the potential gradient are found in reference 15.

The number of charges used to model the system for different gap distance/sphere radius ratios and for different radii ratios is based on a fixed number of charges per unit length and is taken here as 3 charges/cm of arc length. The assignment factor is kept at 1.2.

The calculations of potential and potential gradients are executed for different values of the ratio r_2/r_1 which represents the ratio of the low-voltage sphere to the high-voltage sphere radii. This ratio is varied from 1 to 6. The gap separation g is varied over a wide range, from 0.05 to 100.0 of the high-voltage sphere radius r_1, to determine its effect on the potential and potential gradient distributions.

Computed values of the normalized potential V' and normalized electric field F are given in Table 5.1 at specific points along the line of the minimum gap distance.

The potential and potential gradient are plotted along the line of minimum gap distance for four values of g/r_1 for each value of the ratio r_2/r_1. Fig. 5.24 show the potential distribution for different values of the ratio r_2/r_1 . It is clear from these figures that as the ratio g/r_1 increases, the nonlinearity in the potential distribution increases. The most linear curve is that when g/r_1 is equal to 0.1, and the most nonlinear curve is that when g/r_1 is equal to 100.0. It is clear also from these graphs that as the ratio r_2/r_1 increases for a fixed value of g/r_1, the nonlinearity does not increase much as compared to the effect of the change of the ratio g/r_1 keeping r_2/r_1 fixed.

Typical values of the potential at l/g=0.4 and $r_2/r_1 = 1$ are 0.598, 0.548, 0.189 and 0.024 for g/r_1 equals 0.1, 1, 10 and 100, respectively. The corresponding analytical values taken from [15]

are 0.5984, 0.5482, 0.1893 and 0.0242. It is found that a good agreement between the numerical and the analytical solution is obtained.

Fig. 5.25 shows the potential gradient distribution along the line of the minimum gap distance for different values of the ratio r_2/r_1 and different ratios of g/r_1 for $r_1=1$ cm. It is clear from these graphs that as the ratio g/r_1 increases, the normalized electric field decreases and at the same time the assymetry in the field increases. Typical values of the electric field at $r_2/r_1 = 1$ and $g/r_1 = 0.1$ are 10.345 and 10.345 for l/g equals 0.0 and 1.0, respectively. While at $r_2/r_1 = 1$ and $g/r_1 = 100$ are 1.0001 and 0.0101 for l/g equals 0.0 and 1.0, respectively. These graphs also show that as the ratio r_2/r_1 increases for a fixed g/r_1, the normalized potential gradient increases slightly so that the effect of this ratio can be neglected. Typical values of F at $l/g=0.4$ and $r_2/r_1 = 1$ are 9.852, 0.895, 0.042 and 0.0006 for g/r_1 equals 0.1, 1, 10, and 100, respectively. The corresponding analytical values taken from [15] are 9.8549, 0.8950, 0.0420, and 0.0006, respectively. A comparison between the results obtained from the numerical solution and those obtained analytically in [15] indicates that the calculated values of the potential gradient using the CAD package are correct to three decimal places compared to the analytical values. The maximum error between the two solutions is found to be 0.03% of the actual value.

Table 5.1 : Potential and field distribution for external spheres for $r_1 = 1$ cm..

$\dfrac{r_2}{r_1}$	$\dfrac{g}{r_1}$		l/g					
			0.0	0.2	0.4	0.6	0.8	1.0
	0.05	V'	1.0000	0.7984	0.5992	0.4008	0.2016	0.0000
		F	20.3430	20.0130	19.8510	19.8510	20.0130	20.3430
	0.10	V'	1.0000	0.7964	0.5984	0.4016	0.2033	0.0000
		F	10.3450	10.0120	9.8517	9.8516	10.0120	10.3450
	0.20	V'	1.0000	0.7935	0.5967	0.4029	0.2062	0.0000
		F	5.3434	5.0127	4.8569	4.8550	5.0075	5.3363
	0.50	V'	1.0000	0.7799	0.5854	0.4006	0.2110	0.0000
		F	2.3980	2.0423	1.8728	1.8474	1.9699	2.2922
	1.00	V'	1.0000	0.7443	0.5483	0.3773	0.2056	0.0000
		F	1.5168	1.0926	0.8950	0.8349	0.9077	1.2009
1.0	2.00	V'	1.0000	0.6630	0.4642	0.3179	0.1810	0.0000
		F	1.1692	0.6149	0.4101	0.3381	0.3652	0.6011
	5.00	V'	1.0000	0.4814	0.3030	0.2044	0.1258	0.0000
		F	1.0334	0.2624	0.1235	0.0818	0.0832	0.2271
	10.00	V'	1.0000	0.3263	0.1893	0.1268	0.0831	0.0000
		F	1.0091	0.1130	0.0420	0.0240	0.0223	0.1082
	20.00	V'	1.0000	0.1977	0.1078	0.0720	0.0498	0.0000
		F	1.0023	0.0402	0.0126	0.0065	0.0053	0.0523
	50.00	V'	1.0000	0.0905	0.0470	0.0314	0.0023	0.0000
		F	1.0004	0.0083	0.0023	0.0011	0.0008	0.0204
	100.00	V'	1.0000	0.0475	0.0242	0.0162	0.0119	0.0000
		F	1.0001	0.0023	0.0006	0.0003	0.0002	0.0101

Table 5.1---continued

$\frac{r_2}{r_1}$	$\frac{g}{r_1}$		l/g					
			0.0	0.2	0.4	0.6	0.8	1.0
	0.05	V'	1.0000	0.7973	0.5974	0.3988	0.2001	0.0000
		F	20.4540	20.1070	19.9050	19.8420	19.9160	20.1300
	0.10	V'	1.0000	0.7947	0.5947	0.3974	0.2001	0.0000
		F	10.4550	10.1070	9.9077	9.8441	9.9131	10.1210
	0.20	V'	1.0000	0.7894	0.5896	0.3949	0.2001	0.0000
		F	5.4536	5.1043	4.9098	4.8482	4.9134	5.1139
	0.50	V'	1.0000	0.7715	0.5713	0.3842	0.1981	0.0000
		F	2.4927	2.1143	1.9146	1.8460	1.8980	2.0900
	1.00	V'	1.0000	0.7336	0.5305	0.3563	0.1876	0.0000
		F	1.5815	1.1362	0.9216	0.8392	0.8672	1.0395
1.5	2.00	V'	1.0000	0.6531	0.4482	0.2980	0.1619	0.0000
		F	1.2033	0.6336	0.4224	0.3438	0.3517	0.4907
	5.00	V'	1.0000	0.4758	0.2943	0.1931	0.1123	0.0000
		F	1.0438	0.2659	0.1263	0.0845	0.0837	0.1716
	10.00	V'	1.0000	0.3237	0.1854	0.1215	0.0757	0.0000
		F	1.0125	0.1137	0.0427	0.0249	0.0235	0.0779
	20.00	V'	1.0000	0.1968	0.1065	0.0700	0.0466	0.0000
		F	1.0033	0.0403	0.0128	0.0067	0.0058	0.0000
	50.00	V'	1.0000	0.0903	0.0467	0.0309	0.0219	0.0000
		F	1.0005	0.0083	0.0023	0.0011	0.0008	0.0138
	100.00	V'	1.0000	0.0474	0.0242	0.0160	0.0117	0.0000
		F	1.0001	0.0023	0.0006	0.0003	0.0002	0.0068

Table 5.1---continued

$\frac{r_2}{r_1}$	$\frac{g}{r_1}$		l/g
			0.0	0.2	0.4	0.6	0.8	1.0
2.0	0.05	V'	1.0000	0.7968	0.5965	0.3977	0.1993	0.0000
		F	20.5110	20.1560	19.9330	19.8370	19.8650	20.0200
	0.10	V'	1.0000	0.7936	0.5929	0.3953	0.1985	0.0000
		F	10.5110	10.1550	9.9357	9.8399	9.8632	10.0090
	0.20	V'	1.0000	0.7873	0.5861	0.3910	0.1971	0.0000
		F	5.5087	5.1496	4.9347	4.8431	4.8672	5.0114
	0.50	V'	1.0000	0.7669	0.5637	0.3756	0.1914	0.0000
		F	2.5458	2.1529	1.9357	1.8431	1.8588	1.9918
	1.00	V'	1.0000	0.7273	0.5203	0.3445	0.1780	0.0000
		F	1.6203	1.1615	0.9357	0.8394	0.8426	0.9598
	2.00	V'	1.0000	0.6465	0.4379	0.2859	0.1510	0.0000
		F	1.2261	0.6456	0.4295	0.3457	0.3415	0.4358
	5.00	V'	1.0000	0.4714	0.2879	0.1850	0.1036	0.0000
		F	1.0520	0.2685	0.1281	0.0859	0.0829	0.1438
	10.00	V'	1.0000	0.3215	0.1823	0.1173	0.0703	0.0000
		F	1.0156	0.1142	0.0431	0.0255	0.0239	0.0627
	20.00	V'	1.0000	0.1959	0.1052	0.0683	0.0441	0.0000
		F	1.0043	0.0404	0.0129	0.0068	0.0060	0.0285
	50.00	V'	1.0000	0.0901	0.0465	0.0306	0.0212	0.0000
		F	1.0007	0.0083	0.0023	0.0011	0.0009	0.0106
	100.00	V'	1.0000	0.0474	0.0241	0.0159	0.0115	0.0000
		F	1.0002	0.0023	0.0006	0.0003	0.0002	0.0051

Table 5.1---continued

$\frac{r_2}{r_1}$	$\frac{g}{r_1}$		l/g					
			0.0	0.2	0.4	0.6	0.8	1.0
	0.05	V'	1.0001	0.7964	0.5958	0.3969	0.1987	0.0000
		F	20.5610	20.1950	19.9540	19.8330	19.8280	19.9430
	0.10	V'	1.0001	0.7924	0.5910	0.3934	0.1971	0.0000
		F	10.5850	10.2040	9.9570	9.8287	9.8145	9.9185
	0.20	V'	1.0000	0.7850	0.5823	0.3867	0.1940	0.0000
		F	5.5776	5.1984	4.9602	4.8362	4.8161	4.9038
	0.50	V'	1.0000	0.7621	0.5557	0.3668	0.1847	0.0000
		F	2.6010	2.1933	1.9571	1.8390	1.8180	1.8936
	1.00	V'	1.0000	0.7202	0.5089	0.3318	0.1679	0.0000
		F	1.6645	1.1897	0.9502	0.8376	0.8148	0.8807
3.0	2.00	V'	1.0000	0.6384	0.4254	0.2717	0.1389	0.0000
		F	1.2550	0.6604	0.4371	0.3463	0.3279	0.3813
	5.00	V'	1.0000	0.4652	0.2788	0.1742	0.0929	0.0000
		F	1.0643	0.2720	0.1303	0.0872	0.0805	0.1162
	10.00	V'	1.0000	0.3179	0.1772	0.1110	0.0630	0.0000
		F	1.0208	0.1150	0.0438	0.0261	0.0240	0.0476
	20.00	V'	1.0000	0.1943	0.1031	0.0655	0.0402	0.0000
		F	1.0064	0.0406	0.0130	0.0071	0.0063	0.0205
	50.00	V'	1.0000	0.0897	0.0460	0.0299	0.0201	0.0000
		F	1.0014	0.0083	0.0023	0.0011	0.0009	0.0073
	100.00	V'	1.0000	0.0473	0.0239	0.0157	0.0111	0.0000
		F	1.0006	0.0023	0.0006	0.0003	0.0002	0.0035

Table 5.1---continued

| $\dfrac{r_2}{r_1}$	$\dfrac{g}{r_1}$		l/g					
			0.0	0.2	0.4	0.6	0.8	1.0
	0.05	V'	1.0000	0.7960	0.5950	0.3961	0.1980	0.0000
		F	20.5890	20.2320	19.9810	19.8330	19.7860	19.8410
	0.10	V'	1.0001	0.7914	0.5893	0.3913	0.1956	0.0000
		F	10.6380	10.2520	9.9847	9.8247	9.7660	9.8112
	0.20	V'	1.0000	0.7829	0.5786	0.3826	0.1909	0.0000
		F	5.6376	5.2468	4.9860	4.8299	4.7667	4.7969
	0.50	V'	1.0000	0.7570	0.5474	0.3576	0.1779	0.0000
		F	2.6590	2.2357	1.9785	1.8332	1.7750	1.7964
	1.00	V'	1.0000	0.7121	0.4962	0.3179	0.1574	0.0000
		F	1.7144	1.2210	0.9651	0.8336	0.7835	0.8022
6.0	2.00	V'	1.0000	0.6281	0.4101	0.2549	0.1257	0.0000
		F	1.2913	0.6778	0.4452	0.3447	0.3104	0.3267
	5.00	V'	1.0000	0.4555	0.2654	0.1592	0.0796	0.0000
		F	1.0831	0.2773	0.1329	0.0876	0.0756	0.0884
	10.00	V'	1.0000	0.3112	0.1683	0.1005	0.0524	0.0000
		F	1.0301	0.1165	0.0447	0.0267	0.0231	0.0325
	20.00	V'	1.0000	0.1909	0.0986	0.0599	0.0335	0.0000
		F	1.0101	0.0409	0.0133	0.0074	0.0065	0.0126
	50.00	V'	1.0000	0.0888	0.0447	0.0282	0.0176	0.0000
		F	1.0023	0.0083	0.0024	0.0012	0.0010	0.0040
	100.00	V'	1.0000	0.0470	0.0235	0.0152	0.0102	0.0000
		F	1.0009	0.0023	0.0006	0.0003	0.0002	0.0018
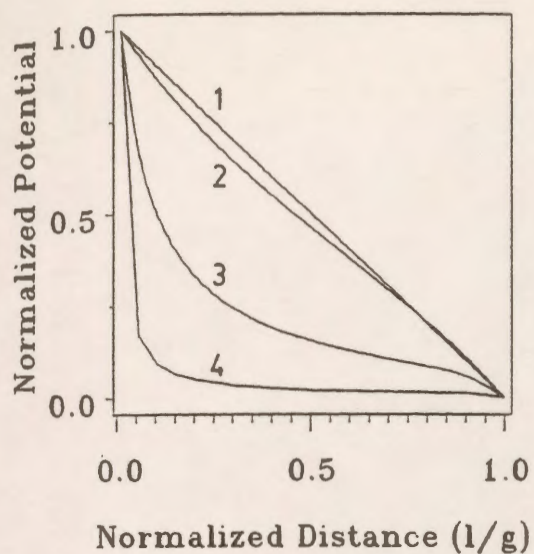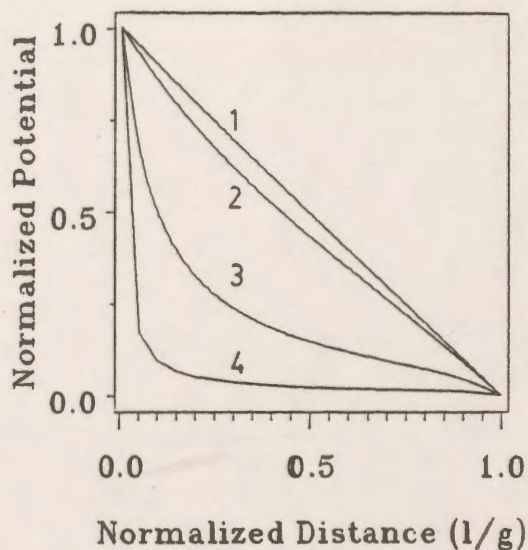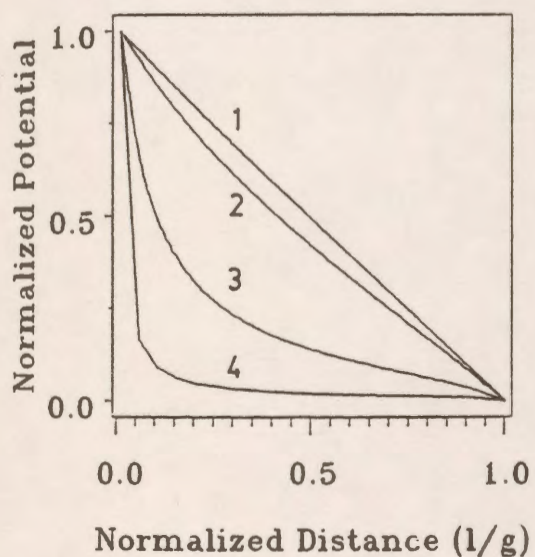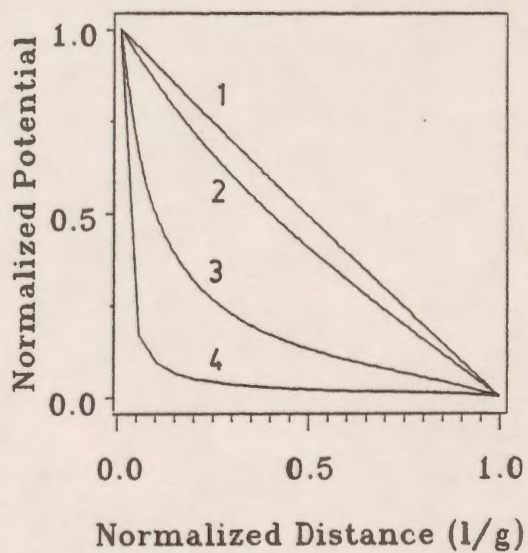
Figure 5.24: Potential distribution along the line of minimum gap (external spheres) for $r_1 = 1$ cm.

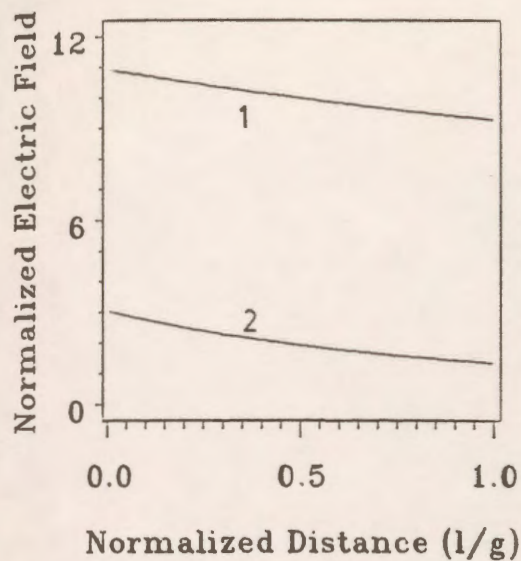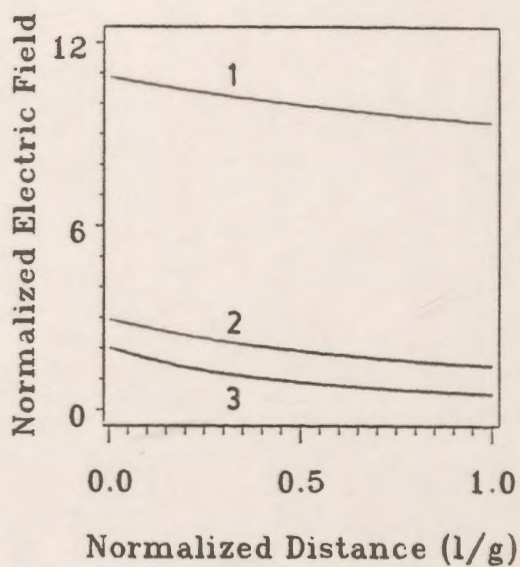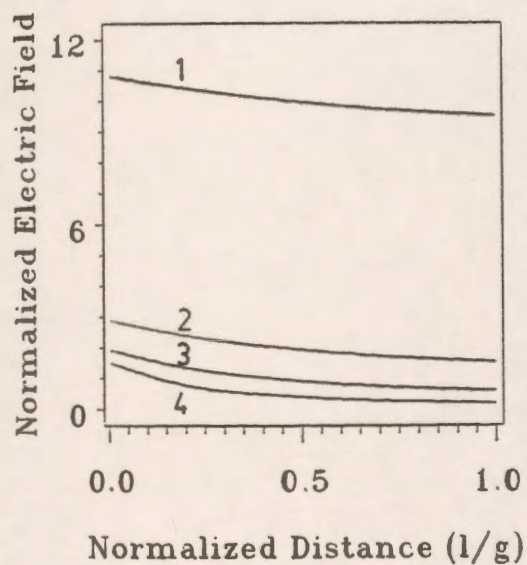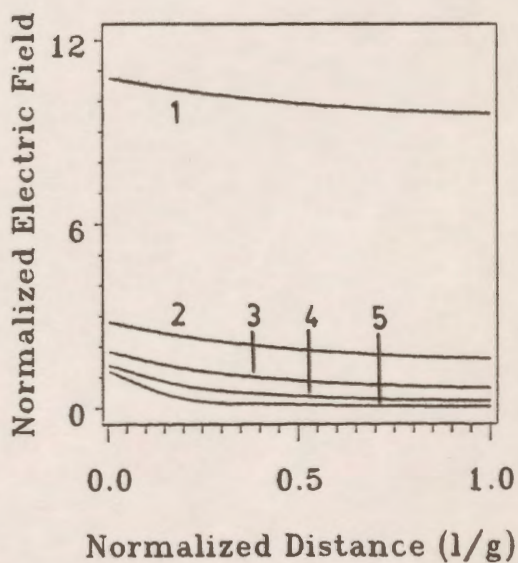|			
(a) $r_2/r_1 = 1$	(b) $r_2/r_1 = 2$	(c) $r_2/r_1 = 3$	(d) $r_2/r_1 = 6$
(1) $g/r_1 = 0.1$	(2) $g/r_1 = 1$	(3) $g/r_1 = 10$	(4) $g/r_1 = 100$
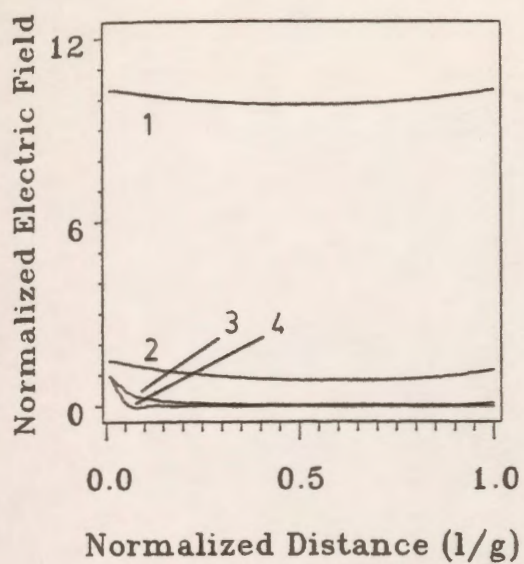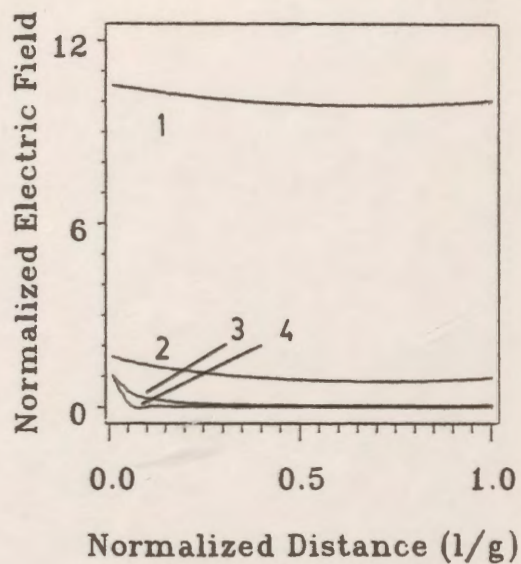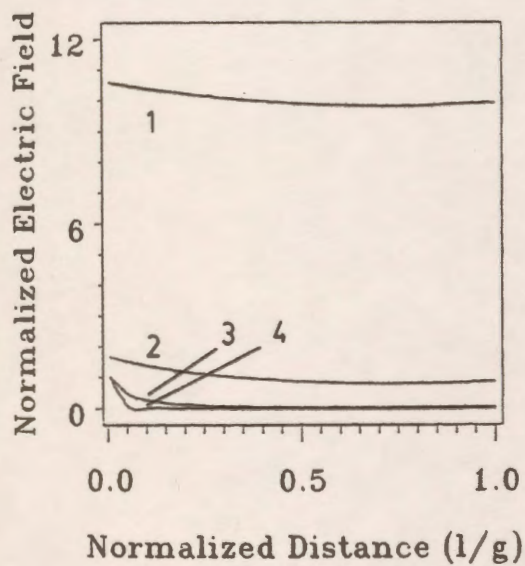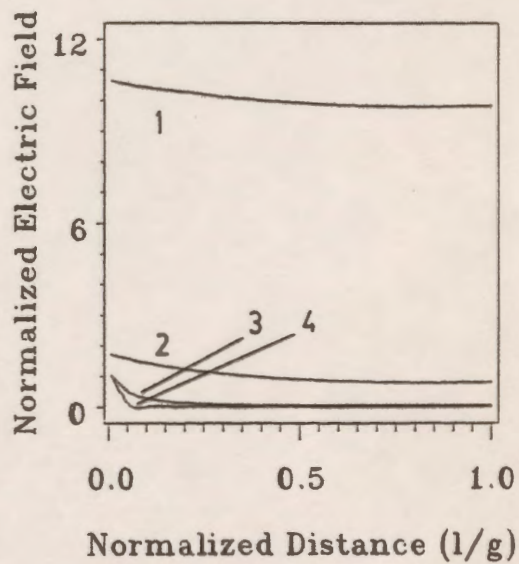
Figure 5.25: Potential gradient distribution along the line of minimum gap distance (external spheres) for $r_1 = 1cm$.

(a) $r_2/r_1=1$ (b) $r_2/r_1=2$ (c) $r_2/r_1=3$ (d) $r_2/r_1=6$
(1) $g/r_1=0.1$ (2) $g/r_1=1$ (3) $g/r_1=10$ (4) $g/r_1=100$

5.4.2 Concentric and Eccentric Internal Spheres

The CAD package is applied to the systems shown in Fig. 5.23b and 5.23c which represent concentric and eccentric spheres, respectively. The inner sphere is held at high-voltage while the outer sphere is connected to low-voltage. The minimum gap distance is represented by g and l is defined as the distance from the high voltage electrode measured along the line of the minimum gap distance. s is defined as the distance between the centers of the spheres. Calculated values of the potential V' and the potential gradient F are given in Table 5.2 for a wide range of g/r_1 and different ratios of r_2/r_1 .

Fig. 5.26 represent the potential distribution along the line of the minimum gap distance for different values of the ratio r_2/r_1 and with different values of the ratio g/r_1. It is obvious from these graphs that as the ratio g/r_1 increases for a fixed value of the ratio r_2/r_1, the nonlinearity in the potential increases, while increasing the ratio r_2/r_1 for a fixed value of g/r_1 decreases the nonlinearity in the potential distribution. Typical values of V' at l/g=0.4 and $r_2/r_1 = 1.5$ are 0.5799 and 0.5001 for $g/r_1 = 0.1$ and 0.5, respectively. The computed analytical values published in reference 15 are 0.5797 and 0.5000, respectively. It is concluded that the results obtained using the numerical technique are matched very well with those obtained by the analytical expressions. The maximum error between the two sets of results is found to be 0.04% of the actual value at the point examined.

Figs. 5.27 show the electric field distribution along the line of the minimum gap distance for different r_2/r_1 and g/r_1 ratios. It is clear from these graphs that as the ratio g/r_1 increases, F decreases while increasing the ratio r_2/r_1 for fixed value of g/r_1 decreases the field value slightly. Typical values of F at l/g=0.4 and $r_2/r_1 = 1.5$ are 10.125 and 2.083 for g/r_1 equal to 0.1 and 0.5, respectively. The recorded values from reference 15 are 10.130 and 2.083, respectively. The maximum error between the numerical and the analytical values is 0.05% of the analytical value at the point examined. For l/g=0.4 and $g/r_1 = 0.1$, the values of F are 10.125, 10.097, 10.069, and

Table 5.2 : Potential and field distribution for internal spheres for $r_1 = 1$ *cm*..

$\dfrac{r_2}{r_1}$	$\dfrac{g}{r_1}$		l/g					
			0.0	0.2	0.4	0.6	0.8	1.0
1.5	0.05	V'	1.0000	0.7931	0.5900	0.3904	0.1938	0.0000
		F	20.9040	20.4950	20.1280	19.8010	19.5120	19.2640
	0.10	V'	1.0000	0.7860	0.5799	0.3808	0.1877	0.0000
		F	10.9130	10.4950	10.1250	9.7982	9.5127	9.2690
	0.20	V'	1.0000	0.7717	0.5596	0.3616	0.1756	0.0000
		F	5.9360	5.4941	5.1169	4.7923	4.5129	4.2775
	0.50	V'	1.0000	0.7273	0.5001	0.3078	0.1429	0.0000
		F	3.0005	2.4791	2.0831	1.7751	1.5307	1.3359
2.0	0.05	V'	1.0001	0.7938	0.5912	0.3917	0.1948	0.0000
		F	20.8380	20.4370	20.0960	19.8100	19.5780	19.4000
	0.10	V'	1.0000	0.7871	0.5818	0.3829	0.1893	0.0000
		F	10.8590	10.4460	10.0970	9.8039	9.5634	9.3755
	0.20	V'	1.0000	0.7740	0.5635	0.3659	0.1787	0.0000
		F	5.8735	5.4432	5.0912	4.8016	4.5649	4.3786
	0.50	V'	1.0000	0.7339	0.5103	0.3183	0.1500	0.0000
		F	2.9241	2.4260	2.0631	1.7911	1.5834	1.4243
	1.00	V'	1.0000	0.6667	0.4286	0.2500	0.1111	0.0000
		F	2.0006	1.3889	1.0203	0.7812	0.6173	0.5007
3.0	0.05	V'	1.0001	0.7943	0.5921	0.3928	0.1956	0.0000
		F	20.7850	20.3890	20.0670	19.8130	19.6280	19.5100
	0.10	V'	1.0001	0.7882	0.5836	0.3850	0.1908	0.0000
		F	10.8050	10.3980	10.0690	9.8092	9.6134	9.4816

Table 5.2---continued

| $\frac{r_2}{r_1}$	$\frac{g}{r_1}$		l/g					
			0.0	0.2	0.4	0.6	0.8	1.0
3.0	0.20	V'	1.0000	0.7763	0.5674	0.3701	0.1817	0.0000
		F	5.8125	5.3931	5.0653	4.8100	4.6162	4.4806
	0.50	V'	1.0000	0.7401	0.5202	0.3285	0.1570	0.0000
		F	2.8520	2.3753	2.0424	1.8048	1.6342	1.5144
	1.00	V'	1.0000	0.6805	0.4484	0.2690	0.1232	0.0000
		F	1.9124	1.3396	1.0083	0.8013	0.6652	0.5733
	2.00	V'	1.0000	0.5714	0.3333	0.1818	0.0769	0.0000
		F	1.5005	0.7653	0.4629	0.3099	0.2219	0.1668
6.0	0.05	V'	1.0001	0.7949	0.5930	0.3938	0.1964	0.0000
		F	20.7300	20.3410	20.0380	19.8180	19.6770	19.6170
	0.10	V'	1.0001	0.7892	0.5855	0.3870	0.1924	0.0000
		F	10.7520	10.3500	10.0410	9.8142	9.6629	9.5874
	0.20	V'	1.0000	0.7785	0.5711	0.3742	0.1848	0.0000
		F	5.7529	5.3438	5.0393	4.8177	4.6669	4.5834
	0.50	V'	1.0000	0.7461	0.5297	0.3385	0.1640	0.0000
		F	2.7839	2.3267	2.0214	1.8163	1.6831	1.6064
	1.00	V'	1.0000	0.6925	0.4662	0.2866	0.1350	0.0000
		F	1.8365	1.2956	0.9946	0.8162	0.7089	0.6479
	2.00	V'	1.0000	0.5967	0.3660	0.2110	0.0948	0.0000
		F	1.4054	0.7285	0.4600	0.3293	0.2586	0.2190
	5.00	V'	1.0000	0.4000	0.2000	0.1000	0.0400	0.0000
		F	1.2004	0.3000	0.1333	0.0750	0.0480	0.0334
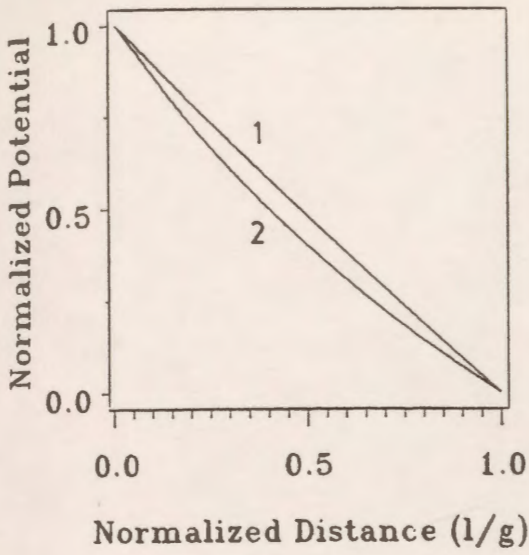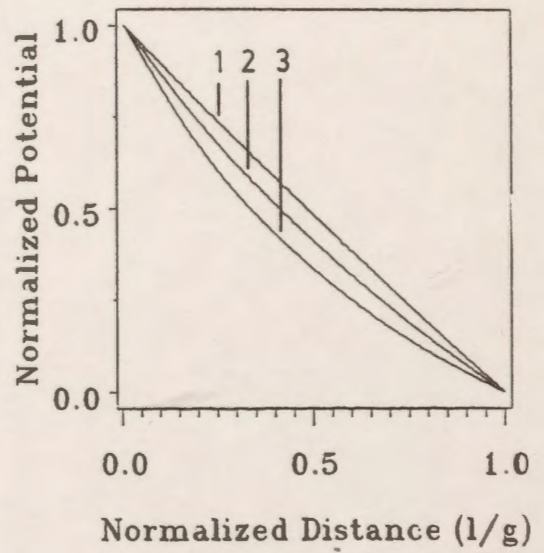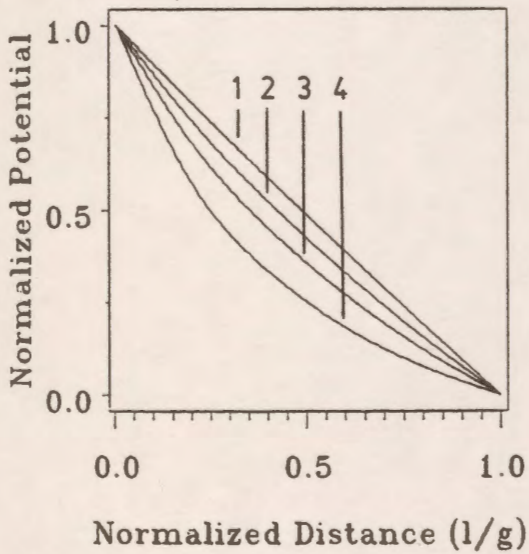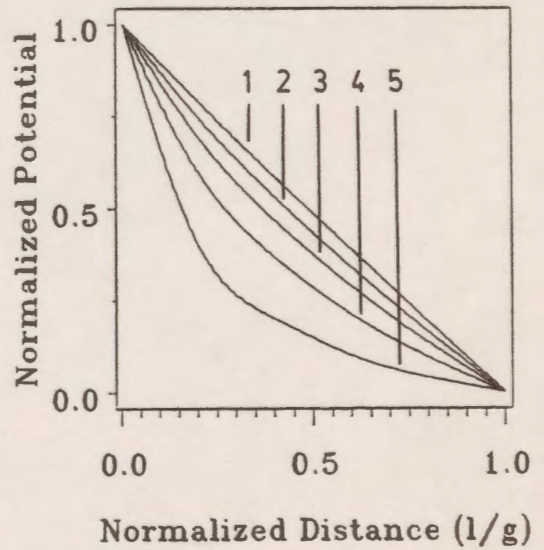
Figure 5.26: Potential distribution along the line of minimum gap distance (internal spheres) for
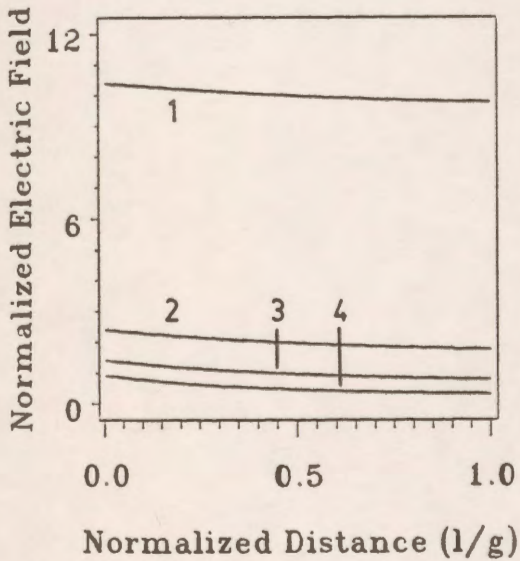$r_1 = 1$ cm.

(a) $r_2/r_1 = 1.5$ (b) $r_2/r_1 = 2$ (c) $r_2/r_1 = 3$ (d) $r_2/r_1 = 6$

(1) $g/r_1 = 0.1$ (2) $g/r_1 = 0.5$ (3) $g/r_1 = 1$ (4) $g/r_1 = 2$ (5) $g/r_1 = 5$
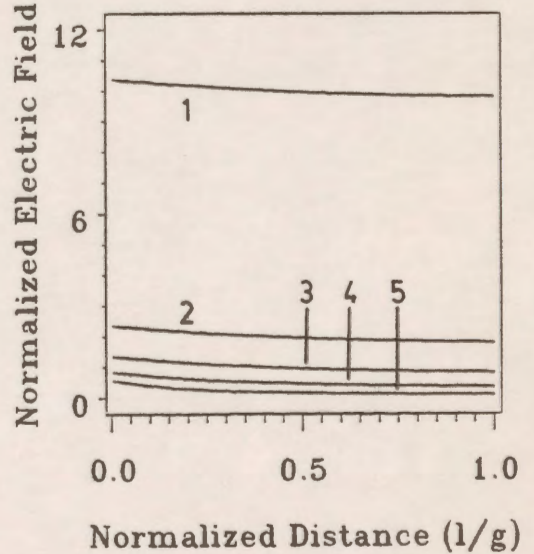
Figure 5.27: Potential gradient distribution along the line of minimum gap distance (internal spheres) for $r_1 = 1$ *cm*.

(a) $r_2/r_1=1.5$ (b) $r_2/r_1=2$ (c) $r_2/r_1=3$ (d) $r_2/r_1=6$

(1) $g/r_1=0.1$ (2) $g/r_1=0.5$ (3) $g/r_1=1$ (4) $g/r_1=2$ (5) $g/r_1=5$

10.041, for r_2/r_1 = 1.5, 2, 3 and 6, respectively. The maximum error between the two solutions is found to be 0.07% of the analytical value at the point examined.

5.4.3 Concentric and Eccentric Internal Cylinders

The CAD package is applied to the systems shown in Figs. 5.23b and 5.23c for concentric and eccentric cylinders, respectively. The parameters l, g and s are kept the same as for concentric and eccentric spheres. Computed values for the normalized potential V' and normalized potential gradient F are given in Table 5.3 for different values of the ratio g/r_1 and r_2/r_1.

Fig. 5.28 shows the potential distribution along the line of the minimum gap distance for a wide range of g/r_1 and r_2/r_1. It is clear from these plots that as the ratio g/r_1 increases for a fixed value of the ratio r_2/r_1, the nonlinearity in the potential distribution increases, while increasing the ratio r_2/r_1 for a fixed value of g/r_1 does not affect the distribution of the potential much. Typical values for V' at l/g=0.4 and r_2/r_1 = 1.5 are 0.590 and 0.550 for g/r_1 equals 0.1 and 0.5, respectively. The computed analytical values published previously [15] are 0.5899 and 0.550, respectively. The maximum difference between the analytical and numerical values is 0.02% of the analytical value.

Fig. 5.29 also shows F for the same values of the ratio g/r_1 and r_2/r_1. The effect of varying the ratio g/r_1 for a fixed value of r_2/r_1 on the distribution of F is very strong. It decreases as g/r_1 increases. Typical values for F at l/g=0.4 and r_2/r_1 =1.5 are 10.061 and 2.054 for g/r_1 equals 0.1 and 0.5, respectively, while the analytical values are 10.0676 and 2.0553. The maximum difference between the two solutions is 0.06% of the actual value. Varying r_2/r_1 and keeping g/r_1 fixed does not affect the distribution of F much. For l/g=0.4 and g/r_1 =0.1, the values of F are 10.061, 10.047, 10.033 and 10.019 while the corresponding analytical values are 10.067, 10.053, 10.039 and 10.024 for r_2/r_1 equals 1.5, 2, 3 and 6, respectively. The maximum difference between the two sets of results is found to be 0.06% of the actual value at the point examined.

Table 5.3 : Potential and field distribution for internal cylinders for $r_1 = 1$ *cm*..

$\dfrac{r_2}{r_1}$	$\dfrac{g}{r_1}$		l/g					
			0.0	0.2	0.4	0.6	0.8	1.0
1.5	0.05	V'	1.0000	0.7967	0.5952	0.3954	0.1970	0.0000
		F	20.4330	20.2370	20.0620	19.9080	19.7740	19.6620
	0.10	V'	1.0001	0.7932	0.5902	0.3906	0.1940	0.0000
		F	10.4460	10.2420	10.0610	9.9017	9.7635	9.6480
	0.20	V'	1.0000	0.7861	0.5801	0.3810	0.1879	0.0000
		F	5.4551	5.2444	5.0607	4.8993	4.7588	4.6420
	0.50	V'	1.0000	0.7649	0.5504	0.3530	0.1703	0.0000
		F	2.4688	2.2416	2.0545	1.8965	1.7614	1.6498
2.0	0.05	V'	1.0001	0.7970	0.5957	0.3960	0.1975	0.0000
		F	20.4060	20.2120	20.0470	19.9090	19.7980	19.7150
	0.10	V'	1.0001	0.7938	0.5912	0.3917	0.1948	0.0000
		F	10.4190	10.2180	10.0470	9.9039	9.7886	9.7018
	0.20	V'	1.0000	0.7873	0.5821	0.3832	0.1895	0.0000
		F	5.4246	5.2183	5.0466	4.9032	4.7856	4.6961
	0.50	V'	1.0000	0.7685	0.5561	0.3591	0.1746	0.0000
		F	2.4298	2.2115	2.0411	1.9038	1.7917	1.7044
	1.00	V'	1.0000	0.7369	0.5146	0.3220	0.1521	0.0000
		F	1.4444	1.2021	1.0303	0.9016	0.8014	0.7236
3.0	0.05	V'	1.0001	0.7973	0.5962	0.3695	0.1979	0.0000
		F	20.3780	20.1870	20.0320	19.9100	19.8220	19.7670
	0.10	V'	1.0001	0.7943	0.5921	0.3927	0.1956	0.0000
		F	10.3930	10.1940	10.0330	9.9062	9.8133	9.7548

Table 5.3---continued

$\dfrac{r_2}{r_1}$	$\dfrac{g}{r_1}$		l/g					
			0.0	0.2	0.4	0.6	0.8	1.0
3.0	0.20	V'	1.0000	0.7884	0.5841	0.3854	0.1911	0.0000
		F	5.3949	5.1929	5.0327	4.9068	4.8117	4.7494
	0.50	V'	1.0000	0.7718	0.5616	0.3650	0.1786	0.0000
		F	2.3933	2.1832	2.0279	1.9100	1.8204	1.7578
	1.00	V'	1.0000	0.7452	0.5273	0.3348	0.1606	0.0000
		F	1.3959	1.1693	1.0189	0.9122	0.8336	0.7766
	2.00	V'	1.0000	0.6937	0.4650	0.2823	0.1303	0.0000
		F	0.9114	0.6501	0.5057	0.4137	0.3501	0.3042
6.0	0.05	V'	1.0000	0.7975	0.5967	0.3970	0.1983	0.0000
		F	20.3490	20.1630	20.0180	19.9120	19.8460	19.8190
	0.10	V'	1.0001	0.7948	0.5930	0.3938	0.1964	0.0000
		F	10.3670	10.1700	10.0190	9.9085	9.8377	9.8073
	0.20	V'	1.0000	0.7895	0.5859	0.3875	0.1927	0.0000
		F	5.3660	5.1681	5.0191	4.9101	4.8373	4.8024
	0.50	V'	1.0000	0.7749	0.5667	0.3705	0.1826	0.0000
		F	2.3592	2.1565	2.0150	1.9152	1.8476	1.8106
	1.00	V'	1.0000	0.7525	0.5387	0.3465	0.1686	0.0000
		F	1.3539	1.1403	1.0074	0.9202	0.8625	0.8282
	2.00	V'	1.0000	0.7129	0.4923	0.3083	0.1469	0.0000
		F	0.8495	0.6165	0.4978	0.4276	0.3828	0.3543
	5.00	V'	1.0000	0.6131	0.3869	0.2263	0.1018	0.0000
		F	0.5588	0.2791	0.1860	0.1395	0.1116	0.0932
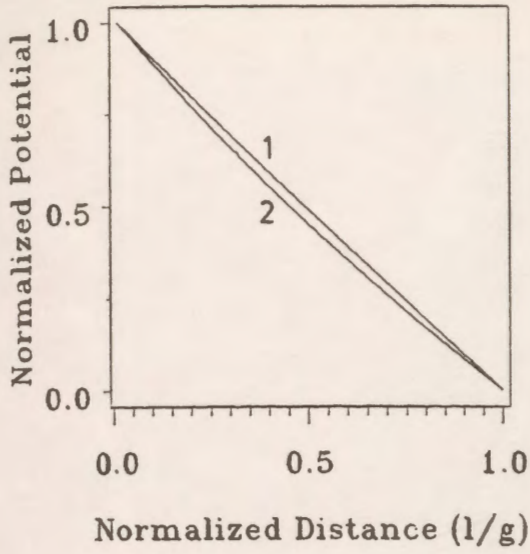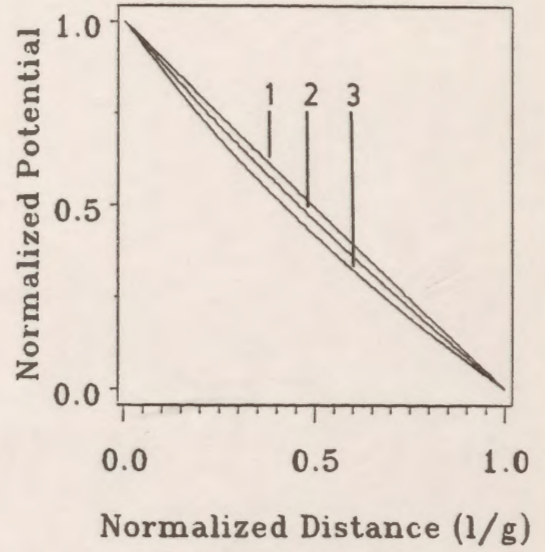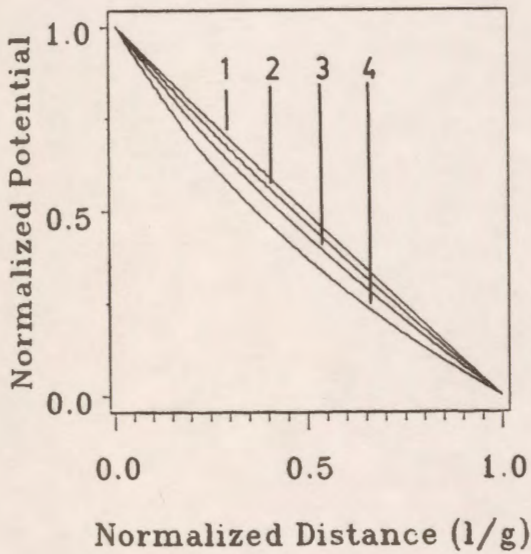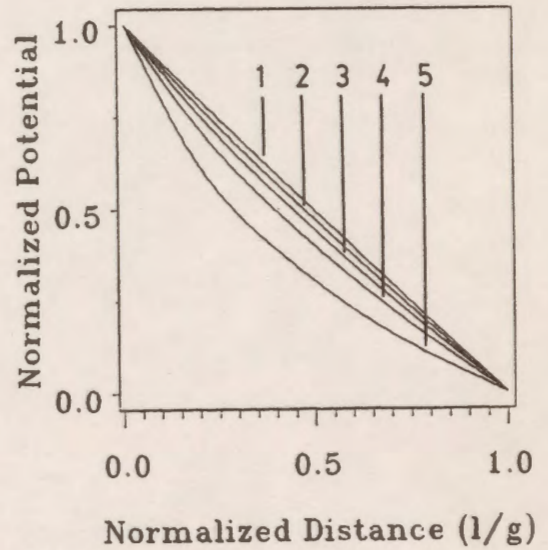
Figure 5.28: Potential distribution along the line of minimum gap distance (internal cylinders) for $r_1 = 1$ cm.

(a) $r_2/r_1=1.5$ (b) $r_2/r_1=2$ (c) $r_2/r_1=3$ (d) $r_2/r_1=6$

(1) $g/r_1=0.1$ (2) $g/r_1=0.5$ (3) $g/r_1=1$ (4) $g/r_1=2$ (5) $g/r_1=5$
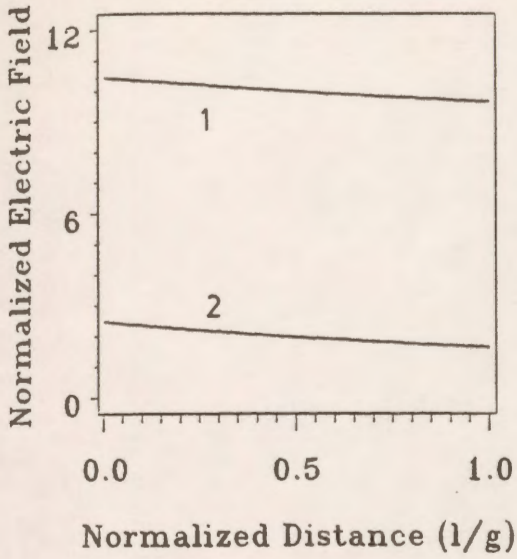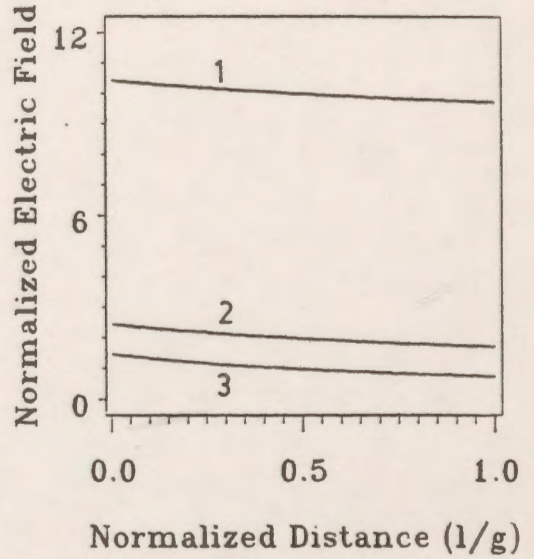
Figure 5.29: Potential gradient distribution along the line of minimum gap distance (internal cylinders) for $r_1 = 1$ *cm*.

(a) $r_2/r_1 = 1.5$ (b) $r_2/r_1 = 2$ (c) $r_2/r_1 = 3$ (d) $r_2/r_1 = 6$

(1) $g/r_1 = 0.1$ (2) $g/r_1 = 0.5$ (3) $g/r_1 = 1$ (4) $g/r_1 = 2$ (5) $g/r_1 = 5$

It is concluded that the potential and potential gradient values computed using the Charge Simulation Computer-Aided-Design package (CAD) are in good agreement with the values computed using the analytical formulas in reference 15 and that the errors in the Charge Simulation method are very small for those standard systems.

Chapter VI

OPTIMUM PARAMETER SELECTION IN THE CHARGE
SIMULATION METHOD

6.1   General

The charge simulation technique is controlled by some modelling parameters which affect the accuracy of the solution of the problem to a great extent. Therefore, it is preferable that a study should be done on a simple geometry in order to examine the effect of the different controlling parameters on the accuracy of the simulation.

This method of modelling electrostatic fields is applied to an electrode geometry in order to evaluate the effect of varying such parameters as the assignment factor, the total number of charges, the number of charges on the curved portion to the total number of charges of the geometry on the accuracy of the method. The effect of the discontinuity in the positions of the charges on the quality measures of the simulation is also examined. Detailed examination of the effect of the assignment factor and the total number of charges for uniform charge distribution on the accuracy of the charge simulation is described. A comparison between full modelling and the use of symmetry and between translational and rotational symmetry regarding the accuracy of the CSM are presented. Recommendations for the ranges of several parameters used in the charge simulation modelling are made.

6.2   Effect of Different Parameters on the Accuracy of the CSM

A charged conductor at potential V above an infinite plane (ground surface) is shown in Fig. 6.1. The conductor has an infinite vertical and horizontal planar regions, joined with a quarter circle transition of radius r (the system has translational symmetry). This system is chosen for study because it has minimal complexity which has both straight and curved portions; it is somewhat practical as a detailed model for the corner (edge) of an electrode and it does not have inherent symmetries which might influence the level of errors. Although a finite region of the conductor near the corner is modelled, the parameters governing the details of representation can be adjusted to examine the effects of the corner in isolation or in proximity to a ground plane, in addition to the effects of other modelling details on the process. Infinite line charges have been used for modelling the field distributions of the electrodes with translational symmetry. The distribution of the line charges are shown inside the conductor which is at the applied potential as shown in Fig. 6.2. For each charge modelling the charged conductor, an image charge of opposite polarity is symmetrically placed with respect to the ground surface as shown in Fig. 6.2.

Table 6.1 shows the effect of the assignment factor (β_a), the total number of charges n and the ratio of the number of charges on the curved portion to the total number of the charges n_c / n on the accuracy of the charge simulation modelling. Keeping the total number of charges fixed at 60 charges, n_c / n at 0.1 and varying the assignment factor from 0.7 up to 1.5, it is found that the assignment factor has a great effect on the accuracy and the best value of the three tried is found to be 1.2. Increasing the number of the total charges from 60 to 120, keeping the assignment factor at 1.2 and n_c / n at 0.1, it is found that both the percentage maximum potential error and the tangential field difference decrease. It should be mentioned here that the errors at the ends of the modelled region are excluded from these considered because these errors are high due to poor modelling near the edges.

The effect of varying the assignment factor and the total number of charges on the accuracy of the CSM is examined for two cases where there is a discontinuity in the alignment of the
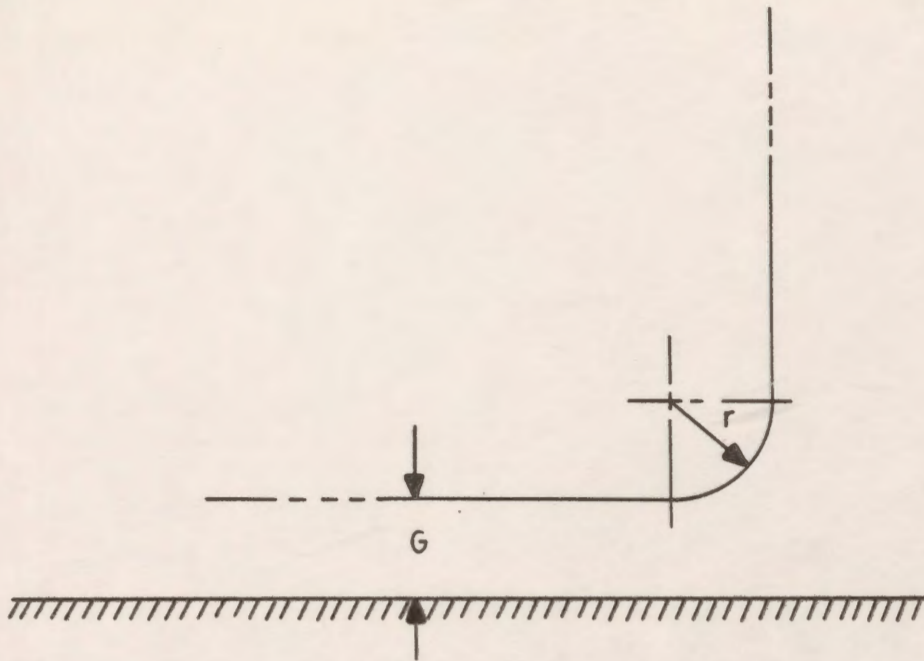
Figure 6.1: An electrode with translational symmetry above an infinite grounded plane.
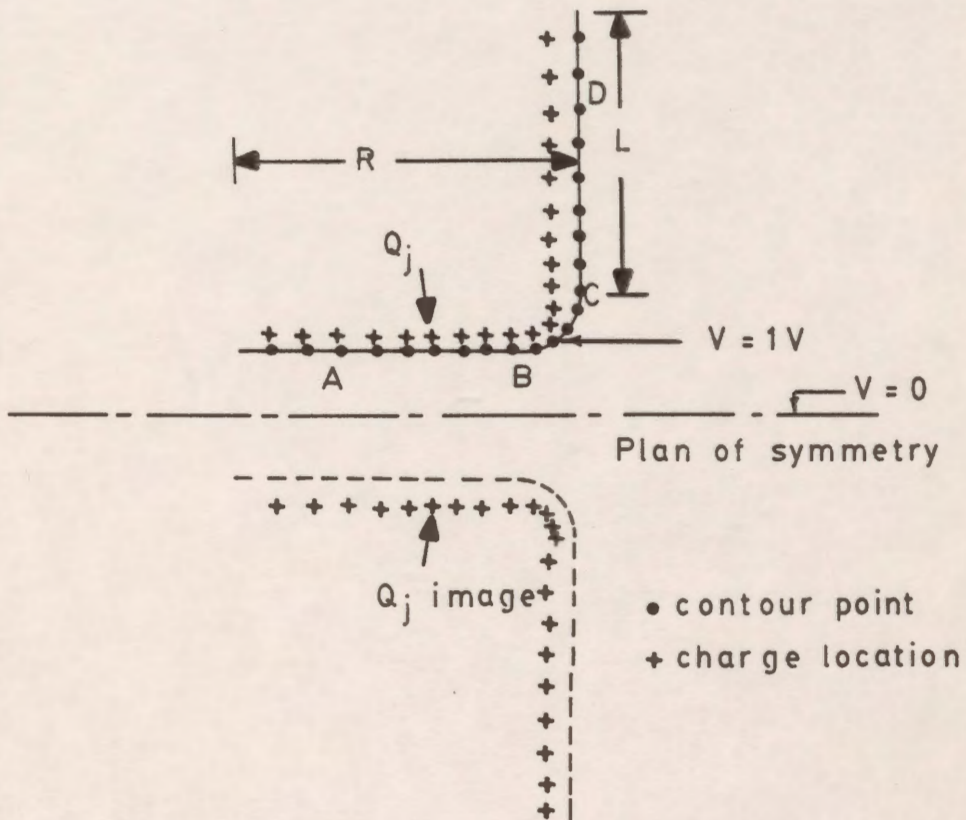
Figure 6.2: The charge simulation model of the system of Fig. 6.1.

charges along the electrode as shown in Fig. 6.3, cases a and b, respectively. The minimum of the maxima of the potential error and the tangential field difference for case a is 0.039% and 0.0184, respectively and they are recorded at n = 120 charges and an assignment factor of 1.2.

In order to evaluate the effect of varying the relative number of charges within the curved portion of the electrode on the accuracy of the simulation, the ratio n_c / n is varied from 0.1 to 0.5 in steps of 0.1 while the total number of charges is fixed at 120 charges and the assignment factor held at 1.2. Table 6.2 describes the effect of varying n_c / n on the potential error and the tangential field difference along the boundary of the whole electrode for cases c and d. It seems from Table 6.2 that the best value of the ratio n_c / n which gives the minima in the percentage potential errors and the tangential field differences is about 0.1.

Another factor which affects the accuracy of the method is the discontinuity in the positions of the charges. Fig. 6.3 shows four conditions for positioning the charges. The first case is to position the charges with a discontinuity between both the horizontal and curved parts, and the curved and the vertical parts (case a). The second case eliminates the discontinuity between the horizontal and curved parts and keeps the other one (case b). In case c, there is a discontinuity between the horizontal and curved parts only. In the last case (case d), no discontinuity is found between the different positions (this case is called the continuous distribution). To study the effect of the different cases on the accuracy of the simulation, the assignment factor is kept fixed at the best value which is 1.2 and the total number of charges is also kept fixed at its highest value which is 120 charges. Also, the ratio n_c / n is kept constant at 0.1.

+ charge location
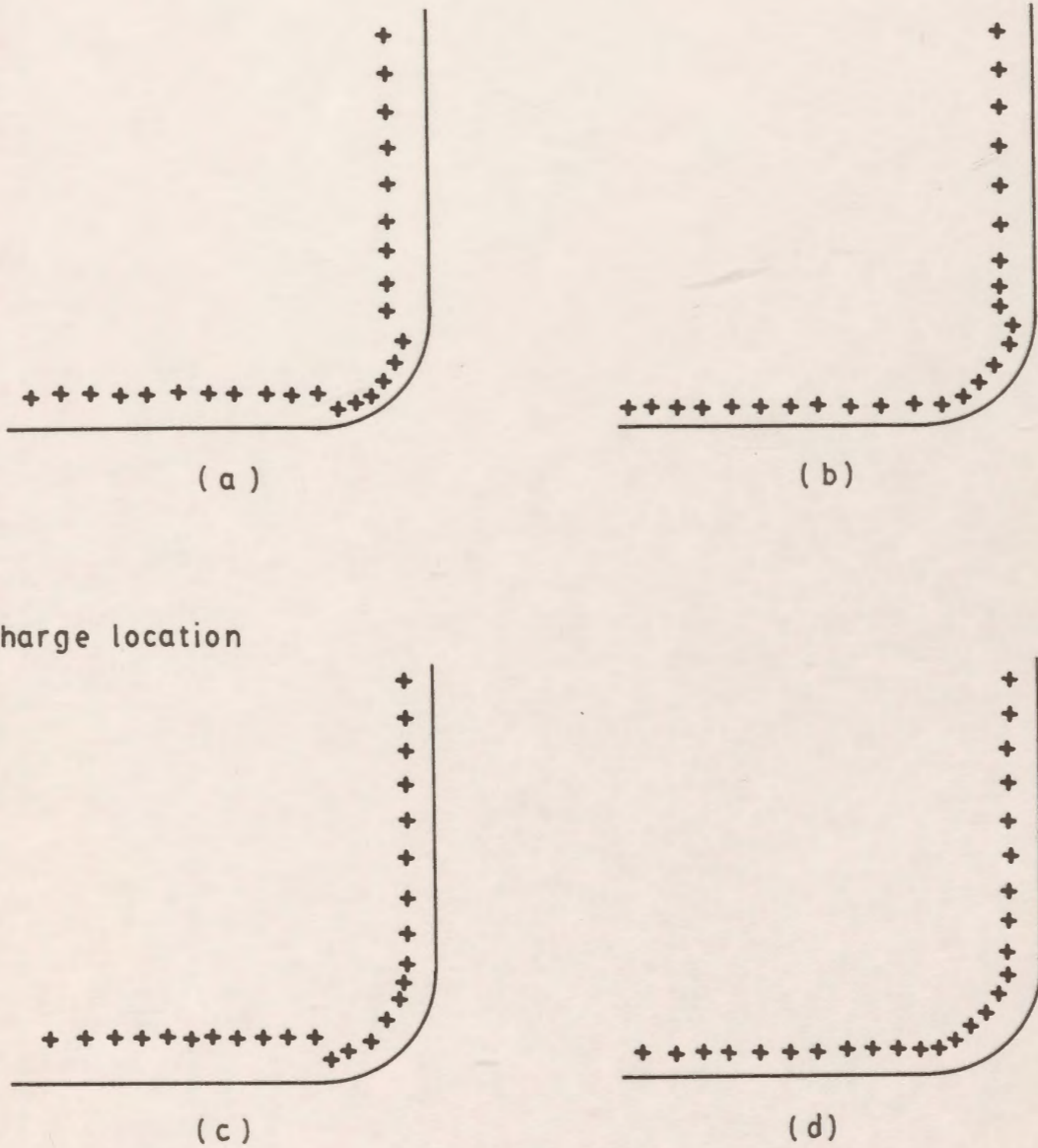
Figure 6.3: Different cases for positioning the charges along the electrode.
(a) double discontinuity in charge alignment
(b) single discontinuity in vertical alignment
(c) single discontinuity in horizontal alignment
(d) continuous charge alignment

Table 6.1: Effect of changing the different parameters on the accuracy of the CSM.

n	β_a	Double discontinuity in charge alignment			Single discontinuity in vertical charge alignment		
		n_c/n	% MPE	MTFD	n_c/n	%MPE	MTFD
	0.7	0.1	0.325	0.0335	0.1	0.208	0.0305
60	1.2	0.1	0.227	0.0352	0.1	0.473	0.0343
	1.5	0.1	0.684	0.0345	0.1	0.973	0.0340
	0.7	0.1	0.160	0.0226	0.1	0.132	0.0208
90	1.2	0.1	0.063	0.0243	0.1	0.061	0.0239
	1.5	0.1	0.163	0.0241	0.1	0.229	0.0239
	0.7	0.1	0.088	0.0179	0.1	0.080	0.0166
120	1.2	0.1	0.039	0.0184	0.1	0.036	0.0182
	1.5	0.1	0.050	0.0184	0.1	0.071	0.0183

Table 6.2 : Effect of varying the ratio n_c/n on the accuracy of the CSM.

n_c/n	Continuous charge alignment		Single discontinuity in horizontal charge alignment	
	% MPE	MTFD	% MPE	MTFD
0.1	0.045	0.0170	0.071	0.0230
0.2	0.388	0.0431	0.495	0.0484
0.3	0.991	0.1130	0.828	0.0827
0.4	1.929	0.1856	1.076	0.1083
0.5	2.395	0.1957	1.677	0.1475

Table 6.3 shows the effect of the discontinuity in the positions of the charges on the accuracy of the CSM. It is obvious from the results that positioning the charges without any discontinuity in alignment reduces the maxima in the potential errors and the tangential field differences (case d).

The potential error and tangential field difference distributions along the electrode surface for case b are shown in Figs. 6.4 and 6.5, respectively. The parameters are kept fixed at the best values. It seems from Figs. 6.4 and 6.5 that the maxima in the values of the errors occur near the transition region of the horizontal and the curved parts. The errors along the rest of the electrode are very small. Fig. 6.6 shows the variation of the percentage maximum potential error on the ratio of the relative number of charges on the curved portion to the total number of charges n_c / n. The lowest of the absolute maximum potential error occurs when n_c / n equals 0.1.

The distribution of the charge density (computed as the product of the electric field and the permittivity of the free space) along the boundary of the electrode is illustrated in Fig. 6.7. It is clear that a higher density of charges are found to be concentrated on the horizontal part while a lower density is found to be on the vertical part of the electrode.

Table 6.3: Effect of discontinuity in position of the charges on the accuracy of the CSM.

Case No.	%MPE	MTFD
Case a	0.039	0.0185
Case b	0.036	0.0182
Case c	0.071	0.0230
Case d	0.045	0.0170
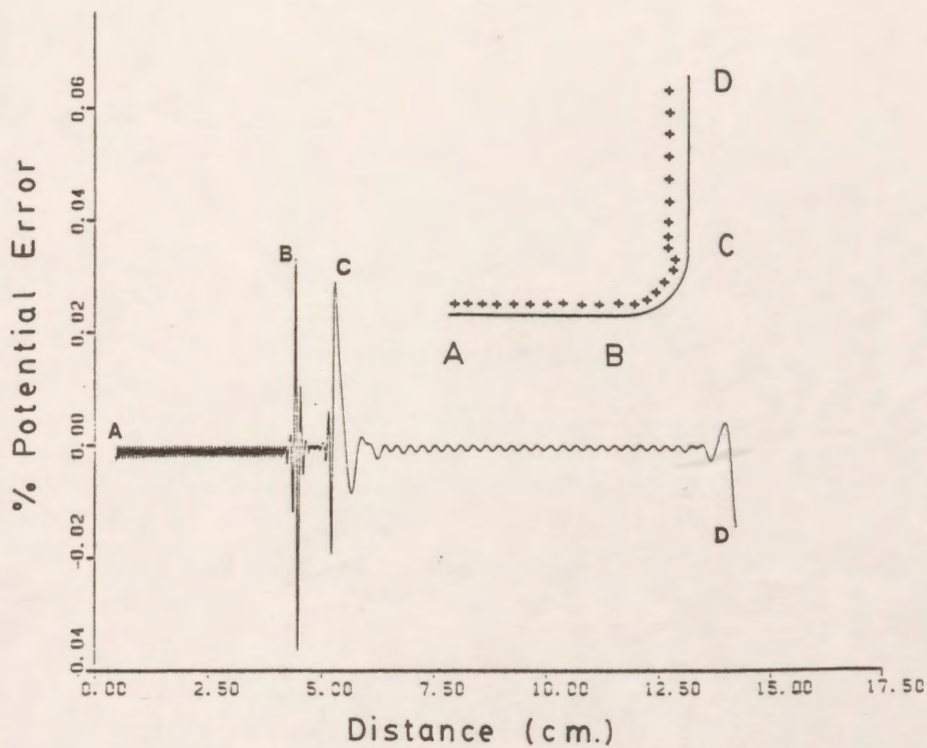
Figure 6.4: Potential error distribution along the electrode surface.
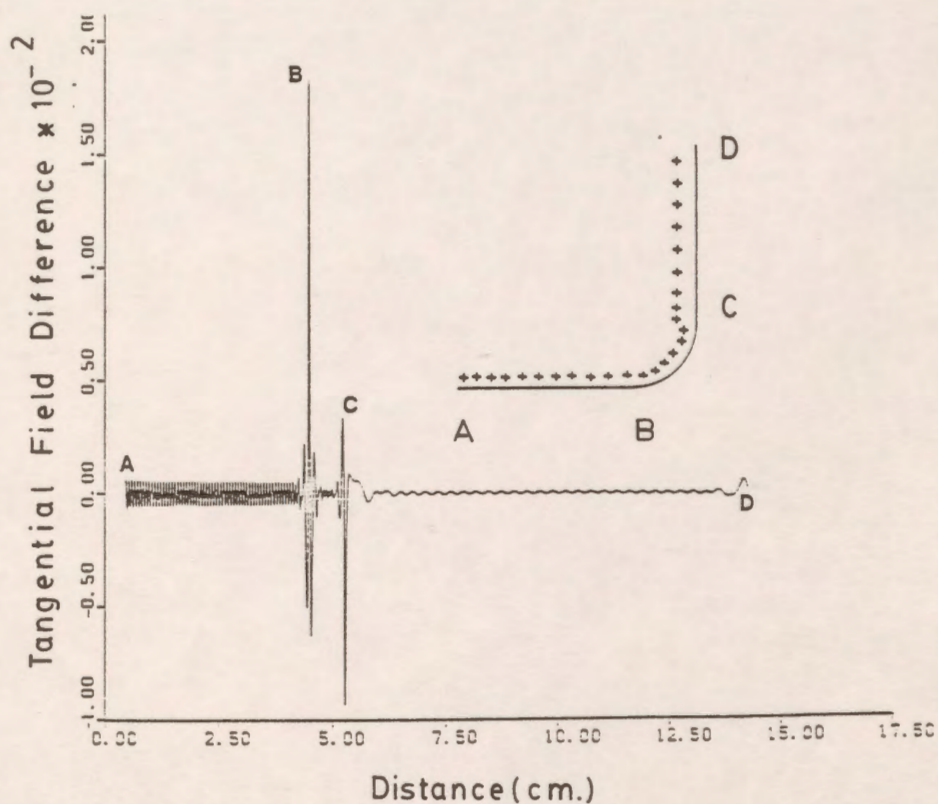
Figure 6.5: Tangential field difference distribution along the electrode surface.
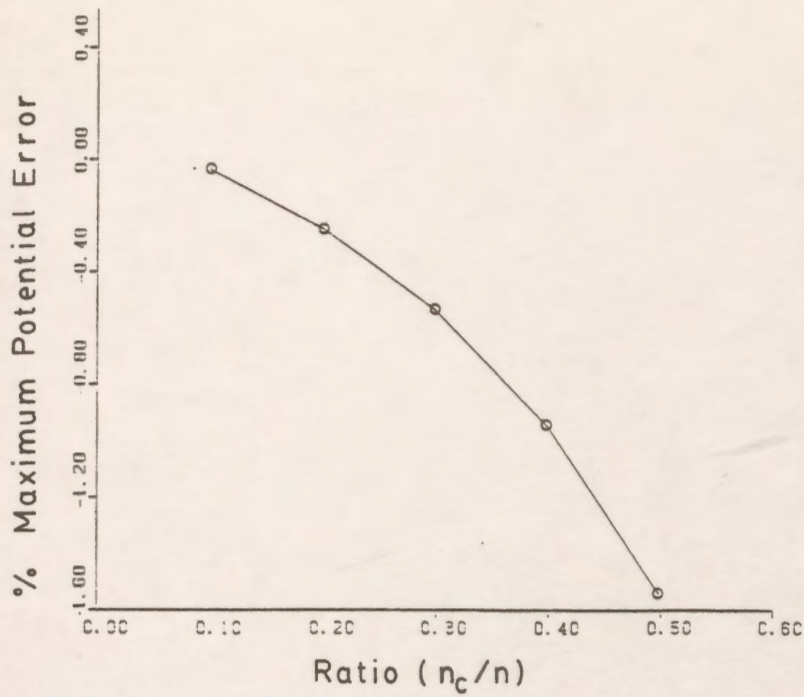
Figure 6.6: Variation of the maximum potential error with the ratio n_c / n.
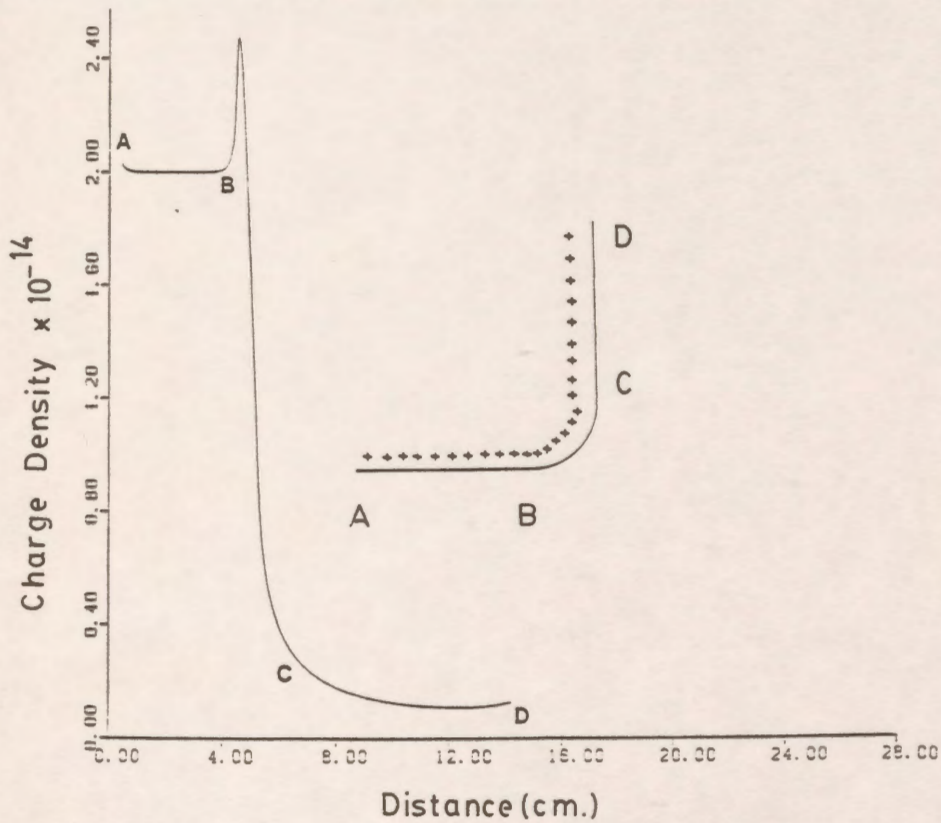
Figure 6.7: Charge density distribution along the surface of the electrode.

6.3 Parameter Selection for A Uniform Charge Distribution

It is found from the above analysis that the continuous alignment distribution of the charges optimizes both the potential errors and the tangential field differences. Therefore, the effect of the assignment factor β_a and the charges per unit length n/L based on a uniform charge distribution on the accuracy of the Charge Simulation method is studied in detail for the system shown in Fig. 6.1.

Figure 6.8 shows the dependence of the maximum potential error recorded along the electrode at fixed values of the charges per unit length (n/L) on the assignment factor. The assignment factor is varied from 0.7 to 2.0 in a step of 0.1 and the results are presented for values of n/L of 6, 10, 14, 20 and 30. It is clear from the graph that as n/L increases, the maximum potential error decreases for the different values of the assignment factor. It is also clear that an increase in the number of charges per unit length beyond 20 does not have a significant influence on the accuracy of the simulation.

Fig. 6.8 also shows that the assignment factor has a large effect on the accuracy of the method. It is noticed that an assignment factor of approximately 1.2 is found to be the best value for all values of the ratio n/L for this specific geometry.

The dependence of the maximum tangential field difference recorded along the electrode on the assignment factor is shown in Fig. 6.9 with the ratio n/L as a parameter. The trend of the tangential field difference curves is the same as those of the potential error curves. It is also found that the best assignment factor for minimum tangential field differences is 1.2.

The potential error distribution along the horizontal, curved and vertical parts of the electrode are shown in Appendix (F). The potential errors near the edges of the horizontal and vertical sections of the electrode are not included. These plots are for regions withdrawn from the edges by almost 33% of the section length and are plotted for n/L=10 and β_a =1.2. It can be seen that except near the transition region between the horizontal and curved parts of the electrode, the potential error seems to be very small and less than 0.01%. The transition region between the
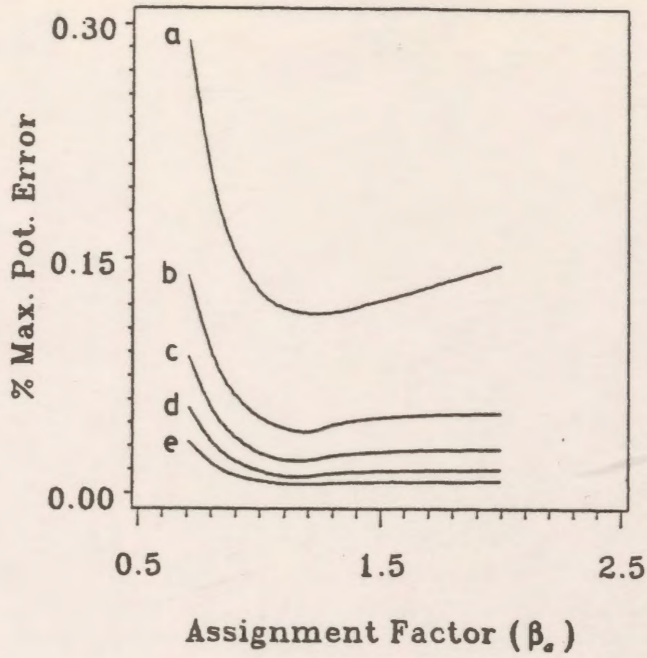
Figure 6.8: Dependence of the maximum potential error on the assignment factor and the charges per unit length.
(a) n/L=6   (b) n/L=10   (c) n/L=14
(d) n/L=20   (e) n/L=30
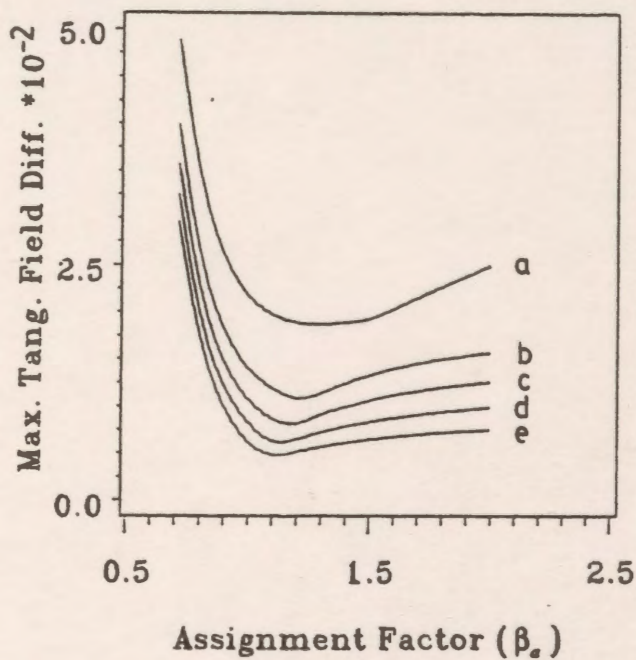
Figure 6.9: Dependence of the maximum tangential field difference on the assignment factor and the charges per unit length.
(a) n/L=6   (b) n/L=10   (c) n/L=14
(d) n/L=20   (e) n/L=30

curved and the vertical parts has little effect on the errors, unlike the other transition, which does have a significant effect.

The tangential field difference distributions along the horizontal, curved and vertical parts are also shown in Appendix (F). Also, except near the transition regions, the tangential field difference values are small and less than 0.01. It should be noted that the maximum values of both the potential errors and the tangential field differences along the electrode have been recorded near the horizontal and curved part transition region.

The recommended values for the assignment factor β_a and the charges per unit length n/L are 1.2 and 10, respectively such that the maximum values of the potential errors and the tangential field differences are small at about 0.05% and 0.01, respectively.

6.4   Effect of the Gap Spacing and the Corner radius on the Accuracy of the CSM

The Charge Simulation method is applied to the system shown in Fig. 6.1 for different gap spacings with n/L=10 and β_a =1.2. The gap spacing is taken as a ratio of the radius of the curved part r. The radius r is kept fixed while G is varied. The maximum potential error and the tangential field difference are plotted as shown in Figs. 6.10 and 6.11, respectively as a function of the ratio G/r for values of G/r from 0.5 up to 10.0. It is found that increasing the gap spacing decreases both the maxima in the potential error and the tangential field difference appreciably. For example, increasing the G/r from 0.5 to 10.0 decreases the maximum potential error from 0.038% to 0.0047% and the maximum tangential field difference from 0.0107 to 0.0013.

Figs. 6.12 and 6.13 show the dependence of the maxima in the potential error and the tangential field difference, respectively on the radius of the curved portion r for two ratios of the gap spacing/corner radius (G/r). The chosen values of the ratio G/r are 0.5 and 10.0 which correspond to the values of G/r for the largest and smallest maxima in the errors for fixed r and variable G. It is clear from these graphs that as the radius r increases, the maxima in the potential error and the tangential field difference decrease for the different values of the ratio G/r.
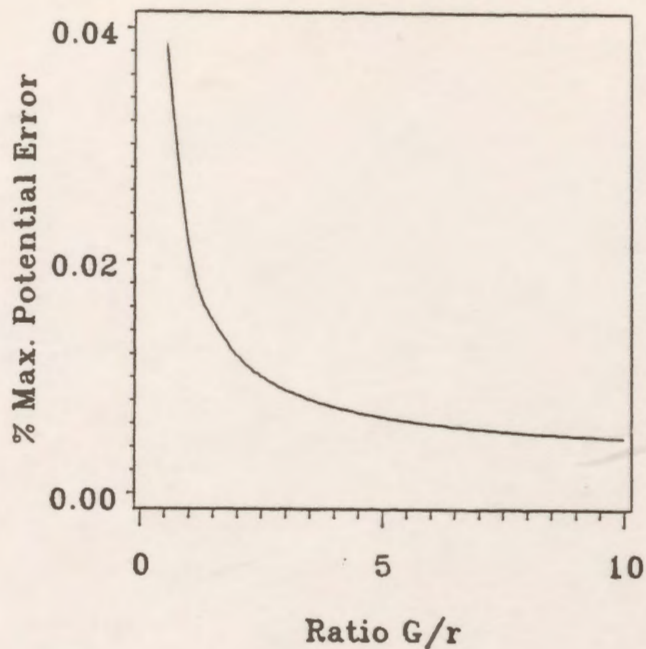
Figure 6.10: Dependence of the maximum potential error on the ratio G/r for r=1 cm.
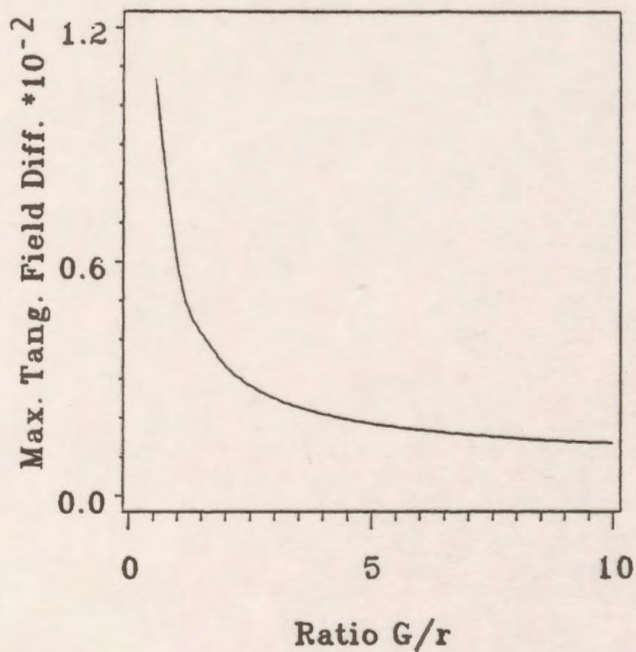
Figure 6.11: Dependence of the maximum tangential field difference on the ratio G/r for r=1 cm.
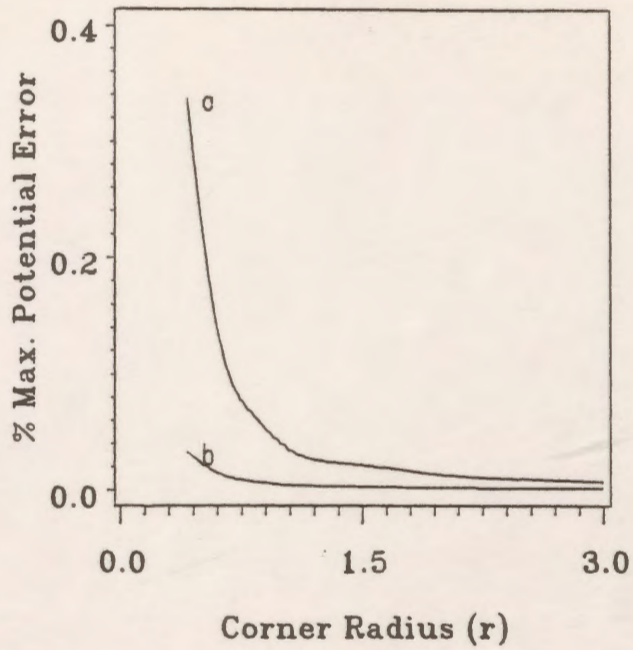
Figure 6.12: Dependence of the maximum potential error on the radius r with G/r as a parameter.
(a) G/r=0.5   (b) G/r=10
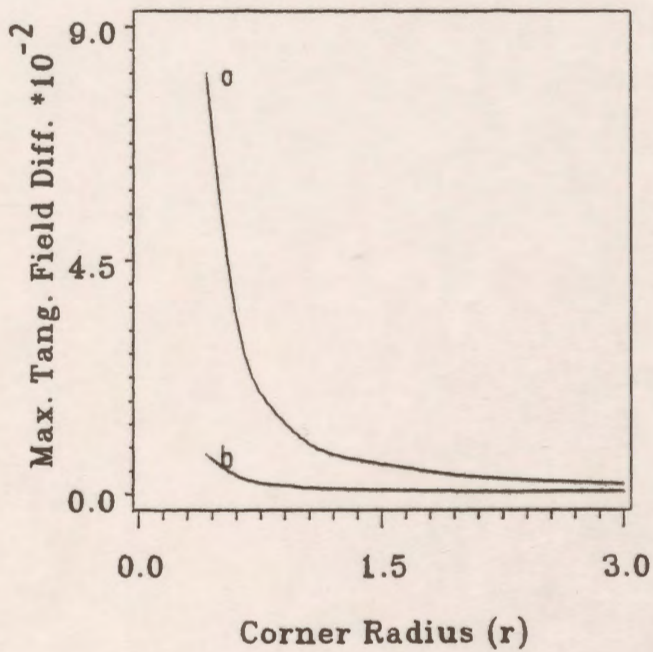
Figure 6.13: Dependence of the maximum tangential field difference on the radius r with G/r as a parameter.
(a) G/r=0.5   (b) G/r=10

6.5   Comparison Between Full Modelling and the Use of Symmetry

The double sided electrode shown in Fig. 6.14 is modelled by using infinite line charges to allow the examination of the differences between full modelling and the use of symmetry. Since the arrangement is symmetrical about the z-axis, two charges of equal value can be positioned symmetrically about the axis of symmetry, and only one half of the system needs to be analyzed for the field. The potential coefficient P_{ij} is computed as the combined effect of both charges on the potential of the i-th contour point and thus the storage requirement is reduced appreciably. The comparison between the two systems is shown in Table 6.4. It is clear from this table that there is no difference between the two systems with respect to the optimum value of the ratio n_c / n, the maximum potential error, and the maximum tangential field difference. The only difference between the two cases (other than the storage requirements) is that the computation time for the double-sides electrode (full modelling) is a little higher than that in the one sided electrode (using the symmetry).
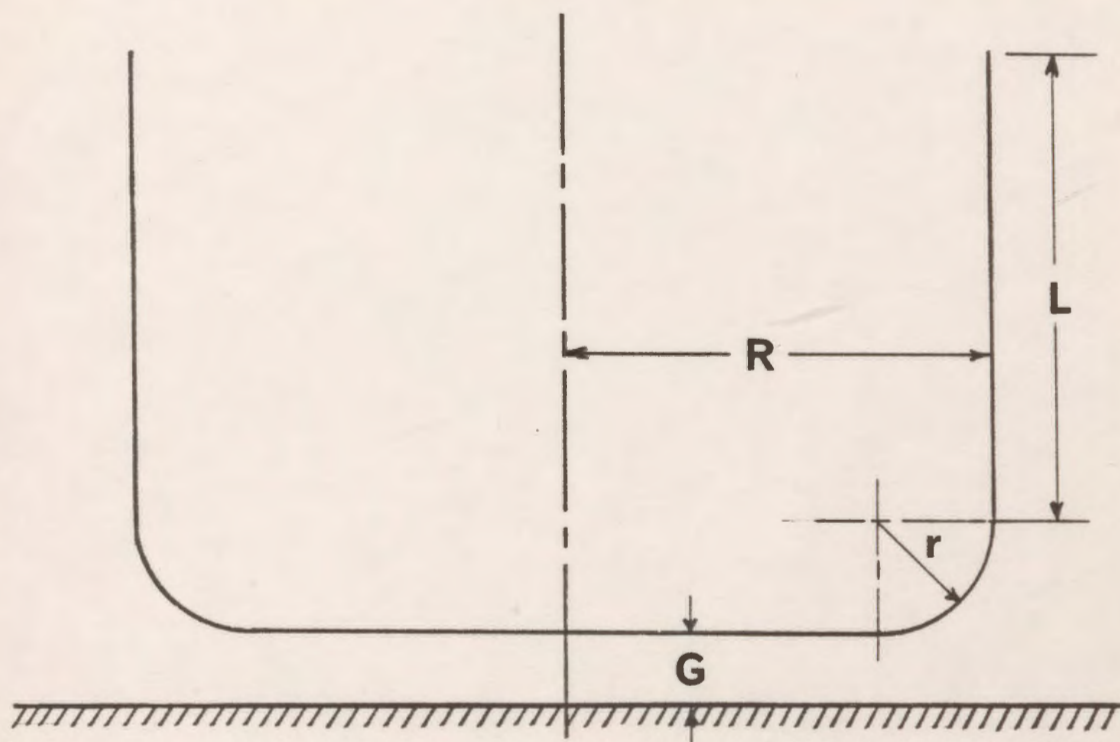
Figure 6.14:   Double sided electrode above an infinite grounded plane.

Table 6.4: Comparison of the full modelling and the use of symmetry regarding the accuracy of
the CSM.

Parameter	Symmetry modelling	Full modelling
n_c / n	0.1	0.1
% Maximum potential error	0.06176	0.06177
Maximum tangential field difference	0.023965	0.023966

6.6 Comparison Between Translational and Rotational Symmetry

The CSM is applied to the system shown in Fig. 6.14 assuming that the electrode has translational symmetry and using infinite line charges for modelling in one case, and assuming that the electrode has rotational symmetry, using ring charges for modelling in the second case. The same number of charges and contour points are used in the two cases. Also, the assignment factor, the relative number of charges on the curved portion as a ratio to the total number of charges and the other parameters which affect the process are kept the same in the two cases. The comparison between the two cases (translational and rotational) regarding the dependence of the maxima in the potential error and the tangential field difference on the ratio R/r which is defined as the ratio of the radius of the electrode to the radius of the curved part is shown in Fig. 6.15 and 6.16, respectively. The ratio R/r is varied from 1.0 which corresponds to a hemispherically capped electrode to 3.0 which corresponds to a busbar.

It is clear from these figures that the potential error and the tangential field difference are higher for the rotationally symmetric case than for the case of translational symmetry for small values of the ratio R/r while there is no significant difference between both cases for large values of the ratio R/r.

The maximum electric field is plotted along the axial gap line as a function of the ratio R/r for translational and rotational cases as shown in Fig. 6.17 for a gap distance of 0.5 cm. It can be seen from this graph that the values of the maximum electric field for rotational symmetry are higher than those for translational symmetry for small values of the ratio R/r. When the ratio R/r approaches 2.0 there is no difference in the maximum field values resulting from translational and rotational symmetry. Using infinite line charges is more advantageous from the computation time point of view.
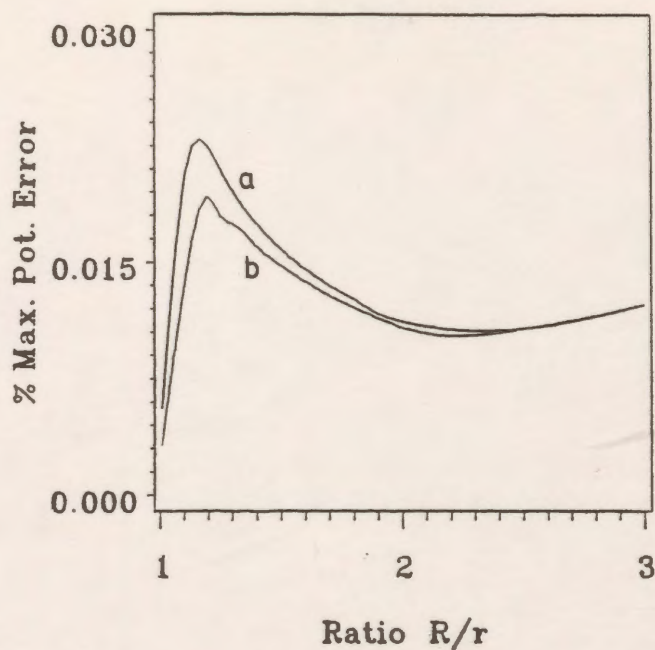
Figure 6.15: Dependence of the maximum potential error on the ratio R/r for rotational and translational symmetry cases for r=1 cm.
(a) rotational   (b) translational
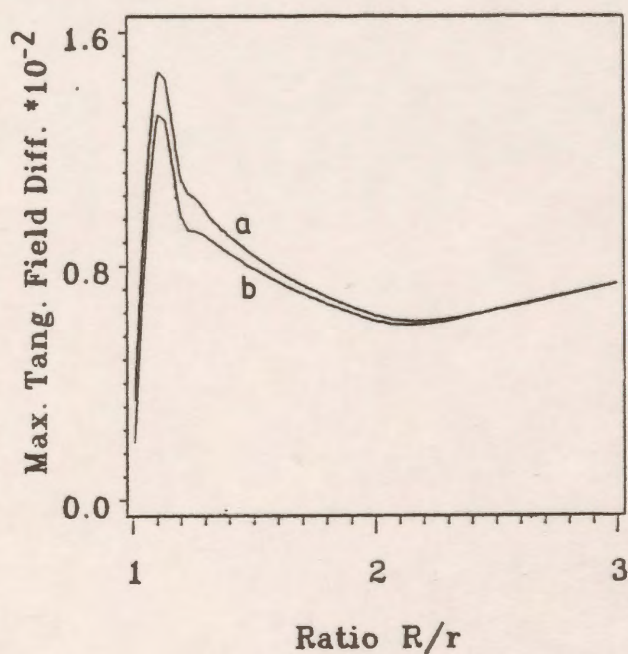
Figure 6.16: Dependence of the maximum tangential field difference on the ratio R/r for rotational and translational symmetry cases for r=1 cm.
(a) rotational   (b) translational
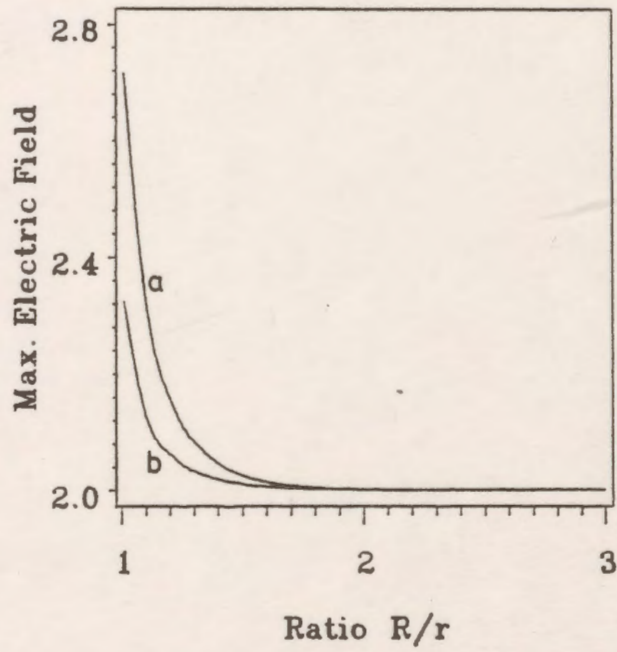
Figure 6.17: Dependence of the maximum electric field along the axial gap line on the ratio R/r for rotational and translational symmetry cases for r=1 cm.
(a) rotational   (b) translational

Chapter VII

APPLICATIONS TO ROTATIONALLY SYMMETRICAL SYSTEMS

7.1   Modelling Simple Electrode Geometries

7.1.1   General

The results of applying the package to several rotationally symmetric electrode shapes are presented to demonstrate the ease with which it can be used to model systems of different geometries and to illustrate some of its useful features [23].

7.1.2   The Test Geometries

The package is applied to five models of electrodes, each representing a charged conductor at potential V_o above an infinite grounded plane. The five models are shown in Figure 7.1(a) through 7.1(e). All the conductors have rotational symmetry and therefore they are modelled by using ring charges. The parameters governing the details of representation can be adjusted to obtain the best modelling of the systems. For each charge modelling the charged conductor, an image charge of opposite polarity is symmetrically placed with respect to the ground surface.

7.1.3   Results

The potential distribution of the rod plane configuration is presented as a sample system for illustrative purposes. The program package is readily used to calculate the potential and the electric field distributions. It is also used to find the potential error on different parts of the electrode.

Fig. 7.2(a) shows the potential error along the hemispherical part of the electrode (part 1) and Fig. 7.2(b) shows the potential error along the cylindrical part of the electrode (part 2). By
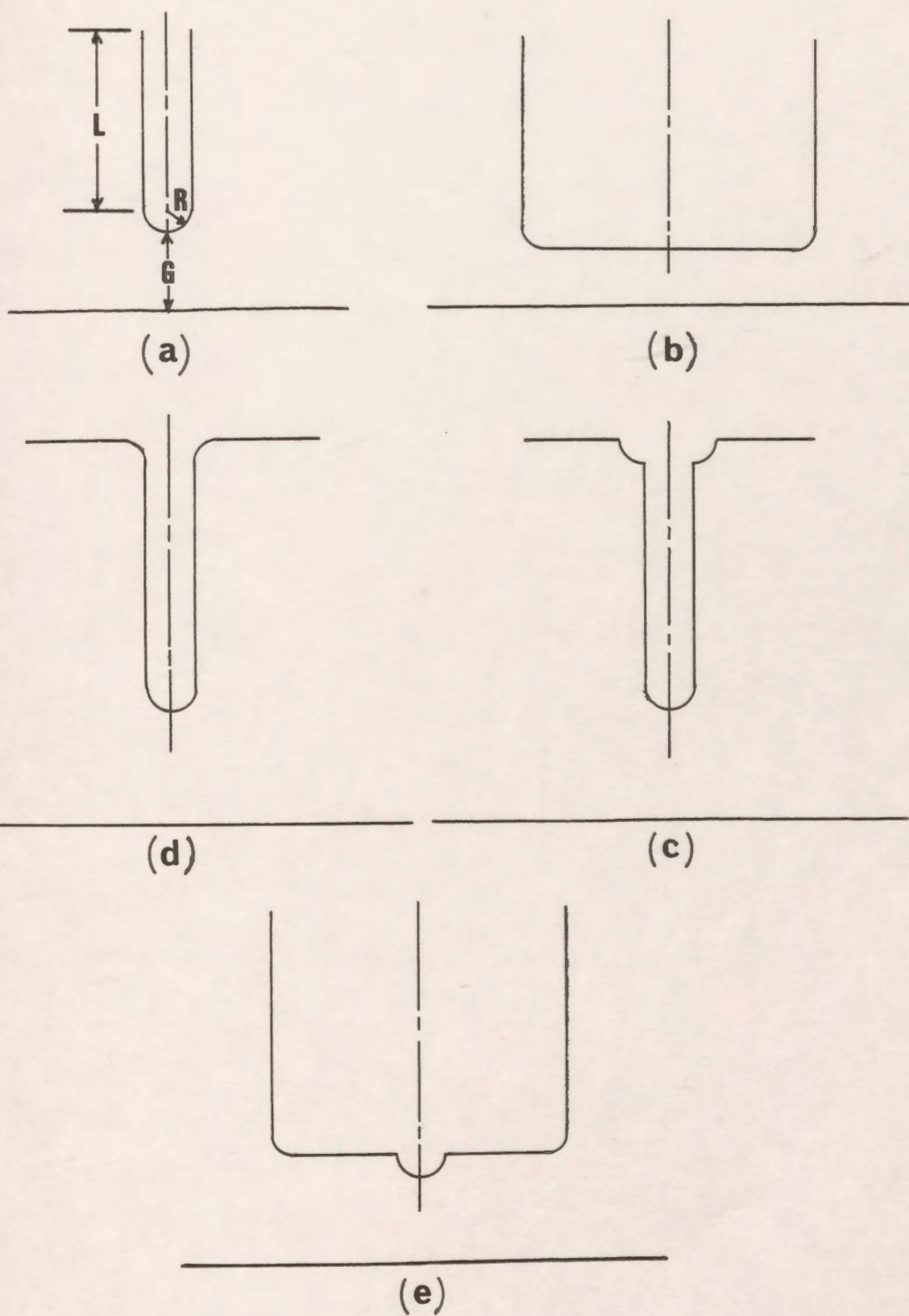
Figure 7.1: A sample of simple electrode geometries.

trial and error adjustment of the parameters affecting the details of representation, the potential error was made to be smaller than that obtained by Yializis et al. [33] and Iravani and Raghuveer [35] for the same dimensions of the electrode. The electrode is modelled by 10 ring charges for the hemispherical part and 30 ring charges to simulate the cylindrical rod. The ratio (G/R) of the gap distance to the radius of curvature is taken as 10 with R equal to 1 cm. The length of the cylindrical rod is G.

Improvement of the accuracy in a certain region can often be achieved by placing a higher density of boundary points near that region. Figs. 7.2(c) and 7.2(d) show the tangential field difference along the hemispherical and the cylindrical parts of the electrode, respectively, and it is also found that these error values are much lower than those obtained in earlier work [35]. Fig. 7.3(a) shows the potential distribution along the axis of symmetry in the region between the ground plane and the tip of the electrode. The total electric field distribution along the axis is also shown in Fig. 7.3(b). Similar results can be produced for the tangential and normal electric field distributions.

The package has been used to iteratively refine example models of electrode systems in order to minimize the errors such as the potential error and the tangential field error along the electrode boundaries and to maximize the quality of the solution.

Curves such as those shown in Figures 7.2(a) through 7.2(d) were examined after each run. Because of such phenomena as the "edge effect" (an increase in error due to poor modelling at the extremities of boundary segments), there is evidently a place for human judgement in assessing results, since simple measures, such as maximum error magnitude, are not universally applicable to all regions. Furthermore, the manner in which several more sophisticated figures of merit should be combined is a matter of opinion which may vary with the system, sub-region or user.

A two-dimensional equipotential field plot is shown in Fig. 7.4.
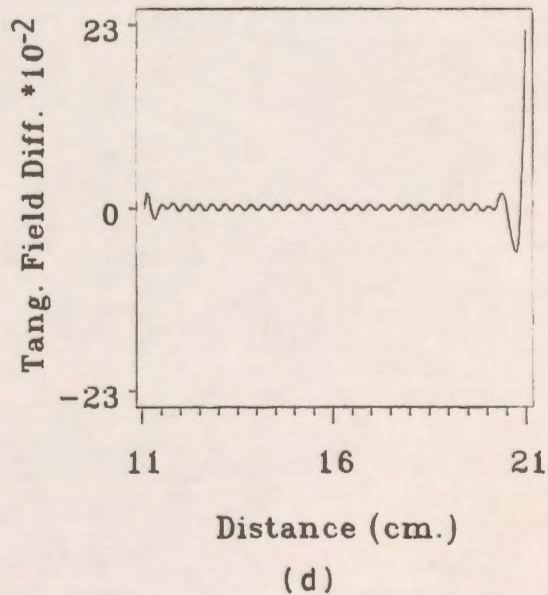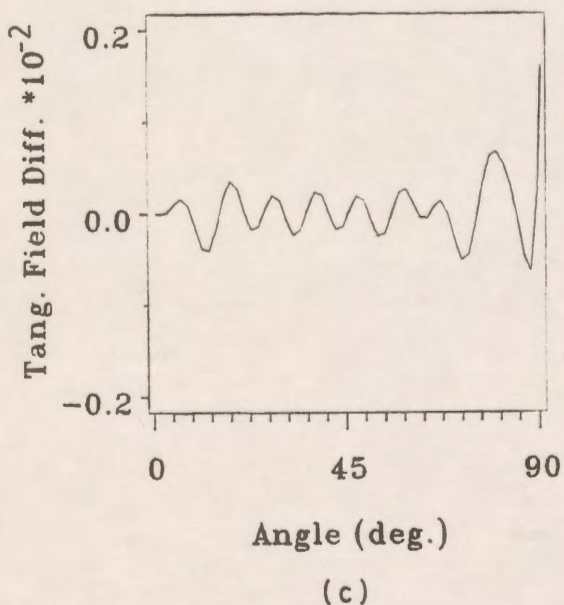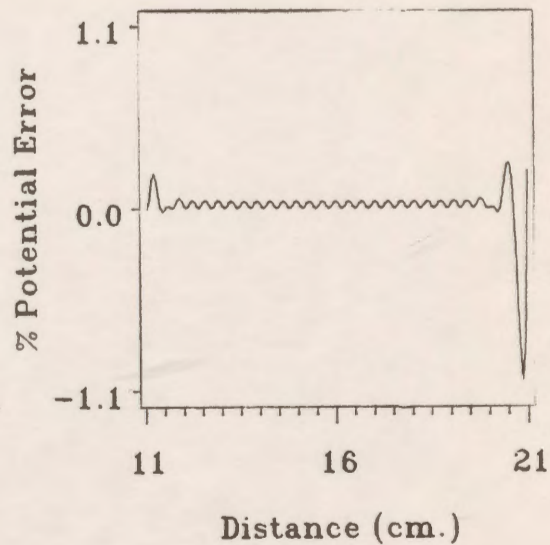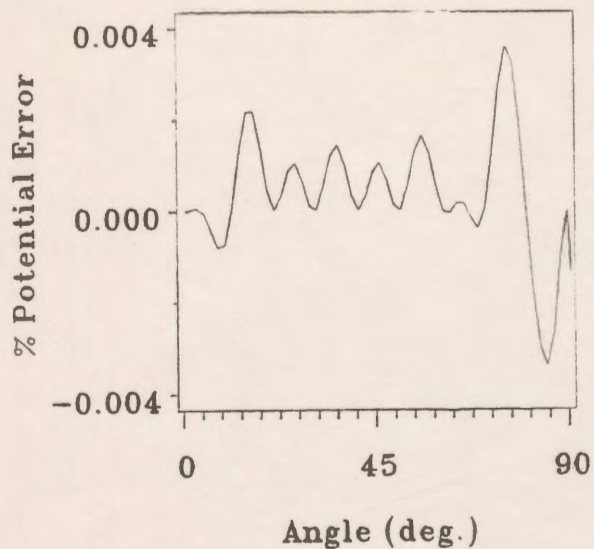
Figure 7.2: Distribution of errors on the electrode boundary.
  (a) potential error - hemispherical part
  (b) potential error - cylindrical part
  (c) tangential field difference - hemispherical part
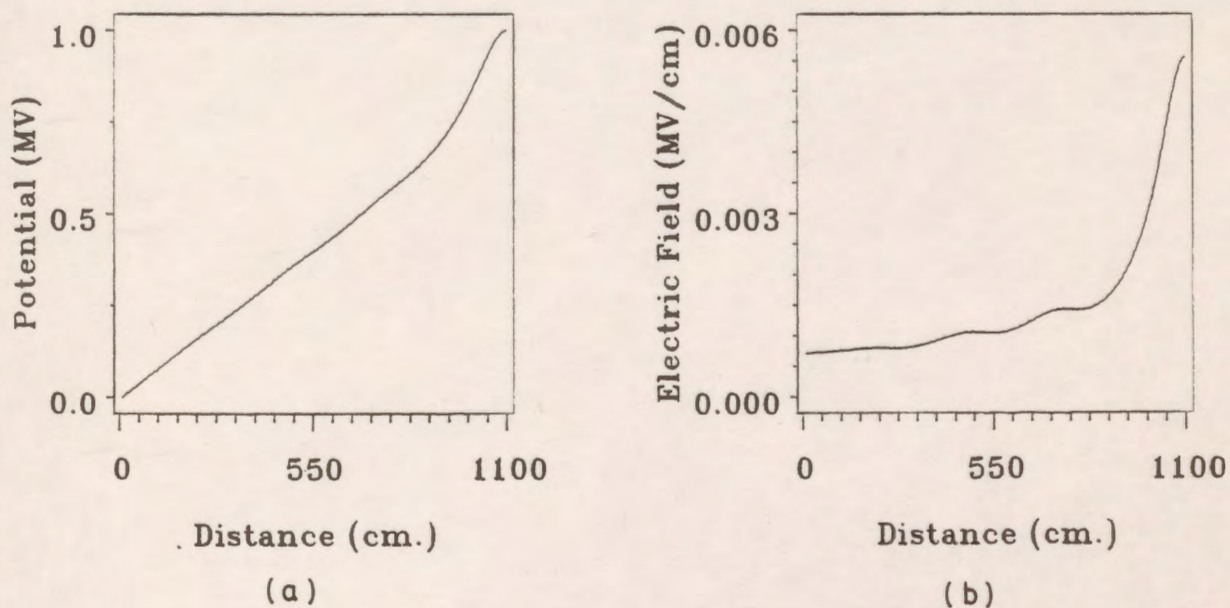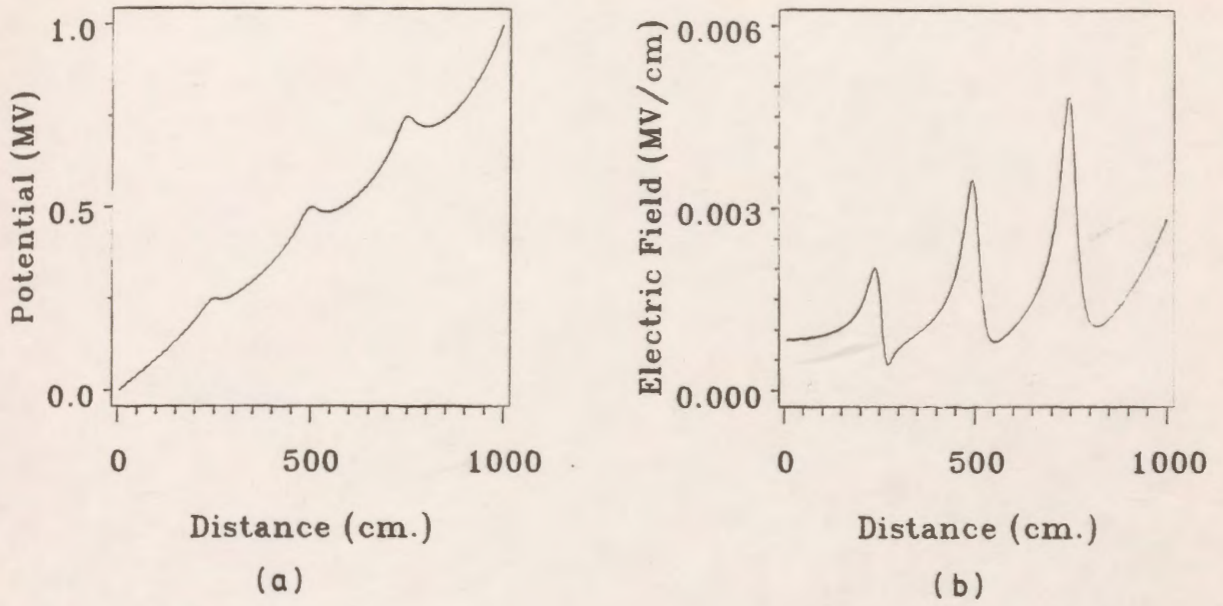 (d) tangential field difference - cylindrical part
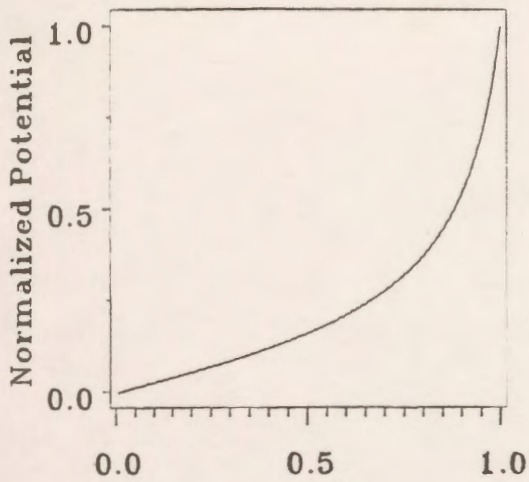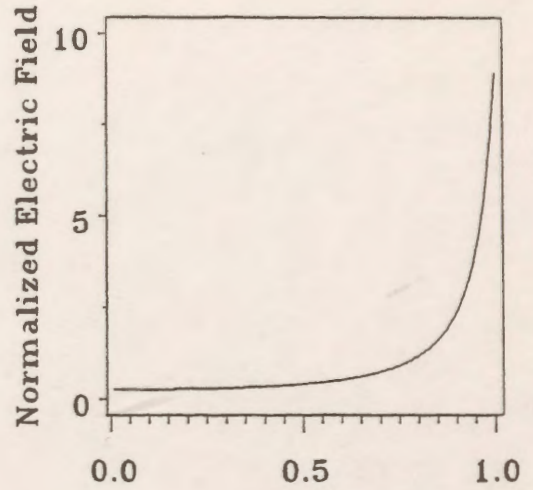
Figure 7.3: Potential and field distributions along the axis.
(a) potential distribution
(b) total field distribution
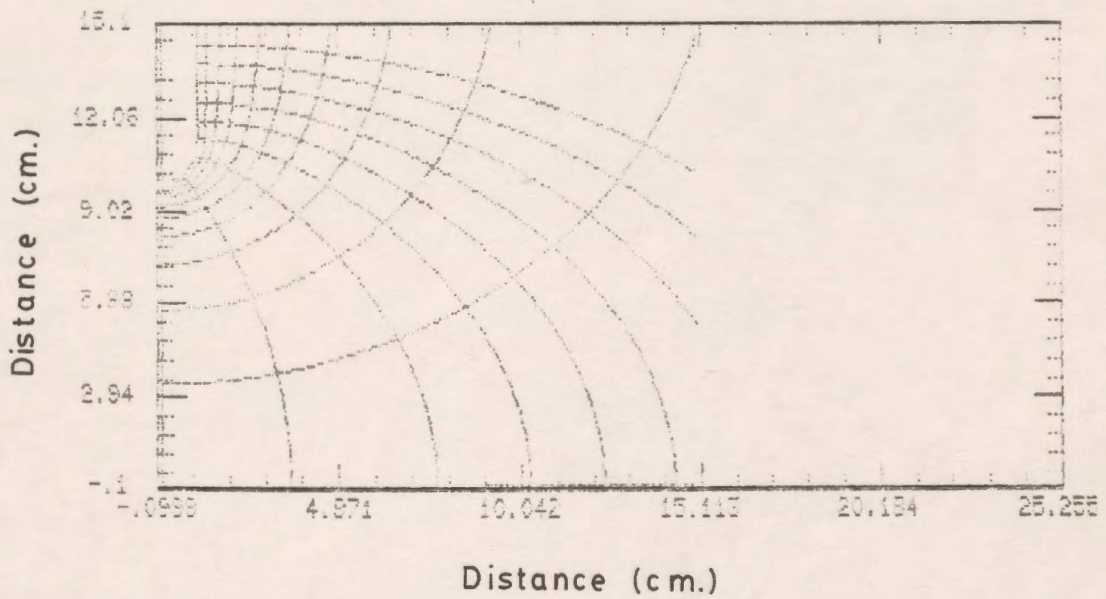
Figure 7.4: Equipotential field plot.

7.2   *Modelling of High Voltage Shielding Apparatus*

7.2.1   General

The Computer-Aided-Design package is applied to two versions of a system used for the shielding of high voltage apparatus. The results presented here include measures of solution errors along portions of the electrode boundaries where maximum errors have been found to occur. More detailed graphical characterization of solution quality measures as well as of characteristics of the fields of the systems studied than have previously appeared in the literature are provided, including an equipotential field map in a planar region of interest.

7.2.2   The Shielding Geometry

Fig. 7.5 shows an electrode arrangement used for the shielding of high voltage apparatus. The potential of the uppermost high voltage electrode is held at U=1.0 MV. and the potentials of the grading rings are fixed at 75, 50 and 25% of the potential U of the top electrode. All dimensions are in cm.

7.2.3   Areas of Concern

The most important areas which are usually of concern are those which have maximum electric field intensities. These are expected to be near the tips of the top electrode and of the grading rings. For this reason more detailed information about the field in these areas is produced and examined.

7.2.4   Refinement Of The Model

7.2.4.1   The Number And Type Of Modelling Charges

It is found that ring charges appear to be suitable for modelling both versions of the system. The number of charges for the system without the dielectric material is 80, and for the system with the dielectric cylinder, 240. The dielectric cylinder interface is modelled by 80 charges located on each side of it and the electrodes by 80 charges.
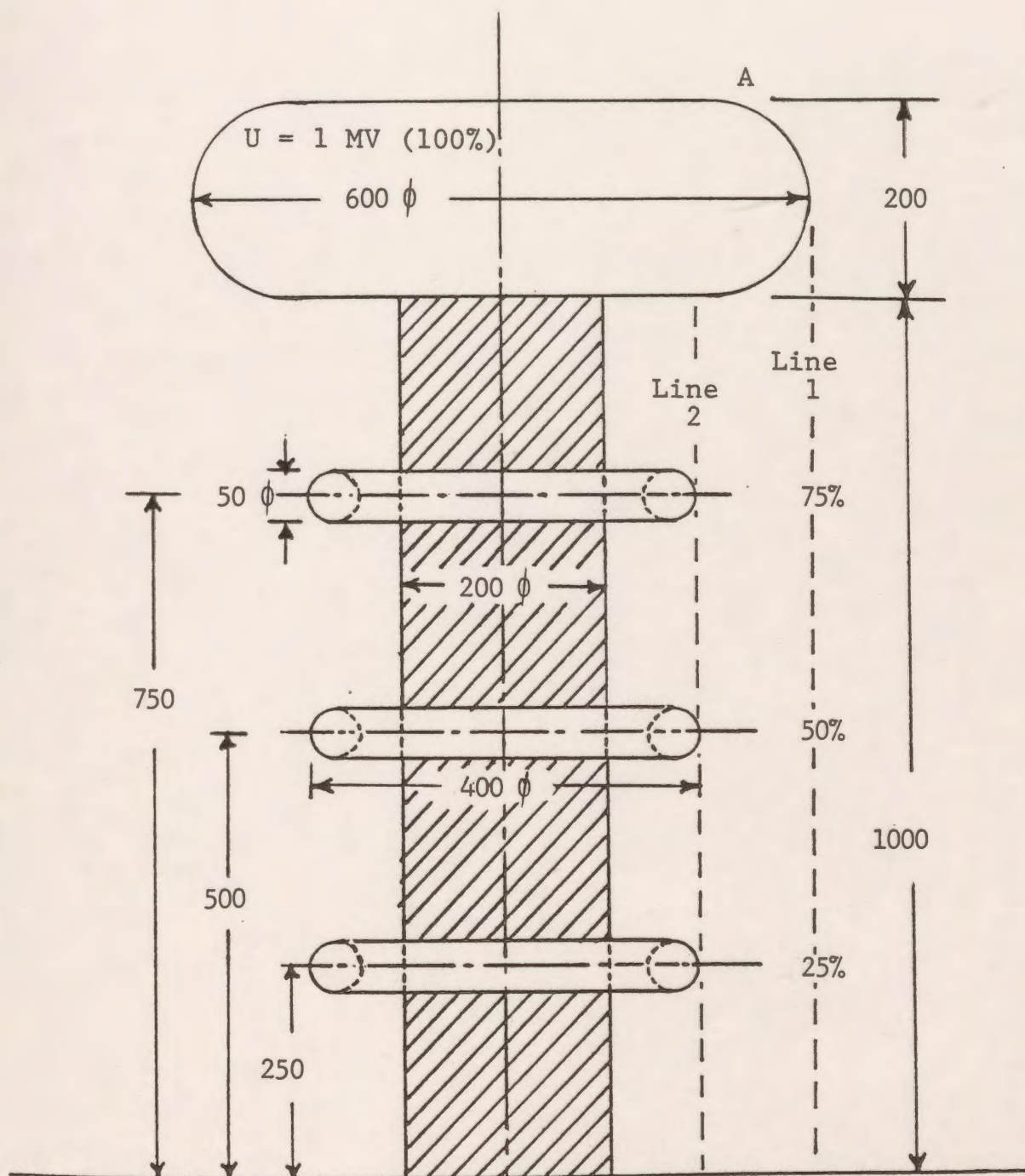
Figure 7.5: High voltage shielding apparatus.

7.2.4.2   Adjusting The Charge Locations

For the most effective application of the CSM the question of a suitable arrangement of the charges and contour points is of importance. The assignment factor is taken between 0.9 and 1.2 along the different sections of the system boundaries.

The accuracy of the calculation depends on the choice of the assignment factor (positioning the charges) and the density of the contour points. If there are abrupt transitions between different sections of the system, or a triple point, the accuracy of the solution will be noticeably affected by the charge placement in these areas. To improve the accuracy, any discontinuity in alignment of the charges adjacent to the transition regions should be avoided. In areas of high interest, the accuracy can usually be improved by an increase in the density of the nearby contour points and charges.

7.2.5   Results

The package is applied to the electrode arrangement shown in Fig. 7.5. The quality of the solution is evaluated by computing the potential error and the tangential field difference. The maximum potential error is found to be about 0.015% near the transition region on the top surface of the top electrode (point "A" in Fig. 7.5). The maximum tangential field difference is found to be as small as 0.0001 near the same area. Figs. 7.6(a) and 7.6(b) show the potential error and the tangential field difference distribution along the horizontal part of the top electrode, respectively. The potential and the total electric field distributions are plotted along a vertical line extending from the ground electrode up to the tip of the top electrode (line-1) as shown in Figs. 7.7(a) and 7.7(b), respectively. The maximum electric field is found to be about 5.57 kV/cm (practically the same as the value reported earlier (5.6 kV/cm) for the same dimensions [21]). Figs. 7.8(a) and 7.8(b) show the potential and the total electric field distributions along a vertical line extending from the ground electrode and passing through the tips of the grading rings up to the bottom of the top electrode (line-2). An equipotential field map is plotted in a region above the first grading ring and is shown in Fig. 7.9.
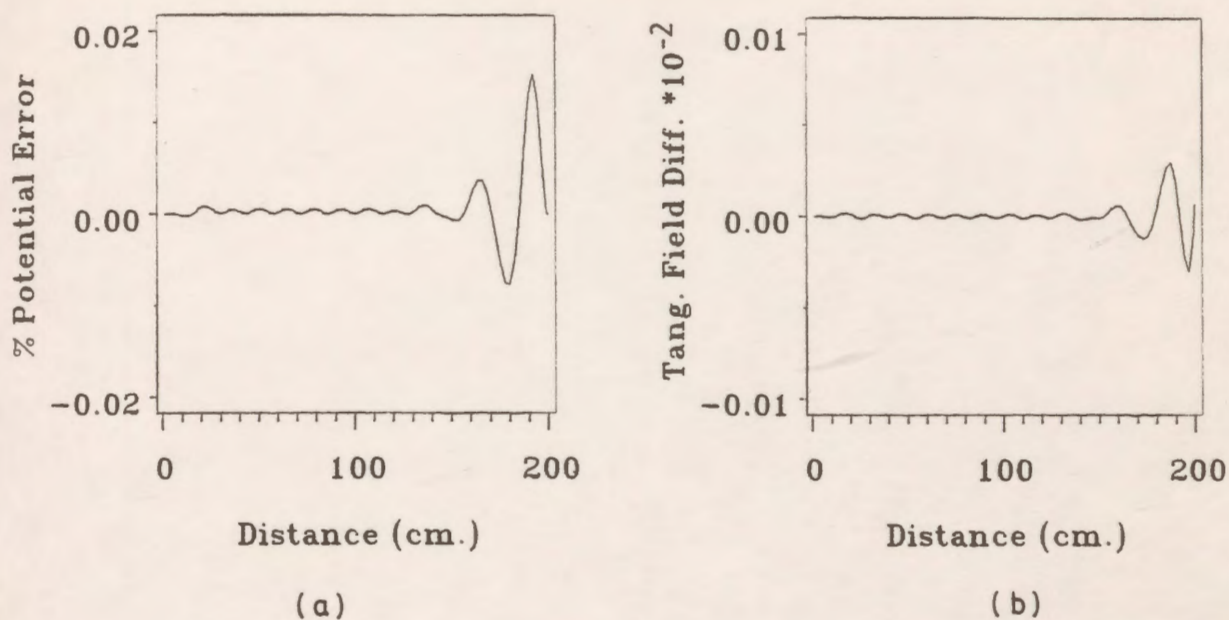
Figure 7.6: Distribution of errors along the horizontal part of the top electrode.
(a) potential error   (b) tangential field error

Figure 7.7: Potential and field distributions along line-1.
(a) potential distribution
(b) total field distribution

Figure 7.8: Potential and field distributions along line-2.
(a) potential distribution
(b) total field distribution
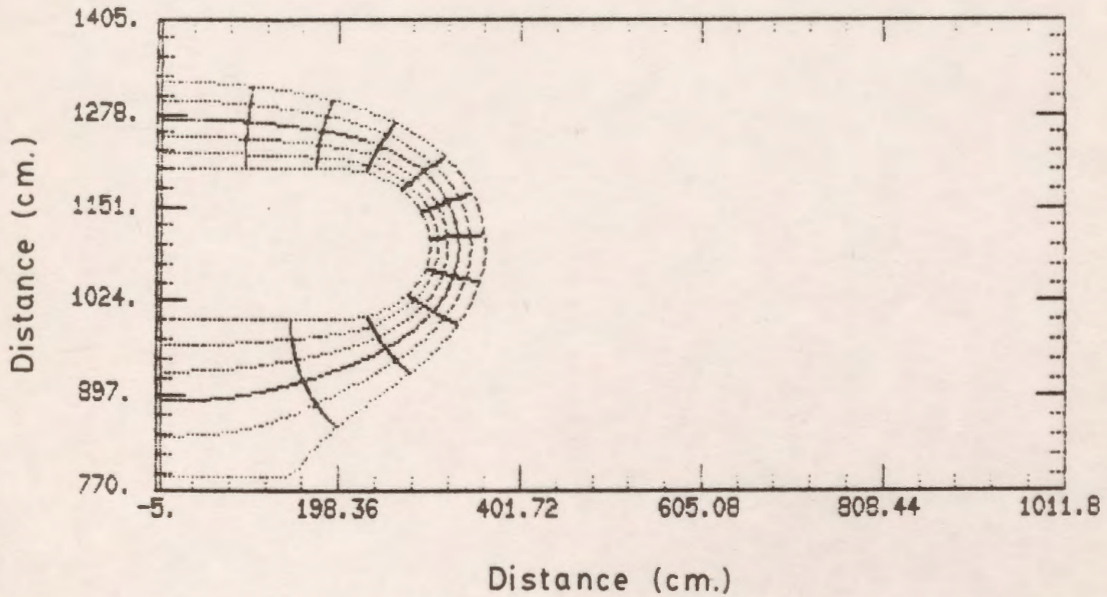
Figure 7.9: Equipotential field plot.

The package is also applied to the same system with a dielectric cylinder as shown in Fig. 7.5 and the quality of the solution is evaluated by computing the various criteria mentioned above. Figs. 7.10(a) and 7.10(b) show the potential and tangential field discrepancies along the interface, respectively and the maxima in the recorded values are $0.8*10^{-3}\%$ and 0.3%. The potential distribution and the tangential field distribution along the interface for the case when the dielectric constant is taken as 6.0 are plotted in Figs. 7.11(a) and 7.11(b), respectively. The maximum tangential electric field is found to be 1.35 kV/cm and the value reported by Singer [21] was 1.36 kV/cm. Also an equipotential field map is plotted for the same region as that of the first version of the system and is shown in Fig. 7.12. The variation of the maximum tangential field strength at the dielectric boundary with the dielectric constant ε_r as a parameter is found to be 1.65, 1.52 and 1.35 kV/cm for ε_r equal to 1.0, 2.2 and 6.0, respectively.
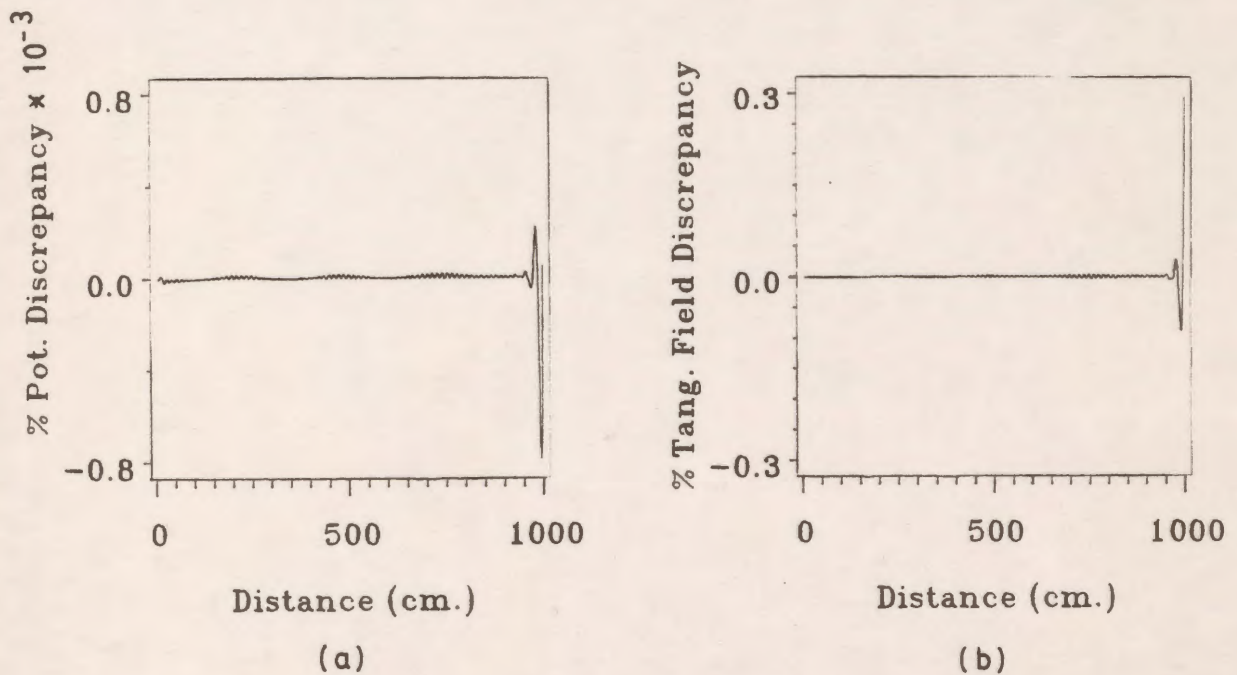
Figure 7.10: Distribution of discrepancies along the dielectric interface.
(a) potential discrepancy   (b) tangential field discrepancy
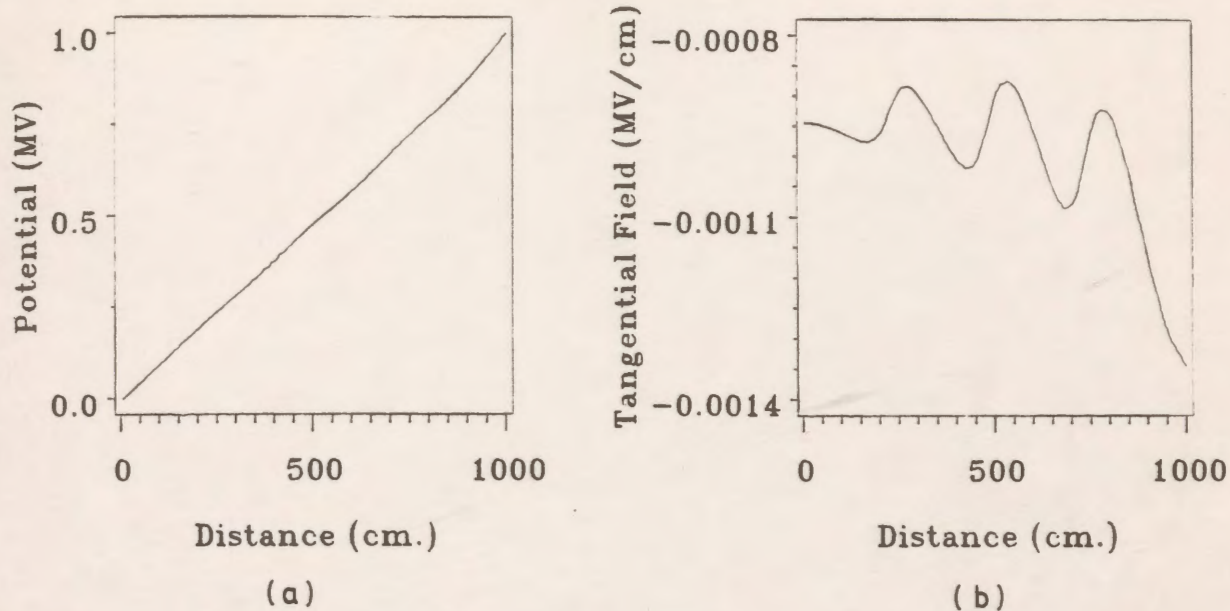
Figure 7.11: Distribution of potential and tangential field along the dielectric interface.
(a) potential   (b) tangential field
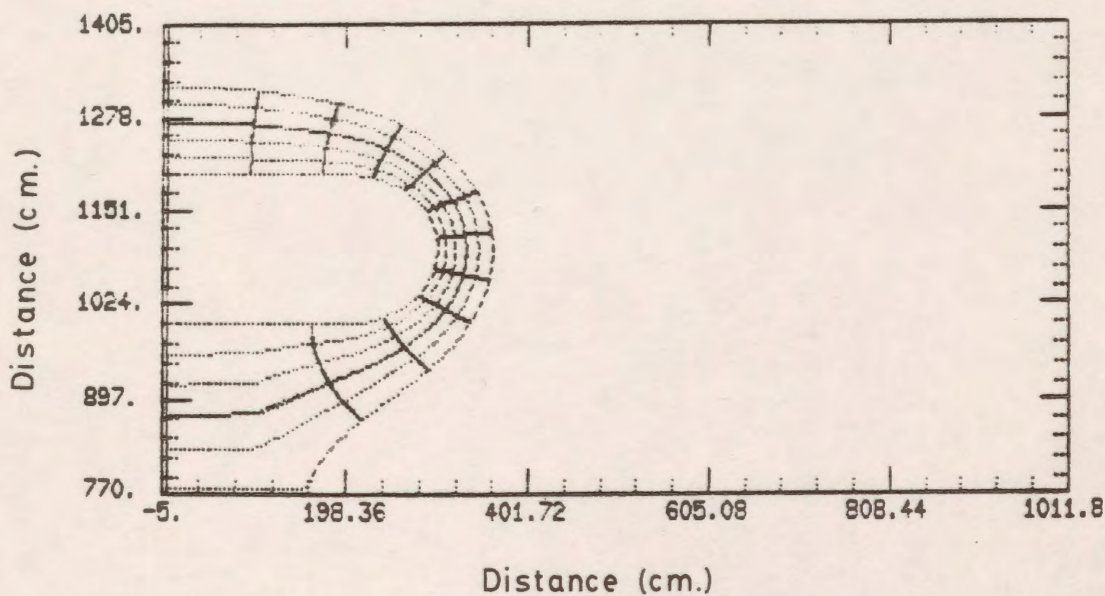
Figure 7.12: Equipotential field plot.

7.3   Calculation of Fields in A Sphere/Slab Arrangement

7.3.1   General

The sphere-sphere or sphere-plane electrode system has long been used for investigation of the electrical breakdown of solid dielectrics. A quantitive estimation of the electric field in the region in which the breakdown occurs is of importance to the interpretation of the experimental results. Flat slab specimens are often tested between a sphere and a plane. Sometimes one face of the slab is given a spherical recess, into which the electrode fits closely. When a slab of higher permittivity than the surrounding region is recessed, the highest electric stress in the medium surrounding the dielectric specimen may be kept much lower than for a plane slab so that there is less likelihood of a discharge originating in the gaseous/vacuum medium rather than in the material of the solid dielectric plate under test [10].

By considering two equal and opposite point charges, Kao [83] calculated the electric field for an infinite dielectric plate between two spherical electrodes. His solution is given as an infinite sequence of charges expressed in terms of applied voltage, radius of the electrodes, thickness of the dielectric plate, and permittivities of the plate and surrounding medium. The results presented by Kao were limited to ratios of plate thickness to electrode diameter between 0 and 1, and ratios of permittivities $\varepsilon_2/\varepsilon_1$ of 1/4, 1 and 4.

Binns and Randall [10] used the FDM in calculating the potential gradients for a dielectric slab placed between a sphere and a plane. The results presented by those authors were for a limited range of slab-thickness to sphere-radius ratios (1/2 and 1). No accuracy measures were provided with the results obtained using the FDM.

Takuma and Kawamoto [45] used the CSM to describe the field intensification at the contact point in various arrangements where a rounded electrode contacts a solid dielectric at zero contact angle. One of these arrangements was the sphere-to-plane dielectric slab. Again, these authors did not present any solution quality measures for the system analyzed by the CSM. They performed calculations for the slab-thickness to sphere-radius in the range from 1 to 16. They also varied

the ratio of the permittivities of the dielectric slab and the surrounding medium to include values greater than unity. Although the electric field strength depends at least as much on the surrounding medium as on the solid dielectric plate itself, they did not examine the fields for permittivity ratios less than 1 (i.e., for cases when the slab permittivity is less than that of the surrounding medium). Also, no analysis and results were provided for a recessed dielectric slab using the CSM.

In the work presented here, the potential distribution and the electric field in a system composed of a sphere and a dielectric slab (plane and recessed) has been calculated using the CAD package. The variation of the electric field on the surfaces of the sphere and the dielectric slab is studied over a wide range of slab- thickness/sphere-radius ratios. The ratio of the permittivities of the dielectric slab and the surrounding medium has been varied to study its effect on the electric field and potential distribution. For convenience in comparison to previously published results, in most of the calculations the distance from the sphere to the earthed plate has been made one half of the sphere radius. The present results are compared with those previously calculated in a more restricted range of slab-thickness/sphere-radius ratios using the Finite Difference method with very good agreement between the two sets of results being observed. Detailed graphical characterization of solution quality measures not presented elsewhere are provided.

Conditions required in order to displace the location of the maximum electric field region away from the inter-electrode gap are presented for the first time.

7.3.2   The System Geometry

Fig. 7.13 shows the sphere electrode and the dielectric slab used in the present study. Fig. 7.13(a) shows a spherical high voltage electrode separated from an earthed plate by a plane dielectric slab. The high voltage electrode has an applied voltage of 1 per unit. The radius of the sphere is R and is assumed fixed at 2 cm. The minimum distance between the sphere and the earthed plate (which is the same as the thickness of the plane slab) is G. The ratio G/R has been

made 1/2 for most of the calculations but is varied from 1/4 to 4 for the generation of some of the results. The ratio of the permittivities of the dielectric slab and the surrounding medium has been varied from 1/30 to 30 to study its effect on the electric field distribution.

Fig. 7.13(b) represents a spherical electrode recessed into the dielectric slab. The ratio G/R is kept constant at the same value used for the unrecessed dielectric plane slab. The thickness of the dielectric slab is represented by D which is the sum of the gap distance G and the recess depth. The fields are calculated for different values of recess depth which is expressed as a ratio of the sphere radius R. Computed fields are presented for recess depths of R/4, 3R/8 and R/2, and for permittivity ratios from 1/4 to 4.

7.3.3   Solution Quality Measures

The Charge Simulation method is applied to the system shown in Fig.7.13(a) for field calculations. Ring charges are used to model the high voltage spherical electrode and the dielectric slab since the system has rotational symmetry about the z-axis. The CAD package capability of allowing the user to change some parameters and keep the others fixed at specified values is used to find the number of charges (or contour points) which results in minimum values of the different potential and field errors and discrepancies. This has been done by assigning a certain number of charges for both the spherical electrode and the dielectric slab and by keeping the charges on the slab fixed and varying those modelling the electrode. Minimum values of overall potential errors (admittedly, a subjective judgement) are reached. The number of charges on the dielectric slab or on the electrode or both are varied until reasonable values of potential discrepancies are obtained without significantly affecting the accuracy of the errors on the spherical electrode. Using this process, the number of ring charges used to model the spherical electrode with the plane slab is found to be 90. Thirty of these charges are used to simulate the spherical electrode, and the other sixty to simulate the interface of the dielectric slab with thirty charges on each side. The radius of the portion of the dielectric slab which is modelled is chosen to be 5 times the radius of the sphere (5R). This corresponds to the same radius chosen by Binns and is used for purposes of comparison.
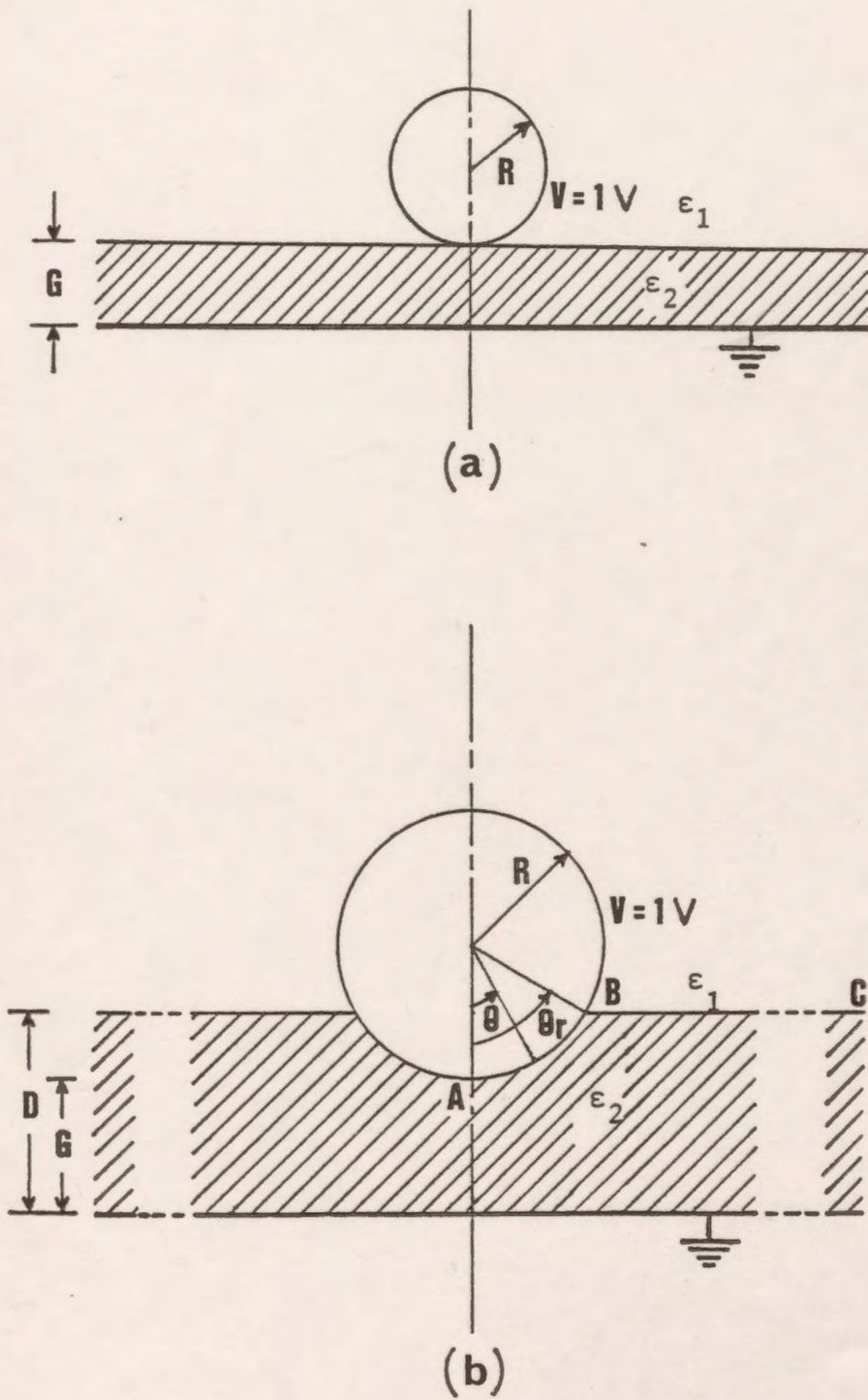
Figure 7.13: Geometries used for charge simulation calculations.
(a) plane dielectric slab   (b) recessed dielectric slab

The maximum potential error and tangential field difference along the electrode are found to be 0.38% and 0.062, respectively and they occur near the triple (contact) point of the sphere, the gas, and the plane dielectric slab. The maximum potential discrepancy, tangential field discrepancy, and normal field discrepancy along the interface of the dielectric are 0.68, 5.0, and 8.6%, respectively and they also occur near the triple point of Fig. 7.13(a).

The charge simulation technique is also applied to the system shown in Fig. 7.13(b). The number of ring charges used to model the spherical electrode and the dielectric slab interface to get minimum values of errors is found to depend on the permittivity ratios and the recess depth of the spherical electrode. It is found to be in the range of 80 to 120 charges. Because the triple point in Fig. 7.13(b) causes some difficulty in simulation and is a region of interest, more detailed graphical characterization of solution quality measures in that vicinity are presented in this work. Fig. 7.14a shows the percentage potential error distribution along the lower part of the sphere (along the arc A-B). A typical value for the maximum percentage potential error is 0.1% and it occurs near the triple point B. The maximum tangential field difference along the arc A-B is 0.1 and it is also found to occur near the triple point B. The potential discrepancy along the interface of the dielectric slab is shown in Fig. 7.14b. It is apparent that the maximum potential discrepancy is about 0.2% near the end of the modelled portion of the infinite dielectric slab while along the rest of the interface it is less than 0.05%. Both the tangential field and the normal field discrepancies along the dielectric interface are plotted in Figs. 7.15a and 7.15b, respectively with maximum recorded values of 7.0 and 18%, respectively.

7.3.4   Computation of Fields

The potential ϕ and the electric field E are computed and presented in a normalized format so that they can be readily used by other researchers. The symbols and notation of reference 10 are retained for reader convenience in comparing both studies. The work presented here is viewed as complementary to that of reference 10 in that the range of G/R is extended here by a factor of 4 over that presented before (in addition to the fact that a different method is used in the calculation).
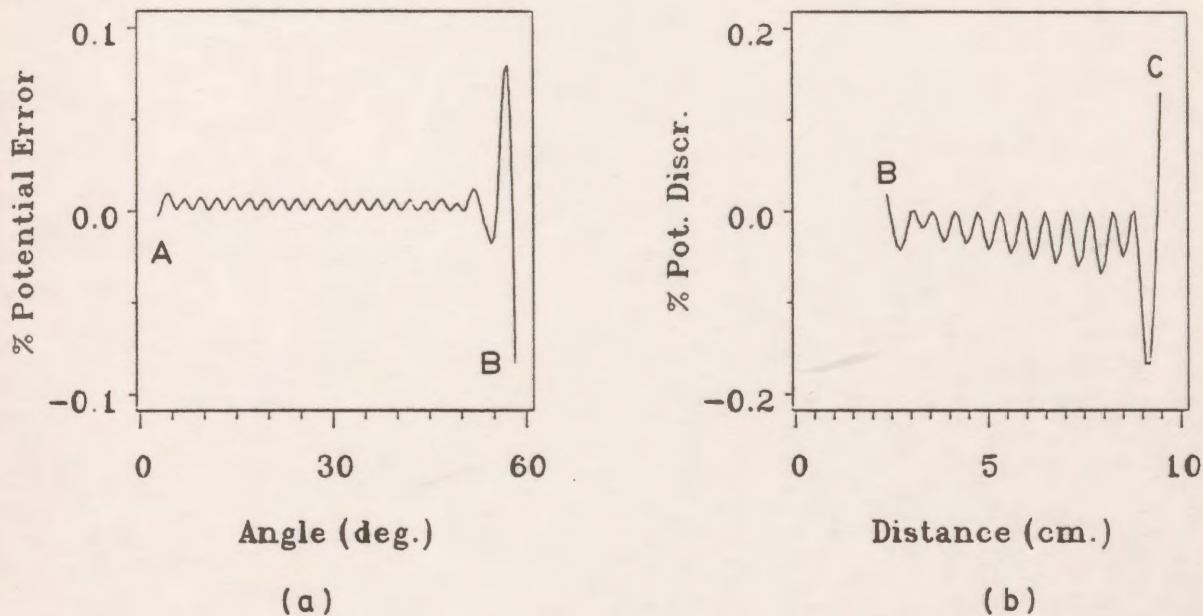
Figure 7.14: Potential error and potential discrepancy distribution for the system of Fig. 7.13(b).
(a) potential error along the arc A-B
(b) potential discrepancy along the dielectric interface
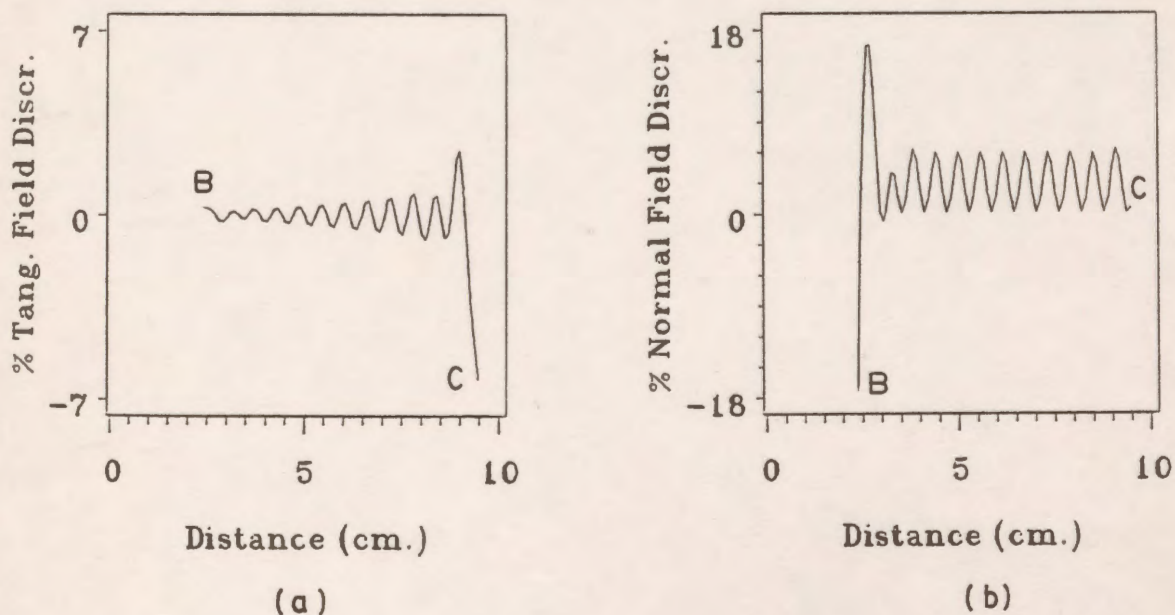
Figure 7.15: Tangential and normal field discrepancies along the surface of the dielectric slab (recessed dielectric slab).
(a) tangential field discrepancy
(b) normal field discrepancy

In the case of the systems shown in Fig. 7.13 where the spherical electrode is raised to a potential V=1, the normalized potential ϕ' and the normalized field components are defined as:

$$\phi' = \frac{\phi}{V}$$

$$E'_n = \frac{E_n}{E_{av}} = \frac{E_n G}{V} = E_n G$$

$$E'_t = \frac{E_t}{E_{av}} = \frac{E_t G}{V} = E_t G$$

where E_n and E_t are the normal and tangential electric fields, respectively and E'_n and E'_t are the normalized normal and tangential field components, respectively. E_{av} is the average field in the gap and is given by $E_{av} = V/G$.

7.3.5   Discussion of Results

7.3.5.1   Plane Dielectric Slabs

The ratio of the permittivities of the surrounding medium and the dielectric slab has been varied and results for the electric field distribution around the spherical electrode are presented for values of $\varepsilon_2/\varepsilon_1$ 4, 1, 1/4 and 1/30 in Fig. 7.16. In all cases the dielectric slab is in contact with both the sphere and the plane. The angle θ is measured from the lowest point on the sphere and increases in the counter-clockwise direction. The field for $\varepsilon_2/\varepsilon_1 = 1$ corresponds to the case where only an upper electrode is present above the grounded plane in a single dielectric medium. Typical values of the normal field for $\varepsilon_2/\varepsilon_1 = 4$, 1, 1/4 and 1/30 at $\theta = 0$ at the surface of the sphere are 8.75, 1.36, 0.29 and 0.035, respectively. The corresponding values of the normal electric field for the same permittivity ratios at G/R = 1 are 13.54, 1.77, 0.322 and 0.0378. These results are much higher than those obtained analytically by Kao and Harker [83] for G/R = 1 and $\varepsilon_2/\varepsilon_1 = 4$. On the other hand, our results are in good agreement with those obtained numerically by Binns et al. [10] and Takuma et al. [45]. The normalized normal values taken from their figures are 13.8 [10] and 14.1 [45] at G/R = 1 and $\varepsilon_2/\varepsilon_1 = 4$, and our value is 13.54.
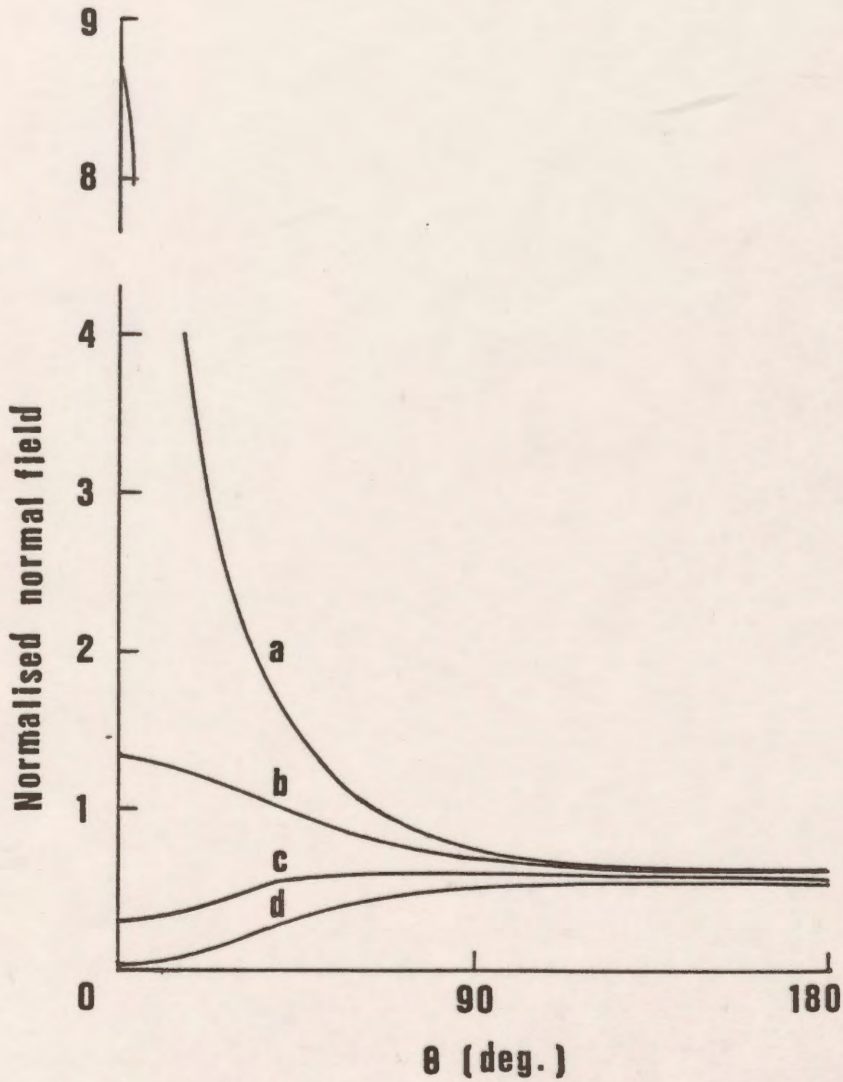
Figure 7.16: Normal field distribution around the sphere for a plane slab for G/R=1/2 and various permittivity ratios.

(a) $\varepsilon_2 / \varepsilon_1 = 4$,   (b) $\varepsilon_2 / \varepsilon_1 = 1$,   (c) $\varepsilon_2 / \varepsilon_1 = 1/4$,   (d) $\varepsilon_2 / \varepsilon_1 = 1/30$

It is clear from Fig. 7.16 that for permittivity ratios $\varepsilon_2/\varepsilon_1$ equal to or greater than 1, the maximum electric field occurs at the contact point and that the field strength becomes higher and much steeper there with increasing $\varepsilon_2/\varepsilon_1$. On the other hand, Fig. 7.16 shows that for permittivity ratios $\varepsilon_2/\varepsilon_1$ less than 1 there can be a maximum in the electric field at a location other than at the contact point. This location is close to $\theta = 90°$.

Fig. 7.17 shows the dependence of the normal field variation at fixed points on the sphere on the permittivity ratio. These fixed points correspond to selected angles θ of Fig. 7.13(a) ($\theta=0°$ (axial point), $30°$, $60°$ and $90°$).

Fig. 7.18 shows the variation of the normalized tangential field along the surface of the plane dielectric slab for different permittivity ratios, out to a distance equal to 1.4R. Typical values of the maximum radial field along the dielectric surface are 0.696, 0.367, 0.265 and 0.21 for $\varepsilon_2/\varepsilon_1$ equal to 4, 1, 1/4 and 1/30, respectively. Good agreement (generally within 1%) exists between these results and [10].

The variation of the normal electric field around the sphere for different gap distance to sphere radius ratios with $\varepsilon_2/\varepsilon_1$ equal to 1/4 is shown in Fig. 7.19. It is clear that as the ratio G/R increases at a constant value of $\varepsilon_2/\varepsilon_1$ the normalized electric field strength increases everywhere. An increase in G/R from 1/4 to 4 corresponds to an increase in the maximum normal field from 0.373 to 4.136. Fig. 7.20 presents the variation of the maximum field on the sphere with the slab-thickness/sphere-radius ratio for different permittivity ratios. The maximum normal field appears to vary linearly with the ratio G/R when that ratio is greater than 1/2. It is clear from this figure that as the permittivity ratio increases at any value of G/R, the maximum field increases. Typically at G/R=2, the maximum field increases from 2.136 to 23.56 as the permittivity ratio $\varepsilon_2/\varepsilon_1$ increases from 1/4 to 4.

Fig. 7.21 shows the variation of the potential along the interface of the dielectric slab for a limited width of the interface (out to 1.4R) for various gap ratios and $\varepsilon_2/\varepsilon_1=4$.
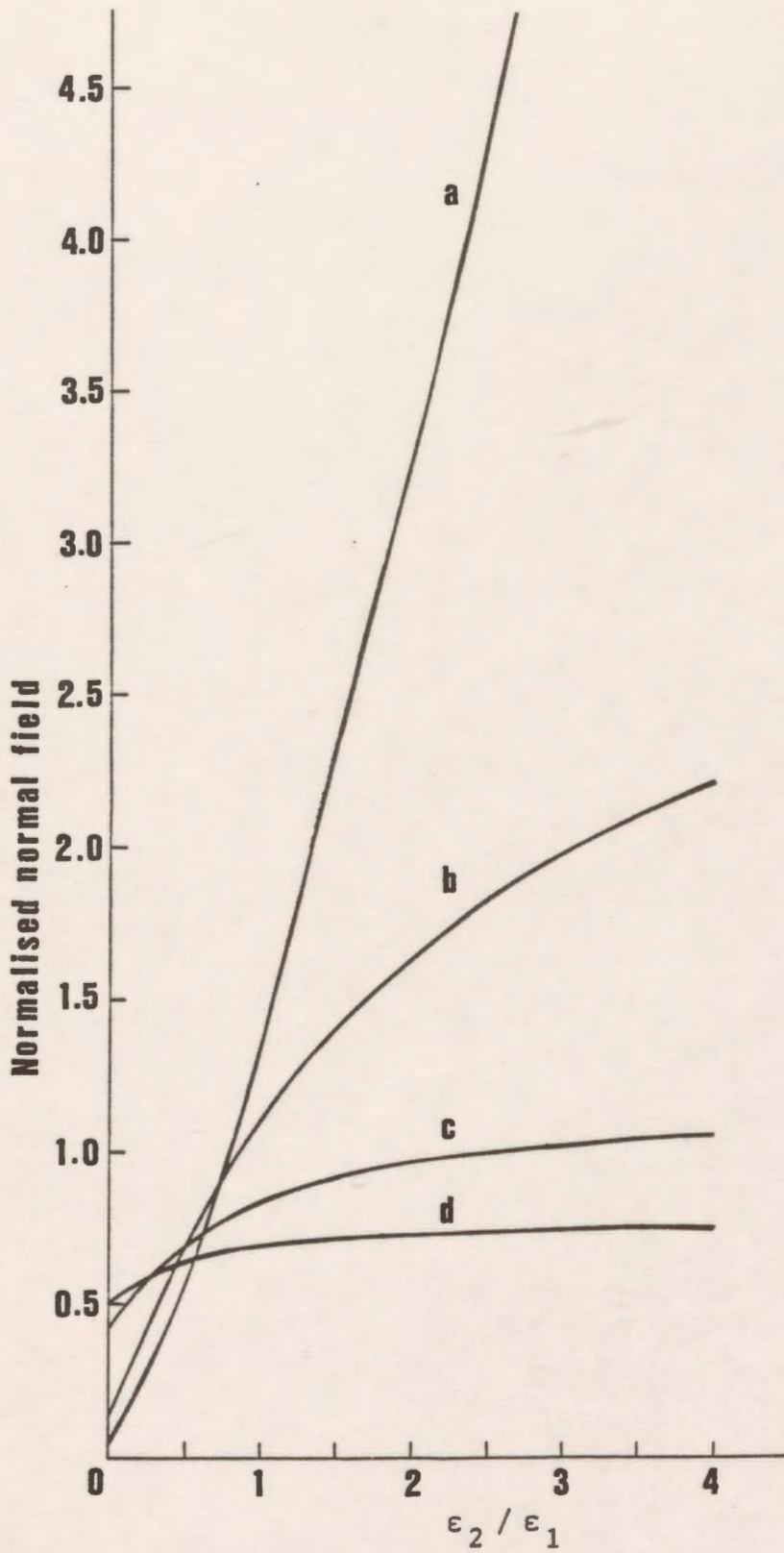
Figure 7.17: Variation of normal field at fixed points on sphere with permittivity ratio for a plane slab for G/R=1/2.

(a) $\theta = 0°$,   (b) $\theta = 30°$,   (c) $\theta = 60°$,   (d) $\theta = 90°$
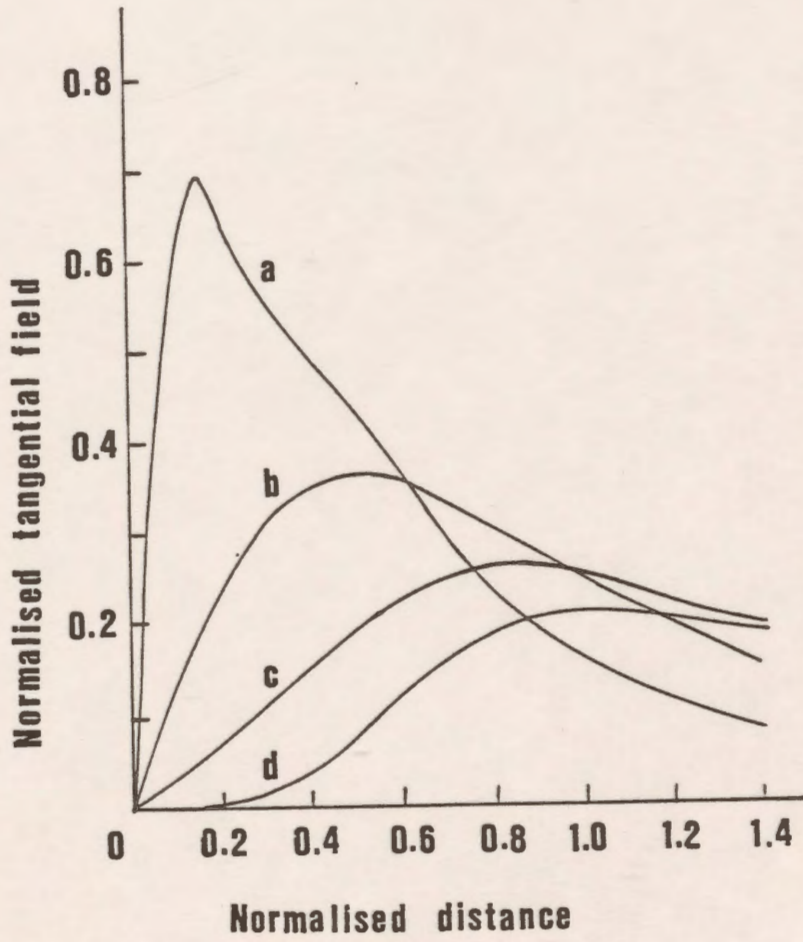
Figure 7.18:   Variation of tangential field on a plane slab for G/R=1/2 for different permittivity ratios.

(a) $\varepsilon_2 / \varepsilon_1 = 4$,   (b) $\varepsilon_2 / \varepsilon_1 = 1$,   (c) $\varepsilon_2 / \varepsilon_1 = 1/4$,   (d) $\varepsilon_2 / \varepsilon_1 = 1/30$
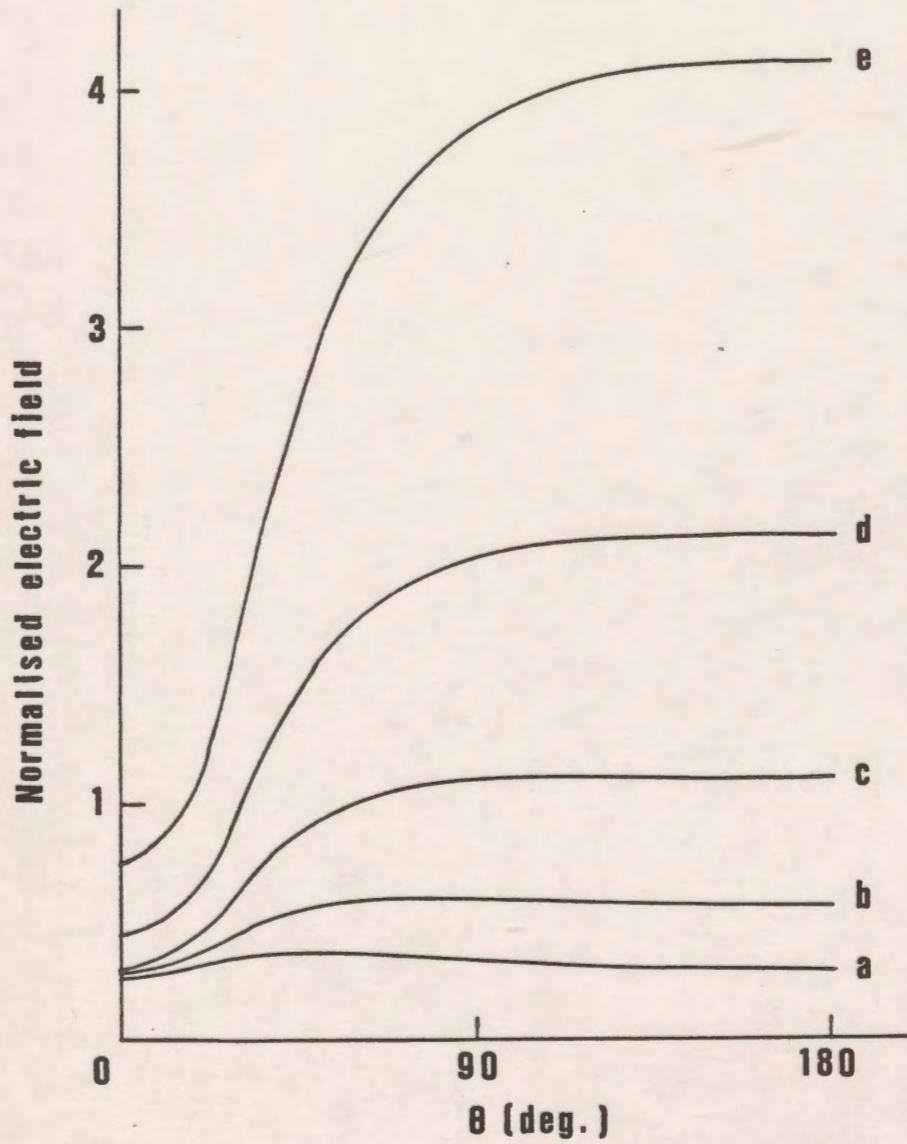
Figure 7.19: Variation of normal field around the sphere with a plane slab for $\varepsilon_2 / \varepsilon_1 = 1/4$ and various G/R ratios.
(a) G/R=1/4, (b) G/R=1/2, (c) G/R=1, (d) G/R=2, (e) G/R=4
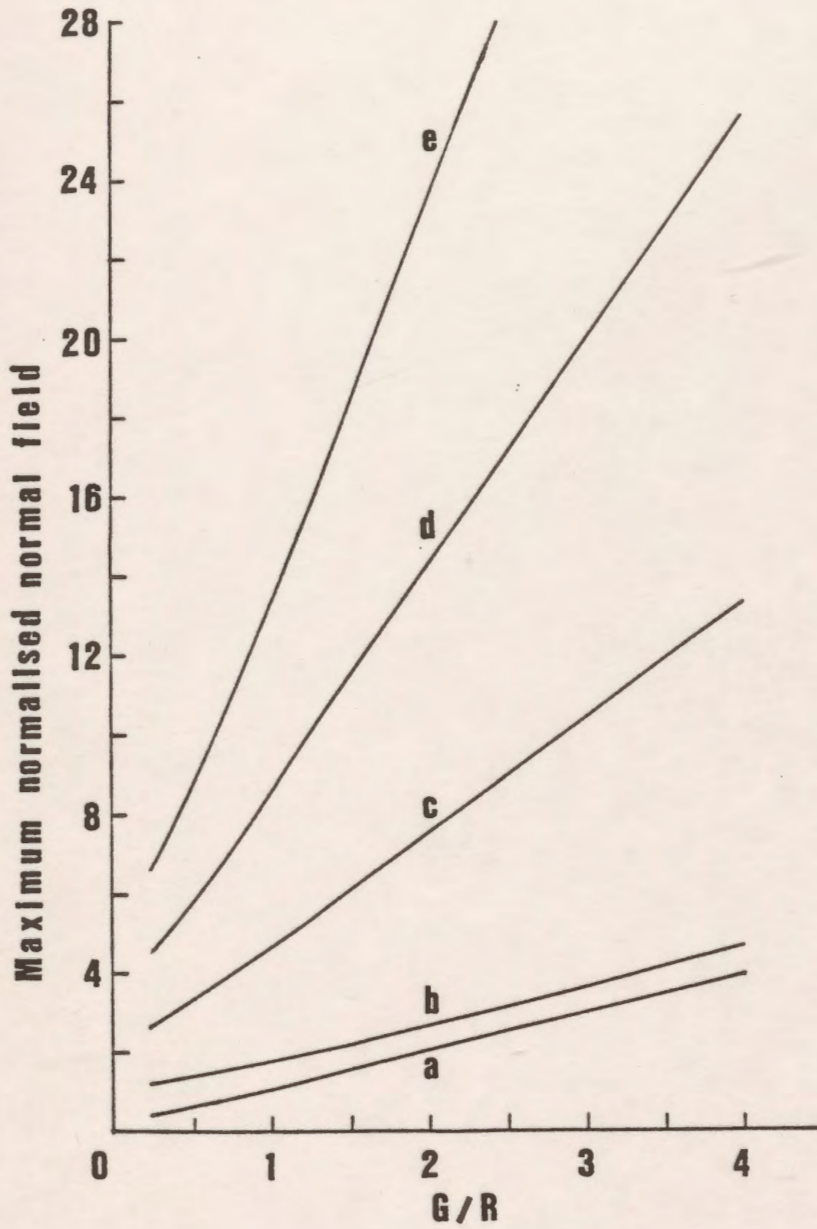
Figure 7.20: Variation of the maximum field on sphere with G/R ratio for different $\varepsilon_2 / \varepsilon_1$ ratios. (a) $\varepsilon_2 / \varepsilon_1 = 1/4$, (b) $\varepsilon_2 / \varepsilon_1 = 1$, (c) $\varepsilon_2 / \varepsilon_1 = 2$, (d) $\varepsilon_2 / \varepsilon_1 = 3$, (e) $\varepsilon_2 / \varepsilon_1 = 4$
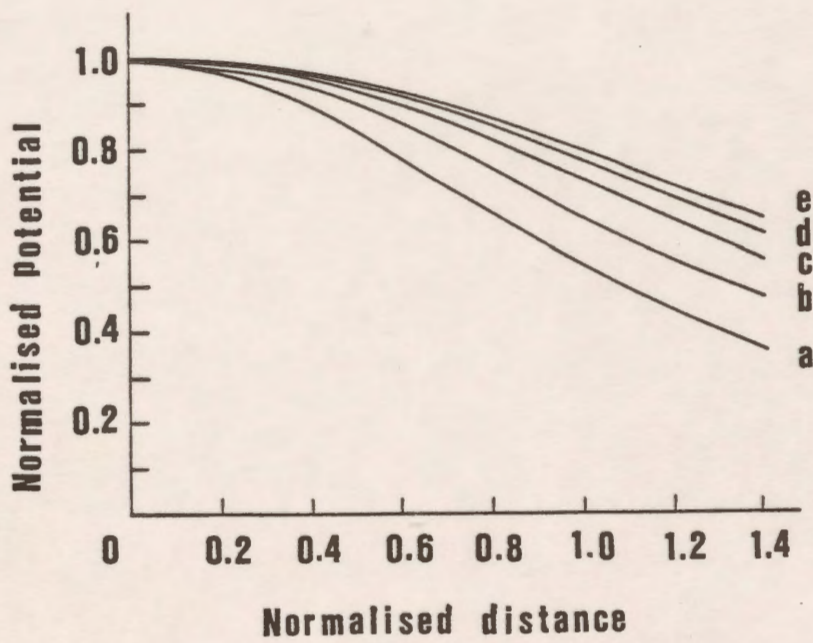
Figure 7.21: Potential distribution on the slab interface for $\varepsilon_2 / \varepsilon_1 = 4$ for different G/R ratios.
(a) G/R=1/4,   (b) G/R=1/2,   (c) G/R=1,   (d) G/R=2,   (e) G/R=4

Table 7.1 summarizes the effect of variation of the permittivity ratios and the slab-thickness/sphere-radius on the maximum electric field strength. It is clear from this table that as G/R increases the maximum electric field decreases at different values of permittivity ratio while the normalized maximum electric field increases. Table 7.1 also shows the location of the maximum electric field for different G/R ratios and different permittivity ratios.

The fine structure of the field resulting from a charge simulation model has small spatial variation in amplitude which are consistent with the spacing of the discrete charges in the model. Fig. 7.22 shows the electric field near a maximum lying close to the top of the spherical electrode. The fluctuations are clearly evident. The maximum electric field for this example occurs at $\theta=172^{\circ}$. However, the estimated location of the maximum in the "smoothed" field (represented by the dashed curve) is at $\theta=180^{\circ}$. This manual inspection procedure was used to estimate the location of the field maxima for the data presented in Table 7.1.

It is evident that for $\varepsilon_2/\varepsilon_1 < 1$, the maximum electric field occurs away from the axis of symmetry.

Figure 7.23 shows the variation in the angle at which the maximum field on the sphere is located. Curves are plotted as a function of gap separation with permittivity ratio as a parameter. The range of values for $\varepsilon_2/\varepsilon_1$ was chosen to cover conditions for which a transition toward the top of the sphere occurs with increasing G/R. For G/R somewhat greater than 1, the field maximum occurs away from the axis.

Table 7.1 : Maximum field (E_{max}) and normalized maximum field (E'_{max}) for different $\varepsilon_2 / \varepsilon_1$ and G/R ratio.

G/R	$\varepsilon_2 / \varepsilon_1$	E_{max}	E'_{max}	θ for E_{max}
	1/30	0.563	0.278	113.0
	1/4	0.764	0.373	43.0
	1/3	0.876	0.438	32.0
	1/2	1.160	0.580	17.0
0.25	1	2.350	1.175	0.0
	2	5.290	2.645	0.0
	3	9.010	4.505	0.0
	4	13.300	6.650	0.0
	30	317.000	158.500	0.0
	1/30	0.545	0.545	180.0
	1/4	0.614	0.614	69.0
	1/3	0.654	0.654	58.0
	1/2	0.748	0.748	40.0
0.5	1	1.360	1.360	0.0
	2	3.290	3.290	0.0
	3	5.650	5.650	0.0
	4	8.750	8.750	0.0
	30	302.000	302.000	0.0
	1/30	0.534	1.058	180.0
	1/4	0.560	1.110	105.0
	1/3	0.574	1.148	90.0
	1/2	0.608	1.216	67.0
1.0	1	0.885	1.770	0.0
	2	2.340	4.680	0.0
	3	4.290	8.580	0.0
	4	6.720	13.440	0.0
	30	272.000	544.000	0.0
	1/30	0.524	2.072	180.0
	1/4	0.537	2.136	180.0
	1/3	0.542	2.168	135.0
	1/2	0.553	2.211	105.0
2.0	1	0.669	2.676	0.0
	2	1.870	7.480	0.0
	3	3.560	14.240	0.0
	4	5.890	23.560	0.0
	30	256.000	1024.000	0.0
	1/30	0.511	4.040	180.0
	1/4	0.521	4.136	180.0
	1/3	0.524	4.192	180.0
	1/2	0.529	4.232	180.0
4.0	1	0.576	4.608	0.0
	2	1.660	13.280	0.0
	3	3.200	25.600	0.0
	4	5.360	42.880	0.0
	30	246.000	1968.000	0.0
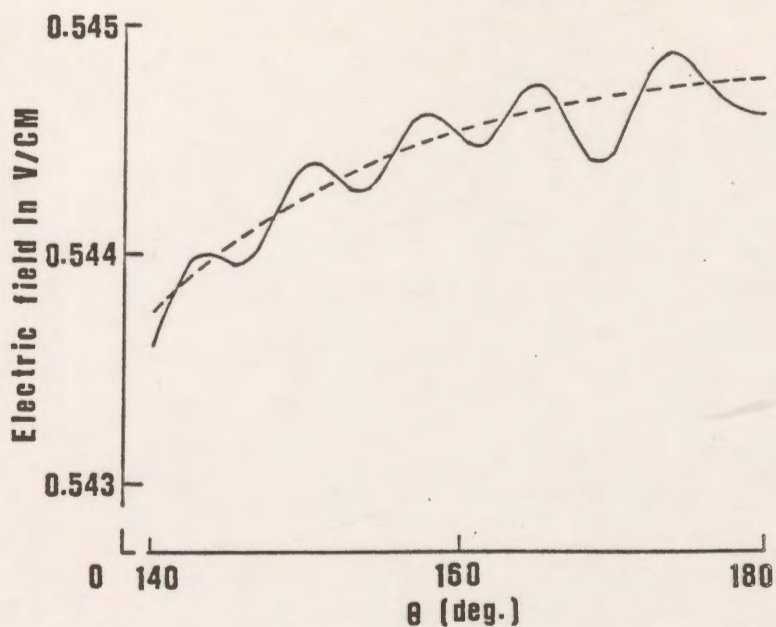
Figure 7.22: Fine structure of electric field distribution near a maximum for G/R=1/2 and $\varepsilon_2 / \varepsilon_1 = 1/30$.
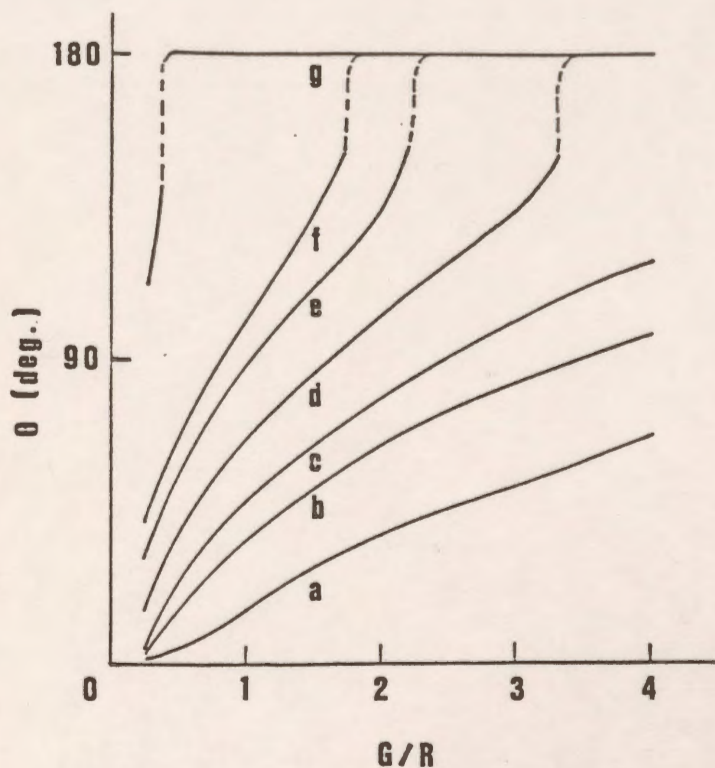
Figure 7.23: Variation of the maximum field location on sphere with G/R ratio for different permittivity ratios.

(a) $\varepsilon_2 / \varepsilon_1 = 1/1.1$, (b) $\varepsilon_2 / \varepsilon_1 = 1/1.3$, (c) $\varepsilon_2 / \varepsilon_1 = 1/1.5$, (d) $\varepsilon_2 / \varepsilon_1 = 1/2$,

(e) $\varepsilon_2 / \varepsilon_1 = 1/3$, (f) $\varepsilon_2 / \varepsilon_1 = 1/4$, (g) $\varepsilon_2 / \varepsilon_1 = 1/30$

7.3.5.2   Recessed Dielectric Slabs

The CAD package is applied to the configuration shown in Fig. 7.13(b) for various recess depths and permittivity ratios. Figs. 7.24 to 7.26 show the normal field variation around the lower half of the sphere for various permittivity ratios with three ratios of recess depth to sphere radius. The three recess depths are R/4, 3R/8 and R/2. Good agreement has been found between the results presented here and those obtained by Binns et al. for key values as well as for the distribution of the electric field strength around the lower half of the sphere except at the triple point (point B in Fig. 7.13(b)). Since the field at a triple point is usually singular (undefined) any comparison of the accuracy at that point is not meaningful.

Figs. 7.27 and 7.28 show the normal field distribution around the lower half of the high voltage spherical electrode for $\varepsilon_2/\varepsilon_1 = 4$ and 1/4 for a plane slab and for slabs of different thicknesses each recessed to accommodate a fixed electrode geometry, with G/R = 1/2. At the interface between the media, the gradient suffers a discontinuity. It is clear from Fig. 7.27 that the maximum (normal) field on the sphere is reduced when the dielectric slab is recessed for $\varepsilon_2/\varepsilon_1$ equal 4. It is also observed that as the depth of recess is increased the maximum normal field is decreased.

Fig. 7.28 indicates that for a permittivity ratio $\varepsilon_2/\varepsilon_1 = 1/4$, the maximum (normal) field on the sphere is increased when the dielectric slab is recessed. With increasing recess depth, the maximum field strength increases slowly.
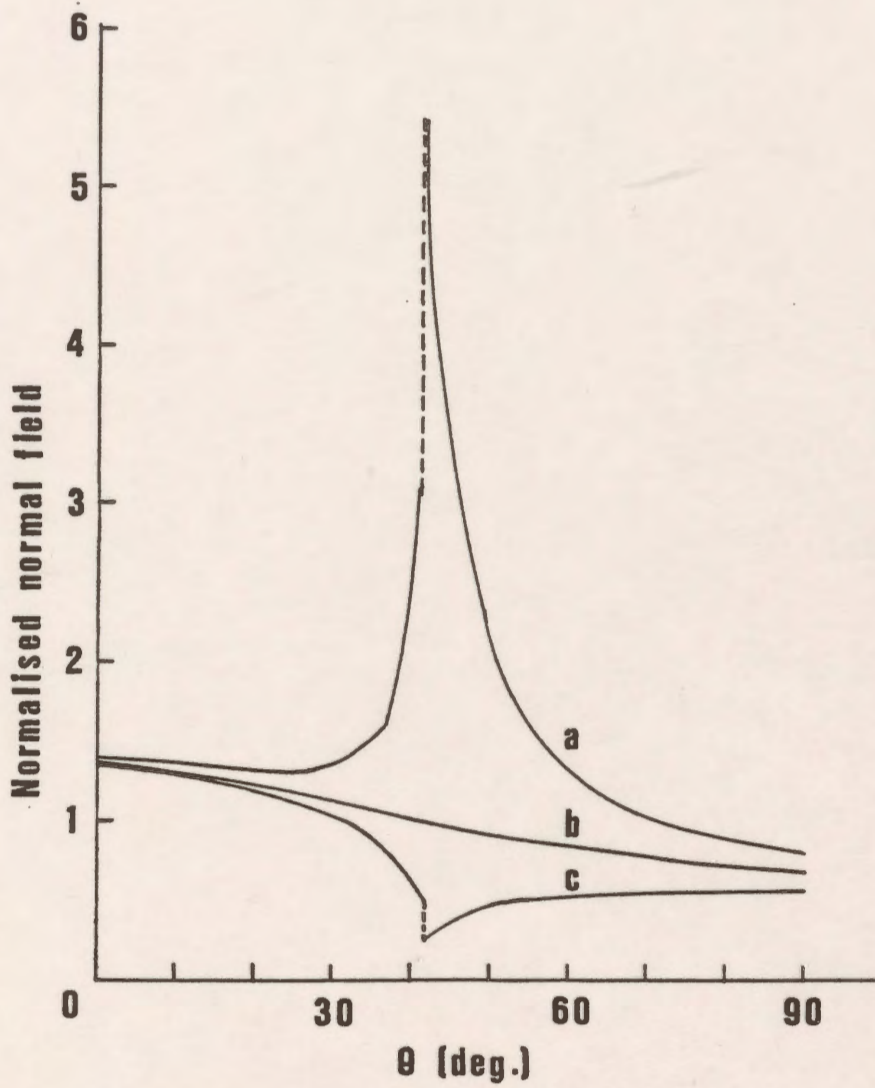
Figure 7.24: Variation of normal field around lower half of sphere for various permittivity ratios with a recess depth R/4 and G/R=1/2.

(a) $\varepsilon_2 / \varepsilon_1 = 4$, (b) $\varepsilon_2 / \varepsilon_1 = 1$, (c) $\varepsilon_2 / \varepsilon_1 = 1/4$
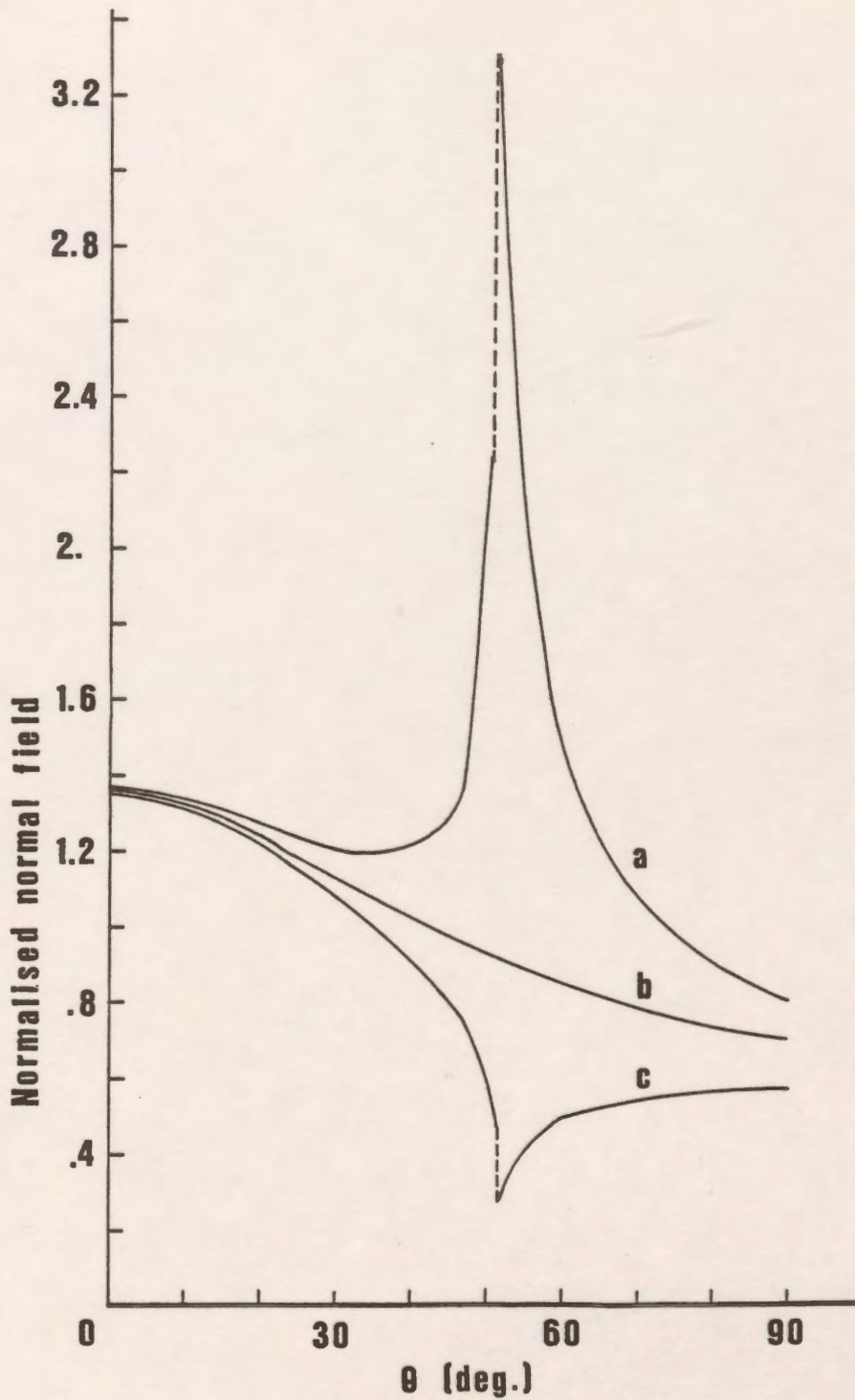
Figure 7.25: Variation of normal field around lower half of sphere for various permittivity ratios with a recess depth 3R/8 and G/R=1/2.

(a) $\varepsilon_2 / \varepsilon_1 = 4$,   (b) $\varepsilon_2 / \varepsilon_1 = 1$,   (c) $\varepsilon_2 / \varepsilon_1 = 1/4$
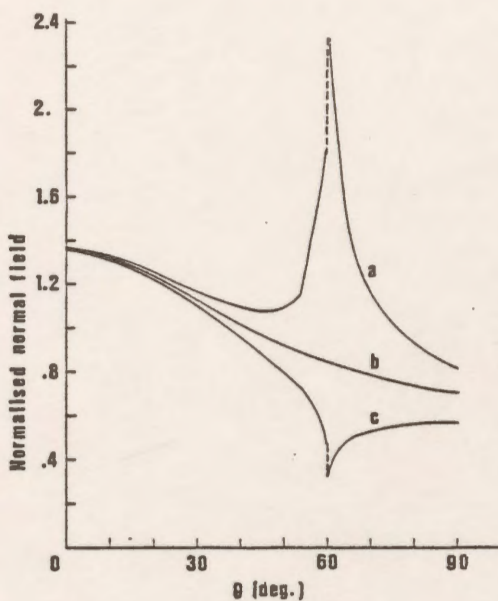
Figure 7.26: Variation of normal field around lower half of sphere for various permittivity ratios with a recess depth R/2 and G/R=1/2.
(a) $\varepsilon_2 / \varepsilon_1 = 4$,   (b) $\varepsilon_2 / \varepsilon_1 = 1$,   (c) $\varepsilon_2 / \varepsilon_1 = 1/4$
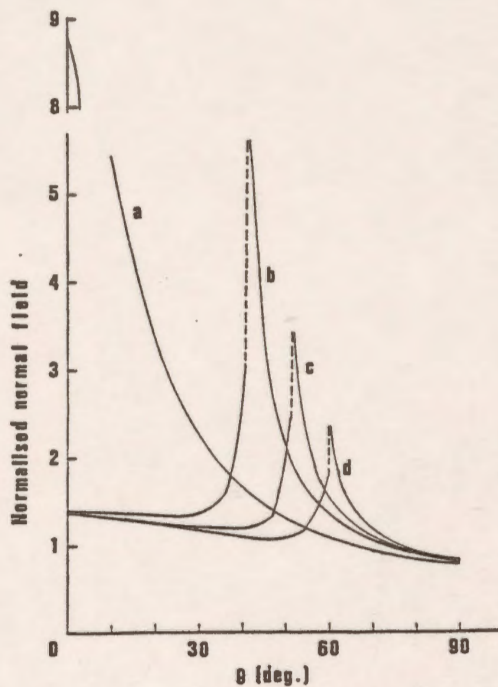
Figure 7.27: Variation of normal field around lower half of sphere with various recess depths for $\varepsilon_2 / \varepsilon_1 = 4$ and G/R=1/2.
(a) plane slab,   (b) recess depth R/4,
(c) recess depth 3R/8,   (d) recess depth=R/2
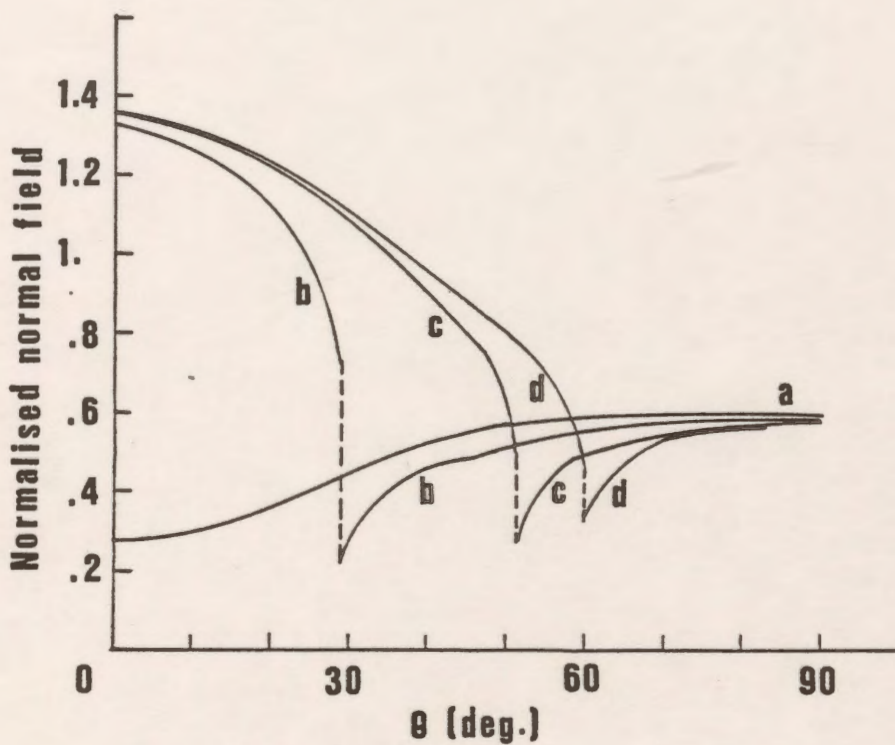
Figure 7.28: Variation of normal field around lower half of sphere with various recess depths for $\varepsilon_2 / \varepsilon_1 = 1/4$ and $G/R = 1/2$.

(a) plane slab,   (b) recess depth R/4,

(c) recess depth 3R/8,   (d) recess depth R/2

7.4   Triggering Electrode System With Rotational Symmetry

7.4.1   Introduction

The CAD package is applied successfully to a trigatron gap which has been used to form the first gap of an impulse generator. Figure 7.29 shows an assembly of the trigatron gap. The high voltage electrode is a hemispherical capped electrode (or a sphere). The earthed electrode consists of a hemispherical capped electrode in which a hole is drilled out of which projects a metal rod. The annular gap between the rod and the surrounding hemisphere is very small compared to the gap between the main electrodes. The gap between the high voltage electrode and the low voltage electrode is termed the main gap, while the other is called the pilot gap.

When a voltage is applied to the triggering rod the field is distorted in the main gap and the latter breaks down at a voltage appreciably lower than that required to cause its breakdown in the absence of the triggering electrode. For optimum operating characteristics to be obtained the trigger pulse should be positive with respect to the surrounding electrode [84].

The main object is to study the effect of changing the main gap distance and the pilot gap distance on the distribution of the potential and the electric field along the axial main gap line and to study the effect of these parameters on the maximum electric field intensity in the trigger gap.

7.4.2   System Geometry and Modelling

Figure 7.29 shows the triggering gap geometry. The diameter of both the high voltage and the low voltage hemispherical electrodes D is 50 cm. The diameter of the triggering electrode d is 0.6 cm. The main gap G is varied during the study from 1 to 25 cm while the pilot gap distance g has been varied from 0.2 to 1 cm in order to examine their effects on the potential and electric field distributions. The high voltage electrode is held at $V_h = 1$ V and the low voltage electrode at $V_l = 0$. The triggering voltage is $V_t = 0.2$ V.

Since the system is rotationally symmetrical about the z-axis, ring charges are found to be suitable for modelling the spherical parts of the geometry and the cylindrical parts of the high and

low voltage electrodes. The cylindrical part of the triggering electrode is modelled by finite line charges.

The first approach for modelling the system is done by modelling all sections of the geometry and the accuracy of the simulation is checked. The second approach is conducted by modelling only a part of the system. This part is represented by the dashed window in Fig. 7.29. It consists of the spherical part of the high voltage electrode and half of the spherical part of the low voltage electrode including the triggering electrode. The internal and external boundaries of the high and low voltage spherical electrodes are modelled in this approach. The accuracy is checked again and it is found that there is no significant difference in solution quality measures and in the field and potential values between the two approaches.

For more simplicity, a third approach for modelling is conducted by considering the high voltage spherical electrode as a solid spherical part to reduce the number of simulating charges used for modelling and to use a reasonable assignment factor. Again, the internal and external boundaries of the low voltage spherical electrode are modelled for accurate simulation since this region is the most important region. Neglecting the simulation of the internal boundary of the low voltage spherical electrode affects the simulation and the resulting field values to some extent. The accuracy is checked for the third approach and it is found that there is no significant difference in the potential errors and even in the field values calculated along the axial main gap line and the minimum pilot gap line at fixed value of G and g except in the third decimal number of these values.

It is found that simplifying the trigatron gap system for simulation as in the last approach without affecting the accuracy and the field values reduced the number of modelling charges and consequently the computation time. Figure 7.30 shows the modelled part of the triggering system with both the contour points and the corresponding charge locations. The total number of ring and finite line charges used is 175. The internal and the external boundaries of the low voltage electrode are simulated by 130 ring charges, the high voltage electrode by 20 ring charges, the

hemispherical part of the triggering electrode by 5 ring charges and the cylindrical part of the triggering electrode by 20 finite line charges.

The potential ϕ and the total electric field E are computed and presented in a normalized format.

In the case of the system shown in Fig. 7.29 where the high voltage electrode is raised to a potential $V_h = 1$ V and the low voltage electrode is raised to a potential $V_l = 0$, the normalized potential ϕ' and the normalized total electric field E' are defined as:

$$\phi' = \phi / V_h = \phi$$

$$E' = E / E_{av} = E G / V_h = E G$$

where E_{av} is the nominal field in the gap and is given by $E_{av} = V_h / G$.

The distance along the axial main gap l is measured from the tip of the triggering electrode and is given in a normalized format as:

$$l' = l / G$$

where l' is the normalized gap distance.

7.4.3 Results

The pilot gap distance g is kept constant at 0.5 cm and the main gap distance G has been varied from 1 to 25 cm. The potential errors and the tangential field differences along the different sections of the electrodes are checked after each run before computing the potential and field distributions to ensure that the errors are within acceptable limits.

Figure 7.31 shows the normalized potential distribution along the axial main gap line for different values of the main gap distance G. It is clear from this figure that for small values of G the distribution of the potential can be considered linear. When G increases the nonlinearity increases and the most significant effect of changing the gap distance G on the potential distribution appears near the trigger pilot gap.

The distribution of the normalized total electric field along the main gap line with the main gap distance as a parameter is given in Fig. 7.32. It is clear from this figure that as the gap
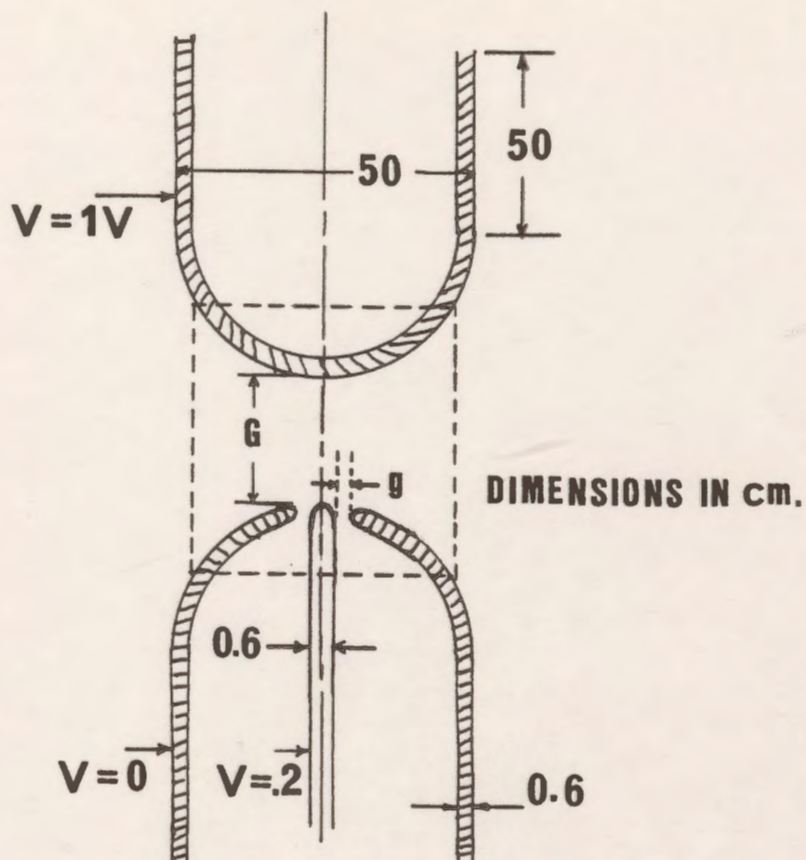
Figure 7.29: Triggering system with rotational symmetry.
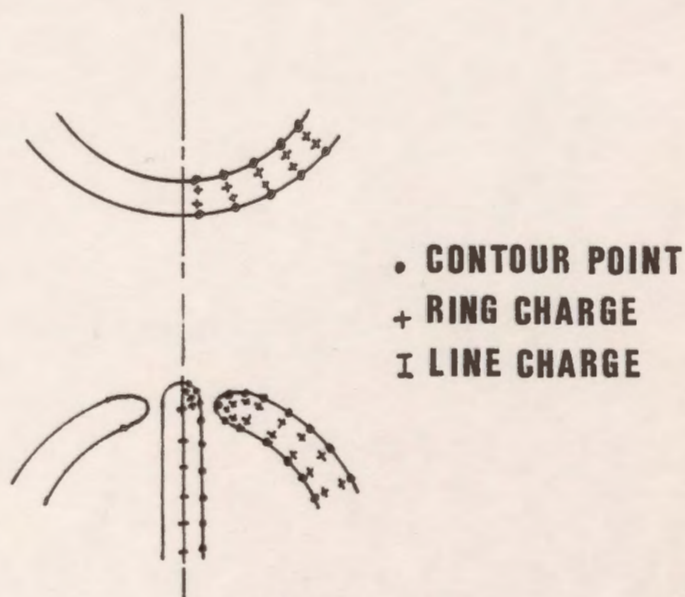
Figure 7.30: Distribution of contour points and charge locations in the triggering system.

distance increases the normalized total electric field near the tip of the triggering electrode strongly increases until at a certain distance from the triggering electrode tip, it decreases for a small distance, then increases again due to the effect of the grounded electrode and after that remains almost constant with a small increase near the high voltage electrode tip.

The main gap distance G is kept constant at 10 cm and the effect of changing the pilot gap distance on the potential and electric field distributions is studied as g varies from 0.2 cm up to 1 cm.

There is no change in the potential distribution due to varying the pilot gap except near the tip of the triggering electrode where the effect of the surrounding low voltage electrode is pronounced as shown in Fig. 7.33. The effect of varying g on the electric field distribution is clear from Fig. 7.34 where the field near the tip of the triggering electrode decreases by increasing the pilot gap.

The electric field is computed along the different sections of the electrodes for each combination of the main gap distance G and the pilot gap distance g to search for the maximum value of the total electric field and the location of that maximum. It should be noted here that the maximum value of the total electric field does not necessarily occur on the main axial gap line or on the tip of the triggering electrode. The location of that maximum changes with both G and g, but always occurs on the hemispherical part of the triggering electrode.

Tables 7.2 and 7.3 summarize the values of the maximum total electric field for different values of G and g. The tables also include the location of these maxima on the hemispherical part of the triggering electrode where the angle θ is measured from the intersection of the cylindrical part and the hemispherical part of the triggering electrode.
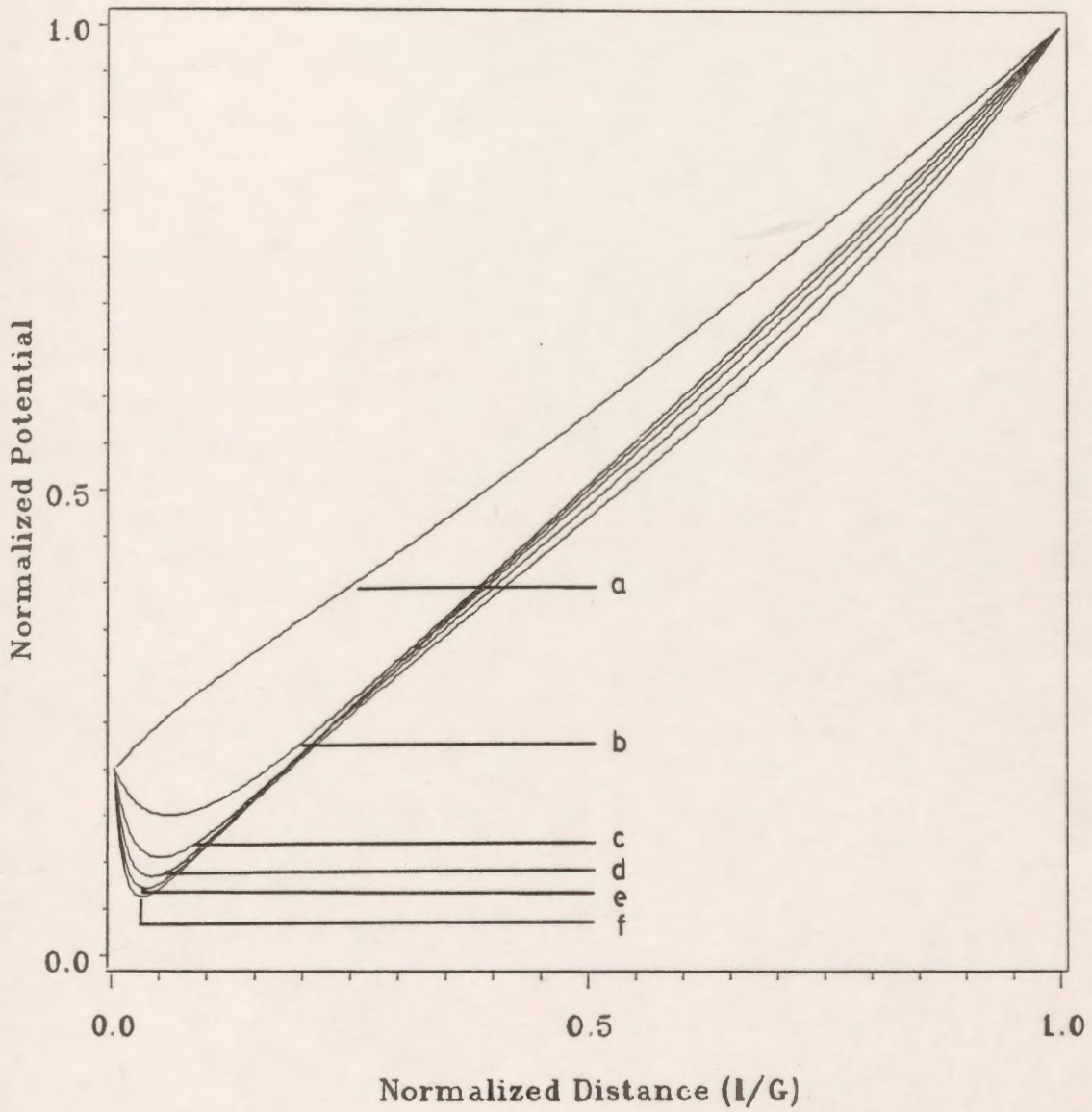
Figure 7.31: Variation of the normalized potential along the axial main gap line for different values of the main gap distance G for g = 0.5 cm.
(a) G=1 cm.   (b) G=5 cm.   (c) G=10 cm.
(d) G=15 cm.   (e) G=20 cm.   (f) G=25 cm.
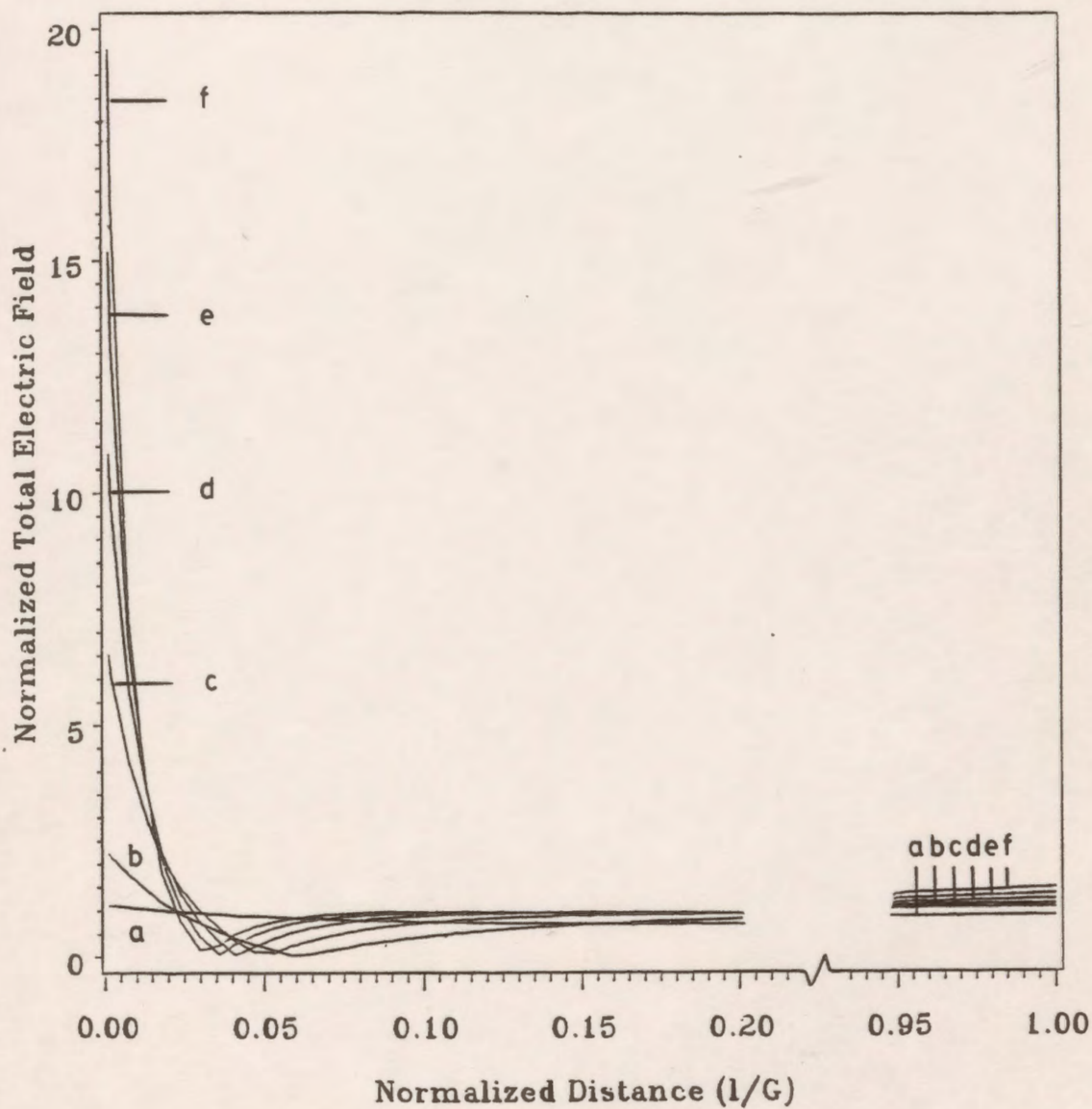
Figure 7.32: Variation of the normalized total electric field along the main gap line for different values of G for g = 0.5 cm.
(a) G=1 cm.   (b) G=5 cm.   (c) G=10 cm.
(d) G=15 cm.   (e) G=20 cm.   (f) G=25 cm.
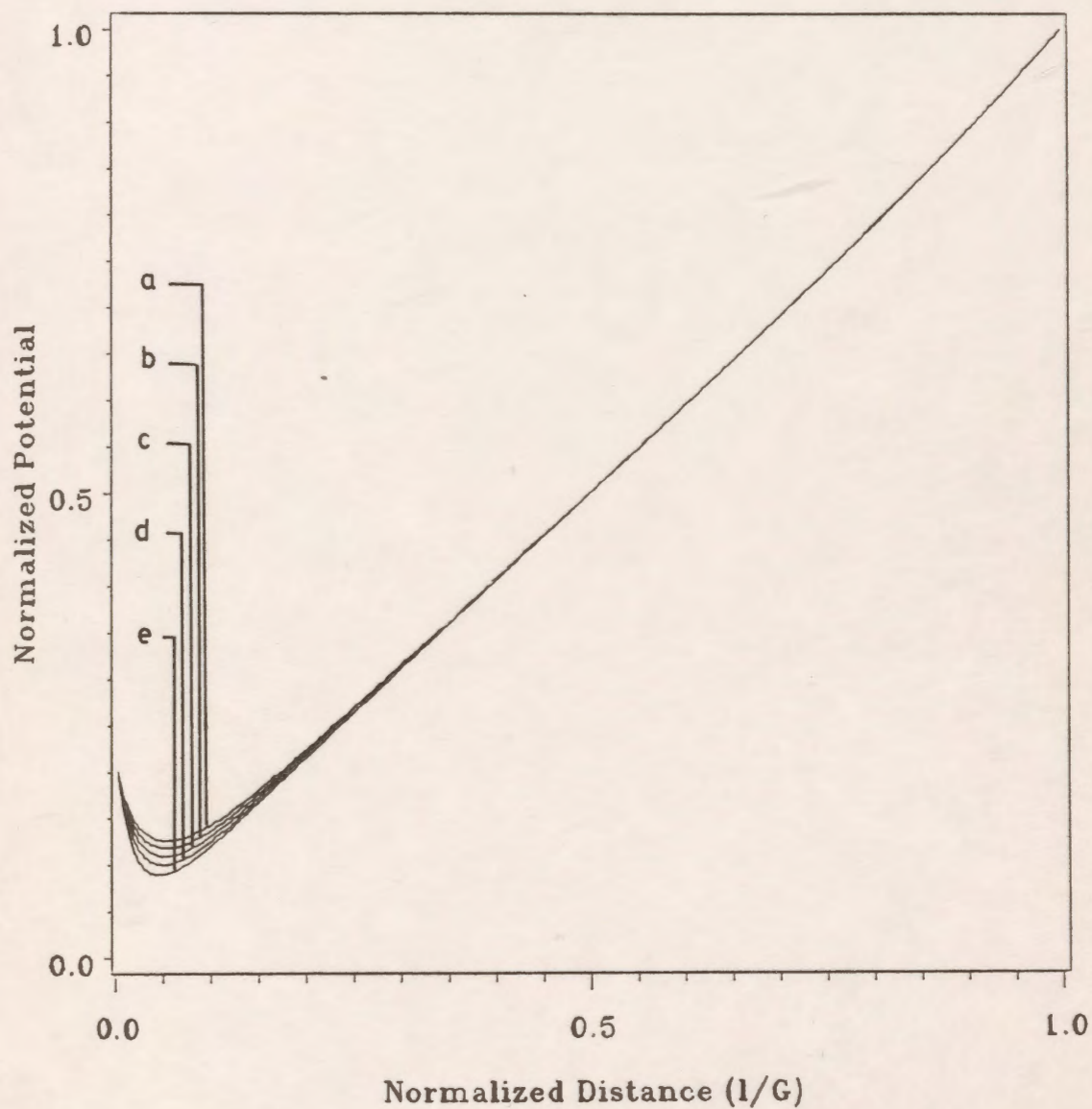
Figure 7.33: Variation of the normalized potential along the main gap line with the pilot gap distance g as a parameter for G = 10 cm.
(a) g=0.2 cm.   (b) g=0.4 cm.   (c) g=0.6 cm.   (d) g=0.8 cm.   (e) g=1.0 cm.
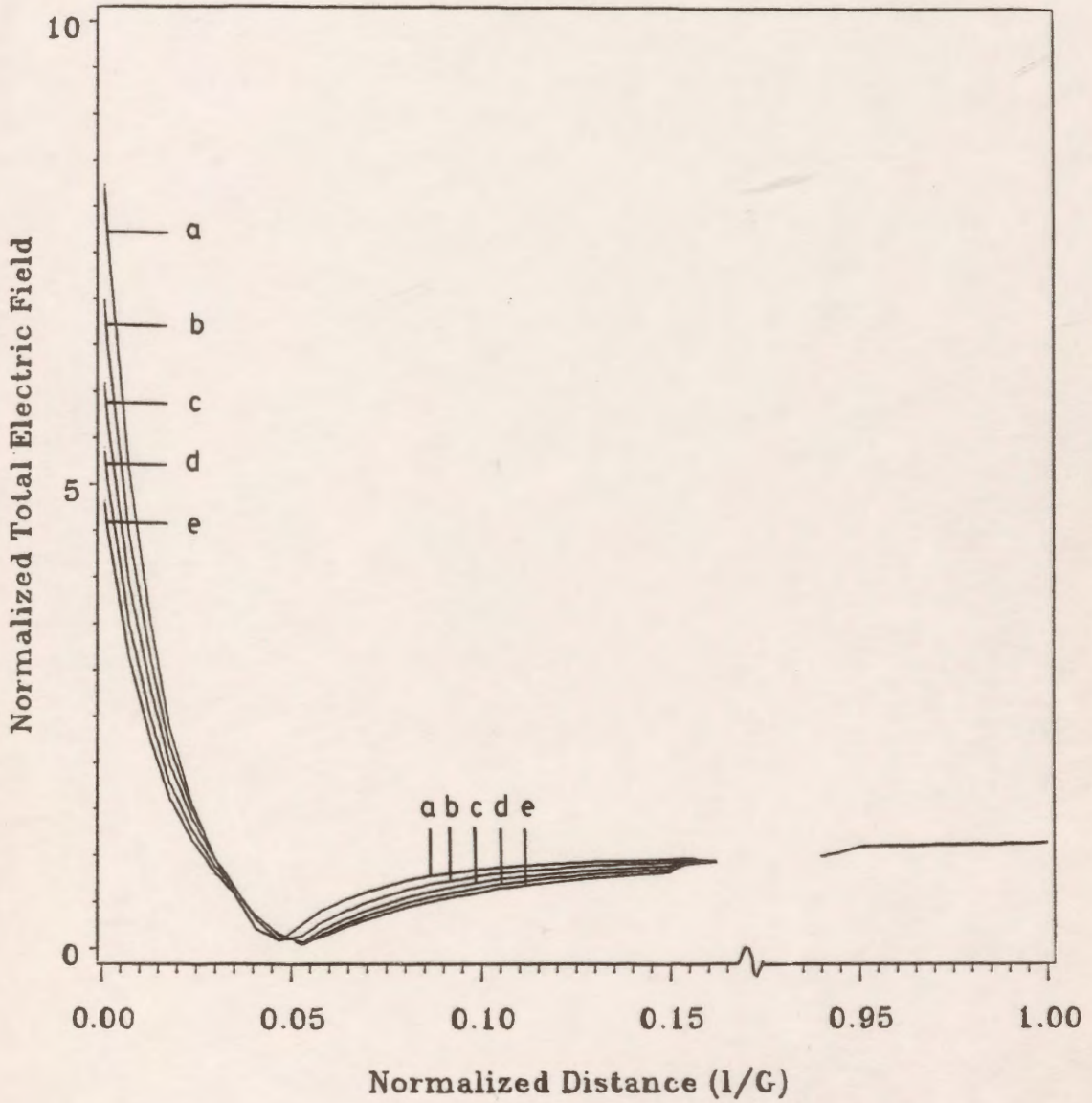
Figure 7.34: Variation of the normalized total electric field along the main gap line with the pilot gap distance g as a parameter for G=10 cm.

(a) g=0.2 cm. (b) g=0.4 cm. (c) g=0.6 cm. (d) g=0.8 cm. (e) g=1.0 cm.

Table 7.2 : Normalized maximum field (E'_{max}) and its location for different values of the main gap distance G.

g (cm)	G (cm)	E'_{max}	θ for E'_{max}
	1	1.115	90
	5	3.740	10
	10	8.113	18
0.5	15	12.561	21
	20	17.040	23
	25	21.544	23

Table 7.3 : Normalized maximum field (E'_{max}) and its location for different values of the pilot gap distance g.

G (cm)	g (cm)	E'_{max}	θ for E'_{max}
	0.2	13.984	5.8
	0.4	9.139	15.6
10	0.6	7.370	20.5
	0.8	6.322	22.0
	1.0	5.573	22.1

7.5   Polymer Long Rod Insulators

7.5.1   Introduction

In recent years the rapidly increasing demand for electric power has resulted in a corresponding increase in high voltage levels and system reliability requirements. This situation imposes very stringent technical and economic requirements on the system as a whole. The modern high voltage components must be designed so as to minimize cost and maximize reliability. The insulation problem of high voltage transmission lines necessitates a thorough investigation for successful operation with minimum interruptions.

Corona current associated with transmission at extra high voltage levels produces radio interference and audible noise that may reach levels higher than those desirable. The energy losses accompanying corona may become unacceptablly high. This intense interference can be avoided if an adequate insulation strength is provided to the high voltage transmission systems.

The potential and electric field distribution is required not only to predict the corona starting voltages, but also to estimate the magnitude and possibly the frequency spectrum of radio interference produced by the corona discharges. It also enables us to determine the breakdown strength of the insulator material.

Although polymeric insulators are still in a stage of development, their advantages are becoming more evident with increasing use in overhead transmission lines. A part from their many advantages that include light weight, ease of handling and lower installation cost, polymeric insulators exhibit unique properties with a smaller surface area and a longer leakage path than conventional ceramic insulators. Because of these two properties, polymeric insulators have superior contamination performance over ceramic insulators [85].

The work presented in this section is based on the use of the Charge Simulation based Computer-Aided Design package to calculate the potential and electric field distribution in and around a polymer long rod insulator string consisting of 22 sheds. Also a study on using grading rings for linearizing the potential distribution along the insulator string and for minimizing the electric field stresses is presented.

7.5.2 Grading of Insulator Strings

Computer-aided design methods have become standard practice in various fields of engineering. The complexity of power system insulation design certainly demands such a sophisticated technique [86]. The engineer can be aided in the electrical design aspect of the problem by having access to a means of calculating the potential fields of complex geometries like those of the polymeric insulators including grading rings for normalizing the potential distribution.

Insulators used on ac transmission and distribution lines attain lengths which are long enough so that the power frequency voltage distribution may become a design consideration [87]. The non-uniformity of the voltage distribution on suspension insulators, bus supports, equipment bushings or polymer insulators may be so severe that grading rings are required to reduce corona to tolerable levels. This non-uniformity is especially pronounced in long rod polymer insulators.

Grading rings have been used for linearizing the potential distribution along a string of insulators. However, the effectiveness of such a scheme is limited by other considerations such as clearance, ring dimensions, string length, etc. [86].

On most polymer insulators, rings are necessary on both ends of the insulator for voltages of 500 kV and above. For voltages between 230 and 500 kV, the need for grading rings depends on the radio noise level that can be tolerated.

Grading rings when properly designed also control the potential gradient in the insulator. There is at least one recommendation that a ring be used on the energized end of the insulators for 230 kV applications [88]. For voltages above 230 kV, most manufacturers supply grading rings to protect the insulator.

Rings provide additional protection to the metal end fittings of composite insulators from damage by power arc flashovers. Test results show composite materials to be more resistant to damage from power arcs than porcelain or glass. The addition of a ring can thus fulfill part of the function of the arcing horns [88].

Another application of the grading rings is to inhibit dry band arcing activity near the metal end fittings. This should help prevent surface degradation of composite insulators in very wet locations [88].

7.5.3   Modelling of the Polymer Insulator

The practical geometry of the polymer insulator string is shown in Figure 7.35. The upper conductor is usually connected to the cross arm end of the tower and therefore, it is assumed to be at the ground potential (zero potential). The lower conductor is at the high potential which is assumed here to be 1.0 V. In between is shown a polymeric insulator which consists of a vertical dielectric column and twenty two shed units connected together. The length of the vertical column is equal to the length of one unit.

Figure 7.36 shows the dimensions of the vertical column and one shed in detail. All dimensions are in mm. The distribution of the simulating charges in the insulator units and inside the low and high voltage electrodes is shown in Fig. 7.37.

The number and distribution of the simulating charges are specified arbitrarily and the system of linear equations is solved for the necessary values of the charge magnitudes to satisfy the boundary conditions. This arbitrary distribution of the charges is varied from trial to trial during the simulation for better results and higher accuracies as the technique is sensitive to the location of the charges.

The polymer insulator system is rotationally symmetrical about the z-axis if the presence of the line conductor and supporting tower is ignored. Ring charges were found to be suitable to model the electrodes and the insulator sheds. The following number of charges were found to be the best to model the various parts of the electrodes and the insulator string:

*   high voltage conductor: 15

*   vertical column of the dielectric: 15 (on each side)

*   low voltage conductor: 15
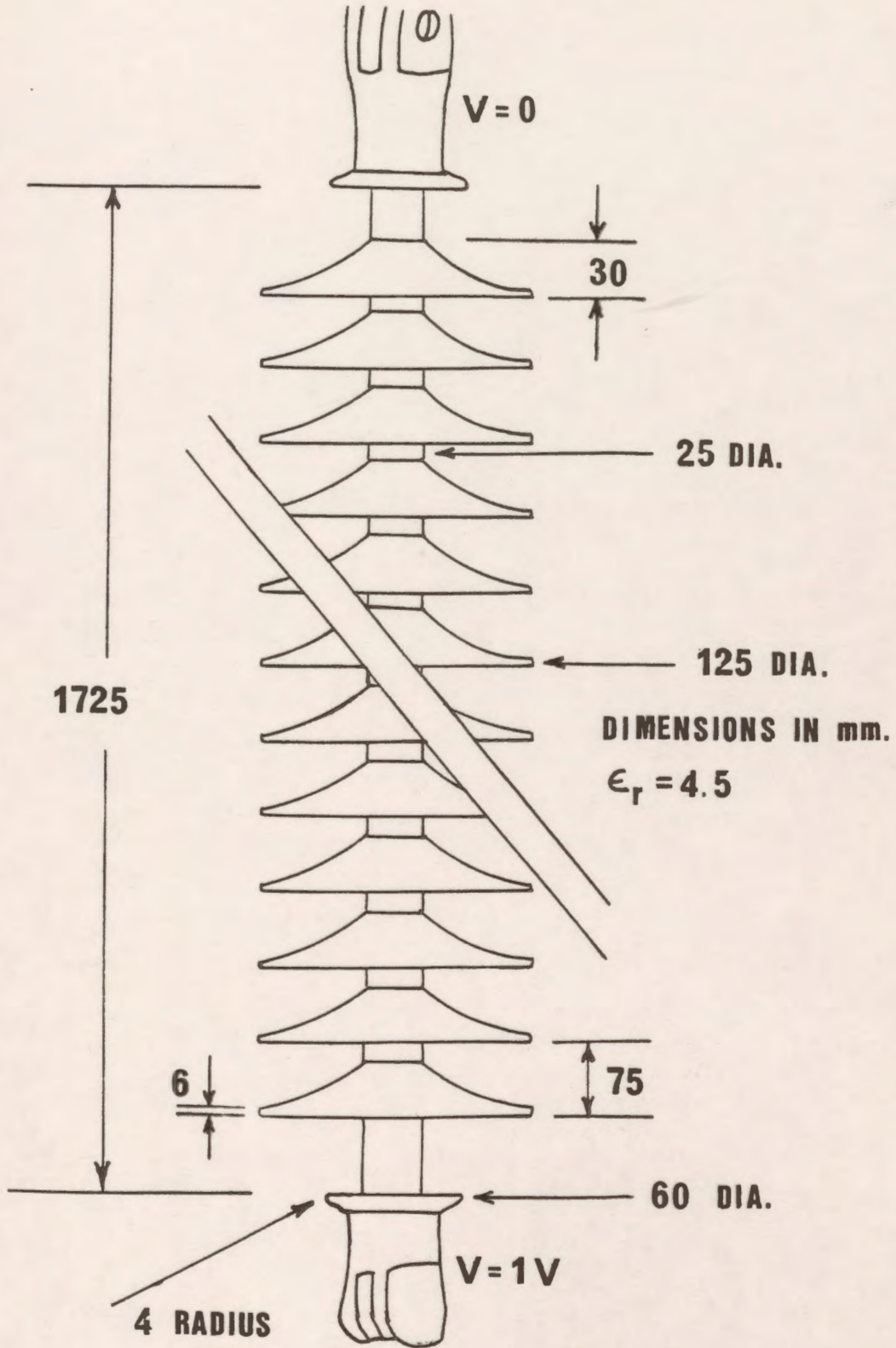
Figure 7.35:   22-Shed polymer insulator string.
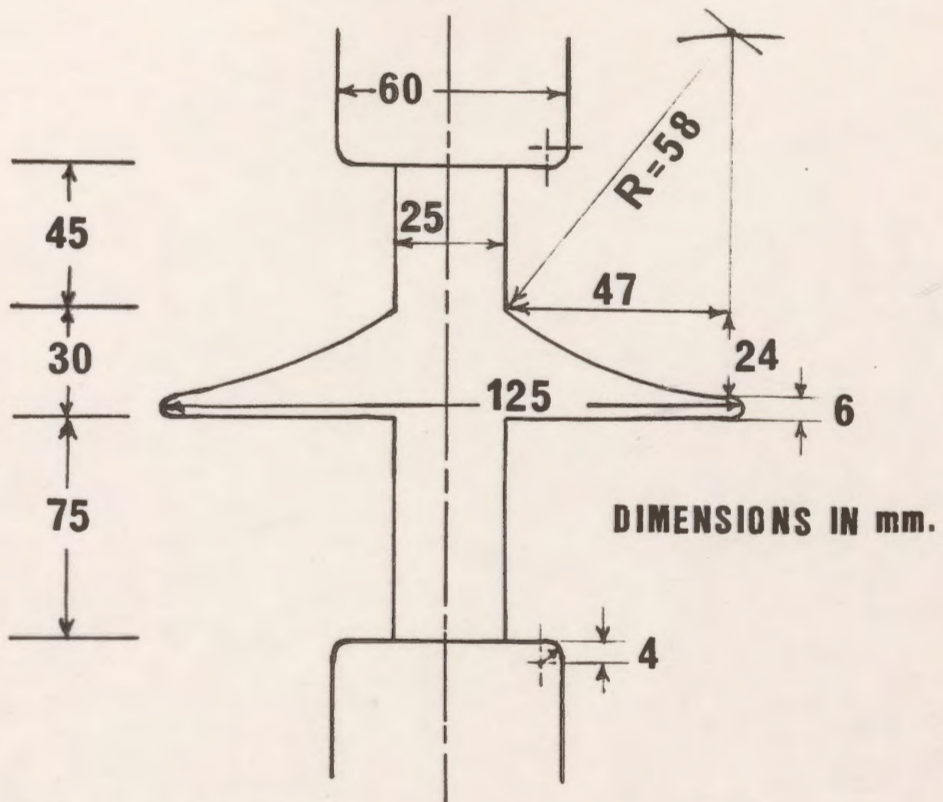
Figure 7.36: Detailed dimensions of a unit.

- • Contour point
- + Charge location
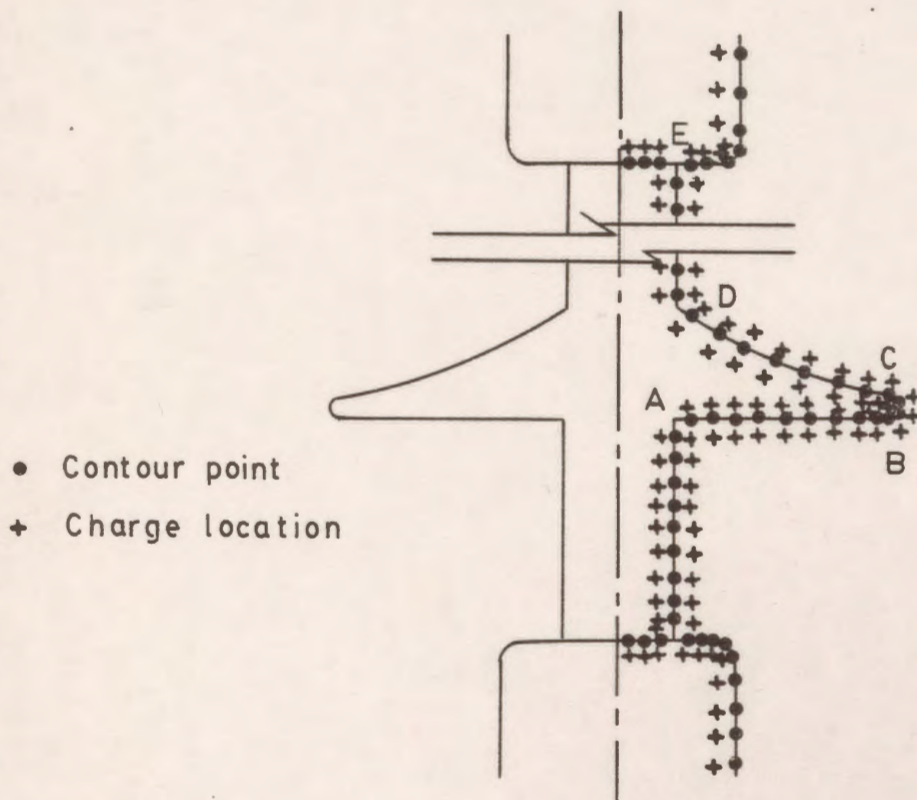
Figure 7.37: Distribution of contour points and charges in the polymer insulator.

The first unit close to the high voltage conductor is modelled by 27 charges on each side and those charges are distributed along the different sections of this unit as:

- horizontal interface of the shed: 15

- half toroidal curved part of the shed: 3

- sloped skirt of the shed: 6

- vertical interface part of the shed: 3

Each unit of the second and third units close to the high voltage conductor is modelled by 18 charges on each side and those charges are distributed along the different sections of the shed as follows:

- horizontal interface of the shed unit: 6

- half toroidal curved part of the dielectric unit: 3

- sloped skirt of the shed unit: 6

- vertical interface part of the unit: 3

The number of charges used to model each unit of the other nineteen units is 8 charges (16 charges for each unit considering those inside and outside the shed). Thus the total number of the charges used to model the electrodes and the entire insulator was found to be 490 considering those charges inside and outside the insulator sheds. This resulted in 490 linear equations that should be solved for the same number of unknown charges.

Although the CAD package developed is flexible enough to accommodate several hundreds of charges, the large number of simultaneous equations places rather severe demands on the memory requirements and the computer processing time. Both the computer time and memory storage considerations present limitations on the number of charges used to model the system.

Introducing the guard ring for linearizing the potential distribution along the insulator length increases the total number of charges used for modelling by 10. Thus the total number of charges becomes 500 charges.

As a preliminary analysis, the polymer insulator string which consists of a vertical dielectric column and 22 sheds is replaced by a vertical dielectric rod having the same dielectric constant and the same diameter as that of the vertical dielectric column of the insulator as shown in Fig. 7.38. The diameters of the grounded and high voltage electrodes are kept the same. The gap between the high and low voltage electrodes which also constitutes the length of the insulator G is varied until it takes the same value as the polymer insulator (1725 mm). The gap/electrode-diameter ratio is varied to illustrate the nonuniformity in the potential distribution for long gaps including insulators. Ring charges were found to be suitable to model that system which also has rotational symmetry around the z-axis.

7.5.4   Results

7.5.4.1   Preliminary Results

The CAD package is applied first to the system shown in Fig. 7.38. The gap/conductor-diameter ratio G/D is varied over a wide range to illustrate its effect on the distribution of the potential and the total electric field along the axial gap line. The results for the potential distribution along the axis are presented in a normalized format in Fig. 7.39 for G/D equal to 0.5, 1.0, 5.0, 15.0, and 28.75. The value of G/D of 0.5 corresponds to almost uniform potential distribution where as the value of G/D of 28.75 (G=1725 mm) corresponds to a very nonuniform potential distribution. It is clear from this graph that most of the potential drop is across the first 5 percent of the insulator length measured from the high voltage electrode for G/D = 28.75. For example, the voltage drop across the first 5 percent of the insulator length for G/D = 28.75 is 71%.

The total electric field distribution along the axial gap line is presented in a normalized format in Fig. 7.40 for the same values of G/D mentioned above. It can be seen from this figure that as the gap distance increases the normalized total electric field increases and this increase in the field is more pronounced near the high voltage electrode and is associated with the nonuniformity of the potential distribution there.
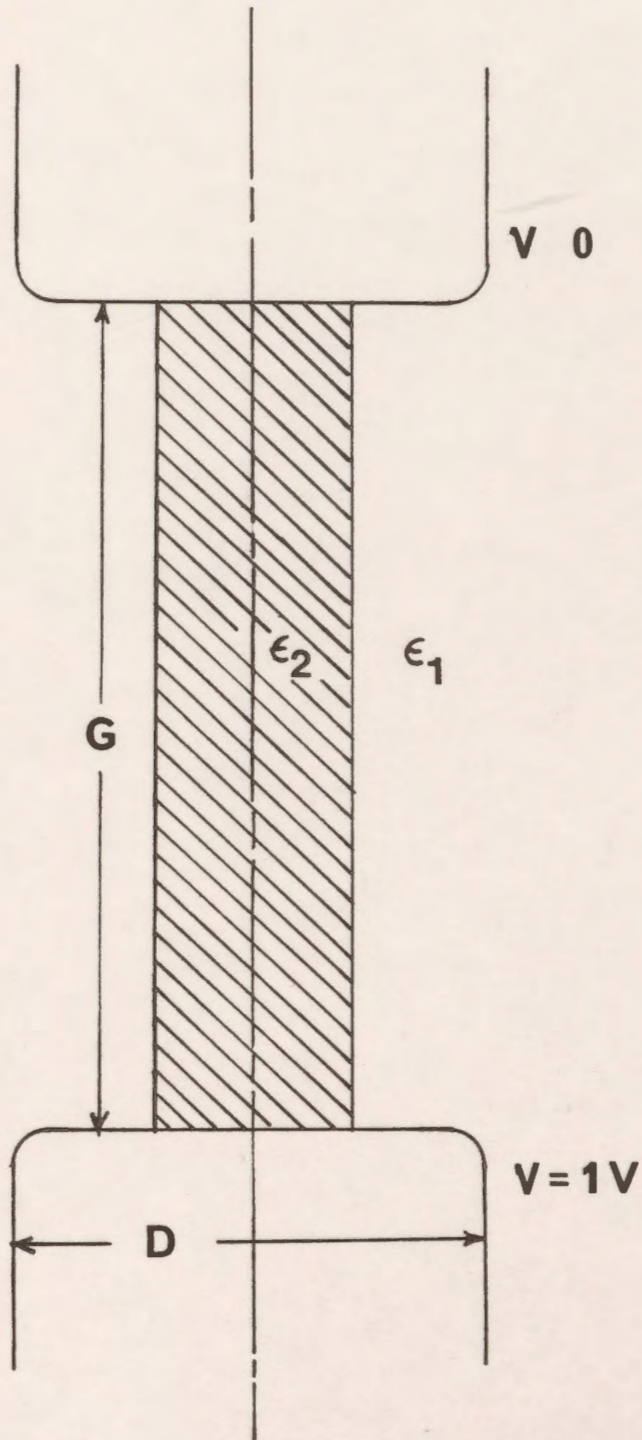
Figure 7.38: A cylindrical rod polymer insulator.
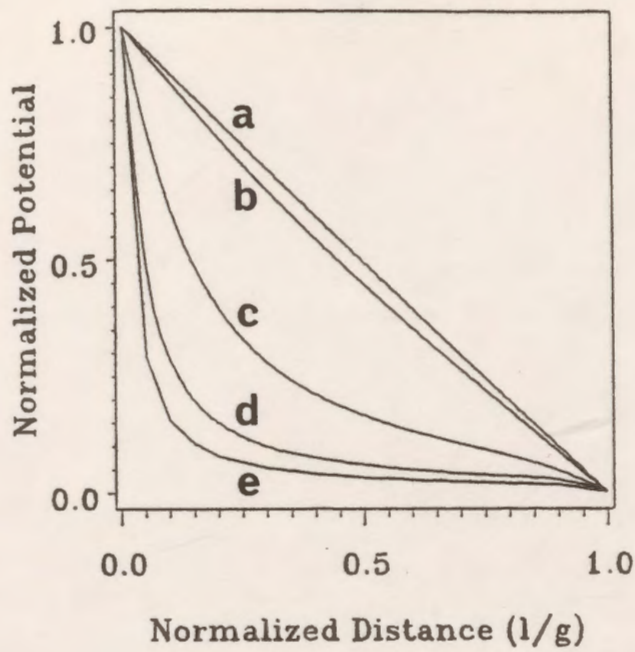
Figure 7.39: Potential distribution along the axial gap line of the rod insulator with G/D as a parameter for D=6.0 cm.
(a) G/D=0.5   (b) G/D=1   (c) G/D=5   (d) G/D=15   (e) G/D=28.75
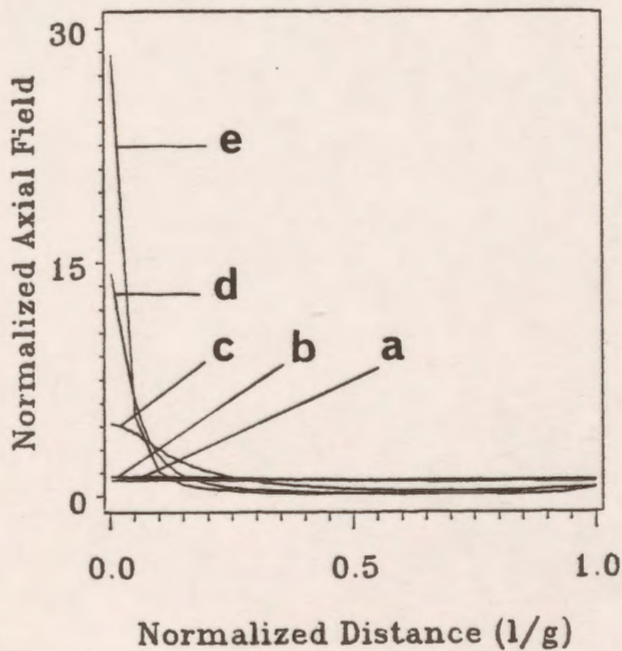
Figure 7.40: Total electric field distribution along the axial gap line of the rod insulator with G/D as a parameter for D=6.0 cm.
(a) G/D=0.5   (b) G/D=1   (c) G/D=5   (d) G/D=15   (e) G/D=28.75

7.5.4.2   Solution Quality Measures

The CAD package is applied to the system shown in Fig. 7.35 which consists of low and high voltage electrodes and a 22 shed polymer insulator. It is required to calculate the potential and the electric field distribution along the axial line of the system and along the different interfaces of the insulator sheds without and including the grading ring for linearizing the potential distribution.

The object of this work also is to determine the size, the diameter and the height of the grading ring that gives the best uniformity of the withstand voltage distribution along the axial length of the insulator. The electric field stress is also evaluated for different values of the guard ring controlling parameters (size, diameter, and height).

The potential error along the different sections of the high voltage electrode is examined and it is found that the maximum value of this error does not exceed 0.15%. Also, the maximum value of the potential difference along the different sections of the grounded electrode is found to be not exceeding 0.0004.

The potential discrepancy distribution along the vertical dielectric column and the different sections of the first three sheds close to the high voltage electrode are presented.

Figure 7.41 shows the potential discrepancy along the initial vertical column section of the dielectric (length=75 mm) with a maximum value of 0.032% near point 'A'. Fig. 7.42(a) illustrates the potential discrepancy along that section which represents the horizontal interface of the first unit. A maximum value of 0.1% is found to be near point 'B'. Fig. 7.42(b) presents the potential discrepancy along the curved periphery of the interfacial part of the first unit. The maximum discrepancy in the potential is about 0.22% close to point 'C'. The potential discrepancy along the sloped skirt of the first unit is shown in Fig. 7.42(c) with a maximum value of about 0.2% near point 'C'. Figure 7.42(d) illustrates the potential discrepancy along the vertical part of the first unit which represents the last part of this unit. The maximum discrepancy along that part is found to be about 0.015% near point 'E'.
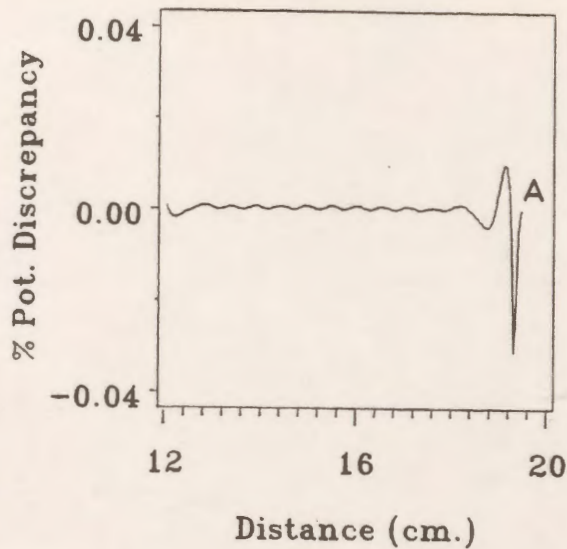
Figure 7.41: Potential discrepancy along the vertical column of the polymer insulator.

The potential discrepancies along the different sections of the second unit, the horizontal, curved periphery, sloped skirt, and the vertical parts are illustrated in Fig. 7.43(a-d) with maximum values of errors of about 0.1, 0.12, 0.08, and 0.05%, respectively. The locations for the maximum errors for the second unit are found to be the same locations as those for the corresponding sections of the first unit.

Figure 7.44(a-d) illustrates the potential discrepancies along the different sections of the third shed of the insulator. The maximum values of the percentage potential discrepancies along the horizontal, curved periphery, sloped skirt and the vertical parts for this unit are 0.4, 0.26, 0.18, and 0.07%, respectively. The percentage potential discrepancies along the different sections of the other sheds are much less than those values.

The potential error distribution along the surface of the grading ring is examined. The maximum recorded value of that error is less than 0.02%.

It is observed that the values of the tangential (or normal) electric field percentage discrepancies along the dielectric interfaces may be extremely high at those locations where the tangential (or normal) electric field components are very small or approach zero.
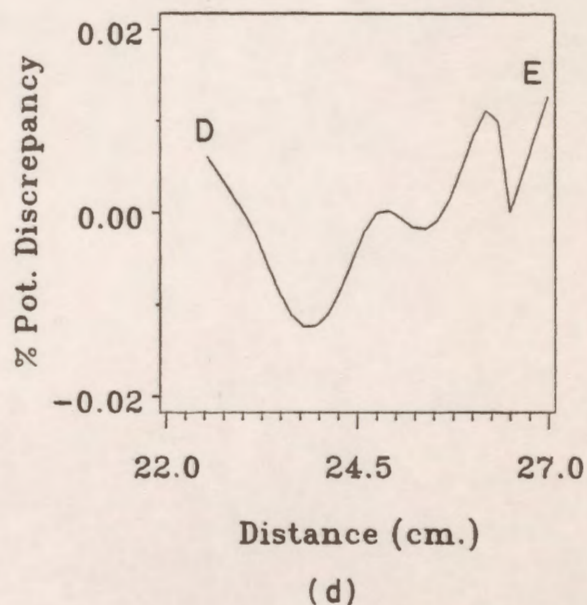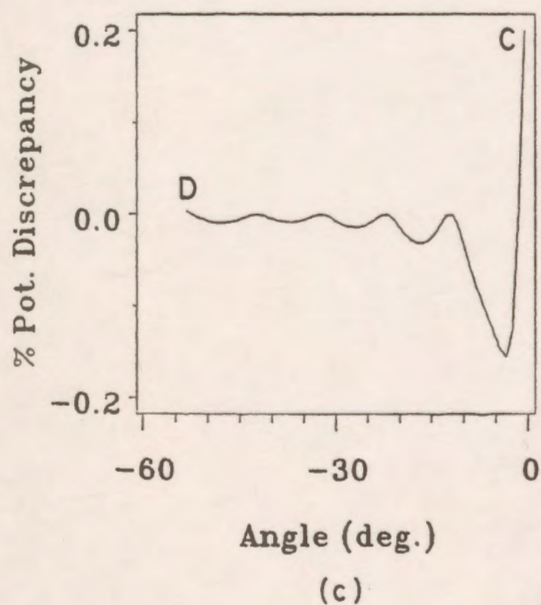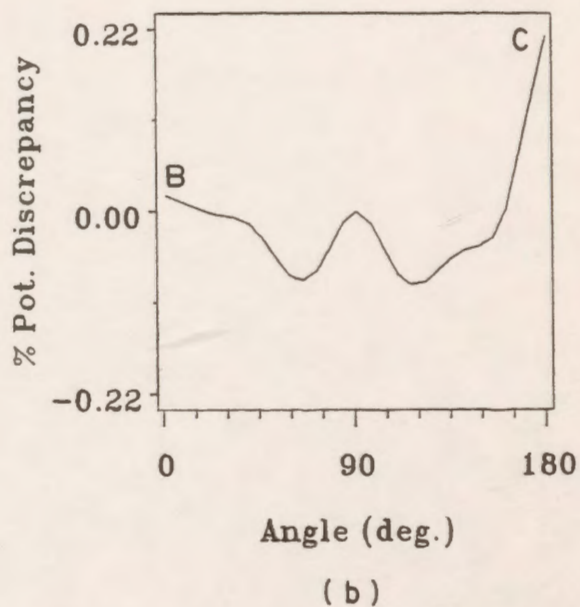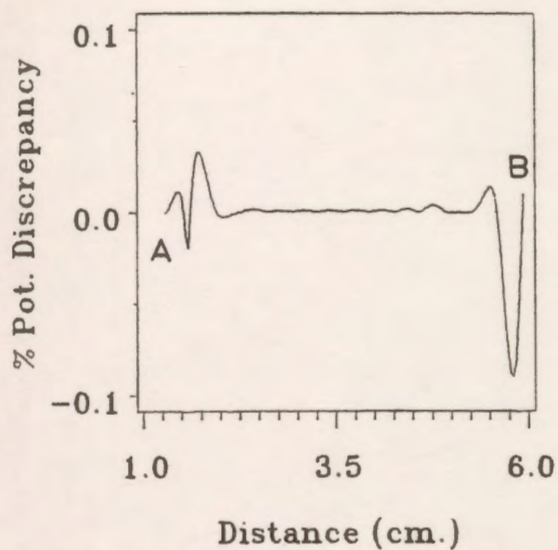
Figure 7.42: Potential discrepancy along the different sections of the first unit.
(a) horizontal part   (b) curved periphery part
(c) sloped part   (d) vertical part
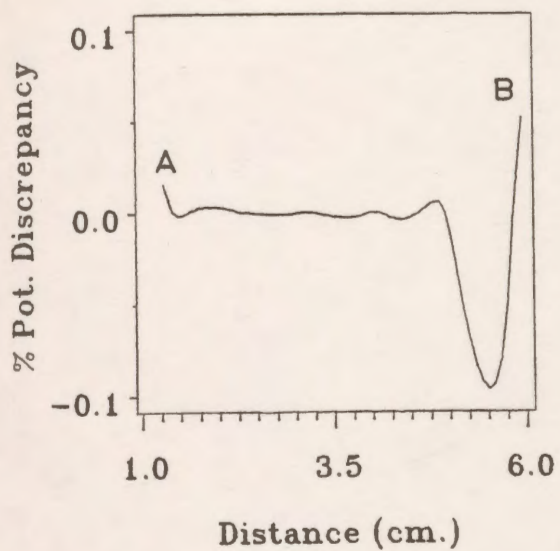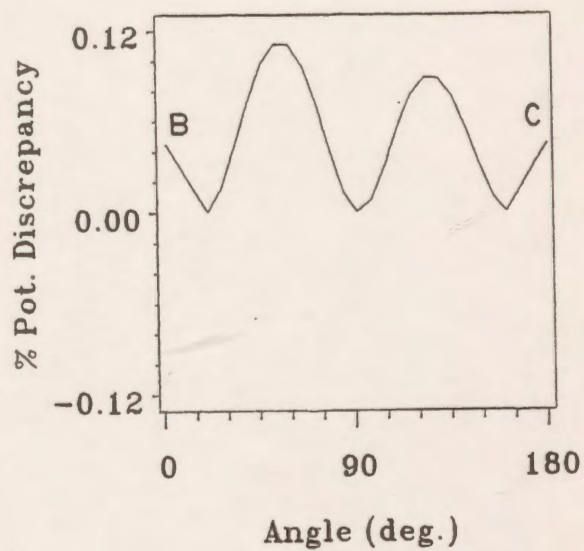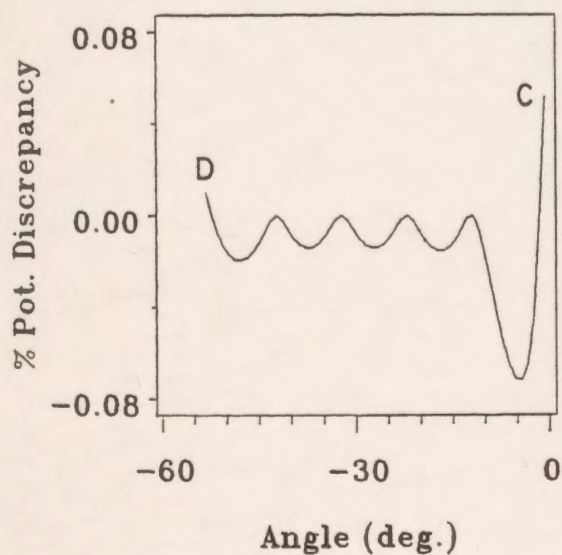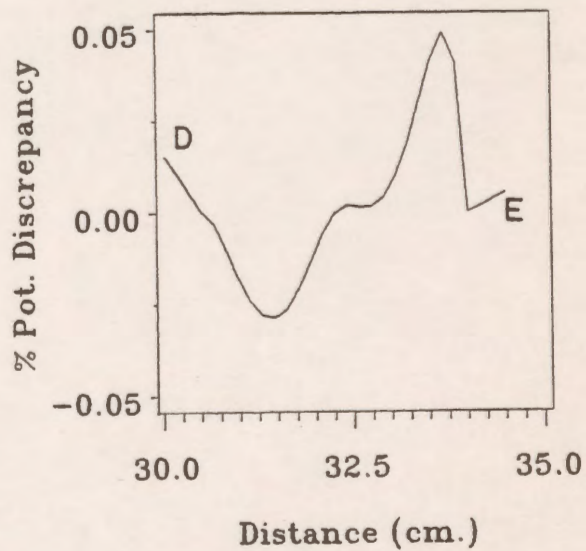
Figure 7.43:   Potential discrepancy along the different sections of the second unit.
        (a) horizontal part   (b) curved periphery part
        (c) sloped part   (d) vertical part
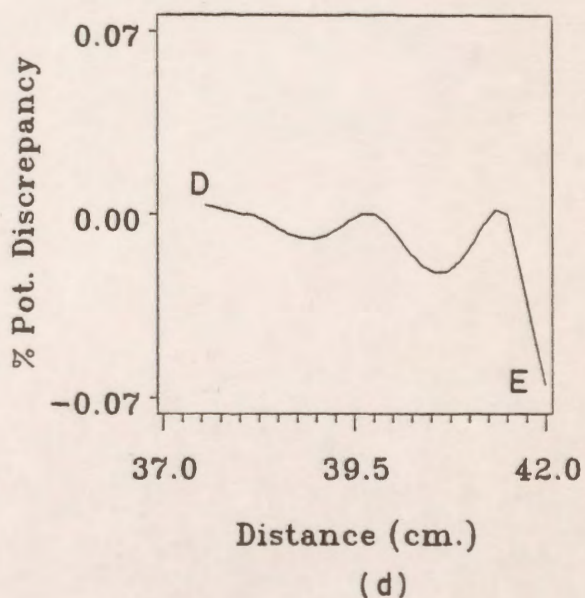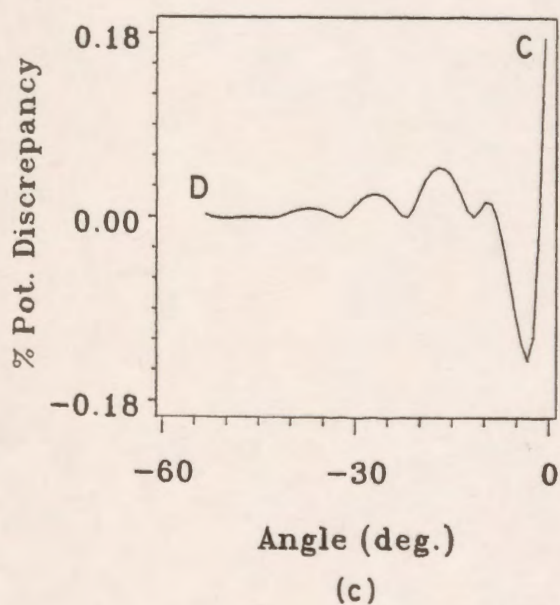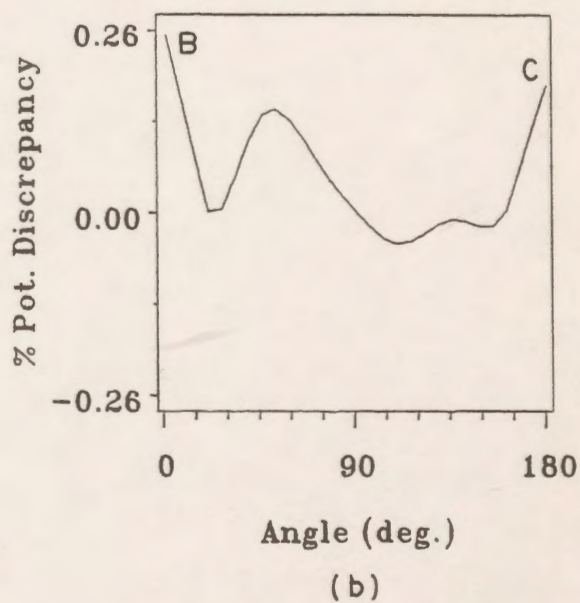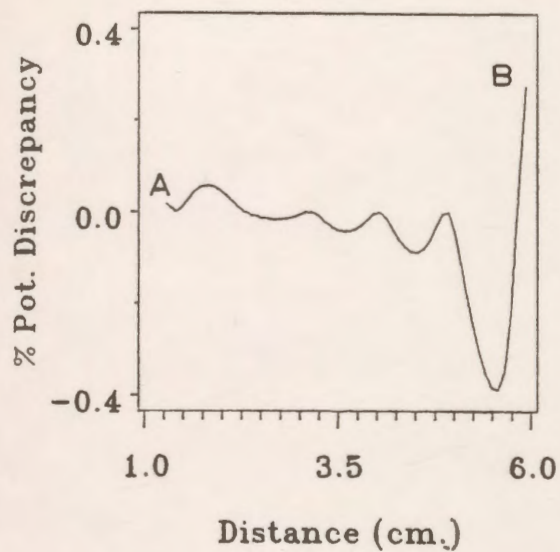
Figure 7.44: Potential discrepancy along the different sections of the third unit.
(a) horizontal part   (b) curved periphery part
(c) sloped part   (d) vertical part

7.5.4.3 Potential and Field Distributions in and Around the Insulator

A design procedure based on the Charge Simulation based CAD package, has been developed for the calculation of both the voltage distribution and the electric field along the axial length of the insulator. Figure 7.45 shows the grading ring where it is placed near the high voltage electrode. The connections between the guard ring and the high voltage electrode are not modelled (ignored to keep the rotational symmetry of the system). The mean radius of the grading ring is denoted by R_g, the cross section (tubing) radius by A_g, and the height of the ring from the high voltage electrode by H_g.

In this work, the size, the radius, and the height of the grading ring are determined to achieve the best uniformity of the withstand potential distribution.
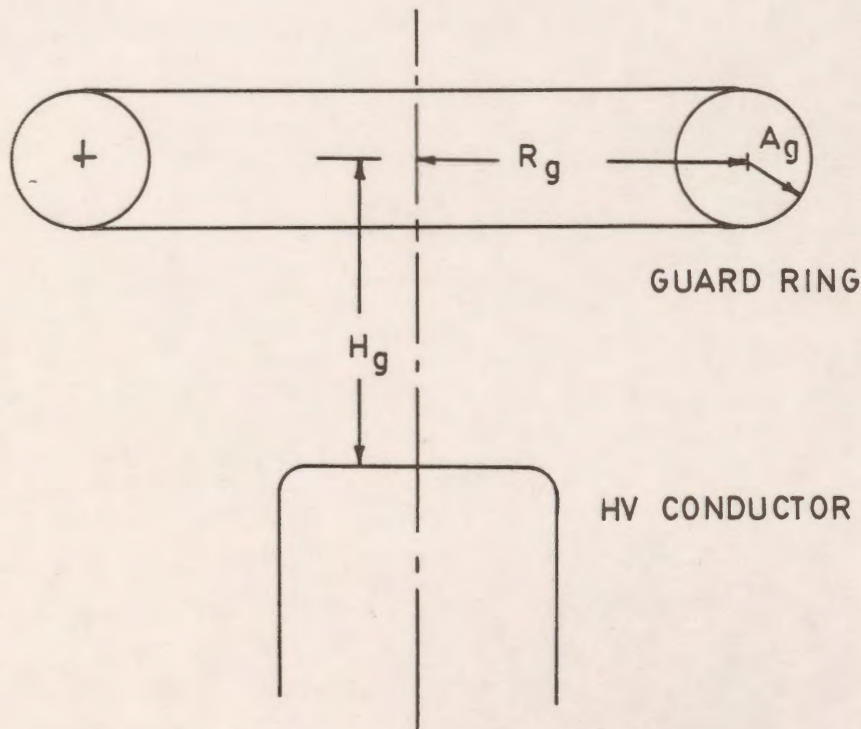
Figure 7.45: Grading ring used with the polymer insulator.

Figure 7.46(a) shows the voltage distribution along the axial length of the insulator for different designs in a normalized format. Fig. 7.46(a), curve 1 shows the voltage distribution without any grading ring. It shows that the voltage distribution along the length of the insulator is highly non-uniform compared to the ideal case of a uniform distribution depicted in Fig. 7.46(a), curve 5. For example, at the location on the axis of the insulator corresponding to 5% of the total length from the high voltage electrode the ideal uniform distribution yields 0.95 pu of the applied voltage (curve 5) while in practice 0.27 pu (curve 1) is obtained. Similarly at the location on the axial length which corresponds to 20% of the length measured from the high voltage electrode, the ideal voltage yields 0.8 pu while in the actual insulator it is 0.07. The high degree of non-uniformity of the voltage distribution is clearly undesirable. It should be noted that the linear voltage distribution (Fig. 7.46(a), curve 5) has the advantage of reducing the electrical stresses at the high voltage electrode and thus provides a better utilization of the insulator.

The axial voltage distribution along the insulator is greatly affected by the different controlling parameters of the guard ring. The effect of varying the radius R_g of the guard ring on the voltage distribution is shown in Fig. 7.46(a), curve 2, 3, and 4 for three different radii of the ring varying from $R_g=4$ cm to $R_g=20$ cm for a fixed height $H_g=4$ cm and fixed cross section radius $A_g=1$ cm. It is clear that at these values of H_g and A_g, increasing R_g beyond a certain limit (12.5 cm) has no great influence on the improvement on the potential distribution.

The axial electric field distribution along the insulator is illustrated in Fig. 7.46(b) for the same controlling parameters as in Fig. 7.46(a). It is seen that the electric field stress is greatly reduced by introducing the grading ring as seen from curves 2, 3, and 4 as compared to curve 1 in Fig. 7.46(b).

The effect of varying the distance of the grading ring from the high voltage electrode H_g at a fixed ring radius R_g and fixed cross section radius A_g, say at $R_g=12.5$ cm and $A_g=1$ cm is also shown in Fig. 7.47(a), curves 2, 3, and 4 for three different positions of the ring varying from $H_g=1$ cm to $H_g=12$ cm. Generally, an increase in H_g improves the voltage distribution. However,
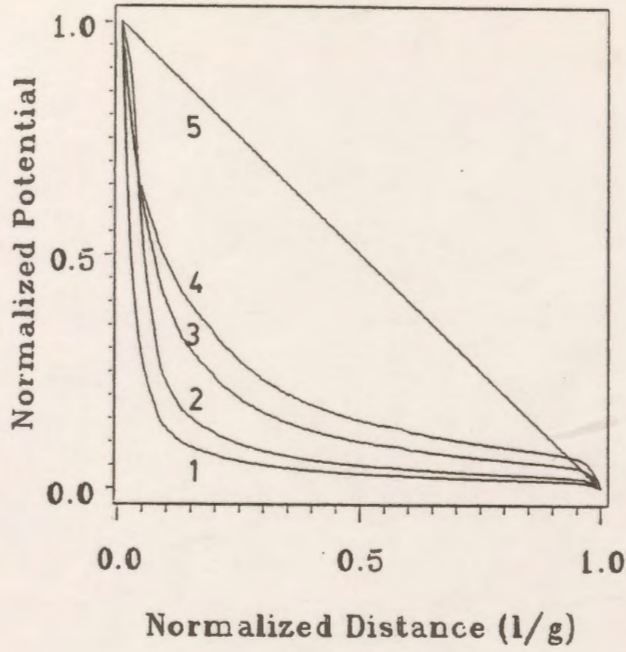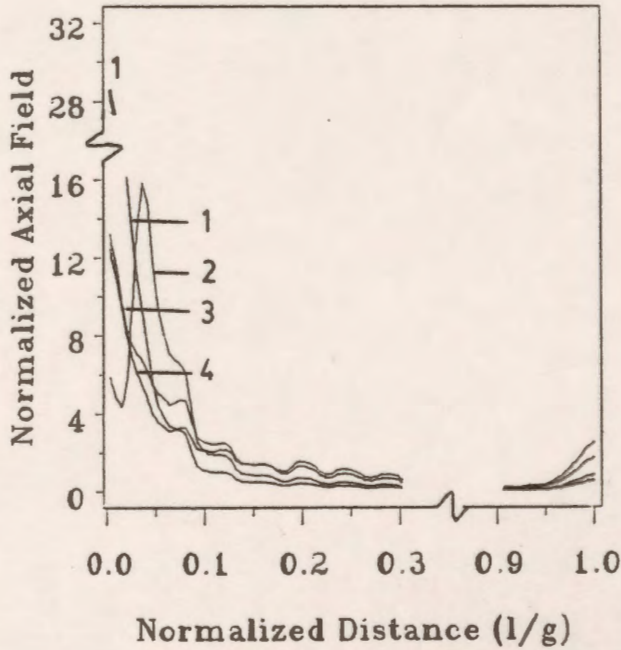
Figure 7.46: Variation of the potential and electric field along the axial line of the insulator with the radius of the guard ring R_g as a parameter for $H_g = 4$ cm and $A_g = 1$ cm.
(a) potential   (b) total electric field
(1) without ring   (2) R_g=4 cm.   (3) R_g=12.5 cm.   (4) R_g=20 cm.   (5) ideal

an upper limit is set on this improvement by the resulting voltage distribution causing some sections to be under stressed and others overstressed (Results for higher values of H_g are omitted for brevity). The axial electric field distribution along the insulator is also shown in Fig. 7.47(b), curves 2, 3, and 4 for the same values of R_g, A_g and H_g as in Fig. 7.47(a). It is clear that the field stress is strongly affected by varying the height position of the ring.

The effect of varying the cross section radius A_g of the grading ring on the potential distribution at a fixed value of R_g and H_g, say R_g=12.5 cm and H_g=12 cm is shown in Fig. 7.48(a) curves 2, 3, and 4 for three different values of A_g varying from A_g=1 cm to A_g =4 cm. It is clear from these curves that the radius A_g has a great influence on the improvement of the potential distribution. However, limits are imposed on the higher values of the radius A_g for economical and weight considerations. Fig. 7.48(b) curves 2, 3, and 4 illustrate the axial electric field distribution for the same parameters as in Fig. 7.48(a). It can be seen from these curves that the electric stress is greatly reduced by increasing A_g.

Finer examinations of the potential and field distributions along the axis of the insulator are carried out to obtain the best design values of the different controlling parameters of the grading ring. Fig. 7.49(a) curves 2, 3, and 4 show the potential distribution at R_g=12.5 cm, A_g=4 cm for another three values of H_g varying from H_g=12 cm to H_g=16 cm. Also, the electric field distribution at these values is illustrated in Fig. 7.49(b), curves 2, 3, and 4.

Figure 7.50(a) curves 2, 3, and 4 show the potential distribution when H_g=16 cm and A_g=4 cm for three different values of R_g varying from R_g=12.5 cm to R_g=18.75 cm which correspond to R_g=2 times the shed radius to 3 times the shed radius. The axial electric field distribution at these values is also shown in Fig. 7.50(b) curves 2, 3, and 4.

It is found that the best distribution of the potential along the axial length of the insulator occured for R_g=15 cm, A_g=4 cm, and H_g=16 cm.
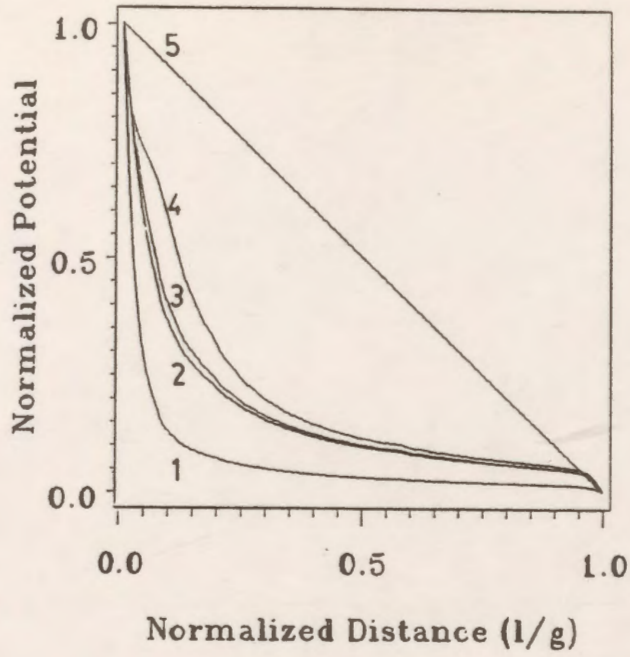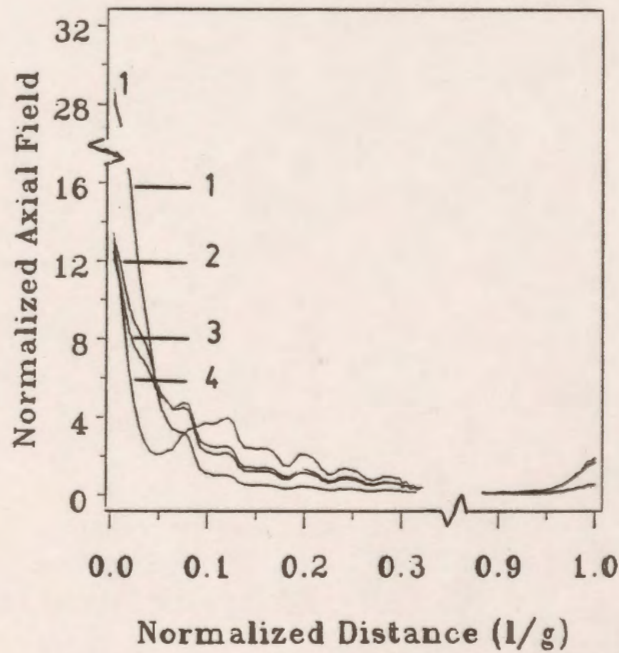
Figure 7.47: Variation of the potential and electric field along the axial line of the insulator with the height of the guard ring H_g as a parameter for $R_g = 12.5$ *cm* and $A_g = 1$ *cm*.
(a) potential   (b) total electric field
(1) without ring   (2) H_g=1 cm.   (3) H_g=8 cm.   (4) H_g=12 cm.   (5) ideal
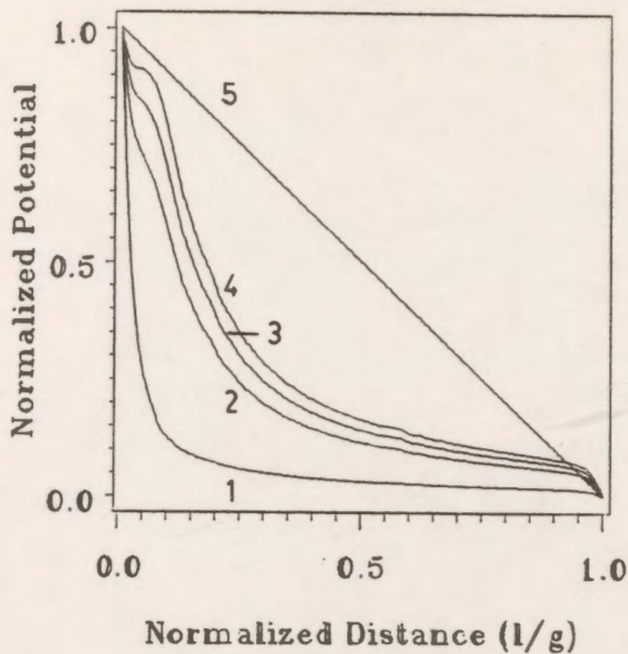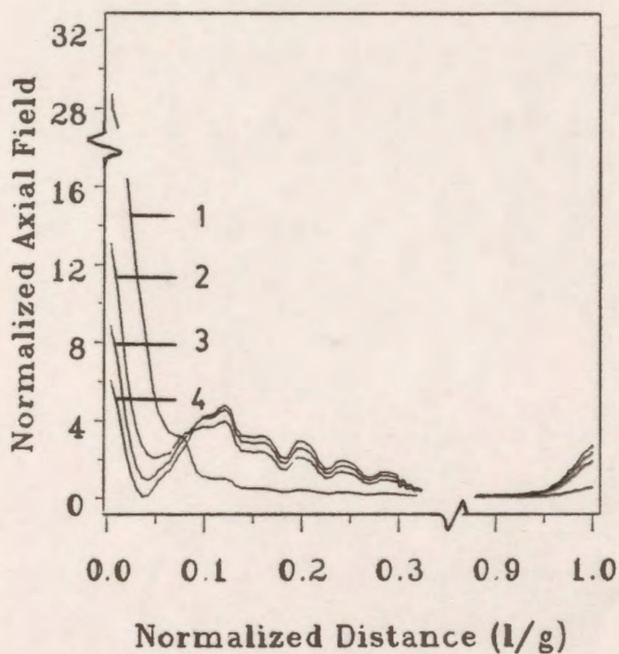
Figure 7.48: Variation of the potential and electric field along the axial line of the insulator with the cross section radius of the guard ring A_g as a parameter for $R_g = 12.5$ *cm* and $H_g = 12$ *cm*.
(a) potential   (b) total electric field
(1) without ring   (2) A_g=1 cm.   (3) A_g=2.5 cm.   (4) A_g=4 cm.   (5) ideal
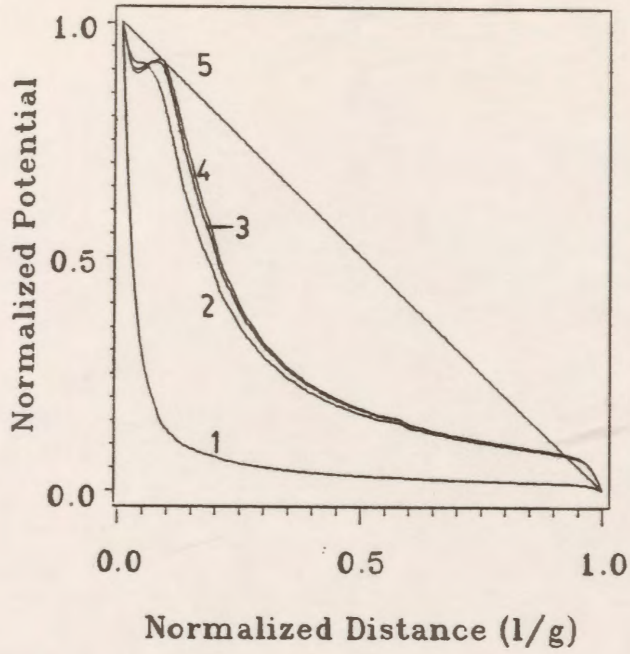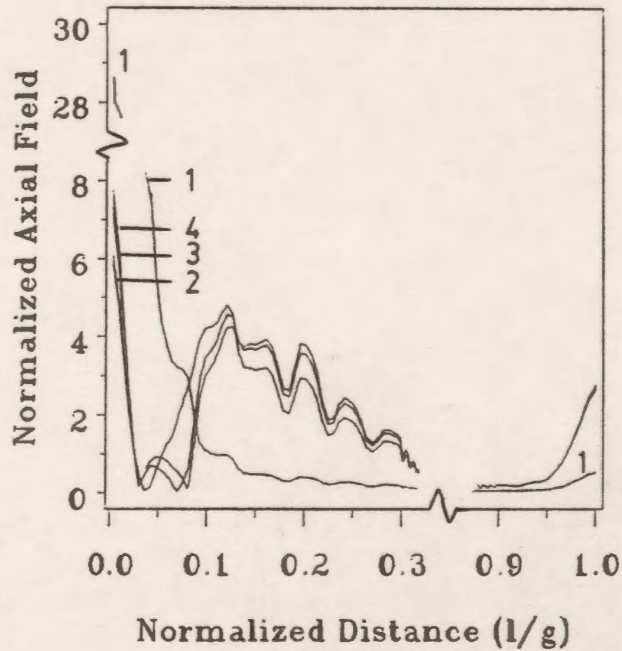
Figure 7.49: Variation of the potential and electric field along the axial line of the insulator with the height of the guard ring H_g as a parameter for $R_g = 12.5$ cm and $A_g = 4$ cm.

(a) potential   (b) total electric field

(1) without ring   (2) H_g=12 cm.   (3) H_g=15 cm.   (4) H_g=16 cm.   (5) ideal
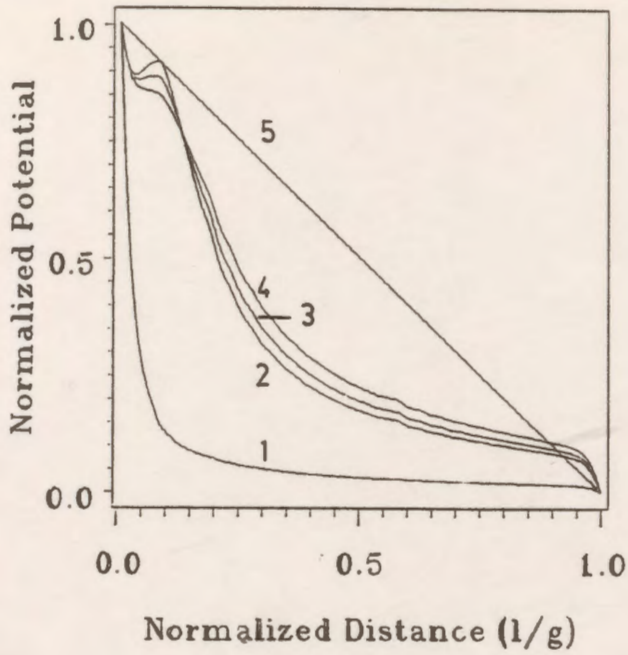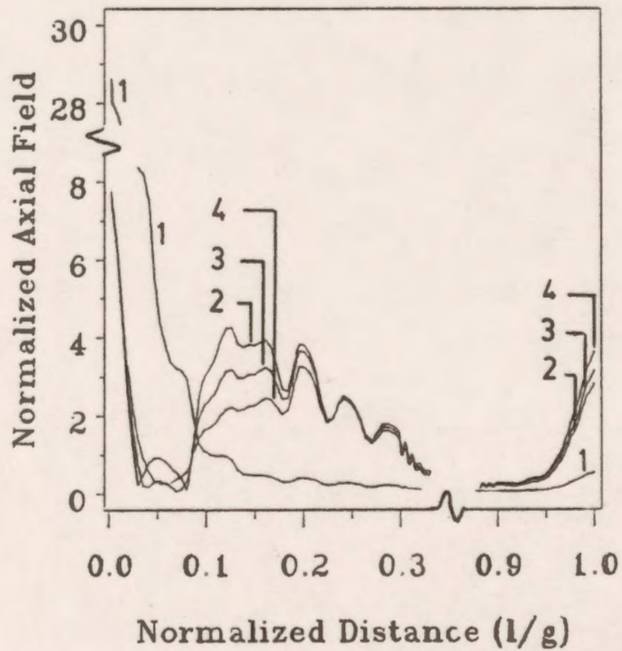
Figure 7.50: Variation of the potential and electric field along the axial line of the insulator with the radius of the guard ring R_g as a parameter for $H_g = 16$ *cm* and $A_g = 4$ *cm*.
(a) potential   (b) total electric field
(1) without ring   (2) R_g=12.5 cm.   (3) R_g=15 cm.   (4) R_g=18.75 cm.   (5) ideal

The potential drop distribution along the polymer insulator units including the vertical dielectric column without and with the guard ring for R_g=15 cm, H_g=16 cm, and A_g=4 cm is shown in Fig. 7.51 curves 1 and 2 respectively. It is clear from this graph that the grading ring decreases the potential drop across the dielectric rod and the units close to the high voltage electrode.

The potential and total electric field distributions along the interfaces of the different units of the polymer insulator are computed without and with the grading ring. The controlling parameters were fixed at their best values, R_g=15 cm, H_g=16 cm, and A_g=4 cm. The results presented here are for the vertical dielectric column, the first three units, a middle unit, and the last unit which is adjacent to the grounded electrode (results for other units are omitted for brevity).

Figures 7.52 to 7.57 illustrate the potential distribution on the vertical column and the sections of the chosen 5 units of the polymer insulator. Curve 1 corresponds to the potential distribution without the guard ring and curve 2 to the potential distribution with the guard ring. The largest potential difference appears across the vertical column of the insulator as shown in Fig. 7.52. The impressed voltage across this section is about 70% of the applied voltage without the grading ring. This drop is decreased to 14% after inserting the guard ring.

The normalized total electric field along the vertical dielectric column and the chosen 5 units of the polymer insulator are also illustrated in Figs. 7.58 - 7.63 without the grading ring (curve 1) and with the grading ring (curve 2). It can be seen from these figures that the field stress is reduced especially along those units which are close to the high voltage electrode by using the grading ring.
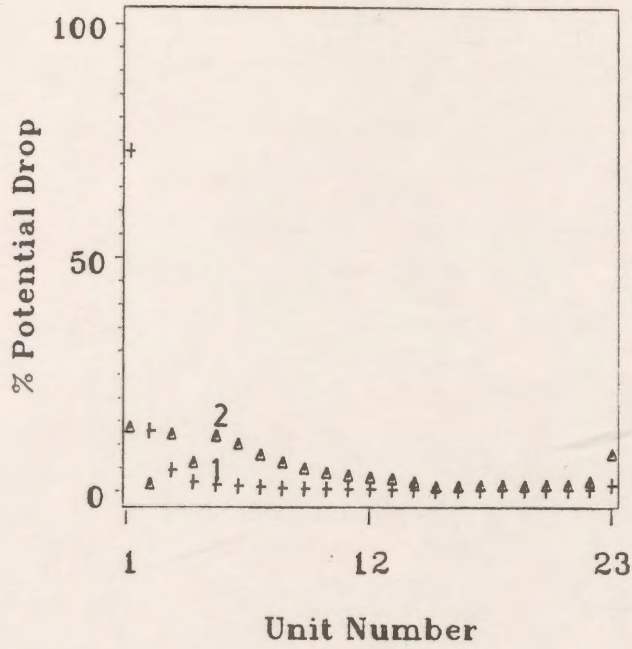
Figure 7.51: Potential drop across the units of the polymer insulator without grading ring (curve 1), and with grading ring (curve 2) for $R_g = 15$ *cm*, $H_g = 16$ *cm* and $A_g = 4$ *cm*.
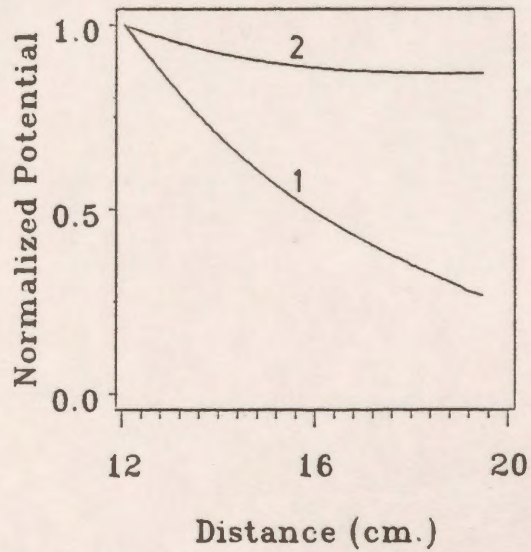

Figure 7.52: Potential distribution along the vertical column of the polymer insulator without grading ring (curve 1), and with grading ring (curve 2).
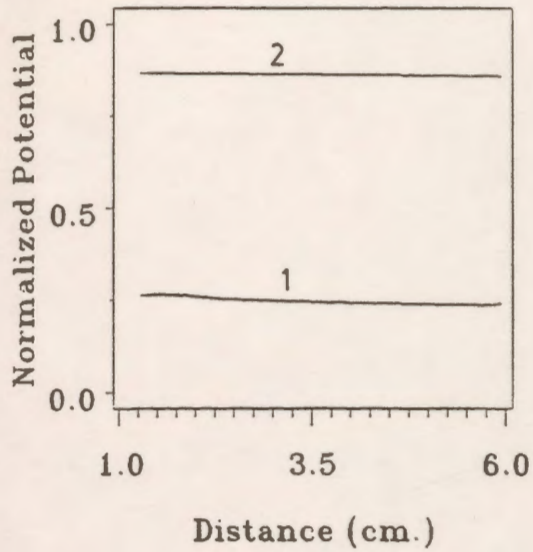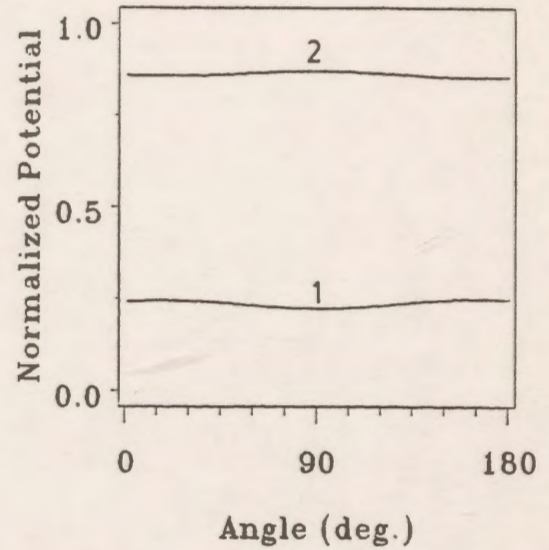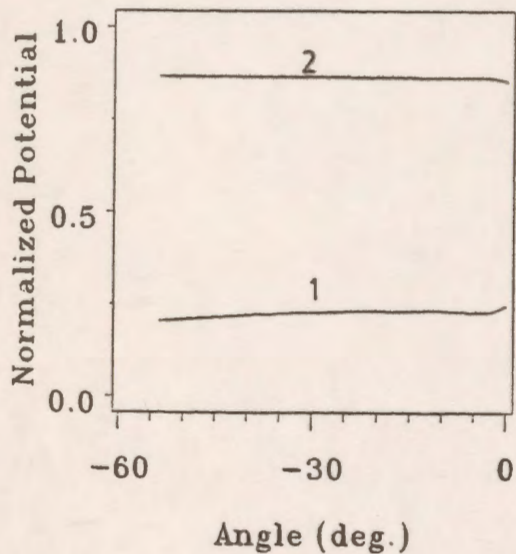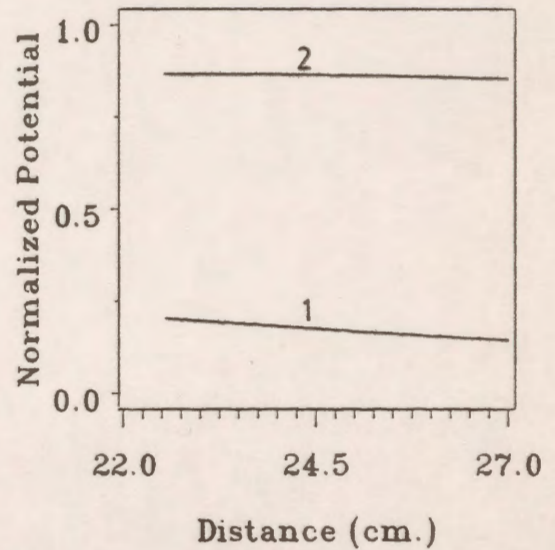
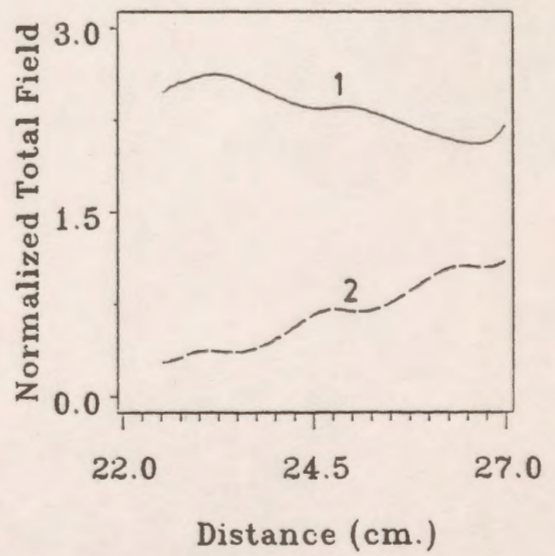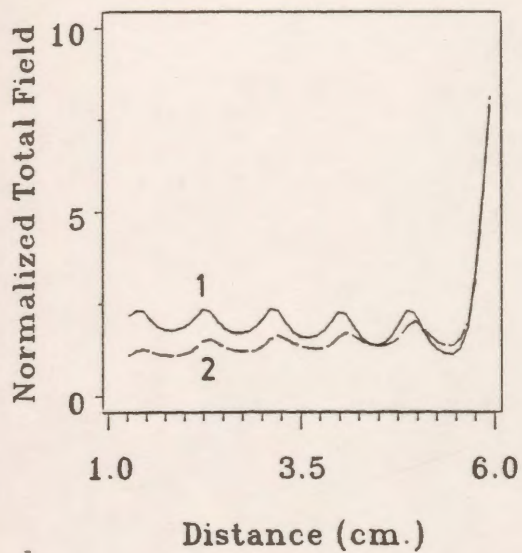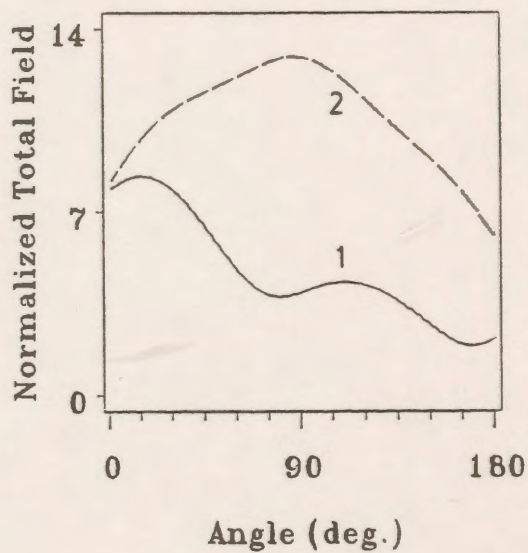*Figure 7.53*: Potential distribution along the different sections of the first unit without grading ring (curve 1), and with grading ring (curve 2).
(a) horizontal part   (b) curved periphery part
(c) sloped part   (d) vertical part
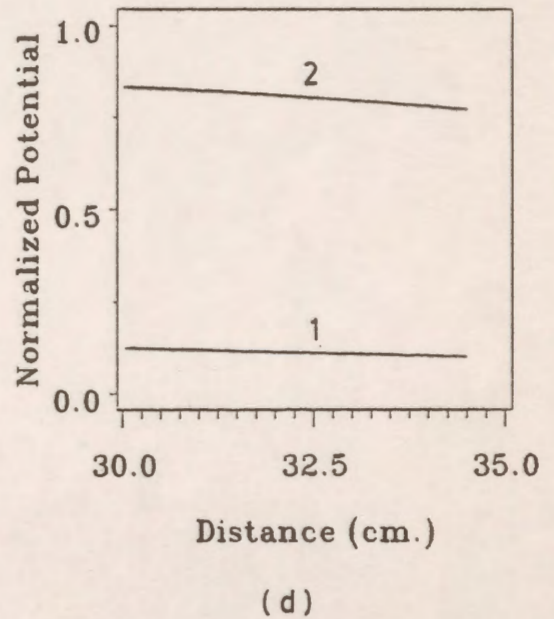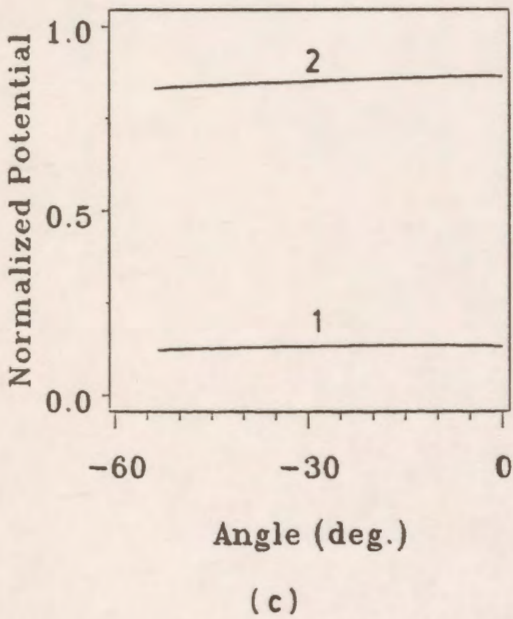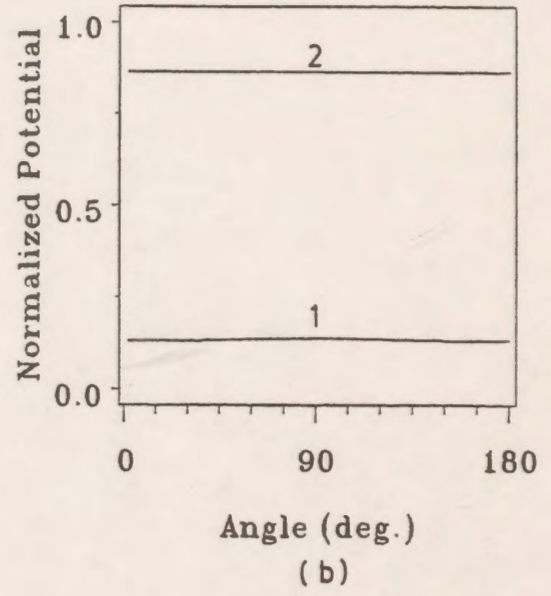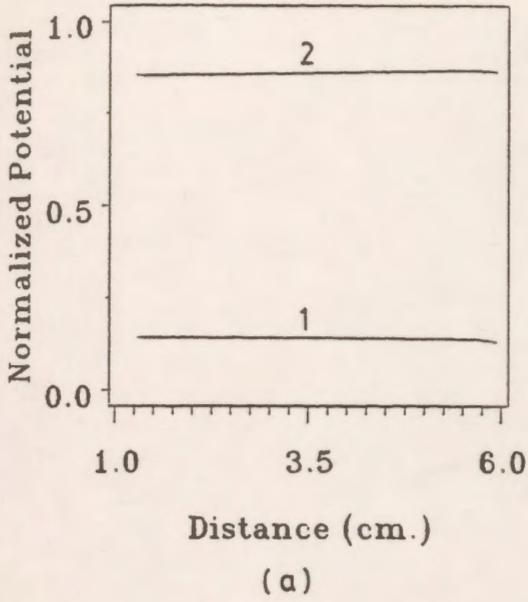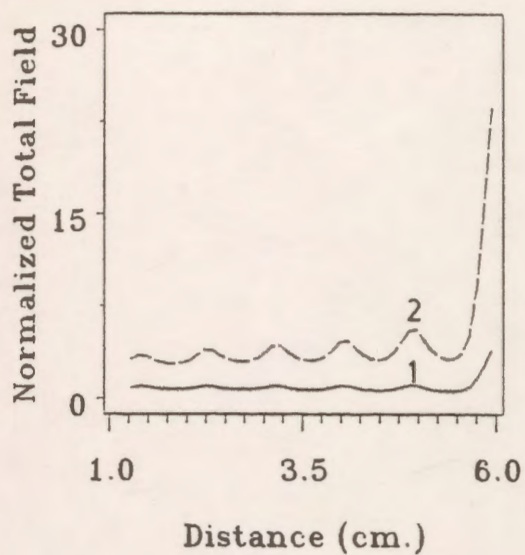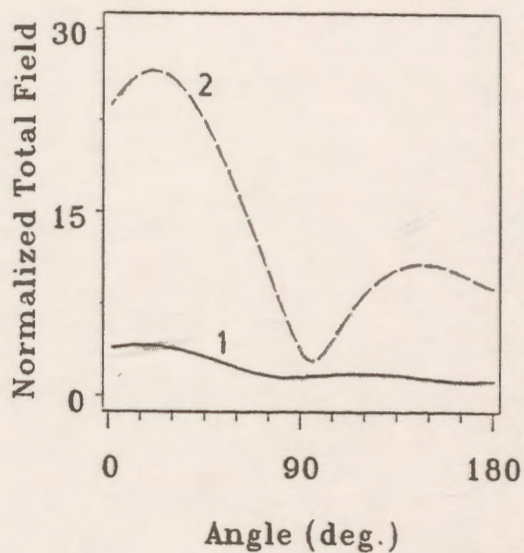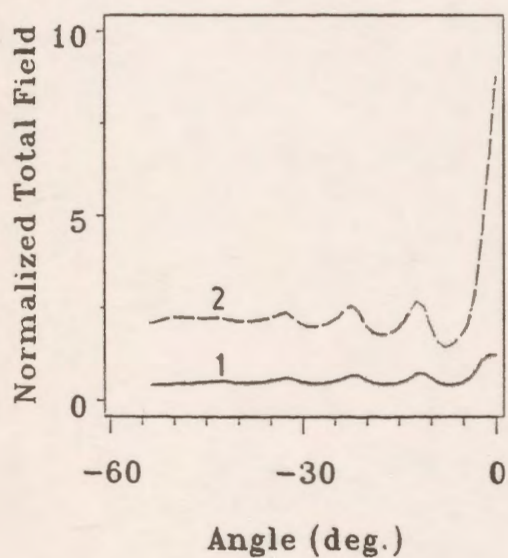
Figure 7.54: Potential distribution along the different sections of unit # 2 without grading ring (curve 1), and with grading ring (curve 2).
(a) horizontal part   (b) curved periphery part
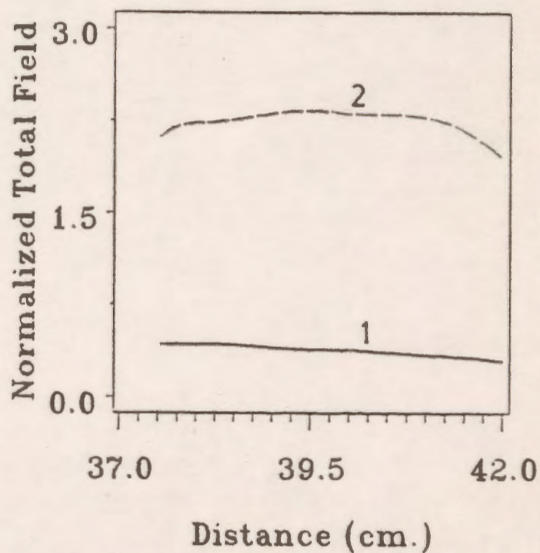(c) sloped part   (d) vertical part
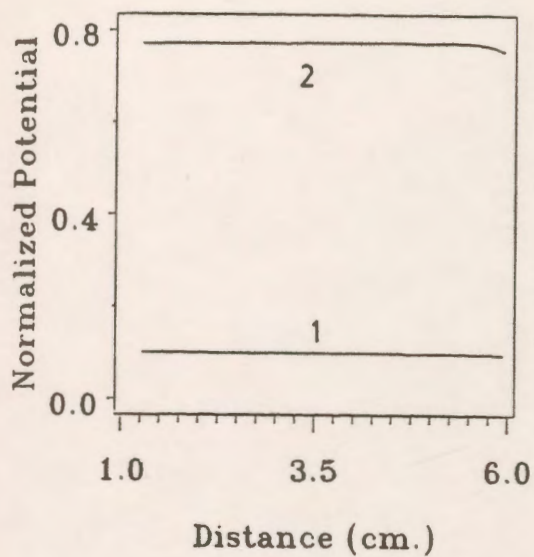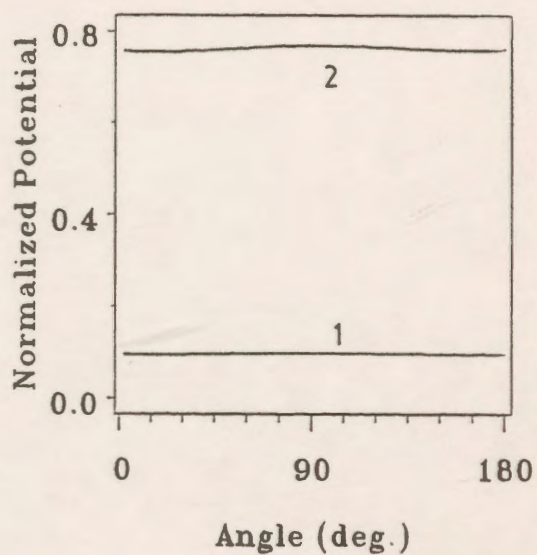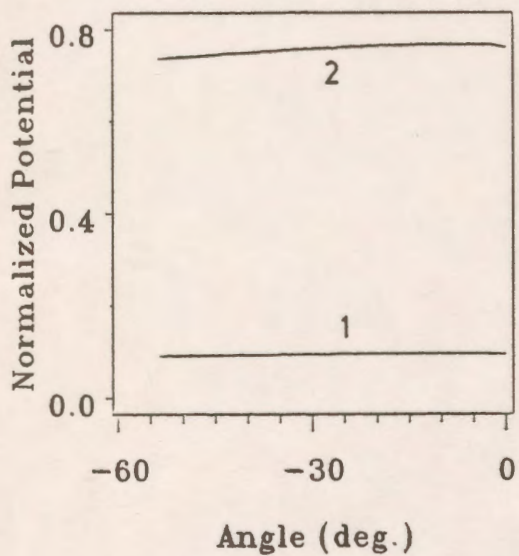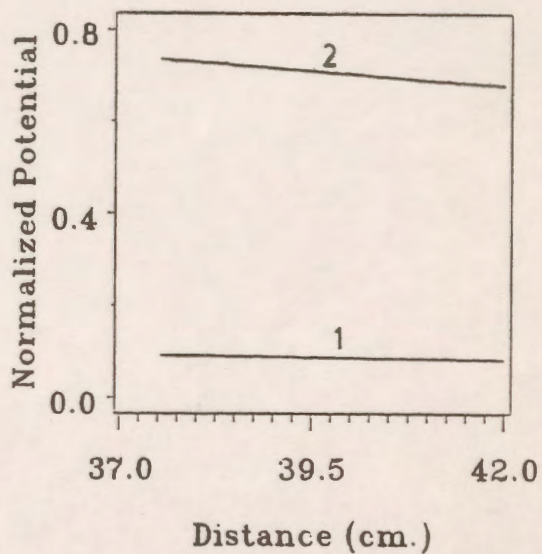
Figure 7.55: Potential distribution along the different sections of unit # 3 without grading ring (curve 1), and with grading ring (curve 2).
(a) horizontal part   (b) curved periphery part
(c) sloped part   (d) vertical part
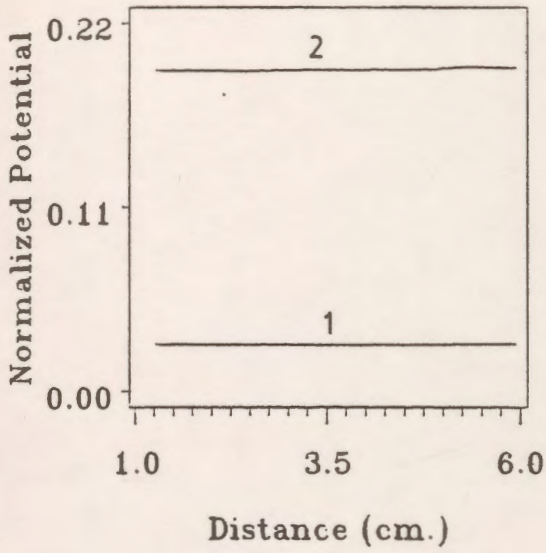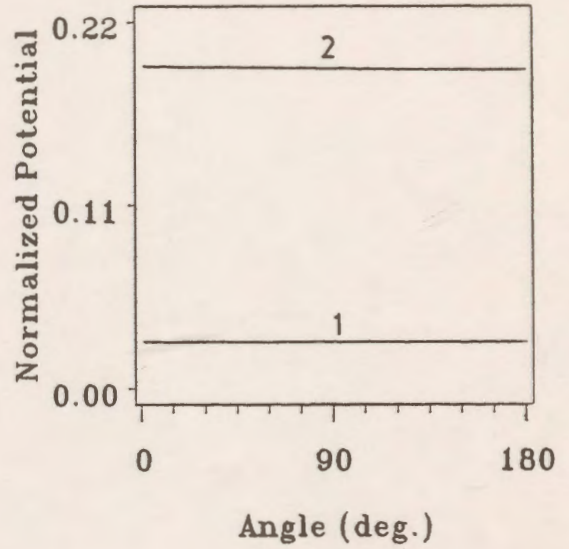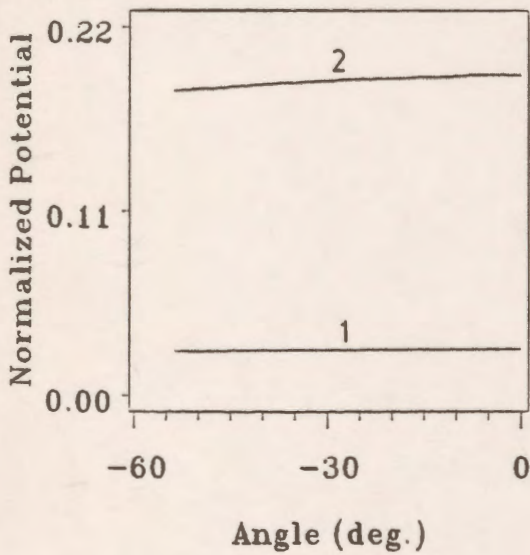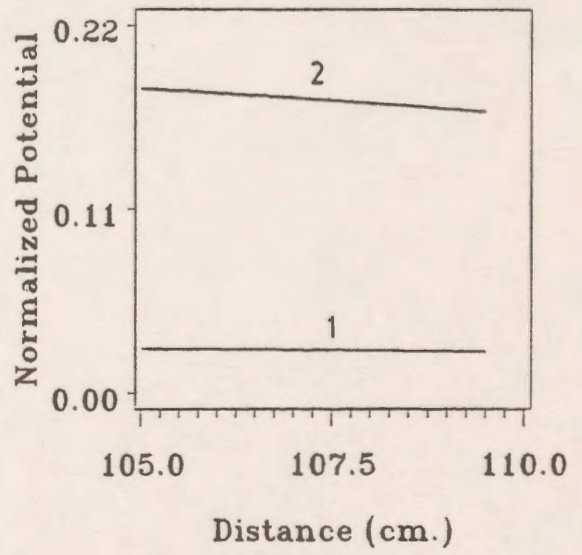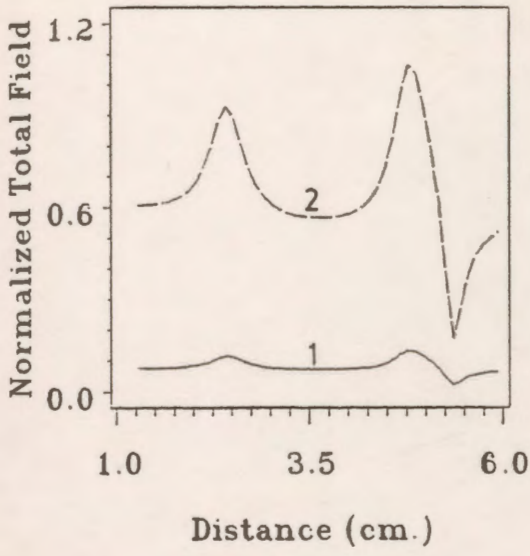
Figure 7.56: Potential distribution along the different sections of unit # 12 without grading ring (curve 1), and with grading ring (curve 2).
(a) horizontal part   (b) curved periphery part
(c) sloped part   (d) vertical part
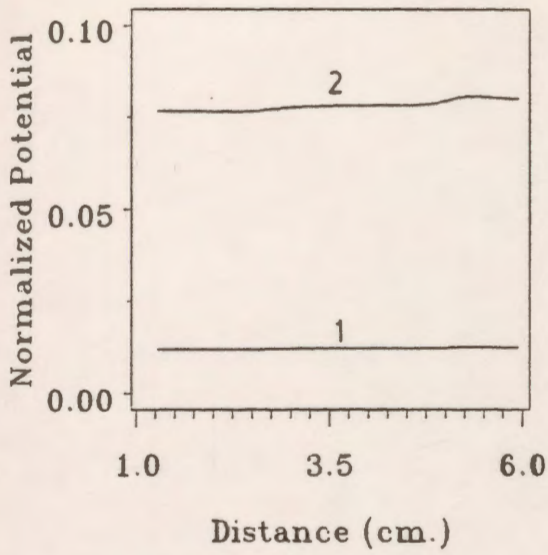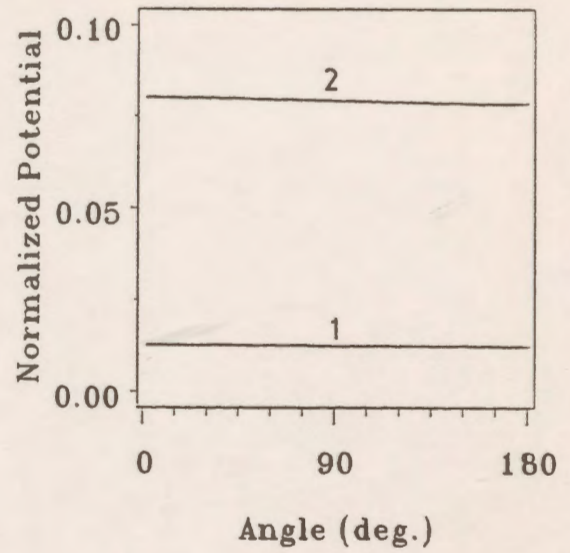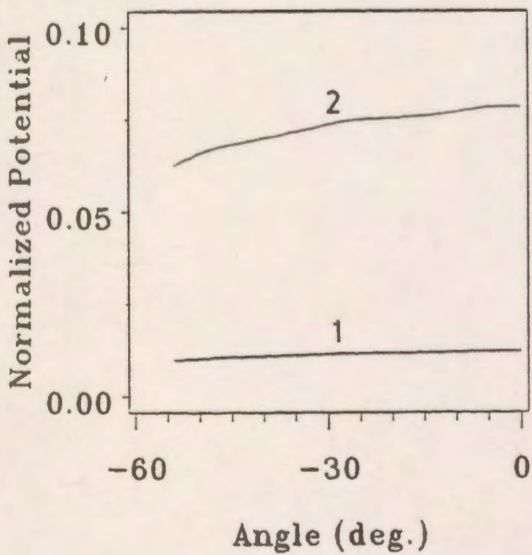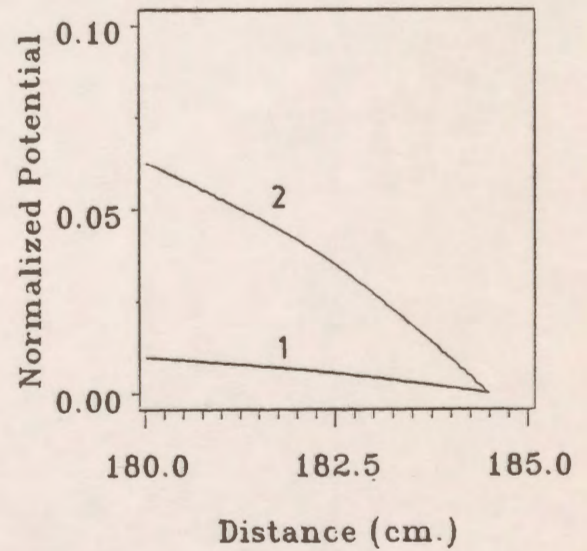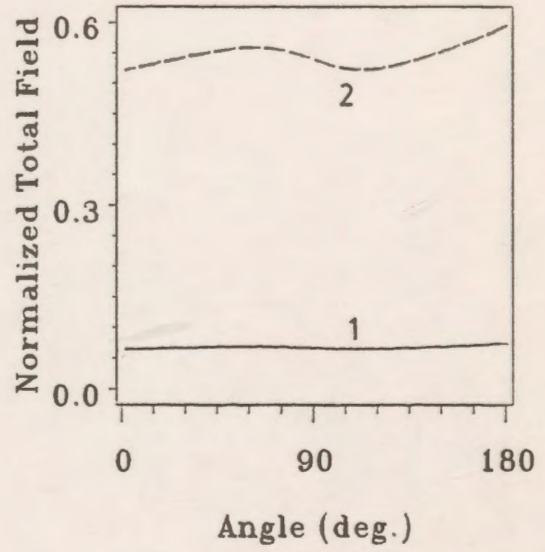
Figure 7.57: Potential distribution along the different sections of the last unit without grading ring (curve 1), and with grading ring (curve 2).
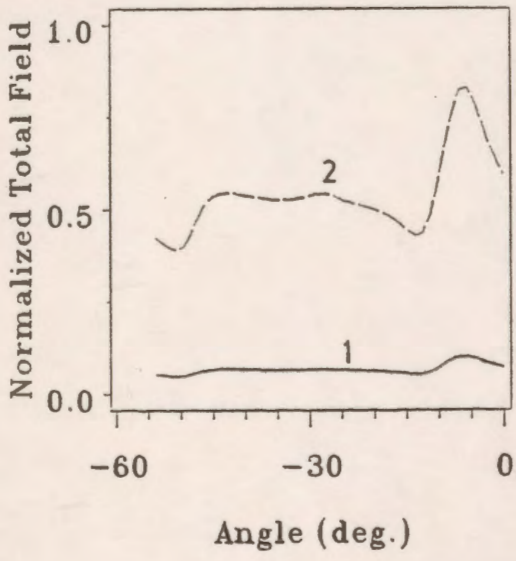(a) horizontal part   (b) curved periphery part
(c) sloped part   (d) vertical part
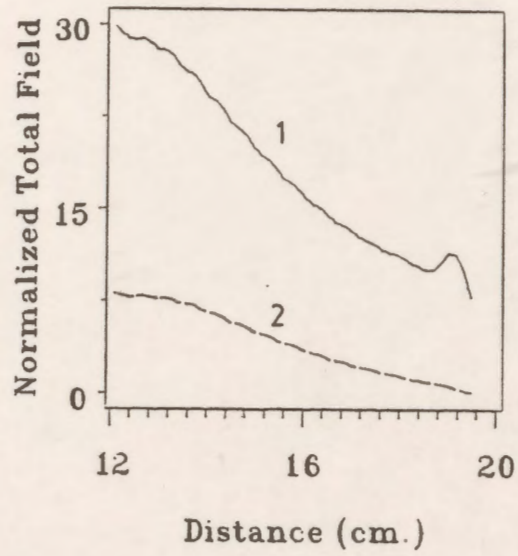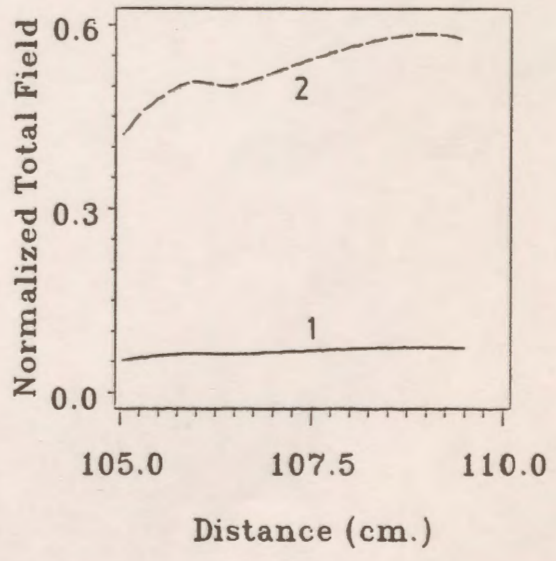
Figure 7.58: Total electric field distribution along the vertical column of the polymer insulator with grading ring (curve 2), and without grading ring (curve 1).
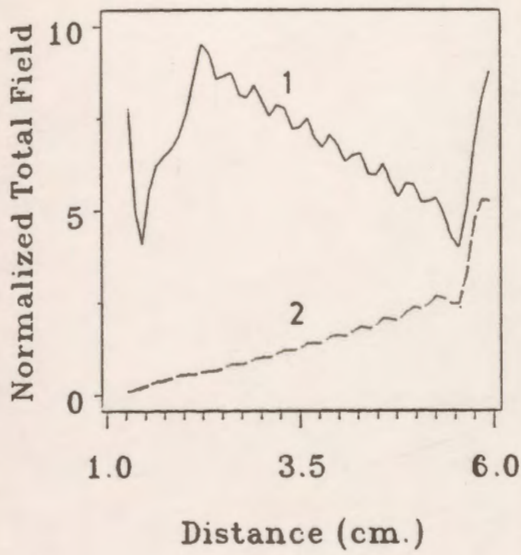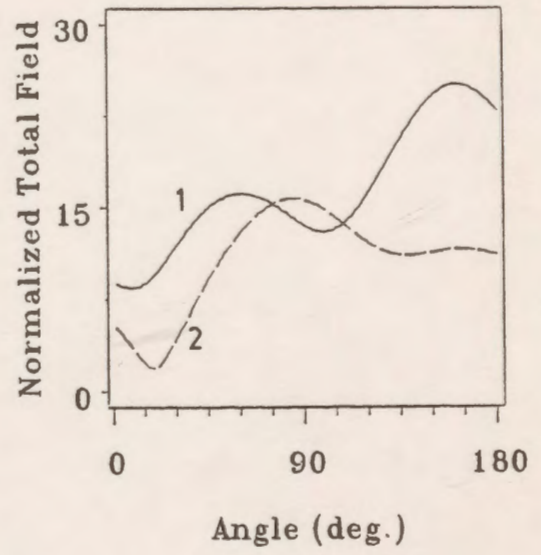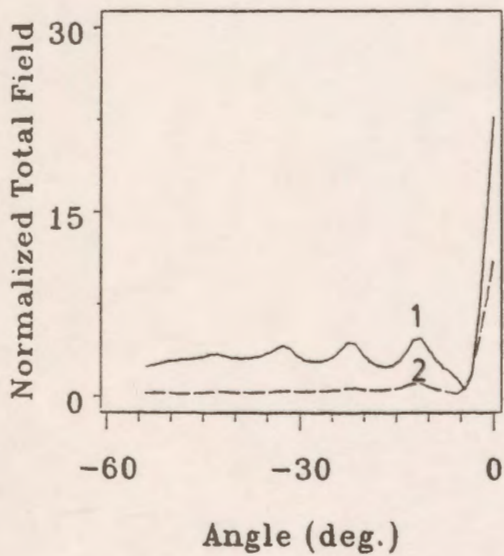
Figure 7.59: Total electric field distribution along the different sections of the first unit without
grading ring (curve 1), and with grading ring (curve 2).
(a) horizontal part   (b) curved periphery part
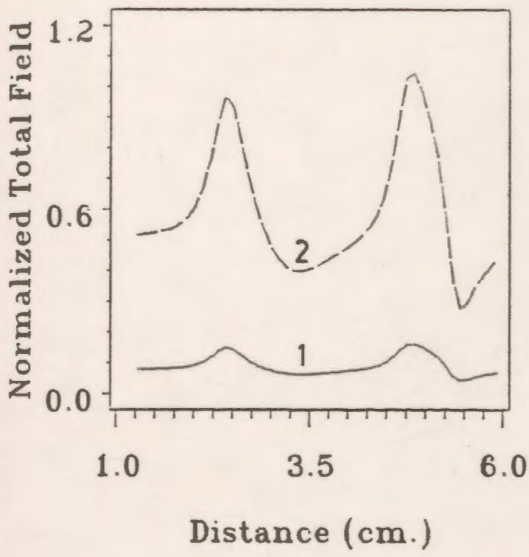(c) sloped part   (d) vertical part
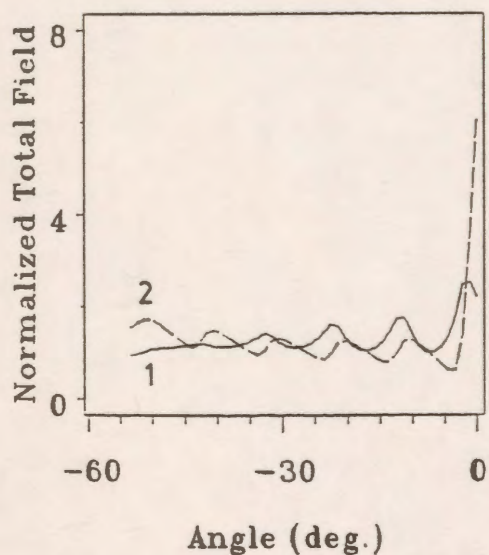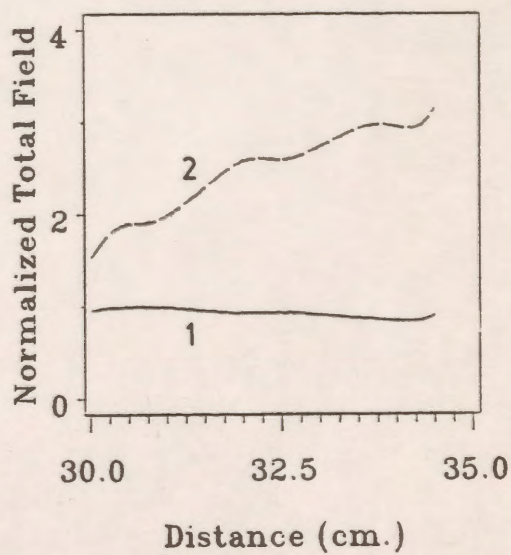
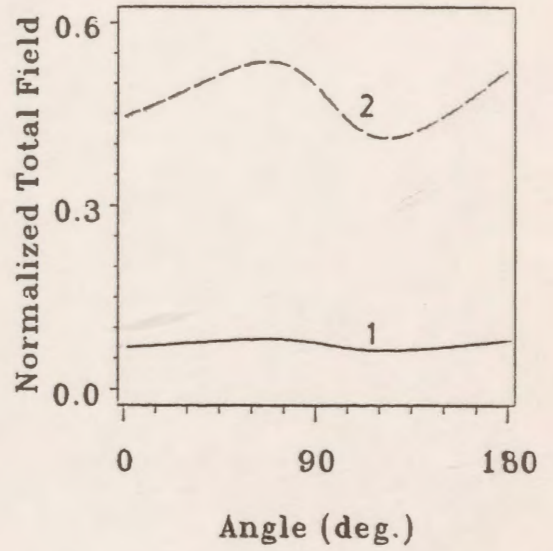*Figure 7.60*: Total electric field distribution along the different sections of unit # 2 without grading ring (curve 1), and with grading ring (curve 2).
(a) horizontal part   (b) curved periphery part
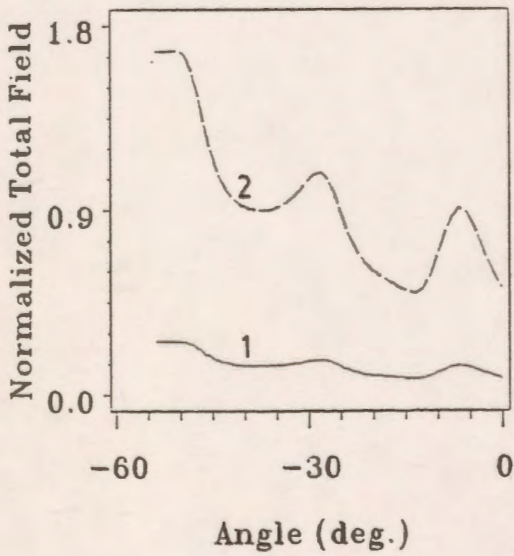(c) sloped part   (d) vertical part

Figure 7.61: Total electric field distribution along the different sections of unit # 3 without grading ring (curve 1), and with grading ring (curve 2).
(a) horizontal part   (b) curved periphery part
(c) sloped part   (d) vertical part

Figure 7.62: Total electric field distribution along the different sections of unit # 12 without grading ring (curve 1), and with grading ring (curve 2).
  (a) horizontal part   (b) curved periphery part
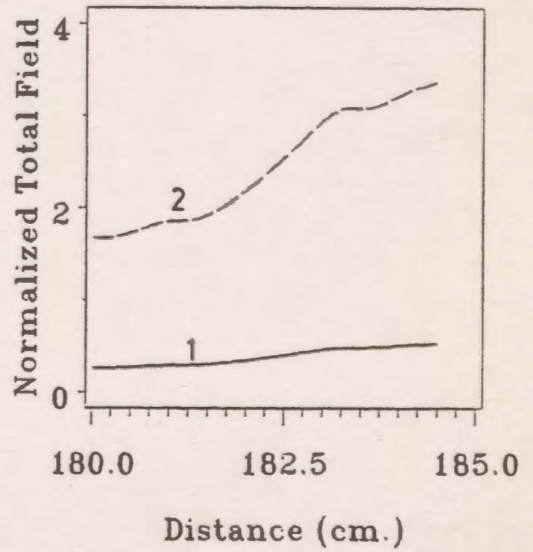 (c) sloped part   (d) vertical part

Figure 7.63: Total electric field distribution along the different sections of the last unit without grading ring (curve 1), and with grading ring (curve 2).
(a) horizontal part   (b) curved periphery part
(c) sloped part   (d) vertical part

It should be mentioned here that the number of charges used for modelling the polymer insulator is not sufficient to get very accurate results for the potential and field distribution. It is expected that acceptable simulation may be reached by using a high number of modelling charges which is estimated to be approximately 2500 based on required values for assignment factor, number of charges per unit length of boundary segment, and on minimizing discontinuities in modelling charge alignment on adjacent boundary segments. The computer time and memory storage requirements present limitations on the number of charges which can reasonably be used to model the system in addition to limitations expected from roundoff error accumulation. A total of 500 charges were used for modelling requiring 90 minutes of CPU time to complete the calculation. Since this level of modelling detail does not produce acceptable levels of all quality measures, the potential and electric field distribution along the axis of a one shed unit with the dielectric cylindrical column was studied using two different total numbers of simulating charges. One corresponding to a poor quality with a total number of modelling charges of 114 and the other to a high quality simulation with 170 modelling charges. It was found that the difference in potential and total electric field distributions between the two cases does not exceed 8% on the axis or along the dielectric interface. This result gives us a measure of confidence in the values of the potential and electric field distributions in and around the polymer insulator using 500 charges for modelling.

Chapter VIII

APPLICATION OF THE CAD PACKAGE TO 3-DIMENSIONAL HV

SYSTEMS

8.1   *Tilted Hemispherical Capped Electrode-Plane Arrangement*

8.1.1   Modelling Concepts

In modelling 3-dimensional systems with non-axial symmetry, the arrangement of contour points and the corresponding charge locations will be different from the case in which the system has symmetry about a common axis. This concept will be illustrated by the application of the package to a tilted upper rod electrode near a grounded plane electrode as shown in Figure 8.1(a).

If the upper rod electrode is in the vertical position ($\theta = 0^{\circ}$), it will have rotational symmetry about the z-axis and it can be modelled by distributing the contour points and the ring charge locations along one side of the boundary (the right side). When this rod is rotated by a certain angle θ, the rotational symmetry will disappear due to the presence of the grounded electrode. In this case the distribution of the contour points and the corresponding simulating charges should be modified in order to compensate for the lack of symmetry. The contour points can be located on the left side boundary and the right side boundary or they can be arranged on four sides of the electrode boundary. The corresponding charges are also arranged to be associated with two sides or four sides of the boundary. Fig. 8.1(b) shows a cross section of the hemispherically capped rod when the charges are used to model both sides of the electrode. The two sets of charges are shifted from each other by a certain amount. Fig. 8.1(c) also shows a cross section of the hemispherically capped rod when the charges are used to model the four sides of the electrode. Whether two or four sides should be modelled depends on how much accuracy in the simulation is required.
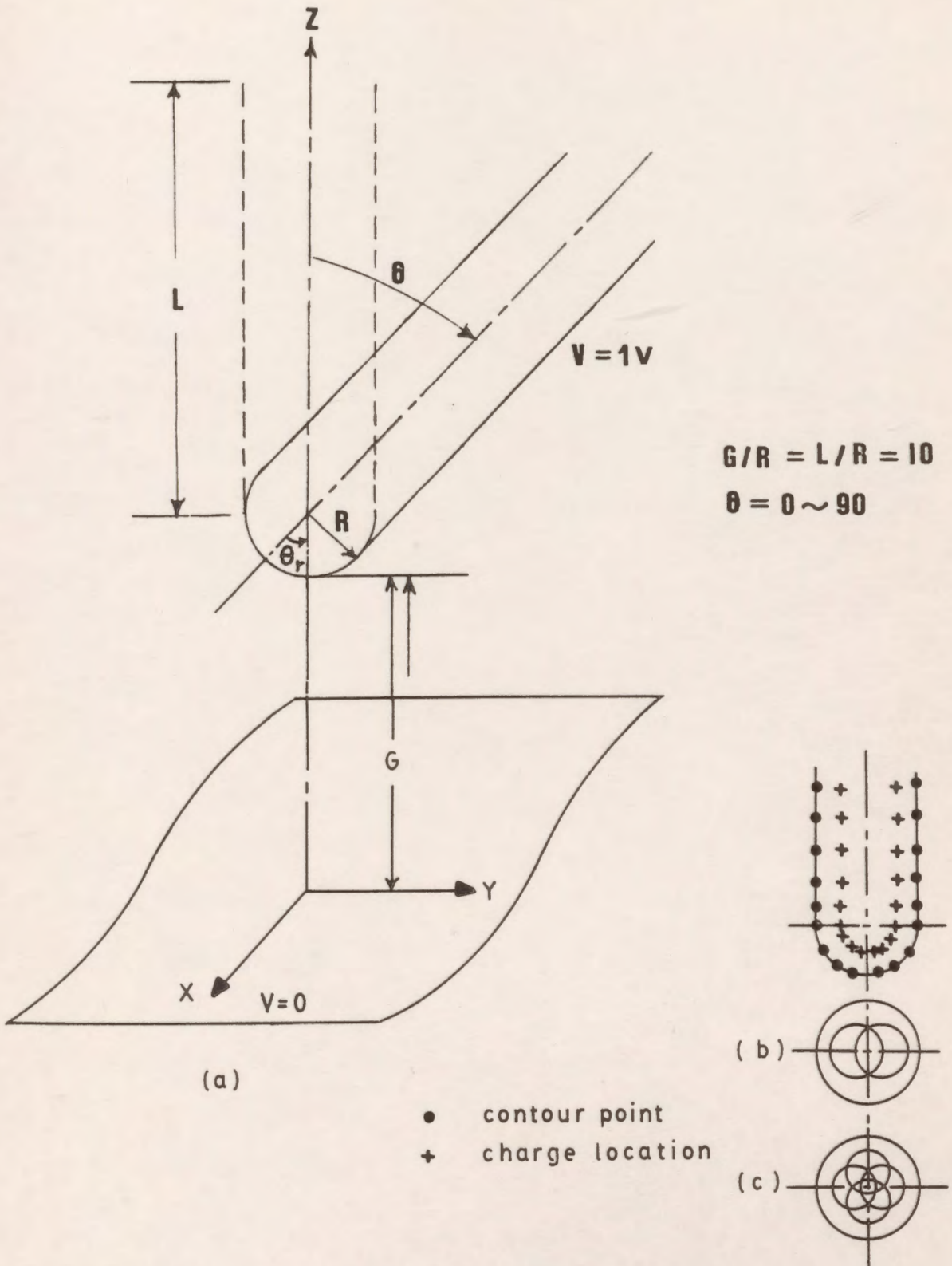
Figure 8.1: A tilted upper rod electrode versus a grounded plane electrode.
(a) the system geometry
(b) rod cross section with two sets of charges
(c) rod cross section with four sets of charges

The package is capable as described before of rotating and translating any section in the model in the three dimensional space and this capability is used in this model. For example, to rotate this electrode by $\theta=45°$, the user has to translate the electrode first to the origin, rotate the electrode by -45° around the x-axis and finally translate it back to the centre of the hemispherical part. This operation may take only one minute of the user's time.

The inclination angle θ is varied from 0° to 90° and the electrode is modelled using only one set of charges to model the right side of the boundary in one case and two sets of charges to model both sides in the other case, to see the difference in errors in both cases. Fig. 8.2(a) shows a computer output for the distribution of contour points and charge locations after rotating the electrode by -45° and using only one set of charges, while Fig. 8.2(b) represents a computer output when modelling both sides of the electrode.

8.1.2   Results

The literature examined reveals no data regarding the normality of the electric field vector to the tilted rod electrode surface. This condition should also be satisfied if an accurate field solution is desired. For this reason all the results include graphs showing the tangential field difference along the electrode surface boundaries which should be as small as possible. Fig. 8.3(a) shows the distribution of the percentage potential error along the right boundary of the hemispherical part for different inclination angles θ when using one set of charges to model the electrode. The tangential field difference distribution along the same part is shown in Fig. 8.3(b). It is clear from these graphs that both kinds of errors are within acceptable limits for this section.

For the left side of the hemispherical part both the potential error and the tangential field difference are plotted as for the right part as shown in Fig. 8.4. The errors increase as the inclination angle increases. The maximum value of the potential error is 1.2% and the maximum value of the tangential field difference is 0.012.
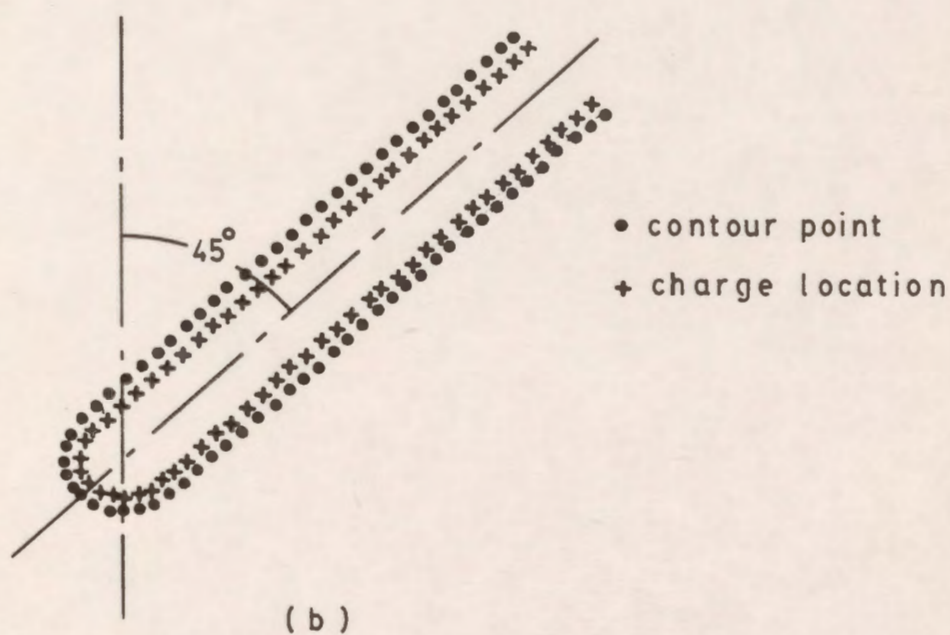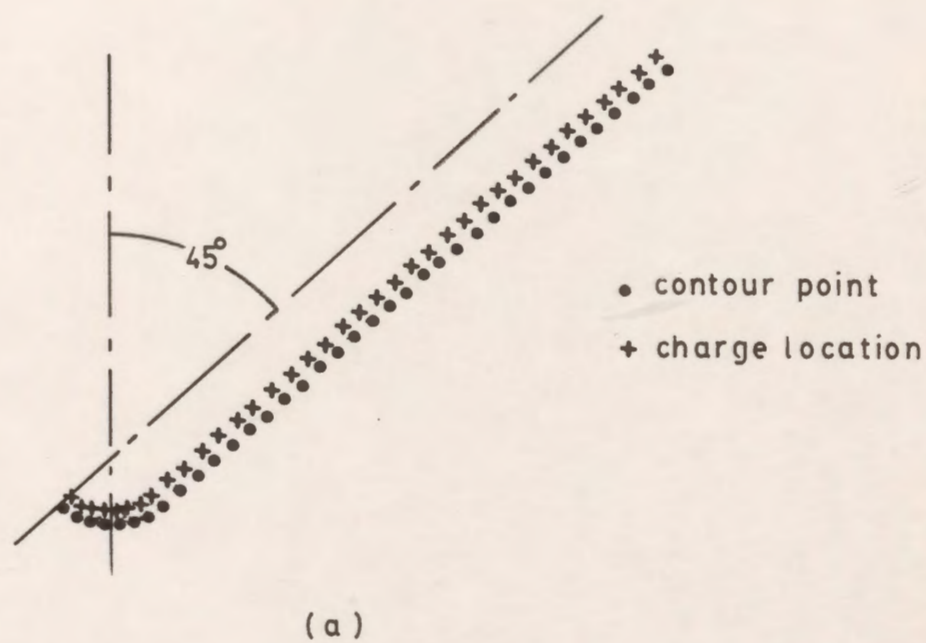
Figure 8.2: Distribution of contour points and charge locations.
(a) modelling one boundary of the electrode
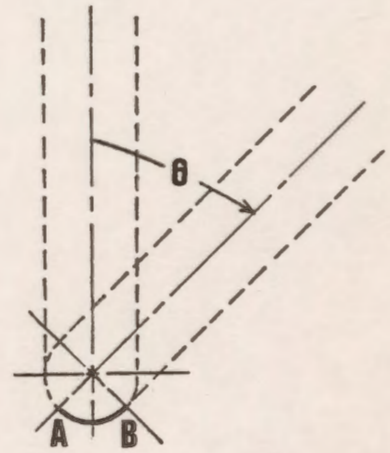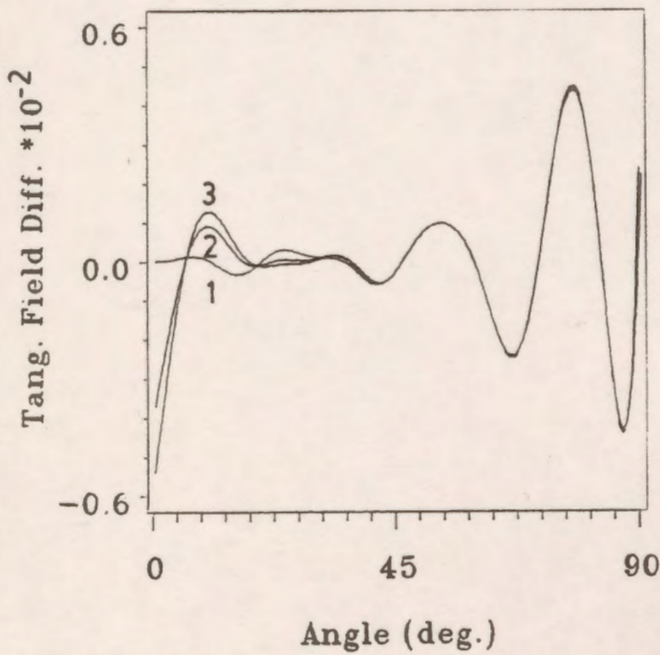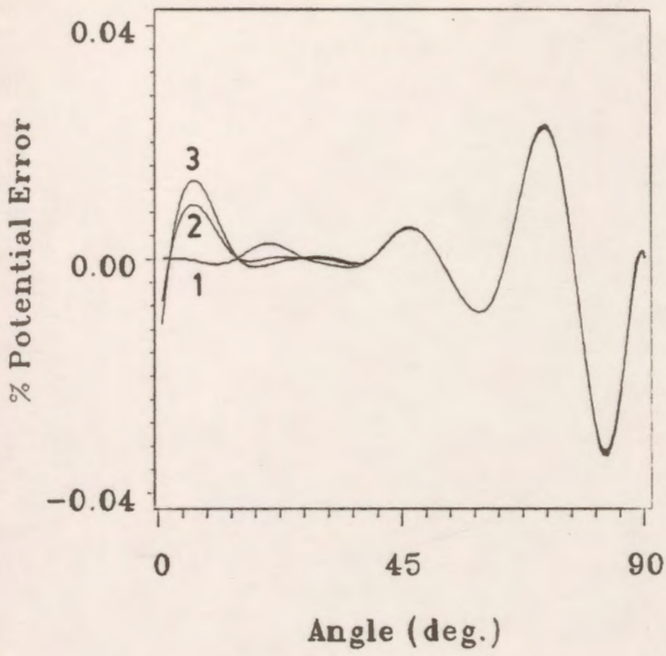(b) modelling two boundaries of the electrode

Figure 8.3: Distribution of errors (section A-B) using one set of modelling charges.
(a) potential error   (b) tangential field difference
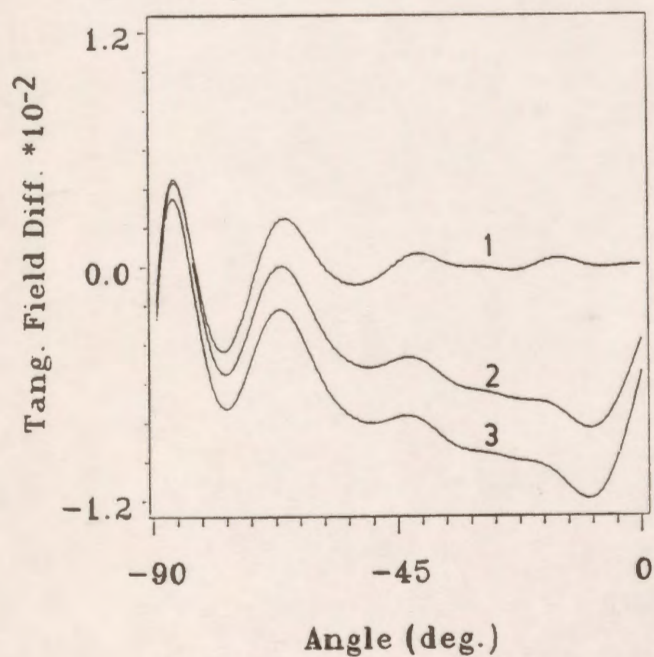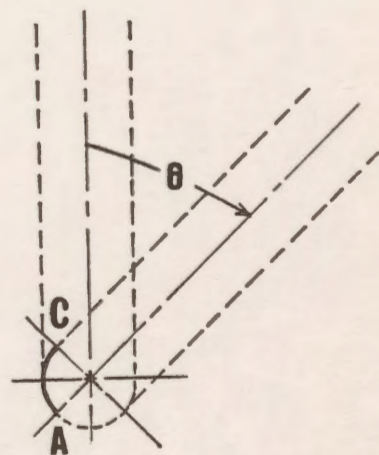(1) $\theta = 0°$ (2) $\theta = 45°$ (3) $\theta = 90°$
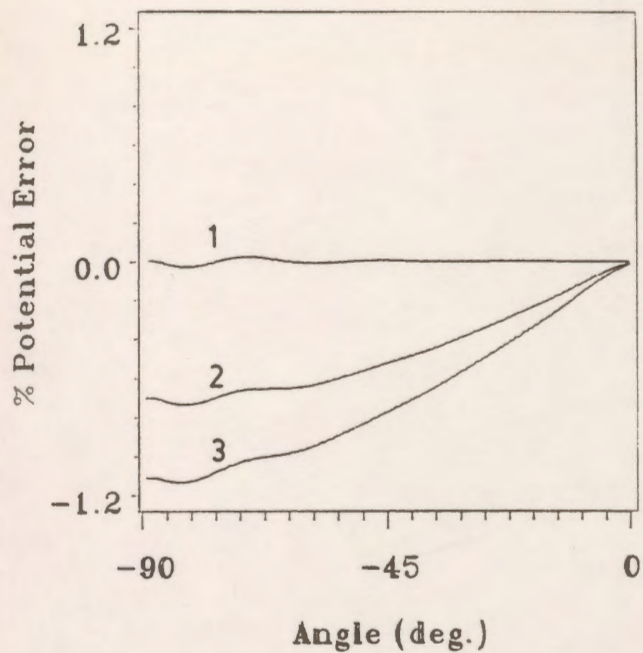
Figure 8.4: Distribution of errors (section A-C) using one set of modelling charges.
(a) potential error   (b) tangential field difference
(1) $\theta = 0°$ (2) $\theta = 45°$ (3) $\theta = 90°$

Fig. 8.5(a) and Fig. 8.5(b) represent the potential error and the tangential field difference distribution along the right section when using two sets of charges for modelling the right and the left sides of the electrode boundaries for different inclination angles. The maximum potential error and tangential field difference are 0.07% and 0.009 respectively at $\theta=90^{\circ}$. The same graphs are plotted for the left side section as shown in Figs. 8.6a and 8.6b and it is clear that the distribution of the potential and tangential field difference are different and much less than those obtained using only one set of charges. The maximum value of the potential error is 0.04% for θ $= 90^{\circ}$ in comparison with 1.2% in the first case.

8.2   Hemispherical Capped Rod and An Infinite Plane Having Another Rod

Another geometry which has several electrodes, each with a different axis of symmetry is considered in this section. This is a hemispherical capped electrode versus a plane with another hemispherical capped rod as shown in Fig. 8.7. The radii of both the electrodes are chosen as 0.01 m and denoted by R. The height of the lower capped electrode H is taken as 0.1 m. The effect of the gap distance (distance between the grounded plane and the upper electrode) G on the results is examined for two values, 0.1 m and 1.0 m. The lower electrode is located D meters along the Y axis apart from the centre (0, 0, 0) on the plane.

This system is modelled by using two sets of ring charges to model each electrode as discussed in the previous example. The upper electrode is held at 1.0 V and the lower electrode is held at 0 volts.

Figure 8.8 shows the field distribution near the upper electrode tip for two different values of the ratio G/R and three different spacings between the lower and upper electrodes. When G = 1 m, the lower rod of H = 0.1 m does not affect the field near the upper rod tip. It is clear from the graph that as the spacing between the electrodes decreases for G=0.1 m, the maximum electric field on the tip of the upper electrode increases and the location of that maximum is displaced toward the right in the direction of the lower hemispherical capped electrode.
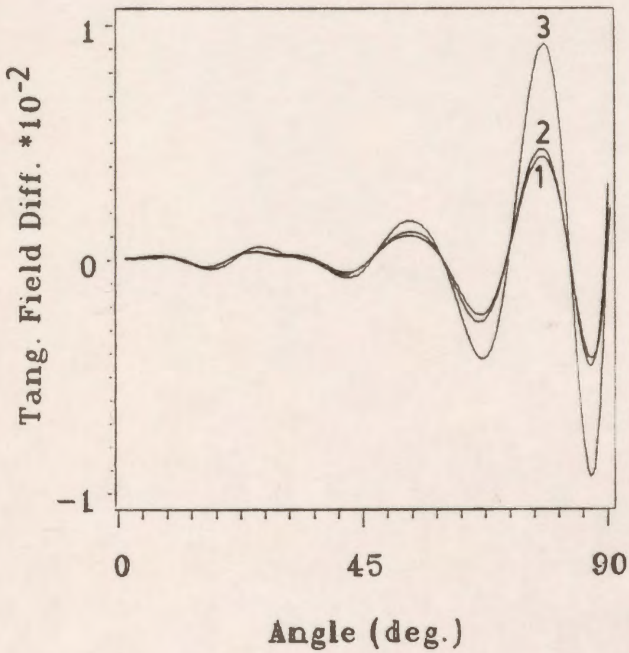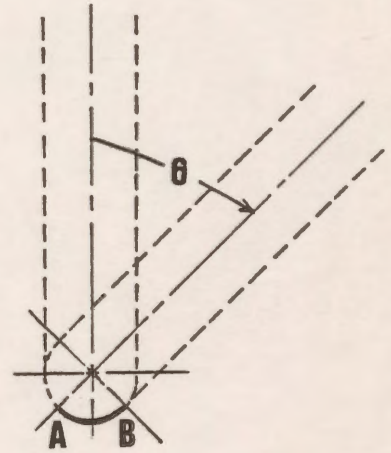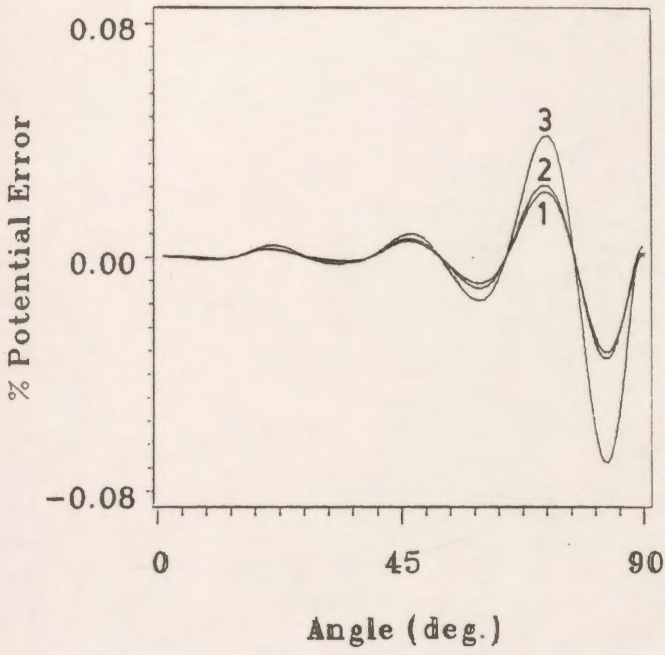
Figure 8.5: Distribution of errors (section A-B) using two sets of modelling charges.
(a) potential error   (b) tangential field error
(1) $\theta = 0°$ (2) $\theta = 45°$ (3) $\theta = 90°$

Figure 8.6: Distribution of errors (section A-C) using two sets of modelling charges.
   (a) potential error   (b) tangential field error
   (1) $\theta = 0°$ (2) $\theta = 45°$ (3) $\theta = 90°$
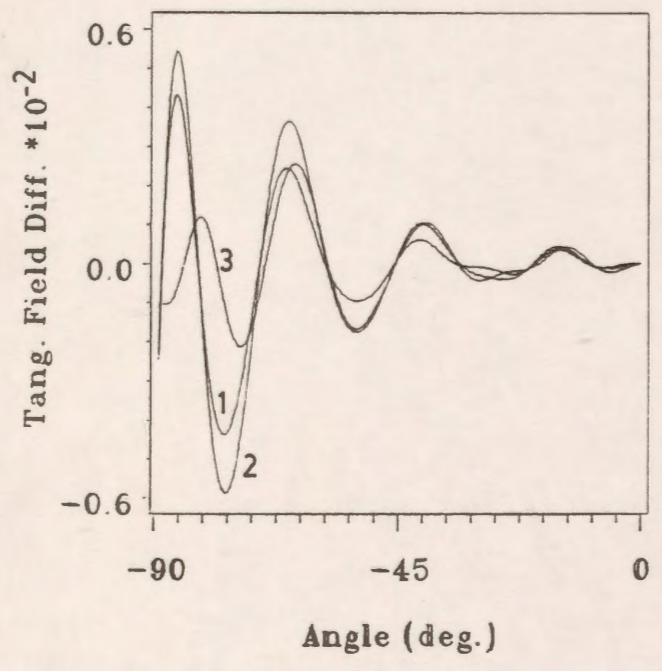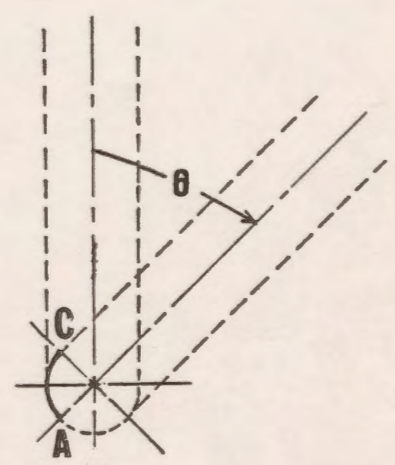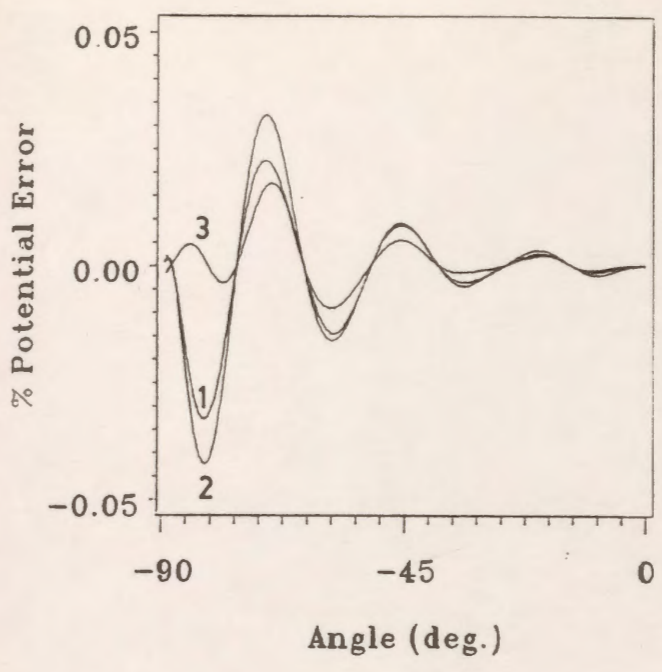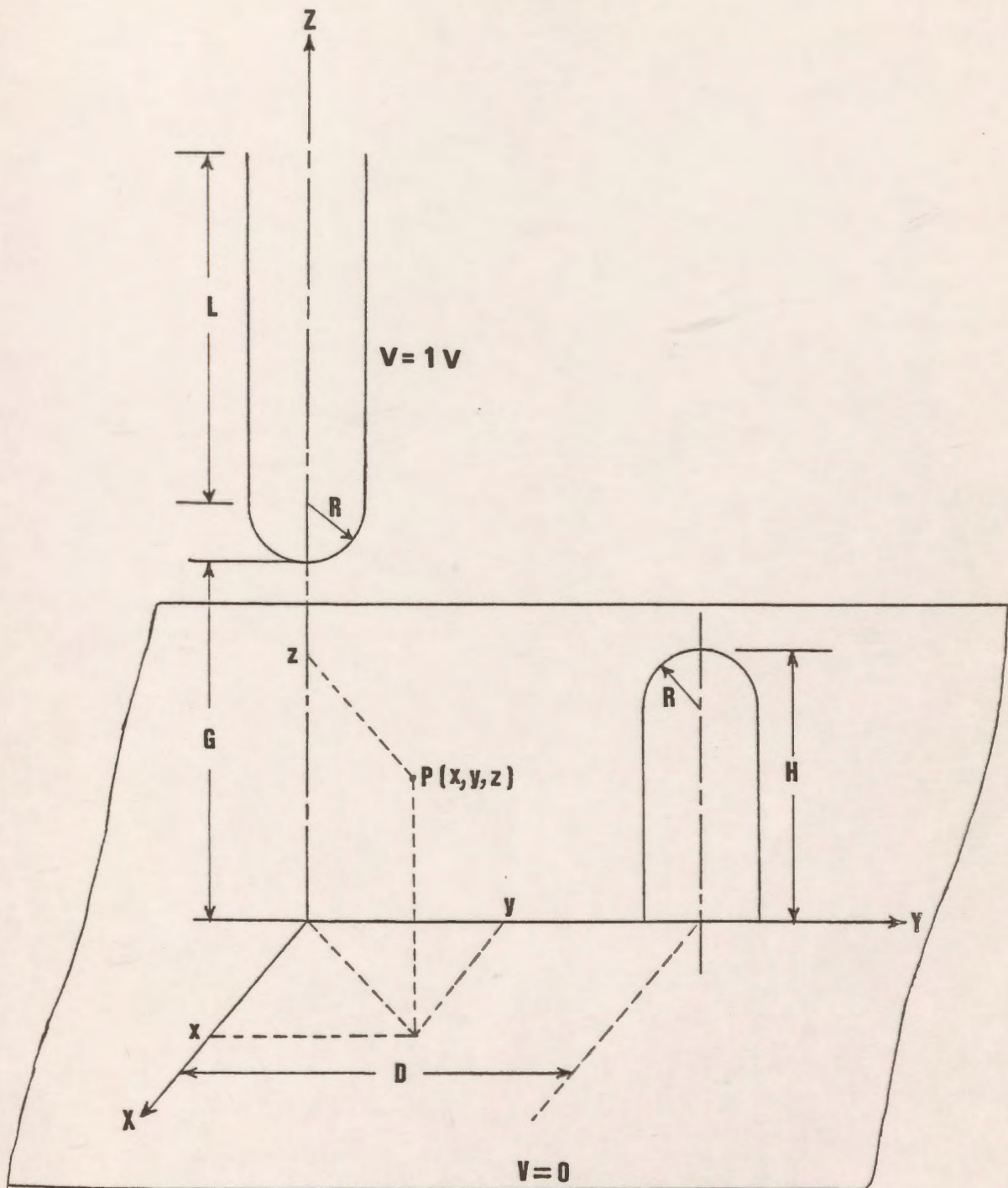
Figure 8.7: Hemispherical capped electrode and infinite grounded plane having another similar rod embedded.
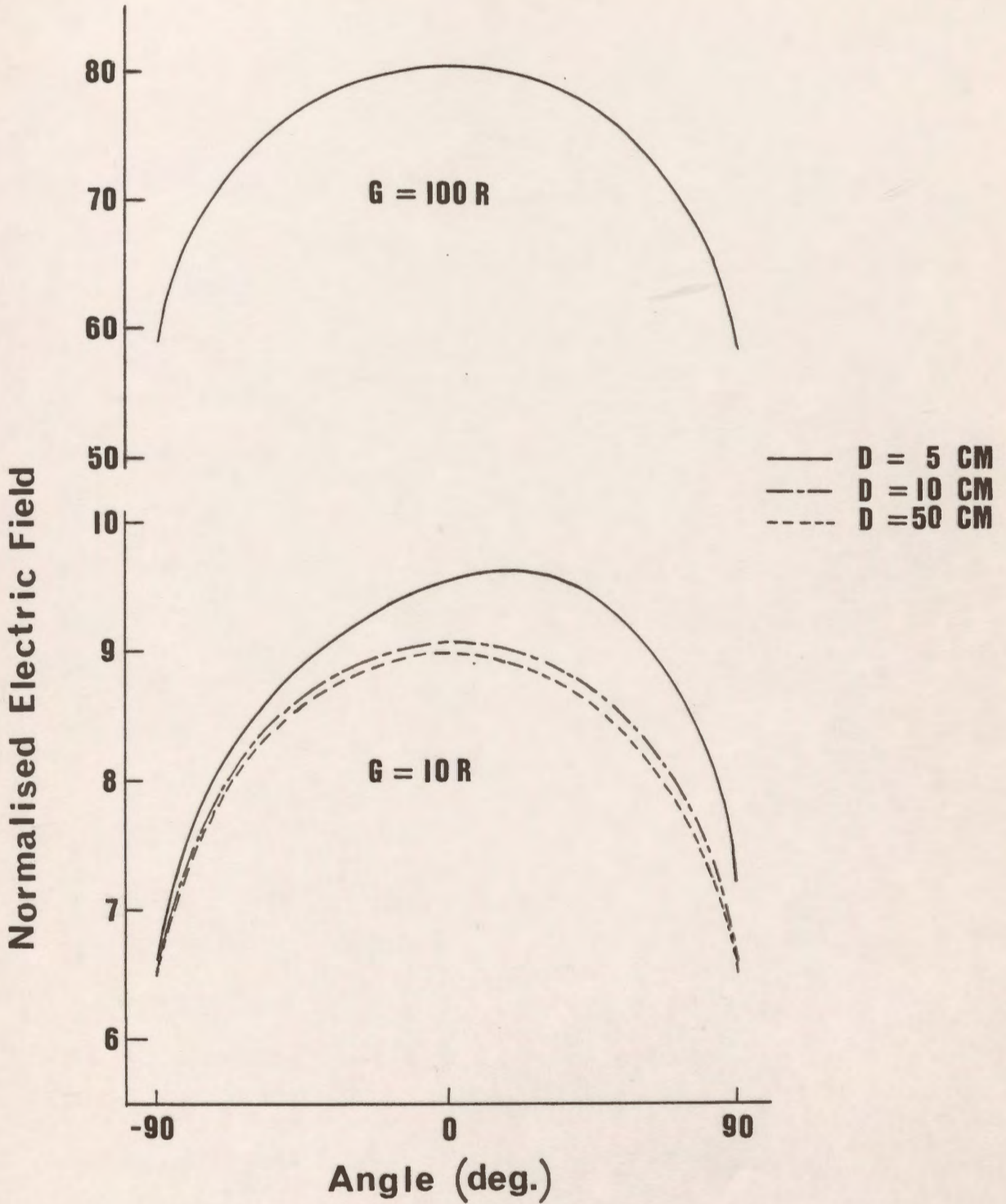
Figure 8.8: Electric field distribution around the hemispherical part of the upper rod for different values of D and G/R ratio.

8.3   *Triggering Electrode System With Non-Axial Symmetry*

The CAD package is applied with great advantage to the calculation of more complicated three-dimensional fields without axial symmetry. The chosen system here for the field analysis is a rod-rod gap with a trigger electrode as shown in Fig. 8.9. The original axial symmetry of the field of the two rods disappears because of the presence of the trigger electrode. The discharge at low voltage between the main electrodes is induced by the small-trigger discharge between the trigger electrode and one of the main electrodes [89].

The radius of the trigger electrode is varied from 0.1 to 0.5 cm in order to study its effect on the maximum electric field. The potential errors and tangential field differences are plotted for the different sections of the trigger electrode on which the maximum errors have been found to occur.

Figures 8.10(a) and 8.10(b) show the potential error and the tangential field difference along the upper hemispherical part of the trigger electrode (indicated by the heavy solid line segment) for a 0.2 cm radius of the trigger electrode. The maximum values of the errors are 0.07% and 0.023 for the percentage potential error and the tangential field difference respectively.

The potential error and the tangential field difference are also plotted for the upper cylindrical part of the trigger electrode (indicated by the heavy solid line segment) as shown in Fig. 8.11 with maximum values of 0.28% and 0.065 near the transition region of the hemispherical part and the cylindrical part.

The potential error and the tangential field difference along the lower two parts of the triggering electrode are shown in Fig. 8.12 and Fig. 8.13. The maximum recorded values of both errors are 0.07% and 0.024 and 0.36% and 0.08 for the hemispherical part and the cylindrical part respectively.

To check that the accuracy of the simulation is within acceptable limits, it is necessary to plot the errors along other sections which did not have boundary points specified.

$$R \quad = 1 \ \text{CM}$$
$$G \quad = 5 \ \text{CM}$$
$$R_t / R \ = 0.1 \sim 0.5$$
$$G_t \quad = 3 \ \text{CM}$$
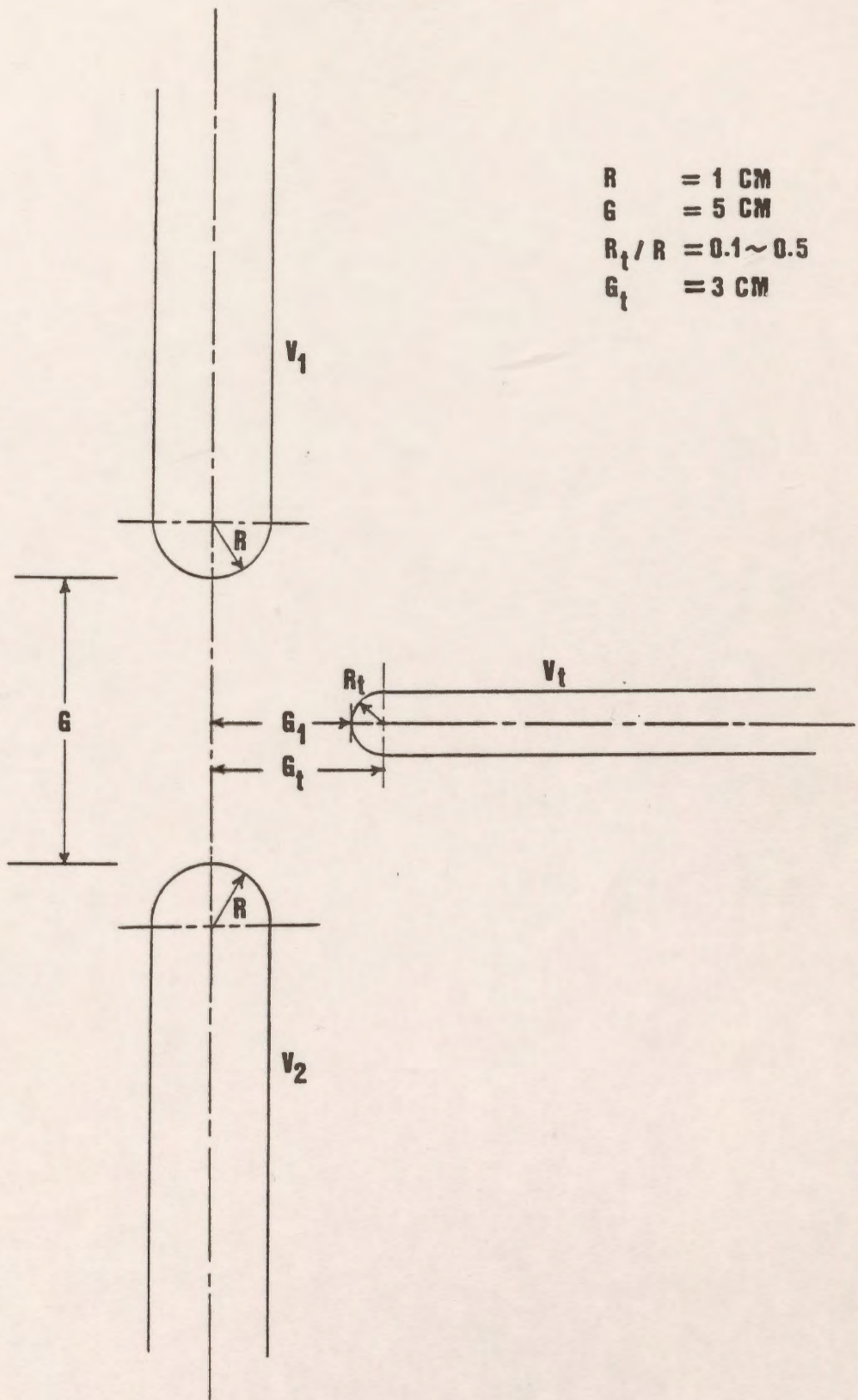
Figure 8.9: Triggering electrode system with non-axial symmetry.
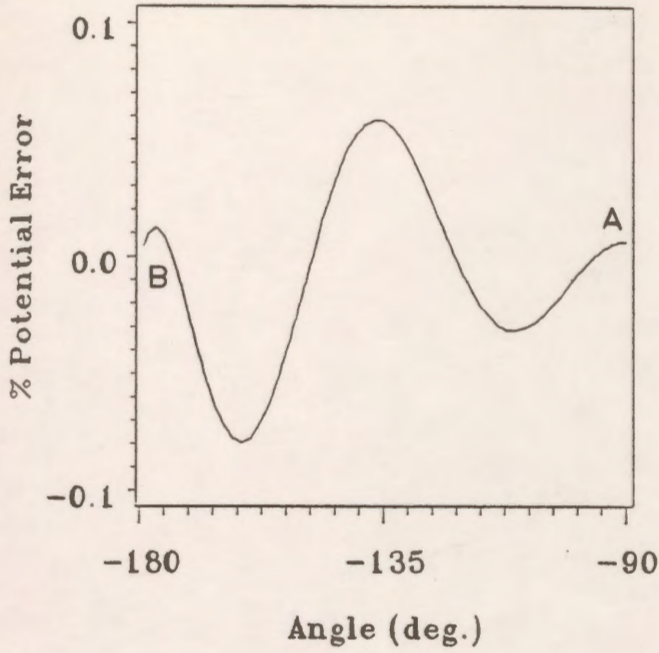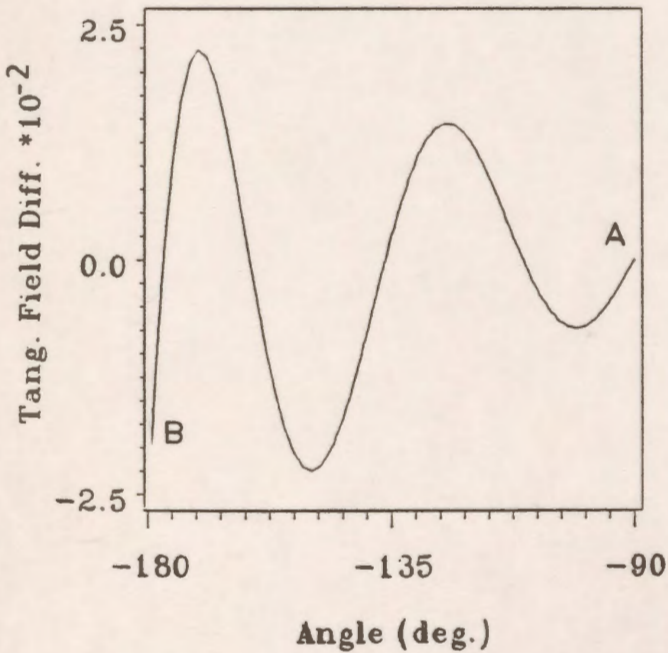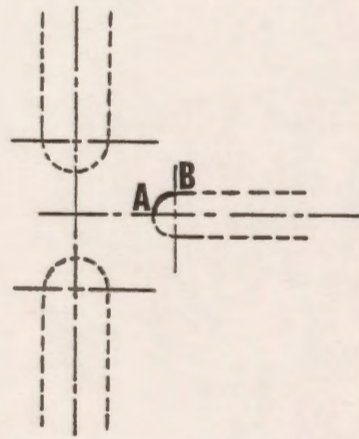
Figure 8.10: Distribution of errors (section A-B).
(a) potential error (b) tangential field difference
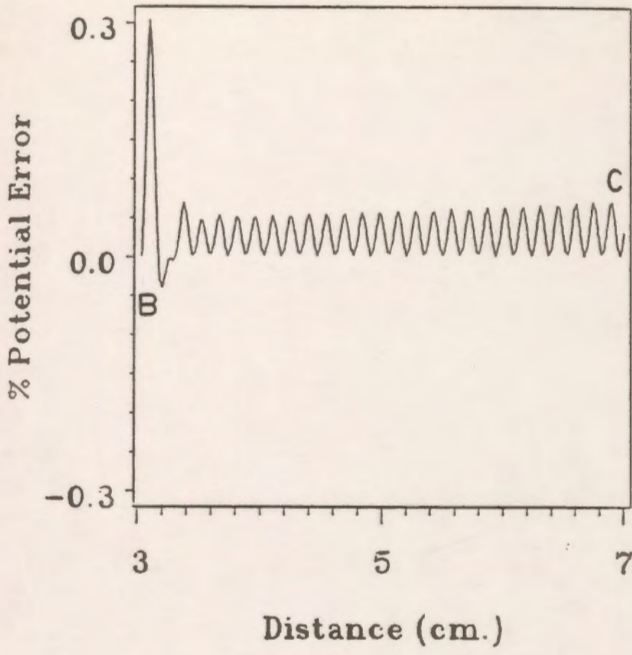
Figure 8.11: Distribution of errors (section B-C).
(a) potential error   (b) tangential field difference

Figure 8.12: Distribution of errors (section A-D).
(a) potential error   (b) tangential field difference

Figure 8.13: Distribution of errors (section D-E).
(a) potential error   (b) tangential field difference

Figs. 8.14(a) and 8.14(b) represent the potential error and the tangential field difference along the upper hemispherical part after rotation by 90° (the heavy line segment). It is felt that the errors are within acceptable limits. The potential error and the tangential field difference are also plotted for the top cylindrical part after rotation by 90° as shown in Fig. 8.15 and the maximum values of the errors are 0.35% and 0.08 and they occur near the transition region.

The electric field distribution around the spherical part of the trigger electrode where the maximum field is found to occur is shown in Fig. 8.16 for different trigger electrode voltages and constant applied voltages of 10 kV and 0 for the main electrodes. The undulating nature of the plots are due to the discrete nature of the simulating charges. It is clear from this figure that as we increase the triggering voltage the electric field increases everywhere along the surface of the electrode. It is also clear that for a 10 kV main gap voltage 10 kV is approximately required for the trigger electrode to initiate the breakdown assuming that the breakdown strength of the air is 30 kV/cm. These results are taken for a 0.2 cm radius of the trigger electrode.

Figure 8.17 shows the variation of the maximum electric field intensity on the spherical part of the trigger electrode with the trigger electrode voltage as a parameter for different radii of the trigger electrode and different applied voltages for the main electrode (the high voltage electrode). It can be seen from this figure that for a fixed applied voltage on the main electrode, the maximum field intensity increases with increasing triggering electrode voltage and decreasing radius.

The effect of the different parameters on the maximum value of the electric field intensity is summarized in Table 8.1. It seems from this Table that the radius of the trigger electrode strongly affects the maximum value of the electric field intensity. It is clear that a thinner triggering electrode will initiate the breakdown at a lower voltage than that of a thicker electrode. The table also shows the approximate voltage required to be applied to the trigger electrode to cause breakdown for each combination of the applied voltage on the main electrode and the radius of the trigger electrode.
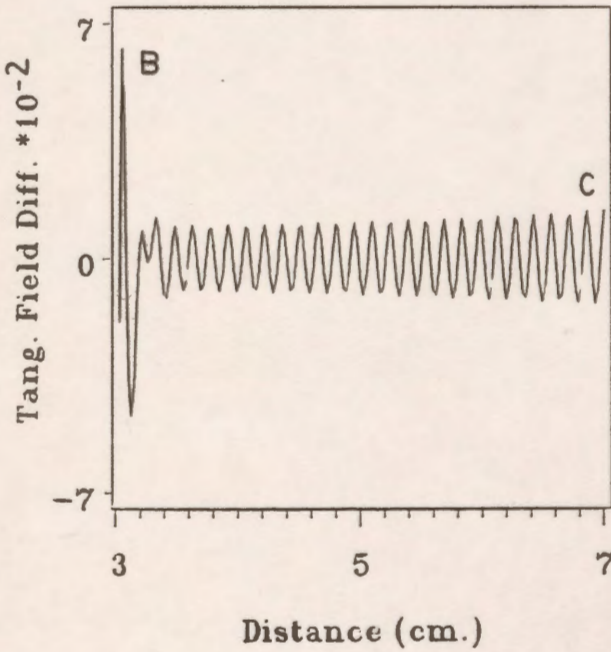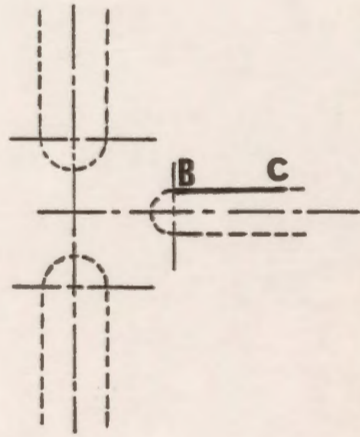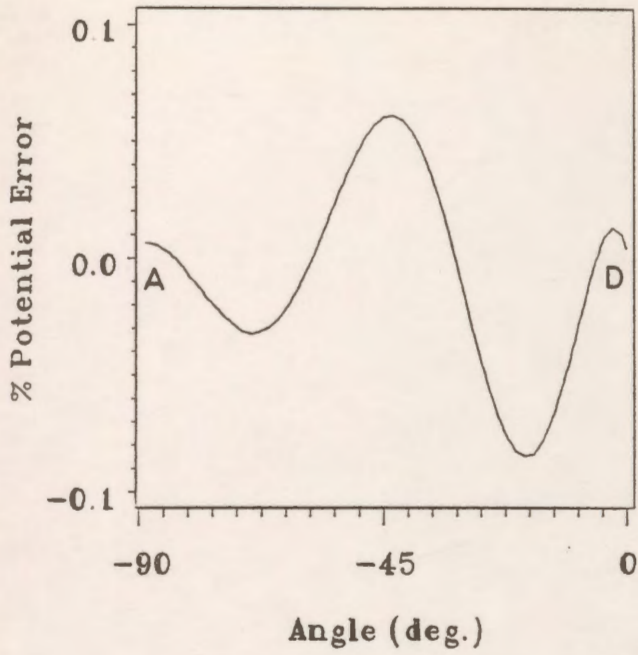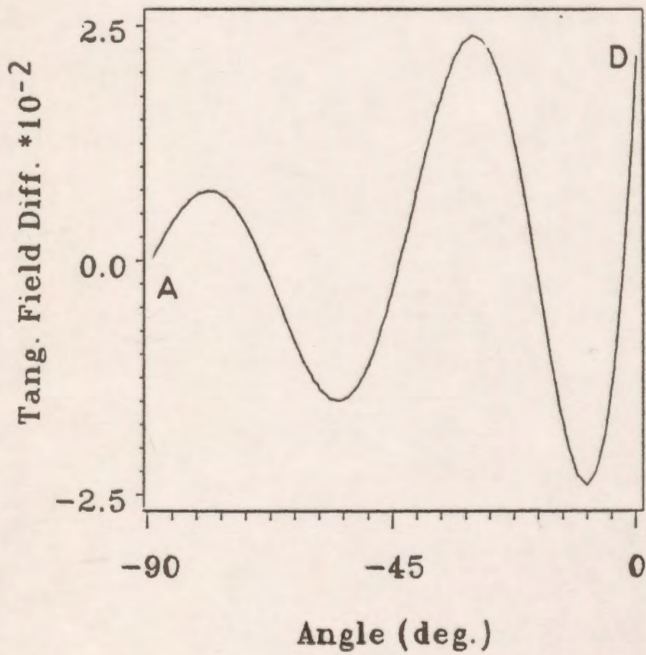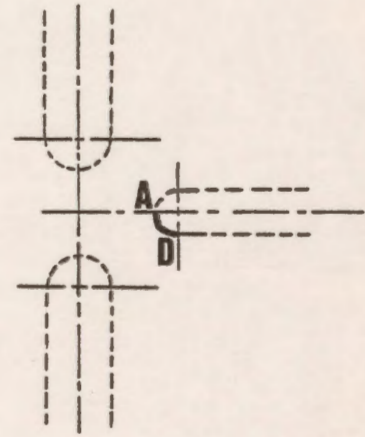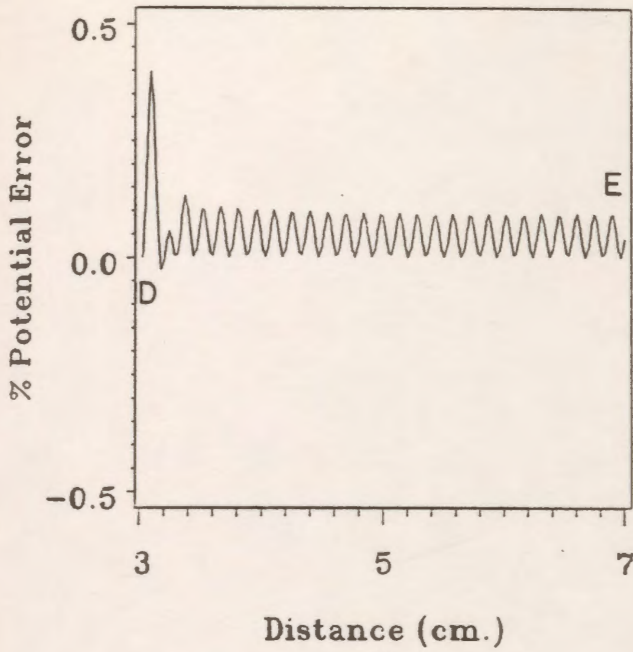
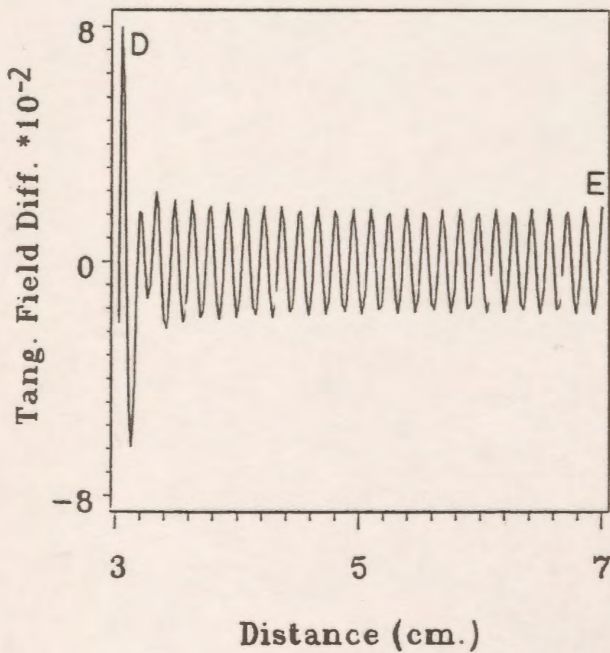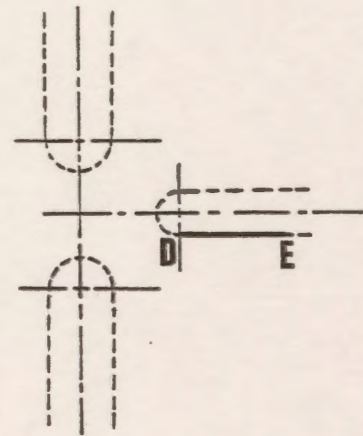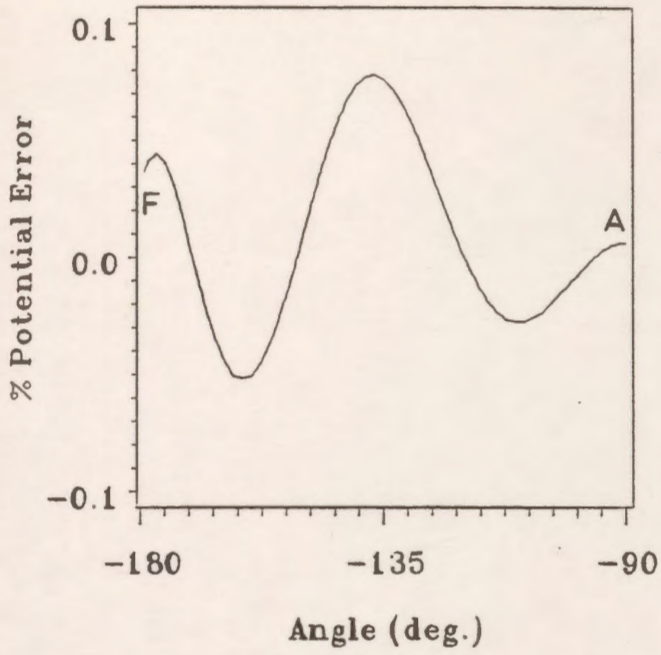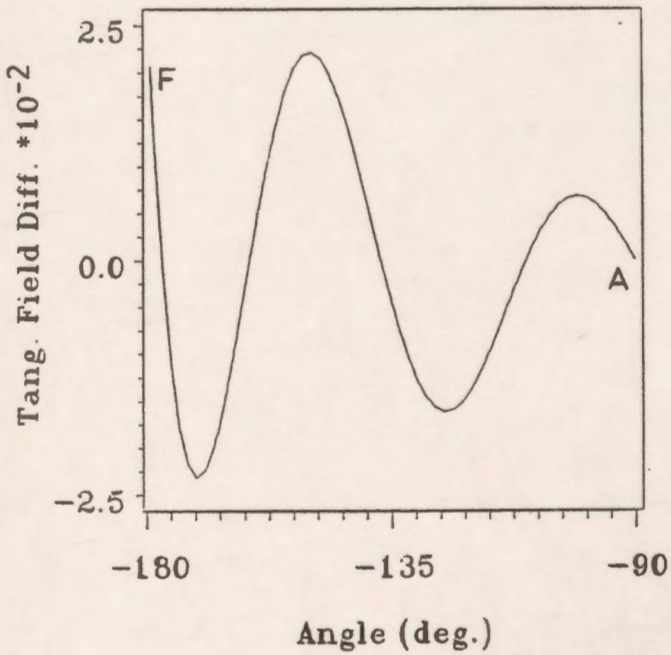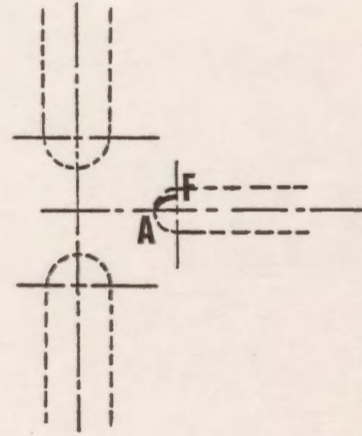*Figure 8.14*: Distribution of errors (section A-F).
(a) potential error   (b) tangential field difference
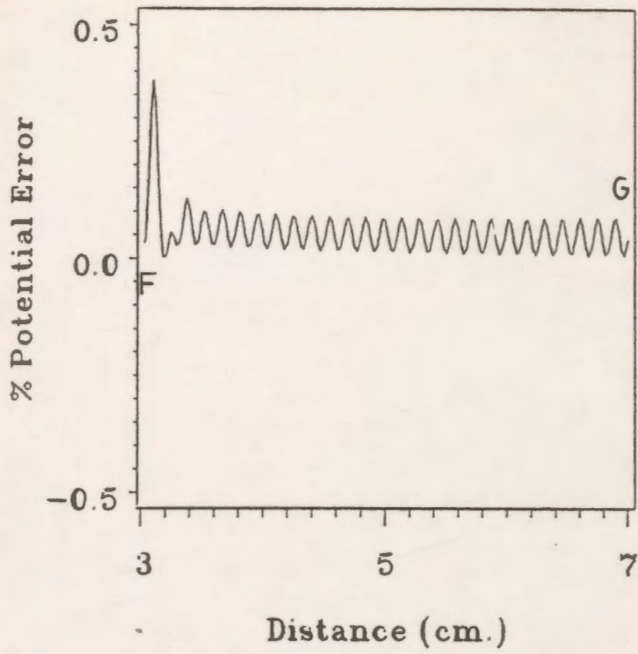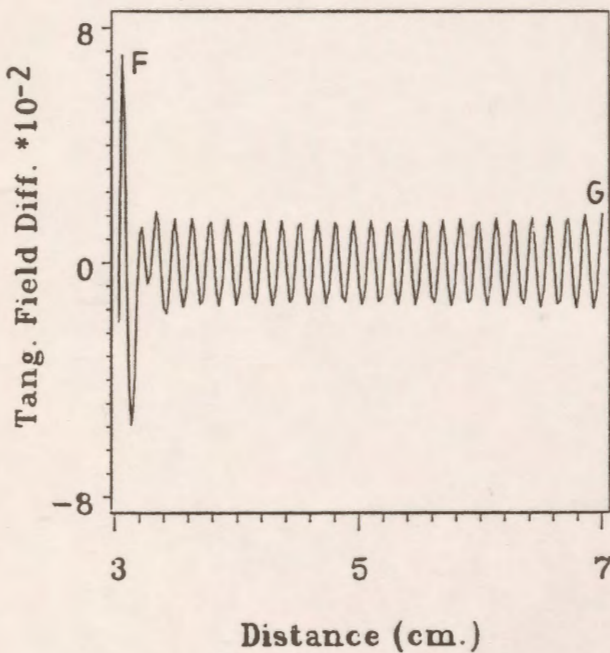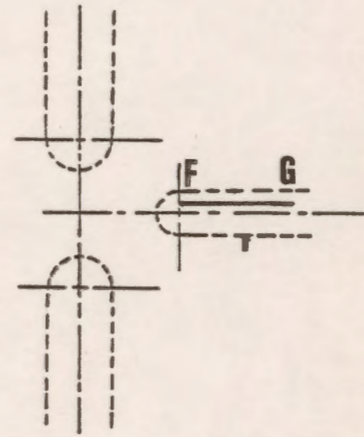
Figure 8.15: Distribution of errors (section F-G).
(a) potential error   (b) tangential field difference
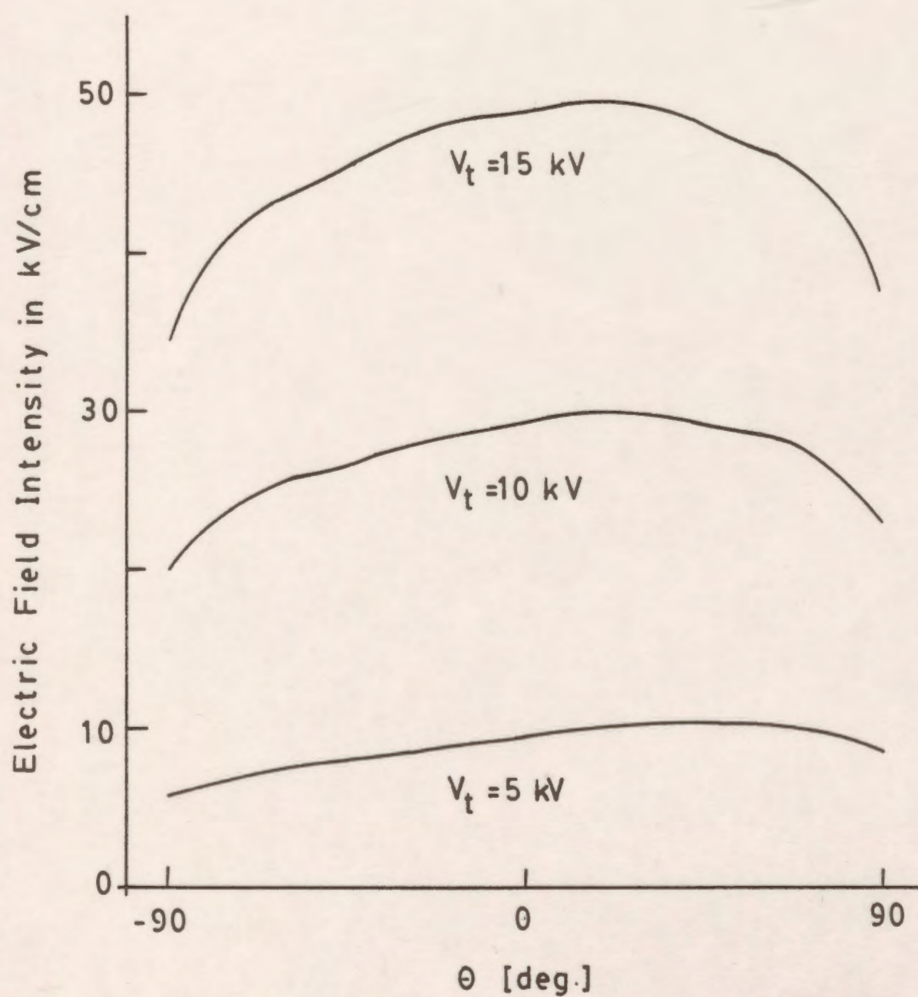
Figure 8.16: Variation of the electric field intensity around the hemispherical part of the trigger electrode for R_t / R=0.2 and V_1=10 kV.
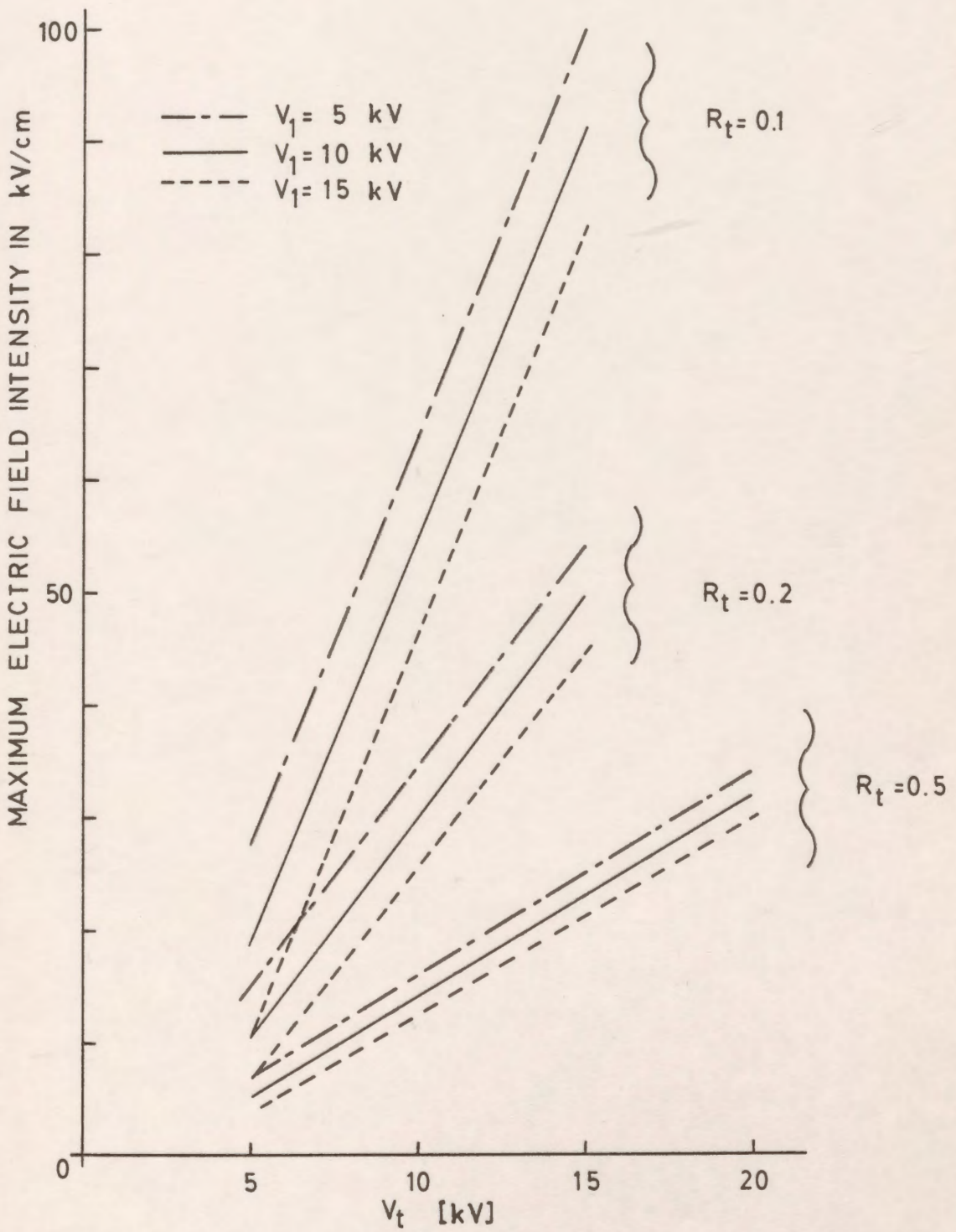
Figure 8.17: Variation of $E_{max.}$ with V_t for different values of V_1 and R_r.

Table 8.1: Effect of different parameters on the maximum value of the electric field intensity.

R_t/R	Applied voltage (kV)			Maximum electric field (kV/cm)			Approximate breakdown (kV)
	V_1	V_2	V_t	E_1	E_2	E_t	
	5	0	5	4.27	1.76	27.62	
			10	3.75	2.41	64.18	5.33
			15	3.24	3.06	100.80	
0.1	10	0	5	9.05	2.90	18.95	
			10	8.54	3.52	55.24	6.50
			15	8.02	4.16	91.78	
	15	0	5	13.84	4.07	10.92	
			10	13.32	4.63	46.47	7.67
			15	12.81	5.27	82.86	
	5	0	5	4.15	1.91	15.00	
			10	3.47	2.78	34.78	8.83
			15	2.80	3.71	54.57	
0.2	10	0	5	8.96	3.00	10.44	
			10	8.29	3.83	30.00	10.00
			15	7.62	4.67	49.76	
	15	0	5	13.78	4.14	6.64	
			10	13.11	4.90	25.35	11.17
			15	12.44	5.74	45.01	
	5	0	5	3.84	2.31	7.07	
			10	2.77	3.75	16.14	17.67
			15	1.71	5.23	25.27	
			20	1.32	6.70	34.42	
0.5	10	0	5	8.75	3.27	5.51	
			10	7.68	4.61	14.13	18.83
			15	6.61	6.03	23.17	
			20	5.54	7.50	32.28	
	15	0	5	13.65	4.29	4.14	
			10	12.59	5.58	12.45	20.00
			15	11.52	6.92	21.20	
			20	10.45	8.30	30.22	

Chapter IX

CONCLUSIONS AND SUGGESTIONS FOR FUTURE WORK

9.1   Conclusions

1.   An implementation of a Charge Simulation based CAD package for high voltage systems has been achieved.

2.   The application of the package to systems which contain single and two-dielectric regions was conducted without spending a significant amount of time defining the geometry for each specific system examined.

3.   The effect of different parameters controlling the charge simulation model has been studied and it was found that for best simulation the discontinuity in alignment of the simulating charges should be avoided. Also, the assignment factor and the number of modelling charges per unit length for best simulation has been found to be at 1.2 and 10, respectively.

4.   The results obtained in modelling the sphere/slab arrangement using the CAD package agreed very well with those obtained previously using the Finite Difference method.

5.   In the sphere/slab arrangement it was found that the maximum electric field strength occurs at the contact point for values of $\varepsilon_2/\varepsilon_1 \geq 1$ while it occurs away from the axis when $\varepsilon_2/\varepsilon_1 < 1$. It is also concluded that recessing the spherical electrode into the dielectric slab at $\varepsilon_2/\varepsilon_1 < 1$ increases the maximum field strength.

6.   The effect of varying the ratio G/R over a wide range on the field distribution for a sphere in contact with a plane slab is examined and it is concluded that as the ratio G/R increases the field around the sphere increases.

7. It is found that the structure of the field resulting from a charge simulation model has small spatial variations in amplitude which are consistent with the spacing of the discrete charges in the model. A manual inspection procedure was suggested to estimate the location of the field maxima.

8. For the rotationally symmetric triggering electrode system it is found that as the main gap distance G increases at fixed pilot gap distance g, the nonlinearity in the potential distribution increases and the most significant effect appears near the tip of the trigger pilot gap. It is also concluded that as G increases the normalized total electric field near the tip of the triggering electrode strongly increases.

9. It is found that varying the pilot gap distance g with G constant does not change the potential distribution except near the tip of the triggering electrode where the effect of the surrounding low voltage electrode is pronounced. The electric field near the tip of the triggering electrode decreases with an increase in the pilot gap distance g.

10. It is found that the maximum value of the total electric field does not necessarily occur on the main axial gap line or on the tip of the triggering electrode. The location of that maximum changes with both G and g, but always occurs on the hemispherical part of the triggering electrode.

11. The potential and field distributions for a 22 - shed polymer insulator without and using a grading ring are calculated. The effects of the different parameters of the guard ring were investigated and it was found that the guard ring has a great effect on linearizing the potential distribution along the insulator.

12. The solution for the field distribution in 3-dimensional systems with and without axial symmetry became more manageable using the CAD package.

13. The field for a tilted upper rod electrode versus a plane electrode was analyzed using the capabilities of the package for rotating and translating the simulated charges. It is found that the simulation quality measures (both the percentage potential error and the

tangential field error) resulting from modelling the two boundaries of the electrode are much better than in the case of modelling one boundary of the electrode.

14. The field for a hemispherical capped electrode versus grounded plane having another hemispherical capped rod was examined using the capabilities of the package for simulating systems of electrodes each having a separate axis of symmetry.

15. The package was applied to a complicated three-dimensional triggering system without axial symmetry and a thorough analysis of field distributions were presented for the first time.

16. More detailed graphical characterization of solution quality measures for the systems studied than have previously appeared in the literature have been presented.

17. The improvements in modelling assessment and presentation of results allow more comprehensive examination of electric field features to be conducted with a modest investment of time and effort. They also allow users to have greater confidence in the validity of CSM models developed for their systems.

9.2 Suggestions For Future Work

1. The accuracy of the Charge Simulation method is in fact dependent on the location of charges and the boundary points and on the density of charges. Therefore, it is suggested to extend the package to include optimization techniques in single and two dielectric systems to simplify the method to the degree of least dependency on the factors mentioned above.

2. Modification can be added to the package in order to include sinusoidal time-varying fields.

3. It is recommended that the package should be extended to model systems which have a space charge associated with it.

4.   For criteria related to, for example, minimizing the tangential electric field in a specified region, the shape of one of the interfaces defined for the model might be changed by the program package in such a way as to satisfy the criteria specified. This would be an invaluable tool for insulator shape design.

5.   A useful application of the package would be to an electric field sensor design.

6.   Some consideration can be given to modelling polymer insulators in a polluted environment by the Charge Simulation based CAD package.

7.   In grading the polymer insulator field distribution, only one guard ring was used near the high voltage conductor. The connections between the ring and the conductor were not modelled for simplicity. Thought can be given to using more than one guard ring and to modelling the connections between those rings and the conductors using the Charge Simulation method.

Appendix A

EXPRESSIONS FOR POTENTIAL AND FIELD STRENGTH IN

3-DIMENSIONAL SPACE

A.1   Point Charge
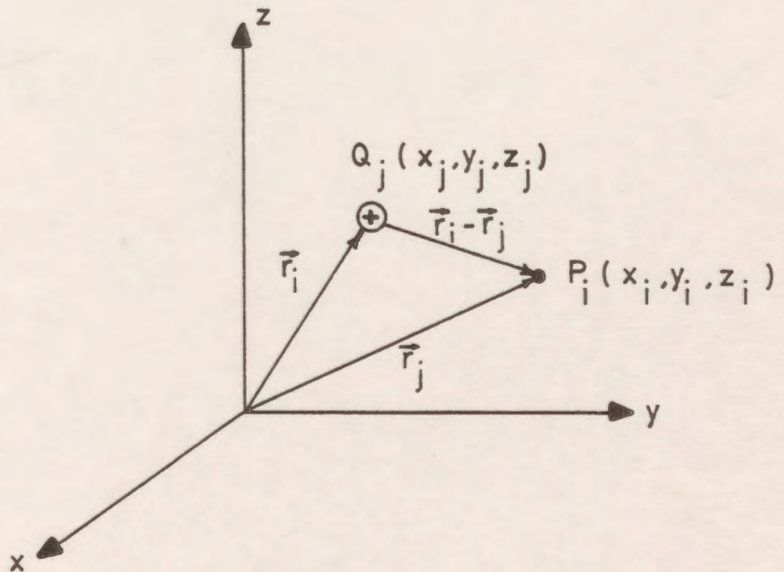
$$P_i = \frac{1}{4\pi\varepsilon_o} \sum_{j=1}^{n} \frac{Q_j}{|\vec{r}_i - \vec{r}_j|}$$

$$E_x = \frac{1}{4\pi\varepsilon_o} \sum_{j=1}^{n} \frac{Q_j (x_i - x_j)}{|\vec{r}_i - \vec{r}_j|^3}$$

$$E_y = \frac{1}{4\pi\varepsilon_o} \sum_{j=1}^{n} \frac{Q_j (y_i - y_j)}{|\vec{r}_i - \vec{r}_j|^3}$$

$$E_z = \frac{1}{4\pi\varepsilon_o} \sum_{j=1}^{n} \frac{Q_j (z_i - z_j)}{|\vec{r}_i - \vec{r}_j|^3}$$

A.2   Semiinfinite Line Charge
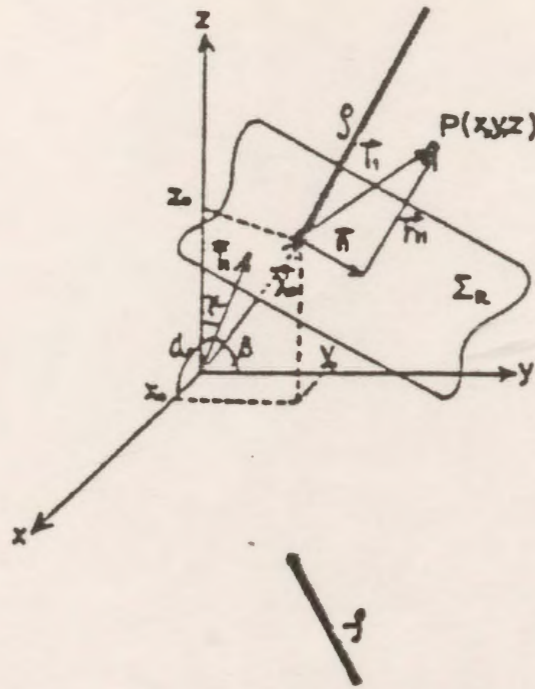
Consider an image charge of density $-\rho$ for the semi-infinite line charge of density ρ with respect to the x-y plane ($z = 0$). Denote by $(\cos\alpha, \cos\beta, \cos\gamma)$ the direction cosines of $\sum R$ where $\sum R$ is a plane normal to the line charge at point (x_o, y_o, z_o). Then the potential coefficient P_v at point P (x, y, z) is

$$P_v = \frac{1}{4\pi\varepsilon_o} \log_e \left\{ \frac{(l_2 - h_2)}{(l_1 - h_1)} \right\}$$

where

$$h_1 = (x - x_o)\cos\alpha + (y - y_o)\cos\beta + (z - z_o)\cos\gamma$$

$$h_2 = (x - x_o)\cos\alpha + (y - y_o)\cos\beta + (z + z_o)\cos\gamma$$

$$l_1 = \sqrt{(x - x_o)^2 + (y - y_o)^2 + (z - z_o)^2}$$

$$l_2 = \sqrt{(x - x_o)^2 + (y - y_o)^2 + (z + z_o)^2}$$

where ε_o is the permittivity of vacuum.

The x, y, and z components F_x, F_y, and F_z of the field coefficient at the point P are

$$F_x = \left(F_{r_1} / r_1 \right) \left(x - x_o - h_1 \cos\alpha \right) + \left(F_{r_2} / r_2 \right) \left(x - x_o - h_2 \cos\alpha \right)$$

$$F_y = \left(F_{r_1} / r_1 \right) \left(y - y_o - h_1 \cos\beta \right) + \left(F_{r_2} / r_2 \right) \left(y - y_o - h_2 \cos\beta \right)$$

$$F_z = \left(F_{r_1} / r_1 \right) \left(z - z_o - h_1 \cos\gamma \right) + \left(F_{r_2} / r_2 \right) \left(z + z_o - h_2 \cos\gamma \right)$$

where F_{r_1}, F_{r_2}, r_1, and r_2 are given by

$$F_{r_1} = r_1 / 4\pi\varepsilon_o l_1 (l_1 - h_1)$$

$$F_{r_2} = -r_2 / 4\pi\varepsilon_o l_2 (l_2 - h_2)$$

$$r_1^2 = l_1^2 - h_1^2, \qquad r_2^2 = l_2^2 - h_2^2$$

A.3   Finite Line Charge
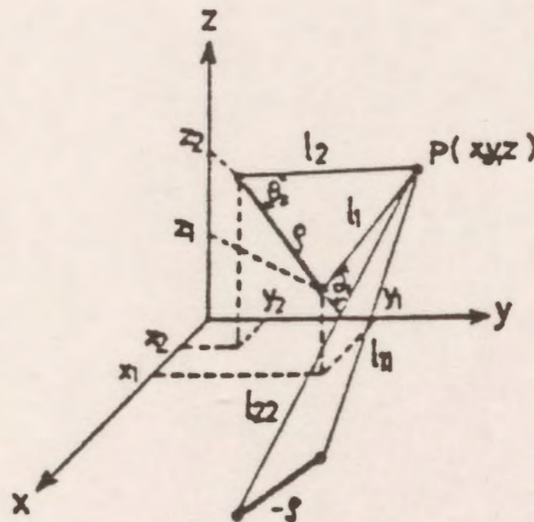
Consider a finite line charge of density ρ and length d with both ends at (x_1, y_1, z_1) and (x_2, y_2, z_2). The potential coefficient P_v at the point P (x, y, z) due to this charge and its image charge $-\rho$ with respect to the plane is

$$P_v = \frac{1}{4\pi\varepsilon_o} \log_e \left\{ \frac{(l_1 + l_2 + d)(l_{11} + l_{22} - d)}{(l_1 + l_2 - d)(l_{11} + l_{22} + d)} \right\}$$

where l_1, l_2, l_{11}, l_{22} and d are given by

$$l_1 = \sqrt{(x-x_1)^2 + (y-y_1)^2 + (z-z_1)^2}$$

$$l_2 = \sqrt{(x-x_2)^2 + (y-y_2)^2 + (z-z_2)^2}$$

$$l_{11} = \sqrt{(x-x_1)^2 + (y-y_1)^2 + (z+z_1)^2}$$

$$l_{22} = \sqrt{(x-x_2)^2 + (y-y_2)^2 + (z+z_2)^2}$$

$$d = \sqrt{(x_1-x_2)^2 + (y_1-y_2)^2 + (z_1-z_2)^2}$$

The x, y, and z components F_x, F_y, and F_z of the field coefficient at the point P are

$$F_x = \frac{1}{4\pi\varepsilon_o}\left\{\left(\frac{x-x_1}{l_1} + \frac{x-x_2}{l_2}\right)T_1 - \left(\frac{x-x_1}{l_{11}} + \frac{x-x_2}{l_{22}}\right)T_2\right\}$$

$$F_y = \frac{1}{4\pi\varepsilon_o}\left\{\left(\frac{y-y_1}{l_1} + \frac{y-y_2}{l_2}\right)T_1 - \left(\frac{y-y_1}{l_{11}} + \frac{y-y_2}{l_{22}}\right)T_2\right\}$$

$$F_z = \frac{1}{4\pi\varepsilon_o}\left\{\left(\frac{z-z_1}{l_1} + \frac{z-z_2}{l_2}\right)T_1 - \left(\frac{z-z_1}{l_{11}} + \frac{z-z_2}{l_{22}}\right)T_2\right\}$$

where T_1 and T_2 are given by

$$T_1 = \frac{1}{l_1+l_2-d} - \frac{1}{l_1+l_2+d}$$

$$T_2 = \frac{1}{l_{11}+l_{22}-d} - \frac{1}{l_{11}+l_{22}+d}$$

A.4   Ring Charge
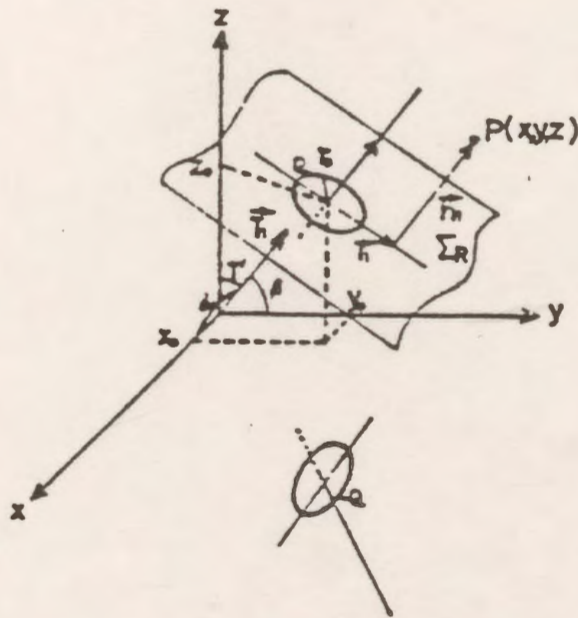
Consider a ring charge Q of radius r_o on the plane $\sum R$ (the directional cosines $\cos\alpha$, $\cos\beta$, $\cos\gamma$) with its center (x_o, y_o, z_o). The potential coefficient P_v of this charge Q and its image charge -Q due to the plane is

$$P_v = \frac{1}{2\pi^2 \varepsilon_o} \left(\frac{K(k_1)}{q_1} - \frac{K(k_2)}{q_2} \right)$$

where K(k) is the complete elliptic integral of the first kind; k_1, k_2, q_1, and q_2 are given by

$$k_1 = 4 r_o r_1 / q_1$$

$$k_2 = 4 r_o r_2 / q_2$$

$$q_1 = (r_o + r_1) + h_1$$

$$q_2 = (r_o + r_2) + h_2$$

where h_1, h_2, r_1, and r_2 are given by

$$h_1 = (x - x_o)\cos\alpha + (y - y_o)\cos\beta + (z - z_o)\cos\gamma$$

$$h_2 = (x - x_o)\cos\alpha + (y - y_o)\cos\beta + (z + z_o)\cos\gamma$$

$$r_1^2 = d_1^2 - h_1^2, \qquad r_2^2 = d_2^2 - h_2^2$$

where

$$d_1^2 = (x - x_o)^2 + (y - y_o)^2 + (z - z_o)^2$$

$$d_2^2 = (x - x_o)^2 + (y - y_o)^2 + (z + z_o)^2$$

The x, y, and z components of the field coefficient at P are given by

$$F_x = (F_{r_1} / r_1)(x - x_o - h_1 \cos \alpha) + (F_{r_2} / r_2)(x - x_o - h_2 \cos \alpha) + (F_{z_1} + F_{z_2}) \cos \alpha$$

$$F_y = (F_{r_1} / r_1)(y - y_o - h_1 \cos \beta) + (F_{r_2} / r_2)(y - y_o - h_2 \cos \beta) + (F_{z_1} + F_{z_2}) \cos \beta$$

$$F_z = (F_{r_1} / r_1)(z - z_o - h_1 \cos \gamma) + (F_{r_2} / r_2)(z + z_o - h_2 \cos \gamma) + (F_{z_1} - F_{z_2}) \cos \gamma$$

where F_{r_1}, F_{r_2}, F_{z_1} and F_{z_1} are given by

$$F_{r_1} = \frac{1}{4 \pi^2 \varepsilon_o r_1} \left\{ \frac{(r_o^2 - r_1^2 + h_1^2) E(k_1)}{q_1 s_1^2} - \frac{K(k_1)}{q_1} \right\}$$

$$F_{r_2} = \frac{1}{4 \pi^2 \varepsilon_o r_2} \left\{ \frac{(r_o^2 - r_2^2 + h_2^2) E(k_2)}{q_2 s_2^2} - \frac{K(k_2)}{q_2} \right\}$$

$$F_{z_1} = h_1 E(k_1) / 2 \pi^2 \varepsilon_o q_1 s_1^2$$

$$F_{z_2} = - h_2 E(k_2) / 2 \pi^2 \varepsilon_o q_2 s_2^2$$

$$s_1 = (r_1 - r_o)^2 + h_1^2$$

$$s_2 = (r_2 - r_o)^2 + h_2^2$$

where E(k) is the complete elliptic integral of the second kind.

Appendix B

DEFINITIONS OF SYMBOLS USED IN CHAPTER IV

The different symbols used in Figs. 4.1 and 4.2 and Tables (4.1), (4.2) and (4.3) are defined as:

R radius of the hemispherical part of the hemispherical electrode or radius of the sphere.

L length of the cylindrical part of the hemispherical capped electrode or length of the dielectric slab.

G gap distance or thickness of the dielectric slab.

n_{ptot} number of total points defining the system

n_{stot} total number of sections which define the system

ε_r relative dielectric constant of the insulator

n_s defines the number of the section

i index for all points defining the geometry

x_i defines the x-coordinate of each point

y_i defines the y-coordinate of each point

z_i defines the z-coordinate of each point

$n_{p(ns)}$ number of points defining each section

$REX_{(ns)}$ displacement of the x-axis of section number ns from the x-reference axis

$REY_{(ns)}$ displacement of the y-axis of section number ns from the y-reference axis

$REZ_{(ns)}$ displacement of the z-axis of section number ns from the z-reference axis

V_{ns} specified potential of each section

$K_{p(ns)}$ index defining the type of interface section (air/dielectric or interface)

$K_{z(ns)}$ index defining the type of charges used in each section

$K_{s(ns)}$ index defining the position of each section with respect to the different axis

$\alpha_{j(ns)}$ the assignment factor for each section

$n_{b(ns)}$ number of boundary points used for each section

Appendix C

TRANSFORMATIONS IN THE THREE-DIMENSIONAL SPACE

C.1   Translation

In a three-dimensional homogeneous coordinate representation, a point is translated from position (x, y, z) to position (x', y', z') with the matrix operation (Fig. C.1)

$$
\begin{bmatrix} x' \\ y' \\ z' \end{bmatrix} = \begin{bmatrix} 1 & 0 & 0 \\ 0 & 1 & 0 \\ 0 & 0 & 1 \end{bmatrix} \begin{bmatrix} x \\ y \\ z \end{bmatrix} + \begin{bmatrix} T_x \\ T_y \\ T_z \end{bmatrix}
\tag{C-1}
$$

Parameters T_x, T_y, T_z, specifying translation distances from the coordinate axes, are assigned any real values. The matrix representation in Eq. (C-1) is implemented in the package in terms of its equivalent three equations as

$$
x' = x + T_x
$$

$$
y' = y + T_y
\tag{C-2}
$$

$$
z' = z + T_z
$$

An electrode is translated in three dimensions by transforming each point used to define the electrode.

We obtain the inverse of the translation matrix in Eq. (C-1) by negating the translation distances T_x, T_y, and T_z.
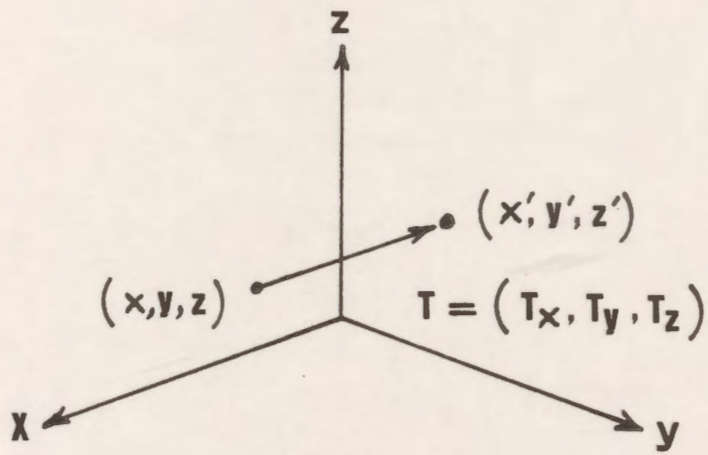
Figure C.1: Translating a point with translation vector (T_x, T_y, T_z).
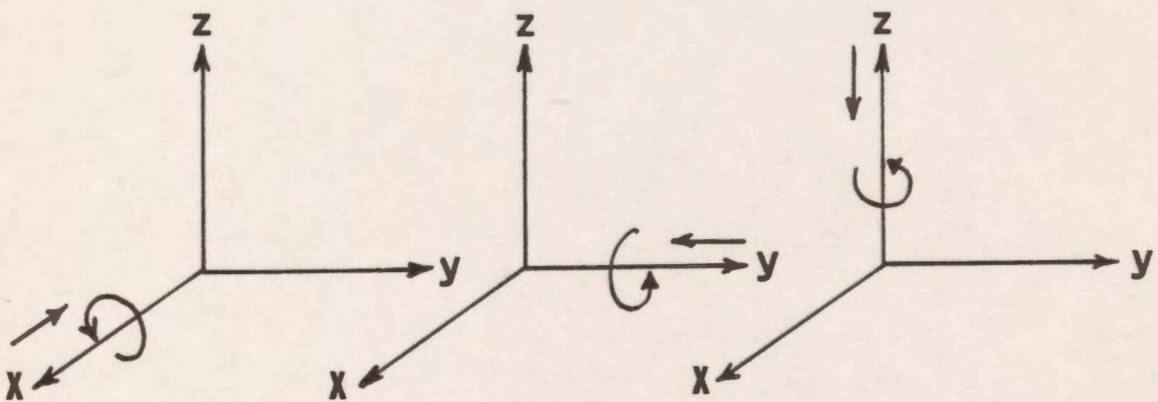

Figure C.2: Rotation of a point around the different axis

C.2   *Rotation*

To specify a rotation transformation for an electrode, we must designate an axis of rotation (about which the electrode is to be rotated) and the amount of angular rotation. For two-dimensional applications, the axis of rotation is always perpendicular to the y-z plane. In three dimensions, an axis of rotation can have any spatial orientation. The easiest rotation axes to handle are those that are parallel to the coordinate axis.

In the package, we adopt the convention that counterclockwise rotations about a coordinate axis are produced with positive rotation angles, if we are looking along the positive half of the axis toward the coordinate origin as shown in Fig. C.2.

In coordinate form, the three-dimensional x-axis rotation equations are expressed as

$$[x'\ y'\ z'] = [x\ y\ z] \begin{bmatrix} 1 & 0 & 0 \\ 0 & \cos\theta & \sin\theta \\ 0 & -\sin\theta & \cos\theta \end{bmatrix} \tag{C-3}$$

Parameter θ specifies the rotation angle. This matrix form can be described in three equations as

$$x' = x$$
$$y' = y\cos\theta - z\sin\theta \tag{C-4}$$
$$z' = y\sin\theta + z\cos\theta$$

The transformation matrix for the y axis rotation is given by

$$[x'\ y'\ z'] = [x\ y\ z] \begin{bmatrix} \cos\theta & 0 & -\sin\theta \\ 0 & 1 & 0 \\ \sin\theta & 0 & \cos\theta \end{bmatrix} \tag{C-5}$$

Which can be represented by three equations as

$$x' = z\sin\theta + x\cos\theta$$
$$y' = y \tag{C-6}$$
$$z' = z\cos\theta - x\sin\theta$$

Also the transformation matrix for the z axis rotation is given by

$$[x'\ y'\ z'] = [x\ y\ z] \begin{bmatrix} \cos\theta & \sin\theta & 0 \\ -\sin\theta & \cos\theta & 0 \\ 0 & 0 & 1 \end{bmatrix} \tag{C-7}$$

Which can be represented by three equations as

$$x' = x \cos \theta - y \sin \theta$$

$$y' = x \sin \theta + y \cos \theta \qquad \text{(C-8)}$$

$$z' = z$$

An inverse rotation matrix is formed by replacing the rotation angle θ by $-\theta$. Negative values for rotation angles generate rotations in a clockwise direction.

Electrodes can be rotated about any arbitrary selected axis by applying a composite transformation matrix whose components perform a sequence of translations and rotations about the coordinate axes. This composite matrix is formed from a combination of the translation matrix (Equation C-1) and transformations C-3, C-5, C-7. The correct sequence of transformations can be determined by transforming coordinate positions of the electrode so that the selected rotation axis is moved onto one of the coordinate axis. Then the electrode is rotated about that coordinate axis through the specified rotation angle. The last step is to apply inverse transformations that return the rotation axis to its original position.

In the special case where the selected rotation axis is parallel to one of the coordinate axis, the desired rotation of the electrode is attained with the equivalent set of three transformations:

1.   Translate the electrode so that the rotation axis coincides with the parallel coordinate axis.

2.   Perform the specified rotation.

3.   Translate the electrode so that the rotation axis is moved back to its original position.

Appendix D

CHEBYSHEV DISTRIBUTION

For the interval [a,b], the Chebyshev distribution of points are defined to be

$$x_k = \frac{a+b}{2} + \frac{a-b}{2} \cos\left(\frac{2k-1}{2n}\pi\right)$$

for k = 1, 2, ... , n Figure D.1 shows the distribution of Chebyshev points for n = 10 on the interval [-1,1].
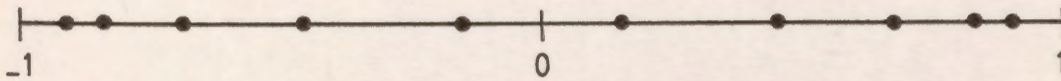
Figure D.1: Distribution of Chebyshev points.

Appendix E

CONSTRUCTION OF A CUBIC SPLINE SCHEME

The construction of a cubic spline interpolatory scheme can be described as follows:

Let $(x_1, f_1), (x_2, f_2), \ldots , (x_n, f_n)$ be the given data of points.

On each subinterval $[x_i, x_{i+1}]$, a cubic spline S(x) has the form

$$S_i(x) = a_i + b_i(x - x_i) + c_i(x - x_i)^2 + d_i(x - x_i)^3$$

$(i = 1, 2, \ldots , n\text{-}1)$

where the coefficients a_i, b_i, c_i, and d_i are to be determined from the definition of cubic splines and interpolatory requirement.

Continuity and interpolation requires that

$$S_i(x_{i+1}) = f_{i+1} = S_{i+1}(x_{i+1})$$

Since cubic splines are twice differentable at the nodes x_{i+1}, therefore

$$S'_i(x_{i+1}) = S'_{i+1}(x_{i+1})$$

$$S''_i(x_{i+1}) = S''_{i+1}(x_{i+1})$$

The conditions $S''_i(a) = S''_{n-1}(b) = 0$ are customarily introduced, and a cubic spline is thereby determined.

Appendix F

POTENTIAL AND TANGENTIAL FIELD ERRORS ALONG THE

ELECTRODE SURFACE OF FIGURE 6.2.
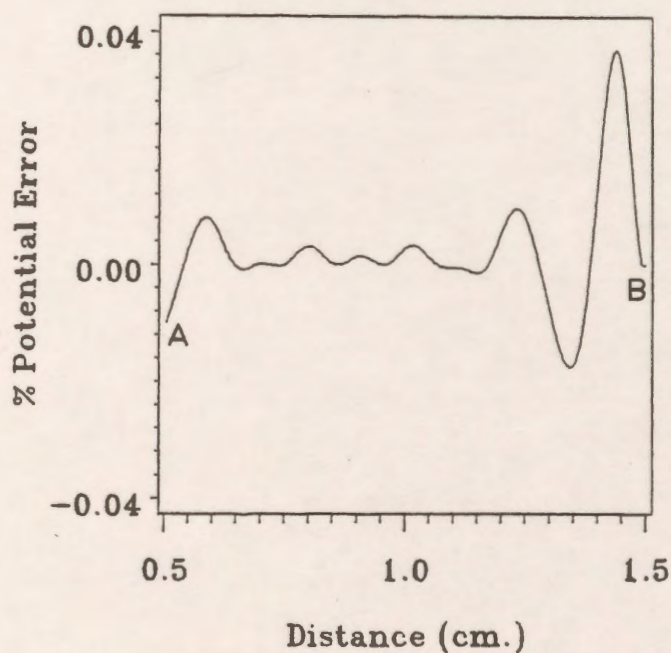
Figure F.1: Potential error distribution along the horizontal part of the electrode of Fig. 6.2.
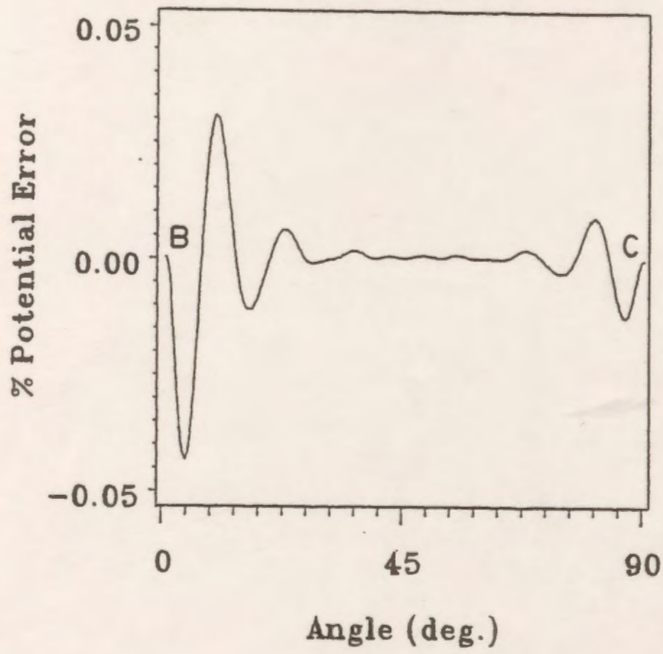
Figure F.2: Potential error distribution along the curved part of the electrode of Fig. 6.2.

Figure F.3: Potential error distribution along the vertical part of the electrode of Fig. 6.2.

Figure F.4: Tangential field difference distribution along the horizontal part of the electrode of Fig. 6.2.
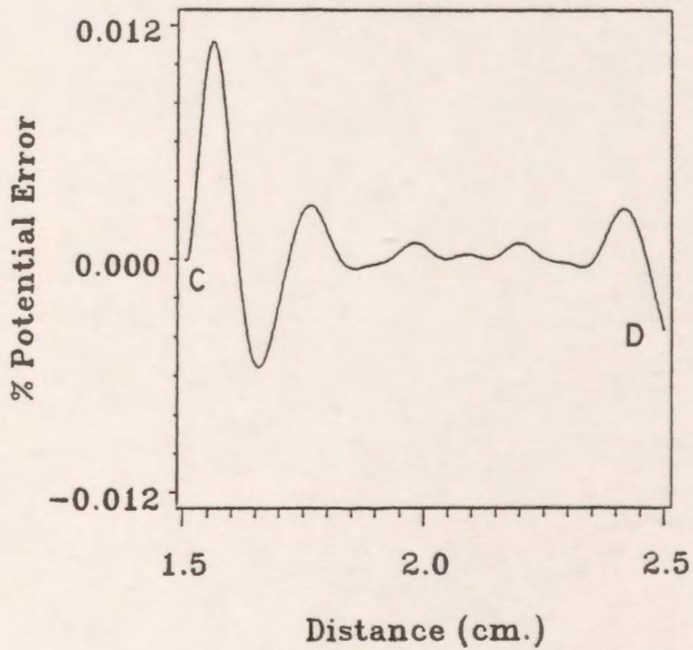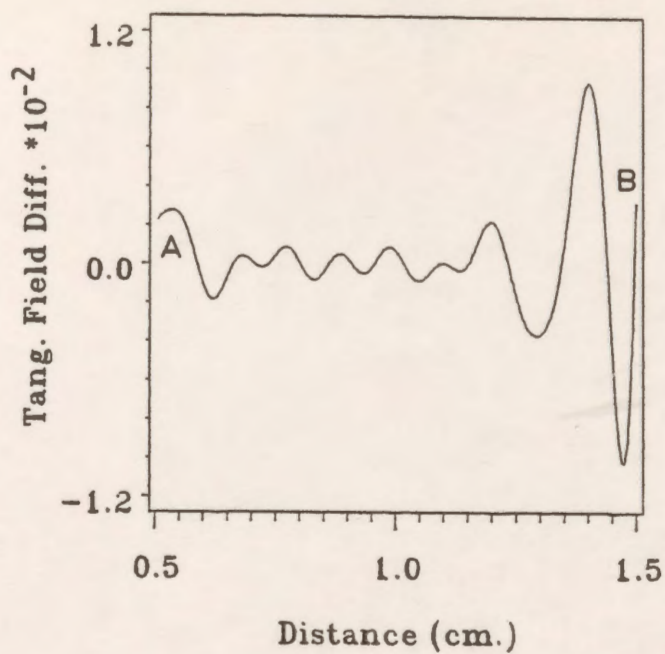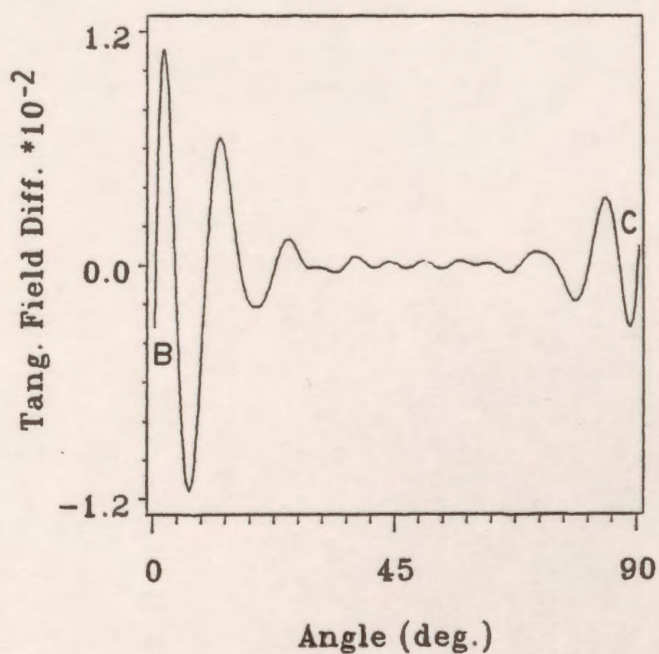

Figure F.5: Tangential field difference distribution along the curved part of the electrode of Fig. 6.2.
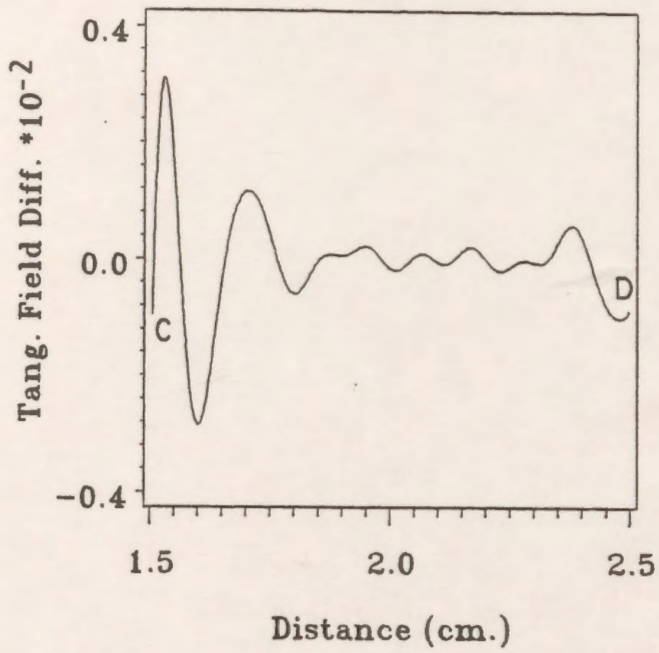
Figure F.6: Tangential field difference distribution along the vertical part of the electrode of Fig. 6.2.

REFERENCES

1.   M. S. Abou-Seada and E. Nasser, "Digital computer calculation of electric potential and field of rod gaps", Proc. IEEE, Vol.56, No.5, 1968, pp.813-820.

2.   E. Kuffel and W. S. Zaengl, "High voltage engineering", Pergamon Press, (1984).

3.   E. Nasser, "Fundamentals of gaseous ionization and plasma electronics" (Wiley-Interscience,1971), chap.11

4.   M. J. Kofoid, "Phenomena at the Metal-Dielectric Junctions of High-Voltage Insulators in Vacuum and Magnetic Field", AIEE. Trans. (Power APP. and Syst.), Vol. 79, pp.991-999, Dec. 1960.

5.   M. J. Kofoid, "Effect of Metal-Dielectric Junction Phenomena on High Voltage Breakdown Over Insulators in Vacuum", AIEE. Trans. (Power APP. and Syst.) Vol. 79, pp.999-1004, Dec. 1960.

6.   C. H. DeTourreil and K. D. Srivastava, "Mechanism of surface charging of high-voltage insulators in vacuum", IEEE Trans. Elec. Ins., Vol. EI-8, pp. 17-21 (1973).

7.   N. G. Trinh, F. A. M. Rizk, and C. Vincet, IEEE Trans. Power Appar. Syst. PAS-99, 2164(1980).

8.   W. H. Hayt, "Engineering electromagnetics", Mcgraw-Hill, (1967).

9.   R. H. Galloway, H. M. C. L. Ryan and M. F. Scott, "Calculation of electric fields by digital computer", Proc. IEE, Vol. 114 pp. 824-829 (1967).

10.   D. F. Binns and T. J. Randall, " Calculation of potential gradients for a dielectric slab placed between a sphere and a plane", Proc. IEE, Vol. 114, pp. 1521-1528 (1967).

11.   I. A. Cermak and P. Silvester, "Solution of 2-Dimensional Field Problems by Boundary Relaxation", Proc. IEE, Vol. 115, pp.1341-1348 (1968).

12.   J. T. Storey and M. J. Billings, "Determination of the 3-Dimensional Electrostatic Field in A curved Bushing", Proc. IEE, Vol. 116, pp. 639-643 (1969).

13.   J. T. Storey, "The determination of axially symmetric fields by digital computation", IEEE Trans. Elec. Ins., Vol. EI-4, pp. 23-30 (1969).

14.   I. A. Cermak and P. Silvester, "Boundary-relaxation analysis of rotationally symmetric electric field problems", IEEE Trans., Vol. PAS- 89, pp. 925-932 (1970).

15.   J. M. Mattingley and M. H. Ryan, "Potential and Potential Gradient Distributions for Standard and Practical Electrode Systems", Proc. IEE, Vol. 118, pp. 720-732 (1971).

16.	H. M. Ryan, J. M. Mattingley and M. F. Scott, "Computation of electric field distributions in high voltage equipment", IEEE Trans. Elect. Insul., Vol. EI-6, pp. 148-154, 1971.

17.	S. I. Bektas, O. Farish and M. Hizal, "Computation of Electric field at a solid/gas interface in the presence of surface and volume charges", Proc. IEE, Vol. 133, pp. 577-586 (1986).

18.	O. W. Andersen, "Finite element solution of complex potential electric fields", IEEE Trans. PAS, Vol. PAS-96, pp. 1156-1161 (1977).

19.	P. P. Silvester, D. A. Lowther, C. J. Carpenter and E. A. Wyatt, "Exterior finite elements for two dimensional field problems with open boundaries", Proc. IEE, Vol. 124, pp. 1267-1270 (1977).

20.	J. Penman, M. D. Grieve and A. F. Wilson, "On the solution of open boundary field problems using the finite element method", Proc. IEE, Vol. 133, pp. 596-600 (1986).

21.	H. Singer, H. Steinbigler and P. Weiss, "A charge simulation method for the calculation of high voltage fields", IEEE Trans. PAS, Vol. PAS-93, pp. 1660-1668 (1974).

22.	P. K. Mukerjee and C. K. Roy, "Computation of fields in and around insulators by fictitious point charges", IEEE Trans. Elect. Insul., Vol. EI-13, pp. 24-31 (1978).

23.	P. H. Alexander and H. M. Ismail, "Implementation of a charge simulation Computer-Aided Design package for high voltage systems", Third Canadian Universities Conference On CAD/CAM, July 2-3, 1987, Ottawa, Ontario, pp. 25-35

24.	H. M. Ismail and P. H. Alexander, "Application of a charge simulation based Computer-Aided Design package to a high voltage shielding system", Nineteenth North American Power Symposium, Edmonton, Oct. 22-23, 1987, pp. 445-453.

25.	M. D. R. Beasley, J. H. Pickles, G. d'Amico, L. Bretta, M. Fanelli, G. Giuseppetti, A. diMonaco, G. Gallet, J. P. Gregoire and M. Morin, "Comparative study of three methods for computing electric fields", Proc. IEE, Vol. 126, pp. 126-134 (1979).

26.	W. R. Smythe, "Static and dynamic electricity", McGraw-Hill, NewYork, (1968).

27.	R. G. Olsen, "Discussion of an optimized charge simulation method for the calculation of high voltage fields" by A. Yializis, E. Kuffel, and P. H. Alexander, IEEE Trans. PAS, Vol. PAS-97, pp. 2439-2440 (1978).

28.	J. H. Pickles, "Monte Carlo field calculations", Proc. IEE, Vol. 124, pp. 1271-1276 (1977).

29.	A. Nicolaide, "A method of distributed charges for solving problems of electromagnetic field in non-homogeneous media", IEEE Trans., PAS 1978 Winter meeting, paper F78,178-6.

30.	H. Steinbigler, "Combined application of finite element method and charge simulation method for the computation of electric fields", Third Int. Symp. on HV Engineering, Milan 28-31 Aug. 1979.

31.   H. Okubo, M. Ikeda and M. Honda, "Combination method for electric field calculations", Third Int. Symp. on HV Engineering, Milan 28-31 Aug. 1979.

32.   H. Parekh, K. D. Srivastava and R. G. Van Heswijk, "Electric field computations for rotationally symmetric electrodes", IEEE PAS, 1977 summer meeting, paper A 77 737-0.

33.   A. Yializis, E. Kuffel and P. H. Alexander, "An optimized charge simulation method for the calculation of high voltage fields", IEEE Trans. PAS, Vol. PAS-97, pp. 2434-2438 (1978).

34.   M. Akazaki and K. Mishijima, "Calculation of three-dimensional axisymmetric fields by charge simulation method", Elect. Eng. in Japan, Vol. 98, pp. 1-7 (1978).

35.   M. R. Iravani and M. R. Raghuveer, "Accurate field solution in the entire interelectrode space of a rod-plane gap using optimized charge simulation", IEEE Trans. Elec. Ins. Vol. EI-17 pp. 333-337 (1982).

36.   M. P. Sarma and W. Janischewskyj, "Electrostatic field of a system of parallel cylindrical conductors", IEEE Trans. PAS, Vol. PAS-88, pp. 1069-1079 (1969).

37.   M. S. Abou-Seada and E. Nasser, "Digital computer calculation of the potential and its gradient of a twin cylindrical conductor", IEEE Trans. PAS, Vol. PAS-88, pp. 1802-1814 (1969).

38.   M. S. Abou-Seada and E. Nasser, "Calculation of the potential gradient of twin-cylindrical bipolar conductors with various geometrical parameters", IEEE PAS winter power meeting pp. 1822-1829 (1971).

39.   H. Parekh, M. S. Selim and E. Nasser, "Computation of electrical field and potential around stranded conductor by analytical method and comparison with charge simulation method", Proc. IEE, Vol. 122, pp. 547-550 (1975).

40.   M. Khaled, "Computation of corona onset using the ring charge method", Proc. IEE, Vol. 122, pp. 107-110 (1975).

41.   T. Takuma, and T. Watanabe, "Optimum profiles of disc-type spacers for gas insulation", Proc. IEE, Vol. 122, pp. 183-188 (1975).

42.   T. Takuma, T. Kouno and H. Matsuda, "Field behaviour near singular points in composite dielectric arrangements", IEEE Trans. Elec. Ins. Vol. EI-13 pp. 426-435 (1978).

43.   T. Takuma, T. Kawamoto and H. Fujinami, "Charge simulation method with complex fictitious charges for calculating capacitive-resistive fields", IEEE Trans. PAS, Vol. PAS-100, pp. 4665-4672 (1981).

44.   T. Takuma, T. Kawamoto and H. Fujinami, "Effect of conduction on field behaviour near singular points in composite medium arrangements", IEEE Trans. Elec. Ins., Vol. EI-17, pp. 269-275 (1982).

45.   T. Takuma and T. Kawamoto, "Field intensification near various points of contact with a zero contact angle between a solid dielectric and an electrode", IEEE Trans. PAS, Vol. PAS-103, No.9, pp. 2486-2493 (1984).

46.   A. Nosseir and A. A. Zaky, "Electrical stresses in three-core cables", IEEE Trans. Elec. Ins. Vol. EI-12 pp. 262-266 (1977).

47.   T. Takashima and R. Ishibashi, "Electric fields in dielectric multi-layers calculated by digital computer", IEEE Trans. Elec. Ins. Vol. EI-13 pp. 37-44 (1978).

48.   T. Takashima and R. Ishibashi, "Expression of electric fields for systems of dielectric-coated cylindrical conductors", IEEE Trans. PAS, Vol. PAS-97, pp. 1847-1852 (1978).

49.   T. Sakakibara, S. Sato, N. Kobayashi and S. Menju, " The application of charge simulation method to three dimensional asymmetric field with two dielectric media", Second International Symposium on Gaseous Dielectrics, Oakridge National Lab., pp. 392-398 March 9-13, (1980).

50.   M. J. Khan and P. H. Alexander, "Charge simulation modelling of practical insulator geometries", IEEE Trans. on Elect. Insul., Vol. EI-17, pp. 325-332 (1982).

51.   A. A. Elmoursi and N. H. Malik, "Field uniformity of a high voltage test electrode system", IEEE Trans. Elec. Ins., Vol. EI-18, pp. 89-92 (1983).

52.   M. R. Iravani and M. R. Raghuveer, "Numerical computation of potential distribution along a transmission line insulator chain", IEEE Trans. Elec. Ins., Vol. EI-18, pp. 167-170 (1983).

53.   H. Anis and A. Mohsen, "Application of the charge simulation method to time-varying voltages", Fourth Int. Symp. on HV Engineering, Athens 5-9 Sept. 1983.

54.   A. S. Pillai, R. Hackam and P. H. Alexander, "Influence of radius of curvature, contact angle and material of solid insulator on the electric field in vacuum (and gaseous) gaps", IEEE Trans. Elec. Ins., Vol. EI-18, pp. 11-21 (1983).

55.   A. S. Pillai and R. Hackam, "Modification of electric field at the solid insulator-vacuum interface arising from surface charges on the solid insulator", J. Appl. Phys., Vol. 54, pp. 1302-1313 (1983).

56.   A. S. Pillai and R. Hackam, "Electric field and potential distributions for unequal spheres using symmetric and asymmetric applied voltages", IEEE Trans. Elec. Ins., Vol. EI-18, pp. 477-483 (1983).

57.   A. S. Pillai and R. Hackam, "Surface flashover of conical insulators in vacuum", J. Appl. Phys., Vol. 56, pp. 1374-1381 (1984).

58.   A. S. Pillai and R. Hackam, "Optimal electrode-solid insulator geometry with accumulated surface charges", IEEE Trans. Elec. Ins., Vol. EI-19, pp. 321-331 (1984).

59.   A. S. Pillai and R. Hackam, "Electric field distribution at solid insulator-vacuum interface of different electrode-insulator geometries", IEEE Trans. Elec. Ins., Vol. EI-19, pp. 502-510 (1984).

60.   A. S. Pillai and R. Hackam, "Improved performance of cylindrical solid insulators with concave curved edges in vacuum", IEEE Trans., Vol. PAS-103, pp. 2418-2427 (1984).

61.   M .M .A. Salama and R. Hackam, "Design of polymer enclosers for high voltage equipment", IEEE Trans. PAS, Vol. PAS-103, pp. 36-43 (1984).

62.   M. M. A. Salama, I. F. M. Hashad, K. D. Srivastava and R. Hackam, "Design of grading rings for air-core power reactors", IEEE Trans. PAS, Vol. PAS-103, pp. 3551-3559 (1984).

63.   M. J. Khan, Computation of electric fields in and around high voltage insulators, M.A. Sc. Thesis, University of Windsor, 1981.

64.   H. Anis, A. Zeitoun, M. El-Ragheb and M. El-Desouki, "Field calculations around non-standard electrodes using regression and their spherical equivalence", IEEE Trans. PAS, Vol. PAS-96, pp. 1721-1730 (1977).

65.   H. H. Rosenbrock, Compt. J., 3, (1960), pp. 175-184.

66.   R. Fletcher and M. J. D. Powell, Comput. J., 6(2), (1963), pp. 163.

67.   Y. L. Chow and C. Charalambous, "Static-field computations by the method of optimized images", Proc. IEE, Vol. 126, pp. 123-125 (1979).

68.   R. Fletcher, "A new approach to variable metric algorithms", The Computer Journal, Vol. 13, pp. 317-322 (1970).

69.   A. Mohsen and K. Abdel salam, "A fast simulation technique for calculating electric fields", IEEE PAS, Paper No. A-77-336-8, (1976).

70.   H. Singer, "Computation of optimized electrode geometries", Third Int. Symp. on HV Engineering, Milan 28-31 Aug. 1979.

71.   D. Metz, "Optimization of high voltage fields", Third Int. Symp. on HV Engineering, Milan 28-31 Aug. 1979.

72.   H. Okubo, T. Amemiya and M. Honda, "Borda's profile and electric field optimization by using charge simulation method", Third Int. Symp. on HV Engineering, Milan 28-31 Aug. 1979.

73.   F. M. H. Youssef, "An accurate fitting-oriented charge simulation method for electric field calculation", Third Int. Symp. on HV Engineering, Athens 5-9 Sept. 1983.

74.   T. Misaki, H. Tsuboi, K. Itaka and T. Hara, "Optimization of three-dimensional electrode contour based on surface charge method and its application to insulation design", IEEE Trans. PAS, Vol. PAS-102, pp. 1687-1692 (1983).

75.   S. Sato and W. S. Zaengl, "Effective 3-dimensional electric field calculation by surface charge simulation method", Proc. IEE, Vol. 133A, pp. 77-83 (1986).

76.   D. Hearn and M. P. Baker, "Computer Graphics", Prentice-hall, (1986).

77.   S. Yakovitz and F. Szidarovszky, "An introduction to numerical computations", Macmillan, (1986), pp. 50-51.

78.   S. Yakovitz and F. Szidarovszky, "An introduction to numerical computations", Macmillan, (1986), pp. 57-72.

79.   G. W. Carter and S. C. Loh, " The calculation of the electric field in a sphere-gap by means of dipolar co-ordinates", Proc. IEE, Vol. 106c, pp. 108-111 (1959).

80.   H. M. Ryan and C. A. Walley, "Field auxiliary factors for simple electrode geometries", Proc. IEE, Vol. 114(10), pp. 1529- 1536 (1967).

81.   A. Pedersen, "Calculation of spark-breakdown or corona- starting voltages in non-uniform fields", IEEE Trans. PAS, Vol. PAS- 86, pp. 200-206 (1967).

82.   M. A. Shallal and J. A. Harrison, "Electric field, potential and capacitance of a sphere-plane electrode system", Proc. IEE, Vol. 116, pp. 1115-1118 (1969).

83.   K. C. Kao and T. Harker, "The calculation of the electric field for an infinite dielectric plate between two spherical electrodes", Proc. IEE, Vol. 109(16), pp.293-298 (1962).

84.   J. D. Craggs and J. M. Meek, "High voltage laboratory technique", Butterworth, (1954).

85.   E. A. Cherney and D. J. Stonkus, "Non-ceramic insulators for contaminated invironments", IEEE Trans. PAS, Vol. PAS-100, pp. 131-142 (1981).

86.   C. T. Wu, T. C. Cheng, and A. Rodriguez, "A study on the use of internal grading to improve the performance of insulators", IEEE Trans. Elec. Ins. Vol. EI-16, pp. 250-257 (1981).

87.   H. M. Schneider, "The influence of voltage grading and insulation length on contamination performance", IEEE Trans. Elec. Ins. Vol. EI-16, pp. 258-262 (1981).

88.   E. A. Cherney, G. Karady, R. L. Brown, J. L. Nicholls, T. Orbeck and L. Pargamin, "Application of composite insulators to transmission lines", IEEE Trans. PAS, Vol. PAS-102, pp. 1226-1234 (1983).

89.   Y. Saito, T. Hino and M. Suzuki, "A dry tracking resistance test method using a trigger discharge", IEEE Trans. Elec. Ins., Vol. EI-3, pp. 18-23 (1968).